The application of inelastic neutron scattering in the investigation of iron-based Fischer-Tropsch catalysts

Alisha Louise Davidson

Submitted in fulfilment of the requirements for the Degree of Doctor of Philosophy

School of Chemistry
University of Glasgow
October 2019

Declaration

This thesis is submitted in part fulfilment of the requirement for the degree of Doctor of Philosophy at the University of Glasgow. This thesis represents the original work carried out by Alisha L. Davidson unless otherwise stated in the text.

The research described herein was carried out at the University of Glasgow in the Department of Chemistry under the supervision of Prof. David Lennon during the period of October 2015 - March 2019.

Alisha Davidson

Abstract

The main aim of this study was to expand on previous projects that have established the use of inelastic neutron scattering (INS) to investigate a range of iron-based Fischer-Tropsch catalysts applied to the hydrogenation of CO at elevated temperature. The project initially makes use of a standard reference hematite catalyst (α-Fe_2O_3) and analyses the temporal behaviour of the hydrocarbonaceous overlayer known to form on the catalyst for an extended period of time on stream (240 h). INS analysis was complemented by other techniques such as X-ray diffraction, Raman spectroscopy and temperature-programmed oxidation (TPO) measurements to establish the complete evolutionary profile of the standard hematite catalyst.

This methodology was also applied to a range of doubly promoted iron-based catalysts that have the potential to be Fischer-Tropsch to olefins (FTO) catalysts. FTO chemistry has gained significant interest over the past several years as it provides a means of supplying lower olefins (C_2-C_4) independently from crude oil. Five catalyst samples were tested over a range of sulfur concentrations (10 – 250 ppm) with a fixed concentration of sodium (2000 ppm). As well as the techniques utilised for the reference catalyst, XANES was applied to determine the form of the sulfur within the catalyst before and after exposure to CO hydrogenation conditions.

Of the five doubly promoted iron-based catalysts tested, one was selected to be analysed as a function of time on stream up to 24 h utilising INS and TPO to investigate how the rate of the hydrocarbonaceous overlayer formation was affected by the inclusion of promoters. Additionally, using the same catalyst, a preliminary measurement was carried out which involved the introduction of CO_2 into the reactant mixture. Once more, INS was utilised to determine how the addition of a CO_2 co-feed would affect the formation of the hydrocarbonaceous overlayer. From a combination of characterisation and reaction testing of the doubly promoted iron catalysts, a scheme is proposed to account for the addition of the promoters, sodium and sulfur, and the role in which these modifiers may play in the FTO process.

Acknowledgements

Many people have contributed to the completion of this Ph.D., whether in the form of personal or technical support, and I would like to thank the following for their contributions.

A special thanks goes to my supervisor, Prof David Lennon, for giving me the opportunity to work on this project and for his guidance and belief in me over the past several years. It has been a pleasure to work under his supervision.

Thanks to Stewart Parker for all his assistance at the ISIS Facility, sharing his insightful knowledge of neutron scattering and for his patience with me throughout all the technical glitches and issues with the beam going down (*which somehow correlated with my presence on site*).

Paul Webb is thanked for his insights and contributions to the project and for his company during beam time measurements at the ISIS Facility.

Thanks to Emma Gibson for her assistance in conducting and working-up of the XANES dataset, to Donald McLaren and Colin How for their assistance with the TEM measurements and to Hervé Ménard for conducting the XPS measurements.

Sasol Technology Ltd. are thanked for the funding of the studentship in particular Bob Tooze. Barbara Walker is also thanked for her incredible organisation when assisting with sample preparation.

A big thanks to all the members of the Lennon Group past and present! To James Campbell, Cédric Boulho, Mairi McAllister, Alastair Boyd and Annelouise McCullagh, for all the great times in and out of the lab! Also, thanks to Andrea Zachariou and Alex Hawkins, for providing me with company on my trips to ISIS and at neutron user meetings.

Finally, none of this would be possible without the love, help and support of all my family and friends, especially to my Mum, Dad, Granny, Gramps and to my brother and sister, Jordan and Shannon Davidson. The moral (and financial) support that everyone has provided me over all these years in education means so much to me and so I dedicate this book to you all.

Contents

Declaration ..... **i**

Abstract ..... **ii**

Acknowledgements ..... **iii**

List of Figures ..... **vii**

List of Tables ..... **xii**

List of Abbreviations ..... **xiii**

Preface ..... **xv**

Chapter 1 – Introduction **1**

1.1. The Fischer-Tropsch Process 1

1.2. Fischer-Tropsch Synthesis 2

1.2.1. Catalysts for Fischer-Tropsch Synthesis 3

1.3. Iron Fischer-Tropsch Chemistry 5

1.4. Role of Carbonaceous Deposits in Metal Catalysed Reactions 6

1.5. Fischer-Tropsch to Olefin Chemistry (FTO) 7

1.5.1. Promoters for FTO Chemistry 9

1.6. Analytical Techniques 12

1.6.1. Inelastic Neutron Scattering 12

1.6.2. Raman Scattering 20

1.6.3. Powder X-ray Diffraction 21

1.6.4. X-ray Absorption Spectroscopy 23

1.7. Project Overview 24

Chapter 2 – Experimental **26**

2.1. Catalyst Preparation 26

2.2. Reaction Testing 27

2.2.1. Micro-reactor Testing 27

2.2.2. Large-scale Reaction Testing 29

2.3. Catalyst Characterisation 32

2.3.1. Pre-reaction Catalyst Testing 32

2.3.2. Post-reaction Micro-reactor 33

2.3.3. Post-reaction Large-scale Reactor 36

Chapter 3 – CO hydrogenation at 623 K: temporal behaviour of the hydrocarbonaceous overlayer on a reference hematite catalyst over an extended period of time-on-stream 38

3.1. Introduction 38

3.2. Characterisation of Catalyst As-prepared 40

3.3. Large-scale Reaction Testing 46

3.3.1. Inelastic Neutron Scattering 49

3.3.2. *Ex situ* Characterisation of the Large-scale Reactor 57

3.4. Micro-reactor Reaction Testing 68

3.4.1. *In situ* Temperature-programmed Oxidation 71

3.5. Discussion 75

3.6. Conclusions 78

Chapter 4 – CO hydrogenation at 623 K: the effect of S concentration on doubly promoted hematite catalyst on the formation of a hydrocarbonaceous overlayer 79

4.1. Introduction 79

4.2. Catalyst Characterisation 82

4.3. Micro-reactor Study 90

4.3.1. *In situ* Temperature-programmed Oxidation 92

4.3.2. *Ex situ* Characterisation 96

4.4. Large-scale Study 104

4.4.1. Large-scale Reactor Testing 104

4.4.2. Inelastic Neutron Scattering 106

4.5. Discussion and Conclusions 119

Chapter 5 – CO hydrogenation at 623 K: investigation of the temporal behaviour of the hydrocarbonaceous overlayer of a prototype FTO catalyst 122

5.1. Introduction 122

5.2. CO hydrogenation at 623 K of a doubly promoted iron catalyst as a function of time on stream 124

5.2.1. Micro-reactor Measurements 124

5.2.2. Large-scale Measurements 128

5.3. CO hydrogenation at 623 K with a CO_2 co-feed of a doubly promoted iron catalyst as a function of time on stream 136

5.3.1. Reaction Testing 136

5.3.2. Inelastic Neutron Scattering 139

5.4. Proposed FTO Model 146

5.5. Conclusions 148

Chapter 6 – Concluding Remarks **150**

Chapter 7 – Future Work **152**

Appendices **153**

Weight Hourly Space Velocity (WHSV) Calculation 153

Iron Time Yield (FTY) Calculation 154

Additional Figures 155

References **157**

List of Figures

Figure 1: Number of patents and articles in relation to the Fischer-Tropsch process published per year vs. US crude oil price($).[2] 2
Figure 2: Proposed model of the hydrocarbonaceous overlayer on a palladium surface by Borodziński *et al*.[43] 7
Figure 3: Various processes available for the production of lower olefins (C_2-C_4) from syngas.[48] 8
Figure 4: The variations of catalytic activity with sulfide content tested under FTS conditions (523 K, 8 bar, 192 h).[64] 10
Figure 5: Percentage of olefinicity of unsulfided and sulfided catalysts as a function of carbon number.[64] 10
Figure 6: Product selectivity (purple – oxygenates, yellow – C_{5+} hydrocarbons, pink – C_2-C_4 olefins, blue – C_2-C_4 paraffins, grey – methane) of a range of iron-based catalyst promoted with varying concentrations of potassium and sulfur.[45] 12
Figure 7: A schematic of the ISIS Facility, which includes the synchrotron, target stations and instruments.[72] 14
Figure 8: A schematic of the MAPS direct geometry spectrometer at the ISIS Facility with the key features highlighted.[69] 15
Figure 9: INS spectra of propyne highlighting resolution differences between a direct geometry spectrometer (MAPS), at different incident energies, and an indirect geometry spectrometer (TOSCA). (a) Measured on TOSCA (black) (b) MAPS, E_i = 60 meV (red) (c) MAPS, E_i = 250 meV (blue), and (d) MAPS, E_i = 600 meV (green). [69] 16
Figure 10: INS spectra recorded at 20 K using TOSCA of (a) methanol (b) background subtracted spectrum of a saturated chemisorbed overlayer of methoxy on η-alumina (1.12 mmol CH_3OH g^{-1}) prepared at 300 K and (c) $Al(OCH_3)_3$.[77] 18
Figure 11: Comparison of the INS spectra (TOSCA) of an industrial Pd catalyst. (a) The deactivated catalyst taken directly from the hydrogenation process and sealed under argon, (b) sample (a) after solvent extraction, (c) same sample as (a) and (b) after in situ hydrogenation up to 1.5 bar of hydrogen equilibrium pressure, and (d) a long-term used, but active catalyst after solvent extraction under the same conditions as the deactivated sample. 19
Figure 12: An example XAFS spectrum for the Fe K edge of FeO indicating the XANES and EXAFS regions. [93] 23
Figure 13: A schematic line drawing diagram of the gas handling apparatus used for the micro-reactor measurements. Abbreviations include MFC – mass flow controller, IR – infrared spectrometer and MS – mass spectrometer. 28
Figure 14: A schematic line drawing diagram of the gas handling apparatus used for the large-scale reaction measurements. Mass flow controllers are indicated by rectangular boxes containing the maximum flow rate (sccm). Other abbreviations include MV – mixing volume, P – pressure gauge, PRV – pressure relief valve, BPR – back pressure relief valve and MS – mass spectrometer. The dotted lines around the schematic show what is encased within the walk in fume hood. [66] 31
Figure 15: Linear plot ($\boldsymbol{y = 0.01101x}$) of the integrated area of the CO_2 trace of the known weights of graphite exposed to TPO conditions against the mass of the graphite calibration material used. The R^2 value is 0.99749. 35
Figure 16: (a) The baseline corrected INS spectra of the varying masses of polystyrene recorded on the MAPS spectrometer at incident energy 650 meV. The spectra were obtained using the 'A' chopper package. (b) Linear plot ($\boldsymbol{y = 8 \times 10 - 19x}$) of the integrated areas of each of the

polystyrene features ν (C-H) present in (a) against the number of hydrogen atoms present in each mass of polystyrene used. The R^2 value is 0.99896. 37
Figure 17: The powder XRD (Co K_α) of the hematite reference catalyst sample (Fe-ref) as-prepared. The red lines are indicative of reflections corresponding to α-Fe_2O_3 reference diffractogram from the programme Highscore Plus.[106] 41
Figure 18: The *in situ* temperature-programmed reduction profile (with hydrogen) of the hematite reference catalyst (Fe-ref). 42
Figure 19: The Raman spectra of (a) the reference catalyst sample (Fe-ref) and (b) a pure hematite sample. 44
Figure 20: The Raman spectra of (a) maghemite (γ-Fe_2O_3) and (b) magnetite (Fe_3O_4) samples. 44
Figure 21: The transmission electron micrograph of the unpromoted α-Fe_2O_3 sample before exposure to CO hydrogenation conditions. The scale bar is indicative of 50 μm 45
Figure 22: High-resolution transmission electron micrograph of the unpromoted α-Fe_2O_3 sample before exposure to CO hydrogenation conditions. The white scale bar is indicative of 5 nm. 45
Figure 23: Mass spectrometer reaction profile for a large-scale reactor of a CO hydrogenation reaction over the reference hematite catalyst (Fe –ref) at 623 K, ambient pressure, for 96 h. The mass traces are labelled on the right hand side. 48
Figure 24: INS spectra (recorded at 650 meV) of the unpromoted α-Fe_2O_3 after CO hydrogenation at 623 K in the large-scale reactor. Spectrum for 3 h on stream obtained by Warringham.[73] 52
Figure 25: INS spectra (recorded at 250 meV) of the unpromoted α-Fe_2O_3 sample after CO hydrogenation at 623 K in the large-scale reactor over a 240 h period. Spectrum for 3 h on stream obtained by Warringhmam.[73] The asterisks highlights the spinon feature. 53
Figure 26: INS spectrum of the Fe-ref sample after exposure to CO hydrogenation conditions at 623 K for 240 h on the large-scale reactor with Gaussian peak fittings (OriginPro 2018) indicating the sp^3 (2932 cm^{-1}) and sp^2 (3048 cm^{-1}) hybridised carbon features. 55
Figure 27: The quantified hydrogen content (μmol g^{-1}_{Fe}) of the features identified in Figure 24: aliphatic, sp^3 hybridised carbon feature at 2932 cm^{-1} (triangles) and aromatic, sp^2 hybridised carbon feature at 3048 cm^{-1} (circles). Data for 3-24 h obtained from Warringham.[73] 56
Figure 28: The *ex situ* X-ray diffractogram (Co K_α) of the unpromoted α-Fe_2O_3 after exposure to CO hydrogenation conditions at 623 K in the large-scale reactor for 48, 96 and 240 h. 59
Figure 29: *Ex situ* Raman spectra of unpromoted α-Fe_2O_3 after exposure to CO hydrogenation conditions at 623 K, ambient pressure on the large-scale reactor for 48, 96 and 240 h on stream. The D and G bands are defined with respect to Table 1. The spectrum was fitted by Guassian line shapes using OriginPro 2018. 61
Figure 30: HRTEM of Fe-ref after exposure to CO hydrogenation conditions at 623 K for 240 h on the large-scale reactor. The d-spacing marked by A is 0.205 nm which is indicative of monocyclic Fe_5C_2. The scale bar is indicative of 5 nm. 62
Figure 31: *Ex situ* temperature-programmed oxidation profiles of unpromoted α-Fe_2O_3 (10 mg) taken from the large-scale reactor after exposure to CO hydrogenation conditions at 623 K, ambient pressure for 48, 96 and 240 h on stream. 65
Figure 32: *Ex situ* temperature-programmed oxidation profiles, displaying oxygen consumption of the catalyst samples using (a) 40 and (b) 10 mg catalyst, after exposure to ambient pressure CO hydrogenation reaction conditions at 623 K for 48 h. The black line is indicative of the measured CO_2 and the red line indicative of O_2 consumption. 66
Figure 33: A comparison of the carbon content (mmol g^{-1}_{Fe}) obtained for the reactive carbonaceous material (α), amorphous carbon (β) and bulk iron carbide (γ) components observed from *ex situ* temperature-programmed oxidation profiles of the samples taken from the large-scale reactor after exposure to CO hydrogenation conditions up to 240 h on stream. Data plotted from 3-24 h obtained from Warringham's PhD thesis[73] and included for comparative purposes. 67

Figure 34: Micro-reactor reaction profile of the upromoted catalysts (10 mg) during a CO hydrogenation reaction, ambient pressure, 623 K for 96 h. 70
Figure 35: *In situ* temperature-programmed oxidation profiles of the unpromoted α-Fe_2O_3 sample with (a) 10 mg (b) 20 mg and (c) 40 mg of catalyst after exposure to CO hydrogenation conditions on the micro-reactor for 48 h. The black line is indicative of the measured CO_2 and the red line indicative of O_2 consumption. 73
Figure 36: *In situ* temperature-programmed oxidation profile of the unpromoted α-Fe_2O_3 sample with 10 mg of catalyst after exposure to CO hydrogenation conditions on the micro-reactor for 96 h. The black line is indicative of the measured CO_2 and the red line indicative of O_2 consumption. 74
Figure 37: A schematic of the composition of the iron FTS catalyst after exposure to ambient pressure CO hydrogenation conditions at 623 K for *ca*. 6h. The hydrocarbonaceous overlayer (purple) is suggested to mediate the transfer of hydrogen, where the final product output is dependent on the supply of hydrogen within the system.[94] 77
Figure 38: Blyholder model of the molecular orbital bonding of CO to a metal site. 80
Figure 39: A comparison of the powder X-ray diffractogram (Cu K_α) of the hematite reference catalyst sample (Fe-ref) as-prepared against the five samples promoted with varying levels of sulfur (10-250 ppm) and a fixed level of sodium (2000 ppm). The red lines are indicative of reflections corresponding to α-Fe_2O_3 reference diffractogram from the programme Highscore Plus.[106] 86
Figure 40: The *in situ* temperature-programmed reduction profile (with hydrogen) of the hematite reference catalyst (Fe-ref) alongside the five samples doubly promoted with varying levels of sulfur and a fixed level of sodium. The dashed lines are indicative of the features of the Fe-ref profile, highlighting the shift to higher temperatures of the promoted samples. 87
Figure 41: Top image is a scanning electron micrograph of catalyst Fe-Na-S_{250} as-prepared. The bottom image is the EDX analysis of the catalyst sample from the image above, detecting the presence of Fe, O, C, Na, and S. 88
Figure 42: Data obtained from analysis using X-ray photoelectron spectroscopy. The top figure displays the ratio of Na:S across all doubly promoted samples and of Fe-ref. The bottom figure displays the atomic percentage of sulfur across all promoted samples and Fe-ref. 89
Figure 43: Micro-reactor reaction profiles with a doubly promoted catalysts, a) 10 ppm & b) 250 ppm of S and a fixed level of Na (*ca*. 2000 ppm) during a CO hydrogenation reaction at ambient pressure and 623 K for 6 h. 91
Figure 44: *In situ* temperature-programmed oxidation profiles of a doubly promoted α-Fe_2O_3 sample (Fe-Na-S_{10}) using (a) 20 mg (b) 30 mg and (c) 40 mg of catalyst after exposure to CO hydrogenation conditions on the micro-reactor for 6 h. The black line is indicative of the measured CO_2 and the red line indicative of O_2 consumption. 94
Figure 45: *In situ* temperature-programmed oxidation profiles of the doubly promoted α-Fe_2O_3 (40 mg) after exposure to CO hydrogenation conditions at 623 K, ambient pressure for 6 h on stream on the micro-reactor. Profiles are offset for clarity. 95
Figure 46: *Ex situ* X-ray diffractograms (Co K_α) of the doubly promoted α-Fe_2O_3 samples and Fe-ref, after exposure to CO hydrogenation conditions at 623 K in a micro-reactor set-up for 6 h. 97
Figure 47: The sulfur K-edge XANES spectra of the reference materials ($FeSO_4$, Na_2SO_3, S, $Na_2S_2O_3$, FeS_2) indicative of sulfur present in various oxidation states. 101
Figure 48: The sulfur K-edge of each of the doubly promoted samples before exposure to reaction conditions. (a) Displays samples Fe-Na-S_{50-250} (b) Displays sample Fe-Na-S_{10} on a reduced scale. 102
Figure 49: The sulfur K-edge of each of the doubly promoted samples after exposure to CO hydrogenation reaction conditions. (a) Displays samples Fe-Na-S_{50-175} (b) Displays sample Fe-Na-S_{10} on a reduced scale. 103

Figure 50: Mass spectrometer reaction profile for the large-scale reactor of a CO hydrogenation reaction over a doubly promoted hematite catalyst (Fe-Na-S_{100}) at 623 K, ambient pressure, for 8 h. 105
Figure 51: INS spectra (recorded at 650 meV) of α-Fe_2O_3 doubly promoted with a fixed level of sodium (2000 ppm) and varying sulfur concentrations (10 – 250 ppm) after CO hydrogenation at 623 K for 8 h in the large-scale reactor.....109
Figure 52: INS spectrum of the Fe-Na-S_{250} sample after exposure to CO hydrogenation conditions at 623 K for 8 h on the large-scale reactor with Gaussian peak fittings (OriginPro 2018) indicating the sp^3 and sp^2 hybridised carbon features.....110
Figure 53: The quantified hydrogen content (μmol g^{-1}_{Fe}) of the features identified in Figure 51: aliphatic, sp^3 hybridised carbon feature at 2932 cm^{-1} (triangles) and aromatic, sp^2 hybridised carbon feature at 3948 cm^{-1} (circles), after exposure to CO hydrogenation conditions at 623 K for 8 h. Data obtained from Warringham[73] for Fe-ref, exposed to the same reaction conditions for 6 h, has been included for comparative purposes between promoted and unpromoted samples.....111
Figure 54: INS spectra (recorded at 250 meV) of α-Fe_2O_3 doubly promoted with a fixed level of sodium and varying sulfur concentrations after CO hydrogenation at 623 K for 8 h in the large-scale reactor. Spectra are offset for clarity.....112
Figure 55: INS spectra (recorded at 650 meV) for (a) the original and (b) repeat measurements of α-Fe_2O_3 doubly promoted with a fixed level of sodium and 250 ppm of sulfur (Fe-Na-S_{250}) after CO hydrogenation at 623 K for 8 h in the large scale reactor. The repeat sample was also exposed to a dehydration step only (c). Spectra have been offset for clarity.....115
Figure 56: INS spectra (recorded at 250 meV) for (a) the original and (b) repeat measurements of α-Fe_2O_3 doubly promoted with a fixed level of sodium and 250 ppm of sulfur (Fe-Na-S_{250}) after CO hydrogenation at 623 K for 8 h in the large scale reactor. The repeat sample was also exposed to a dehydration step only (c). Spectra have been offset for clarity. (d) displays spectra (b) on a smaller y axis range to define peaks present.....116
Figure 57: The momentum transfer dependence (MAPS) of the features present at; 797 cm^{-1} of Fe-Na-S_{250} unreacted (red circles), 941 cm^{-1} of the Fe-Na-S_{250} sample, shown in Figure 56, of the initial (black squares) and repeat (green triangles) measurements. The ν(C-H) stretching region of Fe-Na-S_{250} (blue diamond) is shown for comparison purposes. 118
Figure 58: Mass spectrometer reaction profile in the micro-reactor of a CO hydrogenation reaction over a doubly promoted hematite catalyst (Fe-Na-S_{100}) at 623 K, ambient pressure, for 24 h. 125
Figure 59: The *in situ* temperature-programmed oxidation profiles (40 mg) of a hematite catalyst doubly promoted with sulfur and sodium (Fe-Na-S_{100}) after exposure to ambient pressure CO hydrogenation conditions at 623 K for 0-24 h. 127
Figure 60: A schematic of the potential pathway of the α species observed in the TPO profiles...129
Figure 61: INS spectra (recorded at 650 meV) of a doubly promoted α-Fe_2O_3 (Fe-Na-S_{100}) after ambient pressure CO hydrogenation at 623 K in the large-scale reactor for varying time scales (0 – 24 h). 131
Figure 62: The quantified hydrogen content of the features identified in Figure 61: aliphatic, sp^3 hybridised carbon feature at 2932 cm^{-1} (hollow circles) and aromatic, sp^2 hybridised carbon feature at 3948 cm^{-1} (solid circles) of Fe-Na-S_{100}. 132
Figure 63: A comparison of the quantified hydrogen content (μmol H g^{-1}_{Fe}) of the sp^2 (solid) and sp^3 (hollow) ν(C-H) features from the INS spectra of Fe-Na-S_{100} (circles) and Fe-ref (triangles). 133
Figure 64: INS spectra (recorded at 250 meV) of a doubly promoted α-Fe_2O_3 sample (Fe-Na-S_{100}) after ambient pressure CO hydrogenation at 623 K in the large-scale reactor over a 24 h period. 135
Figure 65: Mass spectrometer reaction profile for large-scale reactor of a CO hydrogenation reaction with a CO_2 co-feed over a doubly promoted hematite catalyst (Fe-Na-S_{100}) at 623 K, ambient pressure, for 12 h.....138

Figure 66: INS spectra (recorded at 650 meV) of the doubly promoted α-Fe_2O_3 (Fe-Na-S_{100}) after ambient pressure CO hydrogenation, with a CO_2 co-feed at 623 K in the large-scale reactor over 24 h period. (b) Enlarged INS spectra from (a) of samples exposed to ambient pressure CO hydrogenation conditions at 623 K between 3 and 12 h. 143
Figure 67: The quantified hydrogen content of the features identified in Figure 66: sp^3 hybridised carbon at 2932 cm^{-1} (hollow circles) and sp^2 hybridised carbon at 3948 cm^{-1} (solid circles) of Fe-Na-S_{100} after exposure to ambient pressure CO hydrogenation conditions at 623 K with the inclusion of a CO_2 co-feed. 144
Figure 68: INS spectra (recorded at 250 meV) of the doubly promoted α-Fe_2O_3 sample (Fe-Na-S_{100}) after exposure to ambient pressure CO hydrogenation at 623 K, with a CO_2 co-feed, in the large-scale reactor over a 24 h period. 145
Figure 69: Adapted model from Warringham *et al*[94] to account for the addition of sulfur and sodium as promoters and their role in FTO chemistry, $t_2 > t_1$. 147
Figure 70(a) The baseline corrected INS spectra of the varying masses of polystyrene recorded on the MAPS spectrometer after the spectrometer upgrade at incident energy 650 meV. The spectra were obtained using the 'A' chopper package. (b) Linear plot ($\boldsymbol{y = 2 \times 10 - 16x}$) of the integrated areas of each of the polystyrene features ν (C-H) present in (a) against the number of hydrogen atoms present in each mass of polystyrene used. The R^2 value is 0.99888. 155
Figure 71: INS spectra (recorded at 650 meV) of the doubly promoted α-Fe_2O_3 after CO hydrogenation, with a CO_2 co-feed at 623 K in the large scale reactor over 3 h period. Peak fitting of the sp^3 and sp^2 hybridised carbon features is shown. 156

List of Tables

Table 1: D and G bands of carbonaceous material observed in Raman spectroscopy. Information reproduced from references. [81,83] 20
Table 2: Diffractometer target materials and Kα radiation values relevant to this project. 21
Table 3: A list of catalysts used within this investigation and their associated chapters within the thesis. 25
Table 4: Tabulated data of surface area and pore volume obtained from BET, particle size (nm) obtained from application of Scherrer equation to XRD diffractogram and mol % of iron from ICP-OES. Parentheses represent standard deviation from triplicate measurements. 40
Table 5: A comparison of the bands observed for Fe-ref and of hematite in comparison to that reported within the literature.[113–116] 43
Table 6: Bands observed in the INS spectra of the Fe-ref sample before and after exposure to CO hydrogenation conditions on the large-scale reactor (Figures 24 and 25) with vibrational assignments. 51
Table 7: Elemental analysis of before and after exposure to CO hydrogenation conditions for 48, 96 and 240 h on stream. The standard deviation from measurements performed in duplicate is shown in brackets. 57
Table 8: A comparison between the quantified carbon (mmol C g^{-1}_{Fe}) obtained from this current study (10 mg catalyst) and that by Warringham[94] (40 mg catalyst) from an *in situ* temperature-programmed oxidation measurement after catalyst exposure to CO hydrogenation conditions for 24 h on stream on the micro-reactor. Carbon content is normalised (g^{-1}_{Fe}) to allow for direct comparison. 71
Table 9: Summary of ICP-OES and BET analysis of Fe-ref (Chapter 3) and of the doubly promoted catalysts utilised within this chapter. BET measurements were performed in triplicate therefore, standard deviation for surface area (m^2g^{-1}) and pore volume (cm g^{-1}) are provided in brackets. Bracketed ICP values are measured values reported by Butterworth Laboratory but below official detection limits and are provided to indicate the varying sulfur concentrations across the samples. 83
Table 10: Tabulated XANES data for reference materials ($FeSO_4$, Na_2SO_3, S, $Na_2S_2O_3$, FeS_2) detailing peak positions and formal oxidation state of sulfur within the compound. 98
Table 11: Tabulated XANES data and assignments of features observed in Figure 49 of the doubly promoted samples after exposure to CO hydrogenation conditions at 623 K for 6 h on the micro-reactor set-up. 100
Table 12: The quantified peak values (μmol H g^{-1}_{Fe}) for the ν(C-H) stretch features observed by inelastic neutron scattering spectra after CO hydrogenation conditions at 623 K for 8 h in the large-scale reactor. 107
Table 13: Comparison of hydrogen concentration (μmol H g^{-1}_{Fe}) of the aliphatic (2932 cm^{-1}) and aromatic (3048 cm^{-1}) features from INS spectra across different catalysts and reaction conditions employed. Numbers marked with (*) are indicative of values obtained by Warringham.[94] 140
Table 14: Bands observed in the INS spectra of the Fe-Na-S_{100} sample after exposure to CO hydrogenation conditions with the inclusion of a CO_2 co-feed, on the large-scale reactor (Figures 66 and 68) with vibrational assignments. 142

List of Abbreviations

DMTO – Dimethyl Ether to Olefins

FT – Fischer-Tropsch

FTO – Fischer-Tropsch to Olefins

FTS – Fischer-Tropsch Synthesis

FTY – Iron Time Yield

HTFT – High Temperature Fischer-Tropsch

LTFT – Low Temperature Fischer-Tropsch

MFC – Mass Flow Controller

MTO – Methanol to Olefins

O.D. – Outer Diameter

RWGS – Reverse Water Gas Shift

Syngas – Synthesis gas

T-o-S – Time on Stream

WGS – Water Gas Shift

WHSV – Weight Hourly Space Velocity

Analytical Technique Abbreviations:

BET – Brunauer-Emmett-Teller

EDX – Energy Dispersive X-ray

EXAFS – Extended X-ray Absorption Fine Spectroscopy

HREELS – High Resolution Electron Energy Loss Spectroscopy

HRTEM – High Resolution Transmission Electron Microscopy

ICP OES – Inductively Coupled Plasma Optical Emission Spectroscopy

INS – Inelastic Neutron Scattering

IR – Infrared Spectroscopy

MS – Mass Spectrometer

NMR – Nuclear Magnetic Resonance

SEM – Scanning Electron Microscopy

TEM – Transmission Electron Microscopy

TPO – Temperature-Programmed Oxidation

TPR – Temperature-Programmed Reduction

XANES – X-ray Absorption Near Edge Spectroscopy

XAS – X-ray Absorption Spectroscopy

XPS – X-ray Photoelectron Spectroscopy

XRD – X-ray Diffraction

Unit abbreviations:

in. - Inch

sccm – Standard Cubic Centimetres per Minute

cm^{-1} – Wavenumber

μm - Micrometres

nm – Nanometres

h – Hours

s – Second

K – Kelvin

°C – Degrees Celsius

ppm – Parts Per Million

a.u. – Arbitry units

eV– Electron Volts

meV – Milli Electron Volts

g^{-1}_{Fe} – Per Gram of Iron

mmol – Millimoles

mol - Moles

Preface

The completion of work undertaken throughout the duration of this project (*October 2015 –March 2019*) is not without its adversities. This project was partly sponsored by Sasol Technology UK and EPSRC. Unfortunately, around June 2017, Sasol Technology UK closed. A close relationship with the industrial partners involved with the project remained however, access to facilities such as XPS, XRD and ICP, were no longer viable. A core aspect of this project utilised inelastic neutron scattering on the MAPS spectrometer at the ISIS Facility. This specific spectrometer was unavailable for a significant proportion of this project (*October 2016 – March 2018*) due to an unexpected fault and repair of the spectrometer occurring as well as the planned upgrade of the instrument.[1] These obstacles created significant challenges throughout the project and are addressed in the relevant aspects of this thesis.

Chapter 1 – Introduction

1.1. The Fischer-Tropsch Process

The Fischer-Tropsch (FT) process is a well-established industrial catalytic reaction involving the conversion of synthesis gas (syngas), a mixture of carbon monoxide (CO) and hydrogen (H_2), into a wide range of hydrocarbon products, including olefins, paraffins and oxygenates.[2] Sabatier, in 1902, was first to publish regarding the conversion of syngas to methane over nickel and cobalt catalysts.[3] In the 1920s Franz Fischer and Hans Tropsch further developed this concept to demonstrate that syngas could be converted into a mixture of higher liquid hydrocarbons, termed "*synthol*", which could be utilised for fuel.[2,4–6] Following from this development, the Fischer-Tropsch process grew rapidly, with the first plant commercialised the following decade in Oberhausen Germany and by 1938, nine plants were in operation with a combined capacity of approximately 660 x 10^3 t per year.[2,5,7] Over the past several decades both academic and industrial interest in the Fischer-Tropsch (FT) process has fluctuated with respect to crude oil prices (**Figure 1**), as it is estimated that the feasibility of FT technology occurs when the price of oil is above approximately $20 per barrel.[8] Nevertheless, in recent years a renewed interest in FT technology has occurred due to several different factors. This includes various environmental and political factors but, crucially, due to limitations of light oil reserves that have led to an increased use in lower quality heavy oils and shale oils, which are highly aromatic and contain a number of heteroatoms and metals.[8] This, alongside the ability to obtain value from coal, natural gas and biomass, has allowed the resurgence of Fischer-Tropsch that is considered as a viable alternative for synthetic fuel production.[2,9]

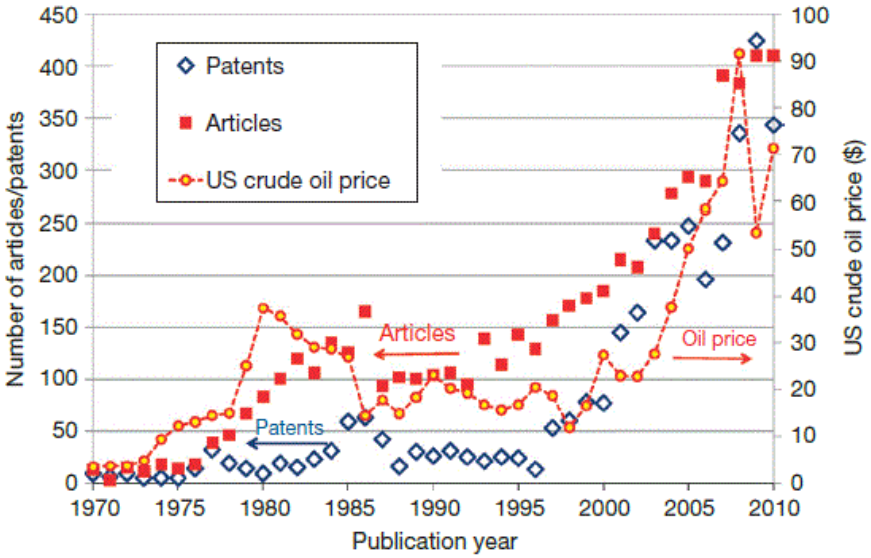

Figure 1: Number of patents and articles in relation to the Fischer-Tropsch process published per year vs. US crude oil price($).[2]

1.2. Fischer-Tropsch Synthesis

Fischer-Tropsch synthesis (FTS) can be defined as an exothermic polymerisation reaction involving the dissociation of dihydrogen and carbon monoxide, on a metal catalyst surface followed by the propagation of CH_x units. *Equation 1.1.* presents the simplified reaction equation of the FTS process, alongside its enthalpy, indicating polymerisation which would lead to a range of hydrocarbon products of various weights and chain lengths.[2]

$$CO + 2H_2 \rightarrow (-CH_2-) + H_2O \qquad \Delta H = -165\ \text{kJ mol}^{-1} \qquad \textbf{(1.1)}$$

Control of the product distribution for FTS is highly dependent on both the reaction conditions and the catalyst used for the process.[2,7,10] Currently there are two operational regimes for FTS – high temperature Fischer-Tropsch (HTFT) and low temperature Fischer-Tropsch (LTFT). HTFT utilises iron-based catalysts and operates in the region of 573 – 623 K. Product distribution for this regime is typically only in the gas phase and consists of low molecular weight olefins and gasoline. On the other hand, LTFT operates between 473 – 513 K and is used for the production of higher molecular weight waxes using primarily cobalt-based catalysts, however, iron-based catalysts also possess the capability for LTFT.[6,7]

The main by-products of FTS are water (H_2O) and/or carbon dioxide (CO_2), which are controlled by the water-gas shift (WGS) reaction (*Equation 1.2.*).[2] This reaction is more

prominent in iron FTS chemistry than cobalt-based systems and can be a means of providing additional hydrogen in syngas consisting of low H_2:CO, which is typically sourced from coal. On the other hand, syngas derived from natural gas will provide a hydrogen-rich supply.[9,11,12] It is essential to have control of the water concentration within the system as it can cause re-oxidation of the catalyst resulting in deactivation.[2,11,13,14]

$$CO + H_2O \rightleftharpoons CO_2 + H_2 \qquad \Delta H = -42 \text{ kJ mol}^{-1} \tag{1.2}$$

Several other undesirable side reactions can occur in the process, such as the formation of methane (CH_4) (*Equation 1.3.*), small amounts of alcohols (*Equation 1.4.*) and the formation of undesired carbon via the Boudouard reaction (*Equation 1.5.*).[14,15] The Boudouard reaction is one of the main mechanisms for carbon deposition (coking) which occurs on the catalyst surface and can eventually lead to deactivation by the formation of inactive carbon, reducing catalytic activity.[16]

$$CO + 3H_2 \rightarrow CH_4 + H_2O \tag{1.3}$$

$$nCO + 2nH_2 \rightarrow C_nH_{2n+2}O + (n-1)H_2O \tag{1.4}$$

$$2CO \rightarrow C_{(ad)} + CO_2 \tag{1.5}$$

1.2.1. Catalysts for Fischer-Tropsch Synthesis

The key components required of a catalyst to have suitable Fischer-Tropsch activity are to be able to have a high capacity of H_2 adsorption plus the ability to dissociatively adsorb CO. Several metal-based catalysts are known to catalyse the Fischer-Tropsch reaction, typically iron, cobalt, ruthenium, nickel and osmium, with rhenium and rhodium also known to exhibit FT activity. However, only iron, cobalt, ruthenium and nickel possess sufficient activity for potential application on a commercial scale.[7,15,17] The catalyst employed is predominantly dependent on the desired product output of the reaction.

Nickel based catalysts are not utilised industrially for Fischer-Tropsch processes for several reasons. Firstly, they are well known as powerful hydrogenation catalysts and therefore produce large quantities of undesirable methane at high temperatures. Moreover, at elevated pressures they are known to produce highly toxic, nickel carbonyl compounds, which over time results in a loss of the active component of the catalyst.[7,9,12,15,17]

Ruthenium on the other hand is the most active and stable FT catalyst which is operational at low reaction temperatures (~150°C) and has an enhanced selectivity towards longer chain waxy hydrocarbons.[17,18] This product distribution is predominantly paraffinic, with a limited production of oxygenates. However, at high temperatures selectivity switches to methane. Despite the many advantages of ruthenium as an FT catalyst, it is currently not a commercially viable option due to its limited availability resulting in a substantially higher price in comparison to that of iron and cobalt metal. [9,12,19]

Of the above mentioned metals potentially viable for commercial application, currently only iron and cobalt based catalysts are used.[12,16] Cobalt-based catalysts have been in operation from commercialisation of the first FT process back in the 1930s and today are commonly used for the production of long chain paraffins.[2,9] As with the likes of nickel and ruthenium catalysts, cobalt can produce excess methane at higher reaction temperatures, therefore is typically only used in LTFT.[9] Cobalt is also a relatively expensive metal and thus is commonly dispersed on a high surface area support such as Al_2O_3 or SiO_2, maximising the available surface area of the metal. Additionally, small amounts of noble metals, *i.e.* Pt or Ru, can be added to the catalyst to enhance the reduction process.[7,12,17]

Iron is the most abundant, and consequently the cheapest, of all of the active FT metals.[7] Its hydrogenation ability is much less than that of other active FT metals and therefore generally has a higher selectivity towards the production of olefinic and oxygenate products over long chain paraffins in comparison to cobalt based systems.[2,15] As mentioned above, iron has the ability to catalyse the WGS reaction and unlike that of cobalt, has access to a wider product distribution as it can be operational in both LTFT and HTFT. However, iron-based systems are more susceptible to deactivation than cobalt systems.[12,20,21] Despite this, significant interest in iron-based systems remains, particularly due to its high abundance, economic viability and ability to produce lower olefins, the latter which could be a sustainable method of producing chemical feedstock in the future.

1.3. Iron Fischer-Tropsch Chemistry

Iron-based FTS catalysts go through an activation or 'induction' period before they can be utilised for an FTS reaction. The activation period typically involves exposing the catalyst precursor to hydrogen, carbon monoxide or syngas during which the catalyst goes through an evolution towards its active phase.[22] The resulting transformation of the catalyst will lead to various different species co-existing, with the composition of each species dependent on the conditions used and promoters that may be contained within the catalyst.[2,13,23–25] Generally, the species present will be a combination of metallic iron (α-Fe), iron oxides (hematite,α-Fe_2O_3; magnetite, Fe_3O_4), iron carbides (Fe_xC_y) and carbonaceous deposits.[22] The final composition of species has been reported to affect catalytic activity, selectivity and overall stability of the catalyst.[26]

The complexity of iron-based FT catalysts during operational reaction conditions has led to a debate within the literature over which species is responsible for the active phase of the catalyst. The identification of the active phase is made difficult by the fact that active iron FT catalysts are air sensitive constraining the application of *ex situ* analysis but this can be overcome with the use of passivation procedures.[27] *Operando* techniques are the preferred method of analysis to preserve the integrity of the catalyst but this can be challenging due to high temperatures and pressures normally utilised for FT chemistry.[20] This analytical predicament alongside the complexity of the catalyst under reaction conditions has led to different proposals of the active phase of iron FT catalysts.

Earlier studies suggested magnetite (Fe_3O_4) to be the active phase.[28–31] A study by Blanchard *et al*.[29] found that spent catalyst samples containing magnetite were most active therefore suggested this to be the active phase. However, iron carbides were also detected but not considered as a possible active phase. Furthermore, Butt *et al*.[28] proposed that Fe_3O_4 is in fact active in the absence of carbide phases. However, a vast proportion of more recent literature has correlated iron carbide formation with the activity of the catalyst suggesting iron carbides to be the proposed active phase. [22,26,32–36] Shroff *et al*.[22] proposed that iron carbides were necessary for FT activity displaying a correlation between increasing catalytic activity and the formation rate of iron carbides, with iron oxides, hematite and magnetite, not displaying any FT activity. Datye and co-workers[34] reported specifically that χ-Fe_5C_2 (Hägg) and Fe_7C_3 are present in an active iron FT catalyst and the presence of ε-carbide may lead to deactivation of the catalyst. Despite Datye proposing ε-carbide being a cause for deactivation, Chang *et al*.[37] investigated several iron carbides (Fe_7C_3, χ-Fe_5C_2 and ε-Fe_2C) and their influence on FT activity and selectivity, concluding

that ε-carbide did display FT activity although significantly less than Fe_7C_3 but in a similar range to that of χ-Fe_5C_2. Overall, this scope of the literature highlights the complexity in defining the specific active phase for iron FTS. However, current literature is generally consistent with iron carbides being the active phase of iron-based systems.

1.4. Role of Carbonaceous Deposits in Metal Catalysed Reactions

Pioneering work by Thomson and Webb first suggested the presence of a hydrocarbonaceous overlayer playing a potentially crucial role in metal catalysed reaction systems, in particular to an olefin hydrogenation reaction. They proposed that hydrogenation occurs by hydrogen transfer between adsorbed hydrocarbon species (M-C_xH_y) and adsorbed olefins, with the metal surface playing a more secondary role.[38] A later review by Webb considered the literature involving investigations of the formation of surface carbonaceous deposits and their role in determining the catalytic behaviour of the surface.[39] One such study by Jackson *et al.*, applied isotopic tracers to investigate the hydrogenation of CO over a rhodium catalyst, and proposed that CO was hydrogenated through the hydrocarbonaceous overlayer on the catalyst surface, rather than directly to methane, with the overlayer acting as a supply of hydrogen and CH_2-units to other reactive species adsorbed on the surface.[40] Another study from Webb's review article[39] by Davis and co-workers,[41] investigated various reactions, including hydrogenation, dehydrogenation and deuterium exchange reactions, and concluded these to be 10 – 1000 times faster in the presence of catalytically active carbonaceous deposits. Overall, the range of studies from Webb's review article highlights the potential benefit of carbonaceous deposits to a reaction scheme and are not just preserved as a mechanism for catalyst deactivation.

Borodziński[42,43] proposed a kinetic model to account for the role of the hydrocarbonaceous overlayer on a palladium surface for the hydrogenation of ethyne-ethene mixtures and is shown in **Figure 2**. It was suggested that the hydrocarbonaceous overlayer creates two active sites on the metal surface, which were labelled A and E with each active site possessing its own specific role in the hydrogenation of ethyne-ethene mixtures. Borodziński proposed that the A sites, as indicated in **Figure 2**, are small sections of palladium surface between the carbonaceous deposits. At this site, only the competitive adsorption of hydrogen and ethyne occur which facilitates the hydrogenation of ethyne to ethene/ethane and the hydro-oligomerisation of ethyne to butadiene. The E sites are larger

spaces on the palladium surface in which all reactants are competitively adsorbed. The hydrogenation of ethene to ethane and the hydrogenation of butadiene to butene/butane occur here.[42,43]

Until recently, a role for hydrocarbonaceous overlayers in FTS chemistry has not really been considered. However, work by Hamilton and co-workers identified the presence of a hydrocarbonaceous overlayer on an industrial grade iron-based FTS catalyst by application of inelastic neutron scattering (INS). Following this, the hydrocarbonaceous overlayer of a series of laboratory prepared iron-based FTS catalysts was studied in an attempt to define its role, if any, in a FTS reaction scheme. By application of Borodziński's model, the role for the hydrocarbonaceous overlayer in terms of FTS and Fischer-Tropsch to olefins (FTO) based chemistry will be discussed in later chapters (**Chapters 3 & 5**).

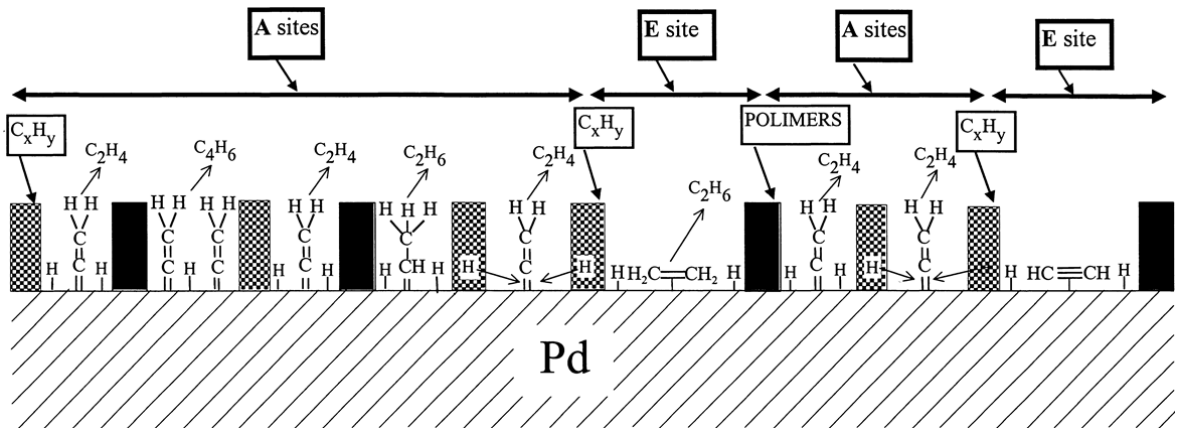

Figure 2: Proposed model of the hydrocarbonaceous overlayer on a palladium surface by Borodziński *et al*.[43]

1.5. Fischer-Tropsch to Olefin Chemistry (FTO)

Short chain olefins (C_2-C_4), such as ethene (C_2H_4), propene (C_3H_6) and butene (C_4H_8), are highly valuable intermediates in the chemical manufacturing industry and can be used for a wide range of derivatives such as the production of plastics, pharmaceuticals and cosmetics.[44,45] Ethene and propene are currently the highest produced organic chemicals, collectively producing 2.3 x 10^8 t per year. [46,47] Due to their diverse applications, this figure is expected to grow as a result of the increasing population resulting in an increase in demand.[46,47] Typically, the production of lower olefins is from cracking of crude-oil. However, this is not sustainable due to several factors, including concerns over the energy required for cracking, the environmental impact and the dependency on the limited supply

of crude oil. This has led to research into alternative sources and processes, in particular those which are derived from syngas obtained from natural gas, coal or biomass, for the production of lower olefins.[45,48,49] **Figure 3** presents various viable options, direct and indirect, for the production of lower olefins from syngas.

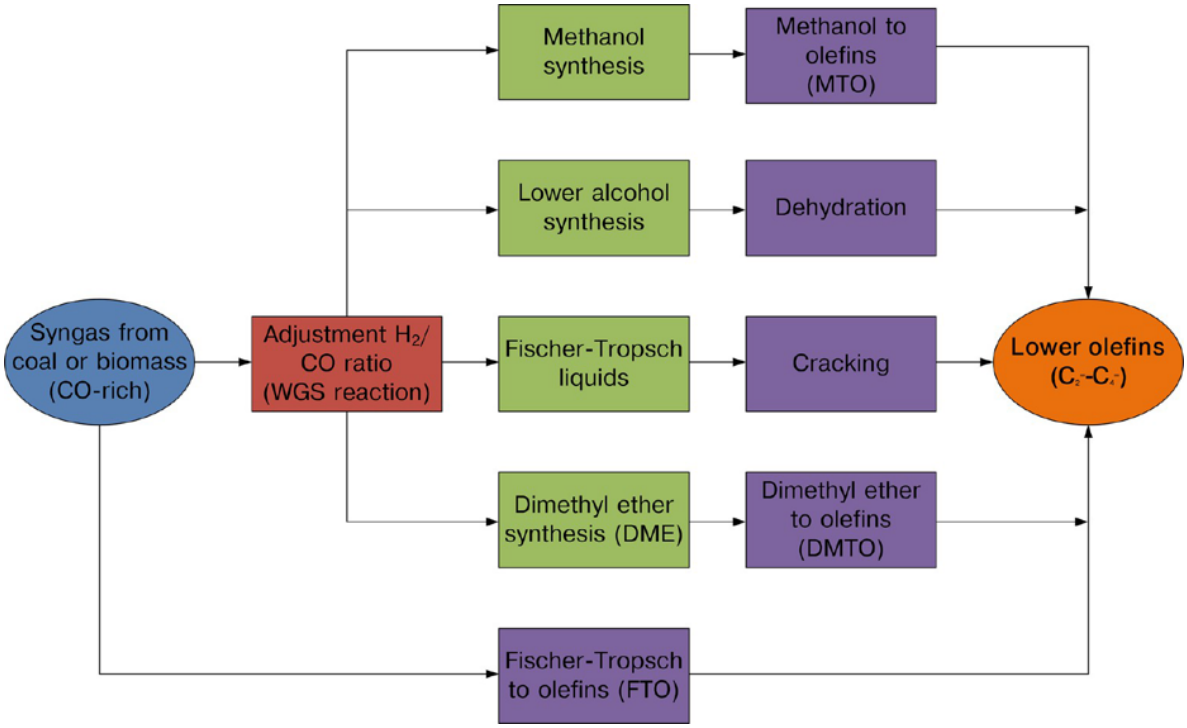

Figure 3: Various processes available for the production of lower olefins (C_2-C_4) from syngas.[48]

The various indirect methods such as methanol to olefins (MTO) and dimethyl ether to olefins (DMTO) can provide high selectivity to the likes of ethene but each of these processes requires additional steps towards the desired olefin outcome. From an economic standpoint, this contributes to higher costs through energy consumption and equipment. Therefore a direct method, such as FTO, provides an alternative route to produce lower olefins that is not only more environmentally enticing but may also be more economically profitable.[48,49]

Iron-based catalysts are more desirable for the FTO process due to iron's high availability and also it naturally possesses a high selectivity towards olefins due to its lower hydrogenation activity in relation to other active FT catalysts.[15,45,49,50]

Whilst there is a vast FTS literature spanning over several decades, FTO is a relatively new aspect, with a small literature available on this subject. Major players in the field of FTO include the likes of de Jong's research group and also researchers from the Dalian institute in China. Initial studies by researchers at the Dalian Institute (2015) on FTO have utilised

zeolites as well as iron catalyst incorporated in carbon nanotubes for the production of light olefins.[51,52] On the other hand, an early study by de Jong's group on FTO (2012) subtly introduced the use of promoters to iron-based catalysts such as sulfur and sodium, enhancing lower olefin production but predominantly focussed on aspects of support materials and their effect on light olefin production.[53] Despite the relatively limited literature currently available on this topic, interest in FTO is expected to grow significantly in the coming years.

1.5.1. Promoters for FTO Chemistry

In FTO chemistry, to improve the selectivity towards lower olefins various promoters to iron-based catalysts have been investigated including zinc[54–56], vanadium[56], manganese[57,58] and alkali metals such as sodium and potassium. [45,50,59] Potassium is commonly added to iron FT catalysts to enhance olefin selectivity whilst decreasing that of methane. It has also been proposed to increase FTS activity as well as WGS activity and causes an increase in carburization.[45,60] Sodium also displays similar properties to that of potassium, with reports of it increasing olefin to paraffin ratios as well as decreasing methane selectivity and an increase in carburization.[50,61] Consequently, Ribeiro *et al*. proposed that the purpose of the addition of alkali metals is to decrease the strength of the CO bond, which in turn increases the coverage of adsorbed carbon leading to increased carburization.[61]

Sulfur has been well established as a poison within the history of the Fisher-Tropsch process.[12,62,63] For example, Bartholomew and Bowman, determined that catalytic activity was reduced in the presence of small volumes of H_2S. Despite this observation, they also noted an increase in activity with a boron promoted iron catalyst, in the presence of sulfur (0.5 ppm H_2S). This was justified by suggesting that the boron prevented the formation of iron sulfides, the suggested cause for deactivation, by selectively adsorbing H_2S.[63] However, more recent investigations have utilised sulfur as a potential promoter in FTO chemistry, with the sulfur incorporated within the catalyst itself. A study by Bromfield and Coville[64] indicated a peak in catalytic activity and selectivity towards lower olefins with the addition of *ca.* 500 ppm of sulfur to an iron-based catalyst (**Figure 4** and **5**). Beyond this concentration, a detrimental loss of catalytic activity was observed.

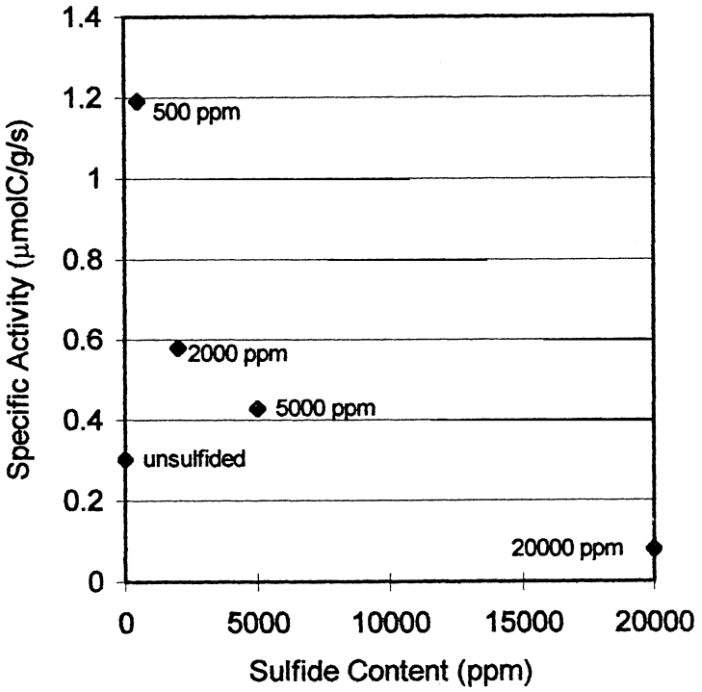

Figure 4: The variations of catalytic activity with sulfide content tested under FTS conditions (523 K, 8 bar, 192 h).[64]

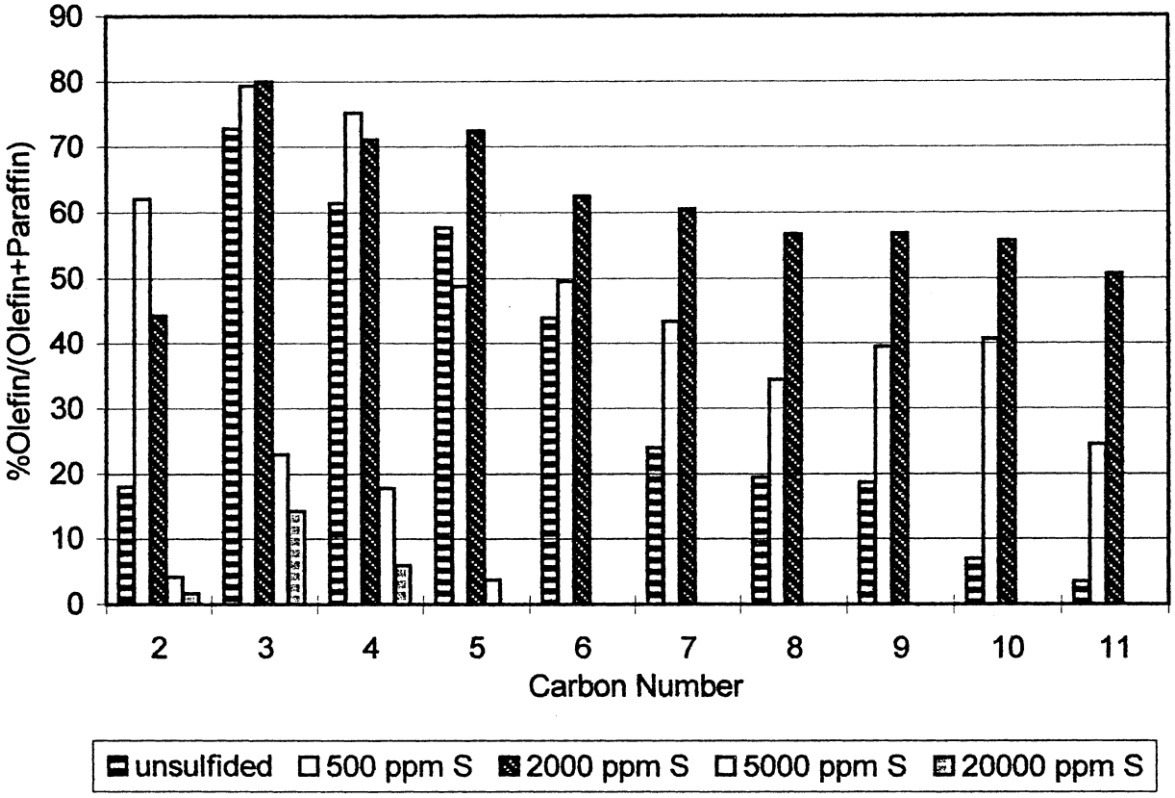

Figure 5: Percentage of olefinicity of unsulfided and sulfided catalysts as a function of carbon number.[64]

The precise role in which sulfur may play in the production of olefins in still under debate within the literature. For example, Galvis *et al.* proposed that the inclusion of small concentrations of sulfur enhances catalytic activity, in agreement with Bromfield and Coville[64], and reduces selectivity to methane, concluding that the sulfur is blocking hydrogenation sites.[50] Conversely Xu *et al*. proposed that the inclusion of sulfur had a negative effect on the catalytic activity by inhibiting CO dissociation and iron carbide formation. Furthermore, Xu illustrates that sulfur causes a decrease in selectivity to long chain hydrocarbons (C_5^+) and the olefin: paraffin ratio and reports a subsequent increase in the selectivity to short chain hydrocarbons (C_2-C_4).[65] Consequently, Yuan and co-workers suggest that the addition of an alkali metal alongside sulfur is crucial for enhancing catalytic activity in comparison to the use of sulfur as a sole promoter.[45]

Galvis' investigation of dual promotion included sodium as the alkali metal, as well as sulfur. Single promotion with sodium displayed reduced methane selectivity and chain growth and, overall, a negative effect on the catalytic activity. However, when combined with sulfur, an increase in selectivity towards lower olefins was observed with a decreased methane selectivity but this resulted in an increase in coke laydown. Overall, Galvis presented lower olefin selectivity in the range of 35 – 51 % (20 bar, 340 °C, H_2:CO = 1). Variations in selectivity were dependent on promoter concentrations and whether or not the catalysts were supported.[50]

Yuan *et al*. utilised potassium, alongside sulfur as a promoter. **Figure 6** presents a summary of the various catalyst tested by Yuan and their product selectivity (10 bar, 340 °C, H_2/CO = 1). From the results, Yuan has proposed that the sole addition of sulfur restrains the carbon chain growth and as a result leads to an increased production of methane, similarly to that observed by Xu.[65] The sole addition of potassium leads to a decrease in methane production and an increase in lower olefins. However, if the concentration of potassium is increased further, beyond its optimal loading, selectivity towards lower olefins is lost and an increase in C_5^+ occurs. By combining both sulfur and potassium this results in an increased catalyst activity of three times that obtained for the unpromoted catalyst.[45] Thus highlighting the importance of the incorporation of both alkali metal and sulfur to enhance selectivity towards lower olefins but also decrease selectivity towards unwanted by-products such as methane.

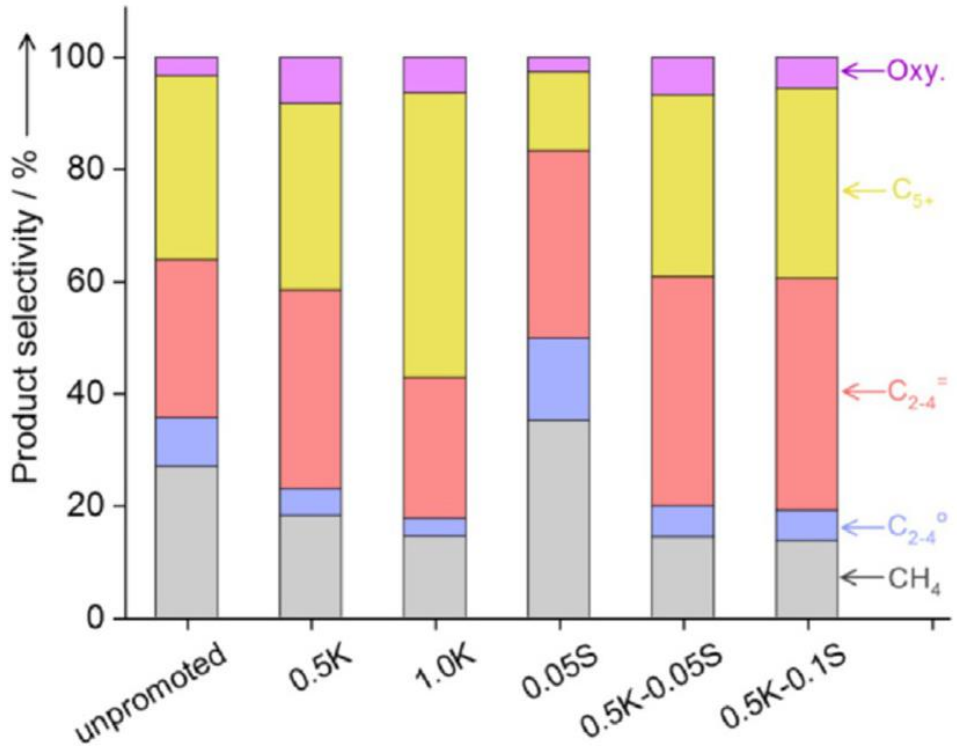

Figure 6: Product selectivity (purple – oxygenates, yellow – C_{5+} hydrocarbons, pink – C_2-C_4 olefins, blue – C_2-C_4 paraffins, grey – methane) of a range of iron-based catalyst promoted with varying concentrations of potassium and sulfur.[45]

1.6. Analytical Techniques

1.6.1. Inelastic Neutron Scattering

Inelastic neutron scattering (INS) is a beneficial spectroscopic technique in heterogeneous catalysis for obtaining vibrational spectra of coked or unsupported metal catalysts which normally present challenges for other vibrational techniques such as infrared spectroscopy (IR) due to their high optical absorbance.[66,67] The advantage of using INS spectroscopy spans from its differences from conventional vibrational techniques, such as IR and Raman spectroscopy, which derive from the properties of the neutron. Neutrons possess a mass (1.009 amu) and have the ability to scatter from the atomic nuclei of the sample. This inelastic scattering process results in transfer of both energy (E cm^{-1}) and momentum (Q $Å^{-1}$) with the degree of scattering given by the neutron cross section (σ). The cross section is not only element dependent but also isotope dependent, with hydrogen having a significantly higher cross section of 80.3 barn (1 x 10^{-28} m^{-2}) in comparison to other elements and isotopes relevant for catalysis which are typically < 5 barn. [68–71] Therefore,

hydrogen will be significantly more visible in the vibrational spectrum than any other atom making INS an ideal technique for the study of hydrogenous modes in catalysis. The application of INS spectroscopy can be complementary to infrared (IR) and Raman.

The intensity of an INS band (S) can be given by the following expression (*Equation 1.6*)[69]:

$$S(Q, n\omega_i) \propto \frac{(QU_i)^{2n}}{n!} \exp[-(QU_{Tot})^2]\, \sigma \qquad \textbf{(1.6)}$$

ω_i is the i^{th} mode at frequency ω,
n=1 for a fundamental, 2 for a first overtone or binary combination, 3 for a second overtone or ternary combination *etc*.,
U_i is the root mean square displacement of the atoms in the mode,
U_{tot} is the total mean square displacement of all atoms in all modes,
σ is the inelastic scattering cross-section of the atom,
Q is momentum transfer that is defined as:

$$Q = k_i - k_f \qquad \textbf{(1.7)}$$

$$k \equiv \frac{2\pi}{\lambda} \qquad \textbf{(1.8)}$$

k is the wavevector ($Å^{-1}$)
λ is the wavelength of the neutron

The magnitude of the U_{Tot} term in *Equation 1.6*, contained within the exponential Debye-Waller factor term, is partly determined by the thermal motion of the molecule. Therefore INS measurements are normally performed at cryogenic temperatures (30 K) to reduce the effect on intensity (S).[69]

This study utilised the ISIS Facility at the Rutherford Appleton Laboratory for a spallation source of neutrons.[72] **Figure 7** displays a schematic of the synchrotron and the target stations at the ISIS Facility. A spallation source involves pulsing a proton beam towards a heavy metal target, either tantalum, tungsten or lead.[67] The ISIS Facility uses tungsten

metal as its target.[70] This results in an atom absorbing a proton, causing a highly excited nuclear state. The decay mechanism results in the production of neutrons which are channelled towards the various instruments. [67,69]

Interestingly, the application of INS has allowed characterisation of the hydrogenous component of iron-based Fischer-Tropsch catalysts.[73,74] This is complementary to other analytical techniques more commonly used for analysis of iron FT samples which focus on either the iron or carbon aspect of the catalytic matrix, *i.e.* XRD, TEM, TPO and Mössbauer spectroscopy. For this investigation, an ambient pressure CO hydrogenation reaction is utilised as a representative FTS reaction.[75] This avoids the formation of any heavy wax residues that may form on the catalyst surface that would otherwise complicate the INS spectra.[76] Despite not being fully regarded as FTS chemistry, due to the fact that no polymerisation takes place, it allows definition of $Fe/H_2/CO$ surface chemistry that is inherently associated with FTS.

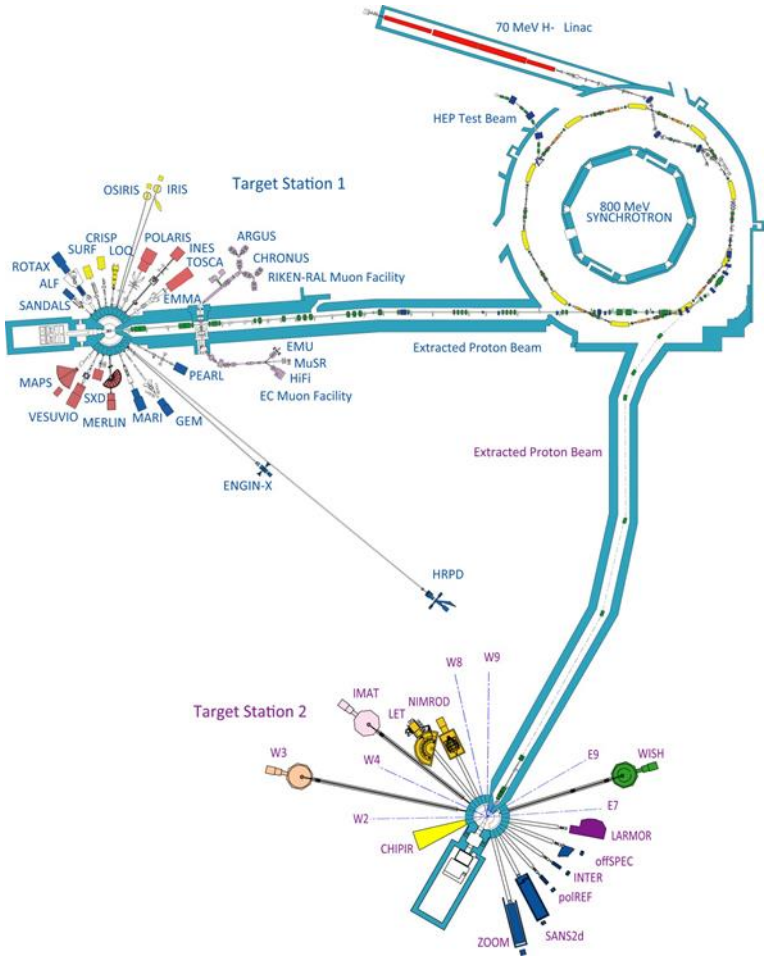

Figure 7: A schematic of the ISIS Facility, which includes the synchrotron, target stations and instruments.[72]

1.6.1.1. MAPS Spectrometer

This study utilised the MAPS direct geometry spectrometer at the ISIS Facility which uses a chopper package to select the neutron incident energies exposed to the sample. A schematic of the instrument is shown in **Figure 8**.[72] Samples are contained within an aluminium sample cell and attached to a sample stick, which is inserted into the instrument via a vacuum sealed sample cryostat. The two choppers involved in the MAPS spectrometer are the Nimonic chopper and the Fermi chopper and sit at a fixed distance from the moderator. The purpose of the Nimonic chopper is to remove gamma rays and un-moderated neutrons as these can cause saturation of the detectors, increasing the background. The Fermi chopper is an aluminium rotor, magnetically suspended in a vacuum and acts as a series of parallel slits. To select the incident energy, the opening time of the slit package is phased to the neutron pulse from the target station. This creates a monochromatic beam which is incident on the sample and the scattered neutrons are recorded on the surrounding detectors. The MAPS spectrometer contains a large detector area, ~16 m^2, within the angle range -30 to 60°. This large number of detectors provides relatively high sensitivity and therefore is particularly suitable for measuring samples with low hydrogen concentrations.[69,72,77,78]

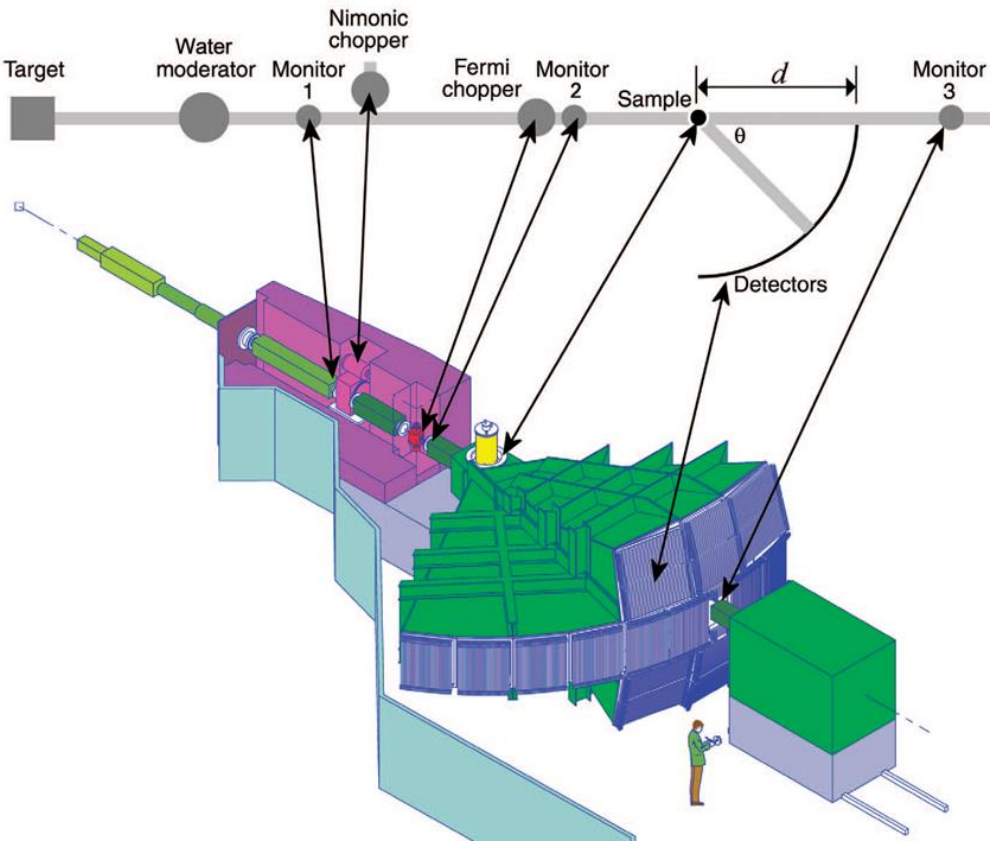

Figure 8: A schematic of the MAPS direct geometry spectrometer at the ISIS Facility with the key features highlighted.[69]

The benefit of utilising a direct geometry instrument, such as MAPS, over an indirect geometry instrument like TOSCA, is that one can access reasonable resolution over the full vibrational spectral range (20 – 4000 cm^{-1}). This can be achieved by altering the incident energy. For example, as shown in **Figure 9**, a small incident energy on MAPS will result in a spectrum comparable to that obtained on TOSCA (*i.e*. similar spectral resolution <1200 cm^{-1}). Upon increasing the incident energy further to 600 meV, will allow access to an increased region of the spectra with increased resolution in comparison to that achievable on TOSCA. However, to record a well-defined spectrum over the full vibrational range, multiple incident energies must be utilised. It is also possible to improve spectral resolution on a direct geometry spectrometer by altering the slit package in the rotor. This in turn will result in a decrease in neutron flux in order to improve spectral resolution.[69]

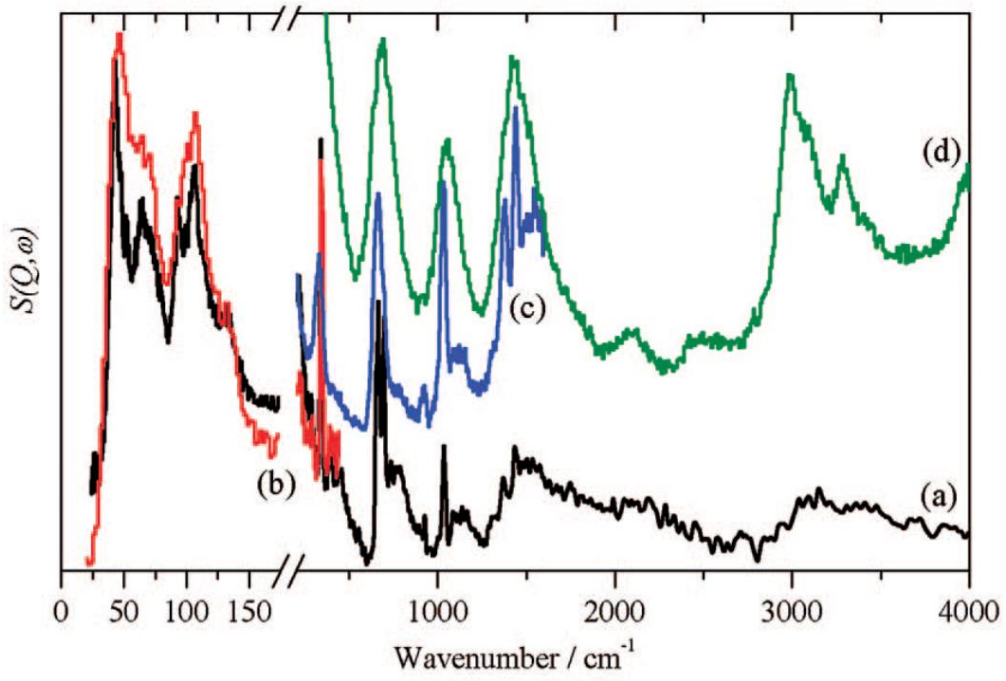

Figure 9: INS spectra of propyne highlighting resolution differences between a direct geometry spectrometer (MAPS), at different incident energies, and an indirect geometry spectrometer (TOSCA). (a) Measured on TOSCA (black) (b) MAPS, E_i = 60 meV (red) (c) MAPS, E_i = 250 meV (blue), and (d) MAPS, E_i = 600 meV (green). [69]

1.6.1.2. Neutron Vibrational Spectroscopy in Catalysis

Neutron scattering is becoming an ever-popular technique in the area of heterogeneous catalysis and can be complementary to other characterisation techniques such as high-resolution energy electron loss spectroscopy (HREELS), X-ray photoelectron spectroscopy (XPS) and infrared (IR) spectroscopy. The chapter titled "*Catalysis*" from "*Neutron Scattering – Applications in Biology, Chemistry and Material Science*" gives an extensive and comprehensive review on aspects of how neutrons can be used within catalysis. Detailed below is a summary of a selection of case studies taken from this book, which highlights the range of catalytic systems which have utilised neutron scattering.[77]

1.6.1.2.1. Catalyst Development - Methyl Chloride Synthesis

Methyl chloride synthesis is a large-scale industrial process, with the final product primarily used as a starting material in the production of higher chlorinated products, silicones and methyl cellulose. Industrially, methyl chloride is prepared via the hydrochlorination of methanol over a solid acid catalyst at elevated temperatures, with selectivity negatively impacted by the side reaction of methanol converting to dimethyl ether (DME). Therefore, it is of interest to develop a new catalyst which increases selectivity towards methyl chloride and decrease selectivity towards DME. INS, alongside other complementary techniques, was used for the development of a new catalyst based on η-alumina and provided information on several aspects including (i) surface acidity of η-alumina, (ii) the interaction of η-alumina and methanol and (iii) the interaction of hydrogen chloride on η-alumina. **Figure 10** examines just one aspect of the application of INS to this process, utilising the TOSCA spectrometer, presenting the interaction of the reactant methanol with η-alumina. **Figure 10 (a)** presents the spectrum of solid methanol, highlighting various bands; < 400, 690-780, 1150 and 1450 cm^{-1}, indicative of methyl torsion, an out of plane O-H bend, a CH_3 rock and a mode resulting from the overlap of a CH_3 deformation mode and the in-plane O-H bend respectively. The relatively weak spectrum, indicative of low-density active sites present on the alumina surface, presented in **Figure 10 (b)**, is of a saturated chemisorbed overlayer of methanol on η-alumina prepared at 300 K. The spectrum is characterised by three features at 84, 1170 and 1460 cm^{-1}, which are assigned to a CH_3 torsion mode, CH_3 rock and CH_3 deformation modes respectively. This spectrum was assigned to chemisorbed methoxy species formed as a

result of dissociative adsorption of methanol. Confirmation of this assignment was achieved by recording an INS spectrum of a model compound, $Al(OCH_3)_3$ as shown in **Figure 10(c)**. The identification of the observed methoxy bands was later used for studying the interaction of the unwanted side-product, DME, with the catalyst surface.

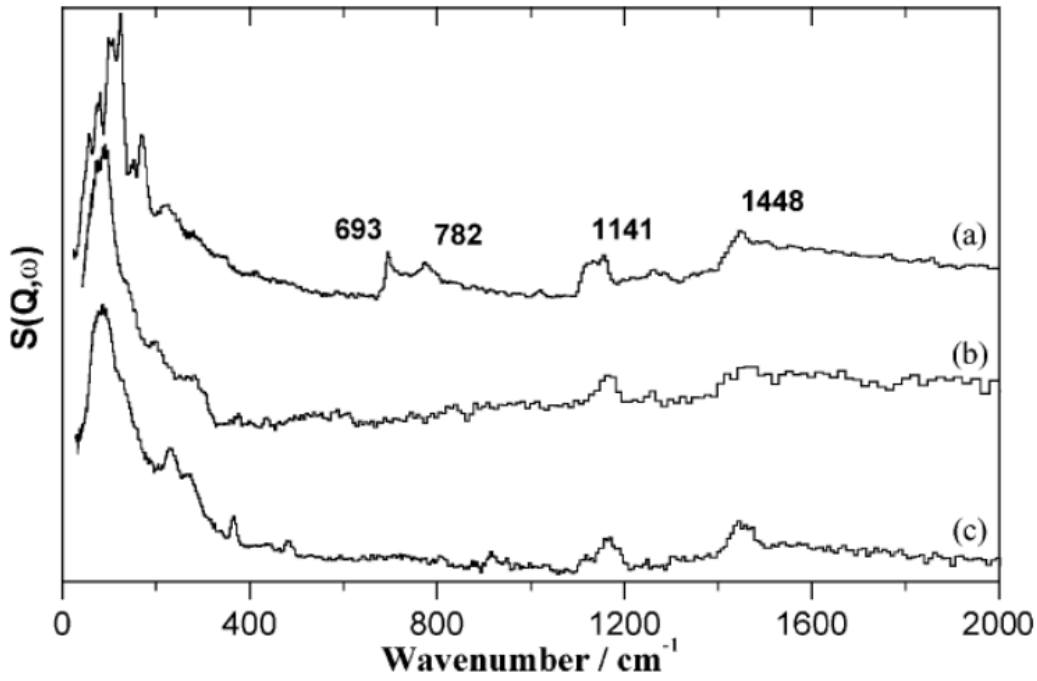

Figure 10: INS spectra recorded at 20 K using TOSCA of (a) methanol (b) background subtracted spectrum of a saturated chemisorbed overlayer of methoxy on η-alumina (1.12 mmol CH_3OH g^{-1}) prepared at 300 K and (c) $Al(OCH_3)_3$.[77]

1.6.1.2.2. Catalyst Deactivation

The application of neutron scattering can also be used for studying aspects of catalyst deactivation. Palladium catalysts are of a high interest for hydrogenation reactions for the synthesis of fine chemicals or intermediates. A well-established palladium catalyst of a large-scale plant was observed to be experiencing an unexpected loss in catalytic activity over time. Several characterisation techniques failed to identify the cause of deactivation *i.e.* no typical poisons identified, no loss of surface area, corrosion phenomena or catalyst coking was observed. Techniques such as IR, Raman and NMR were not applicable for analysis of the catalyst due to specific properties exhibited by the catalyst. **Figure 11 (a)** presents the INS spectra of a spent palladium catalyst taken directly from the reactor and sealed in argon. It shows a significant proportion of weakly adsorbed residual solvent. **Figure 11 (b)** and **(c)** is the same catalyst as in **(a)** after **(b)** solvent extraction and **(c)** exposure to hydrogenation

conditions. Sharp bands of non-extractable, simple molecules are observable in spectrum **(b)**. As these bands are also observable in **(a)** and **(c)**, they are not a result of the solvent extraction process. These species are also not affected by hydrogenation conditions. On the other hand, **Figure 11 (d)** is an active catalyst after solvent extraction which does not display any of the molecular bands observed for the deactivated catalyst. Therefore, the strong bands observed in **Figure 11 (b)** are suggested to be the species responsible for catalyst deactivation. This was confirmed by examining the catalyst at various stages in the deactivation process and correlating the intensities of these bands.

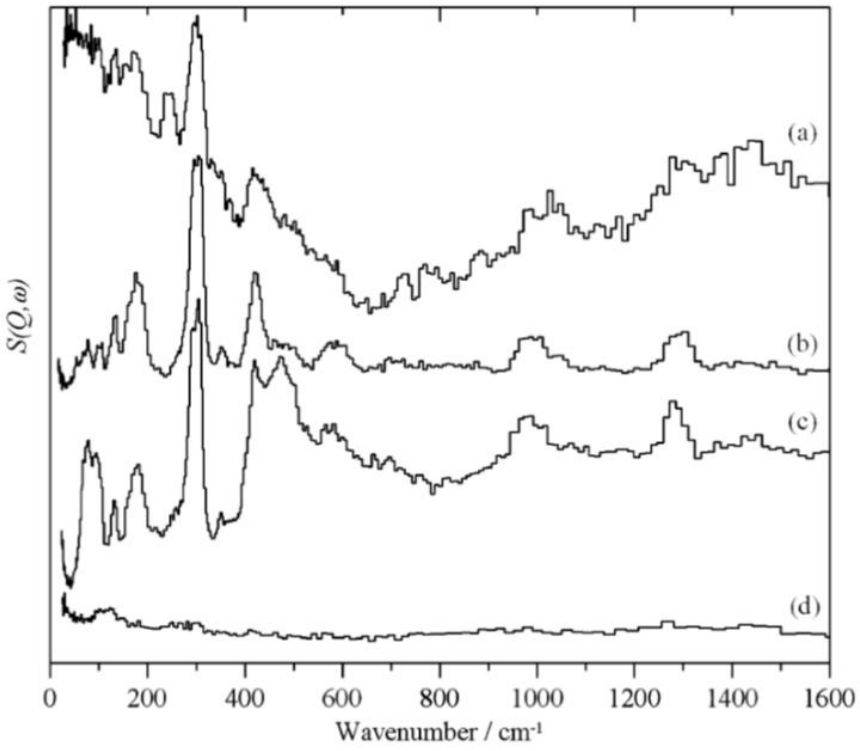

Figure 11: Comparison of the INS spectra (TOSCA) of an industrial Pd catalyst. (a) The deactivated catalyst taken directly from the hydrogenation process and sealed under argon, (b) sample (a) after solvent extraction, (c) same sample as (a) and (b) after in situ hydrogenation up to 1.5 bar of hydrogen equilibrium pressure, and (d) a long-term used, but active catalyst after solvent extraction under the same conditions as the deactivated sample.

1.6.2. Raman Scattering

Raman spectroscopy involves the use of monochromatic radiation to induce inelastic scattering. The process involves the incident beam passing through a sample and measuring the scattered radiation perpendicular to the beam. The incident photon collides with a molecule causing an exchange in energy between the photon and molecules causing the scattered photon to be of a higher or lower in energy than the incident beam.[79] Raman spectroscopy is subjected to selection rules, only allowing transitions where there is a change in polarisability of the molecule.

This project has utilised Raman spectroscopy in the identification of iron oxide phonon modes and the formation of carbonaceous material. Within the literature identification of D and G bands of carbonaceous material, present in the region of 1200-1650 cm^{-1} has been well documented and the relevant bands and assignments are displayed in **Table 1**. [80–82] This technique has been used only to indicate the formation of carbonaceous material on the catalyst and not in a quantitative manner.

Table 1: D and G bands of carbonaceous material observed in Raman spectroscopy. Information reproduced from references. [81,83]

Carbon Peak	Raman Shift (cm^{-1})	Assignment
G	1580	Ideal graphitic lattice
D1	1350	Disordered graphitic lattice (graphene layer edges)
D2	1620	Disordered graphitic lattice (surface graphene layers)
D3	1500	Amorphous carbon
D4	1200	Disordered graphitic lattice

1.6.3. Powder X-ray Diffraction

X-ray diffractometers are composed of an X-ray source, providing monochromatic radiation, a stage, turntables to vary the angle of the incident X-ray beam and an X-ray detector to detect scattered X-rays. The X-rays are generated by a cathode ray tube which involves heating a filament, typically tungsten, to produce electrons; a high voltage is applied to accelerate these towards a target metal. The incoming electrons collide with electrons in the inner shell (K shell) of an atom in the target material, expelling an electron. An electron from a higher energy (L shell) falls into the vacancy emitting characteristic X-rays.[84] The wavelength of the X-ray is dependent on the target material used; the most common of which are Cu, Co, Mo, Fe and Cr. Within this project two different diffractometers were used and contained two different target materials: Cu and Co (**Table 2**). The presence of iron can result in fluorescence with Cu K_α radiation, resulting in poor signal: noise, which may obscure peaks of low intensity. Therefore, Co is the preferred target material for analysis of iron-based catalysts. Unfortunately access to Co K_α radiation was restricted, which resulted in use of Cu K_α radiation for some catalyst samples.

Table 2: Diffractometer target materials and Kα radiation values relevant to this project.

Target Material	K_α radiation (Å)
Copper	1.5418
Cobalt	1.7902

Powder X-ray diffraction (XRD) involves the use of elastically scattered X-rays, for phase identification and particle size determination of crystalline materials.[84] The interaction of a monochromatic X-ray and a sample will result in constructive interference if the conditions of Braggs Law (*Equation 1.9*) are satisfied. If not satisfied, destructive interference occurs resulting in a reduction in the scattered radiation intensity. Powdered materials contain a large number of randomly orientated crystallites, therefore a range of 2θ angles are scanned to ensure all possible diffraction directions of the lattice are obtained.

$$n\lambda = 2d\sin\theta \quad \textbf{(1.9)}$$

n = integer

λ = incident X-ray wavelength

d = interplane spacing

θ = angle between the incident X-ray and the scattering plane

The Scherrer equation can be used to define the size of a crystallite responsible for a particular reflection in a diffractogram and is displayed below (*Equation 1.10*).[85–88] The application of this equation links the width of a reflection from a powder X-ray diffraction to a coherent diffraction domain size, with the increasing width of a reflection correlating with a decrease in the coherent diffraction domain size.[86] For standard laboratory instrumentation, the lower limit for determination of domain size by Scherrer broadening is *ca*. 30 Å, with an upper limit of approximately 1000 Å.[86,87] The value applied for the shape constant (K) is dependent on many factors including the shape of the crystallite, the specific reflection analysed and the form of the reflection width determined *i.e.* integral breadth or the full half width maximum. The shape constant is typically *ca*. 0.9 independently of morphology or reflection index and is expressed in radians, therefore if utilising this value, for dimensional consistency, the reflection width (β) should also be expressed in radians. When applying the Scherrer equation it is important that the reflection width should be only that of the material itself and not from the effects caused by instrumental broadening or from use of non-monochromatic X-ray sources. By using an appropriate standard, the degree of instrumental broadening can be accounted for. The contribution of strain or disorder to the reflection can cause an increased reflection width and results in underestimating the diffracting crystallite size when using the Scherrer equation. Other limitations of the application of this equation include morphological effects and complication of anisotropy.[86,87]

$$d = \frac{K\lambda}{\beta cos\theta} \quad \textbf{(1.10)}$$

d = coherent diffraction domain size

K = shape constant

λ = X-ray wavelength

β = reflection width (2θ)

θ = Bragg angle

1.6.4. X-ray Absorption Spectroscopy

X-ray absorption spectroscopy (XAS) is a technique with application in many fields. Its application in heterogeneous catalysis is beneficial as it can provide both electronic and structural properties of catalysts and can also be used for the study of both crystalline and amorphous materials.[89]

The basic principle of XAS measures the absorption coefficient μ(E), a description of how strongly X-rays are absorbed as a function of X-ray photon energy. As the photon energy is increased there is generally a decrease in the absorption coefficient thus indicating the X-rays are more penetrating. However, when the photon energy coincides with the binding energy of a core orbital there is a sharp increase in the absorption, known as the absorption edge. This absorption edge corresponds with the transition of a core level electron, typically 1s (K edge) or 2p (L_3 or L_2 edge), to a vacant site.[90–92] The energy required for this excitation is element specific; therefore the X-rays can be tuned to a specific absorption edge.[92,93]

A typical XAS spectrum can be divided into 2 sections, XANES (X-ray absorption near edge structure), typically within 30 eV of the absorption edge, and EXAFS (extended X-ray absorption fine structure), as highlighted in **Figure 12**.[93] Each of the sections provides different chemical information on the element of interest. The XANES region of the spectrum is used in determining the oxidation state of the element, whereas EXAFS region can be used in identification of coordination number, distance and species of neighbouring atoms to the absorbing atom.[92,93] This project has utilised XANES for identifying the sulfur species present in iron-based FT catalysts pre- and post-reaction, with measurements taking place at Diamond Light Source.

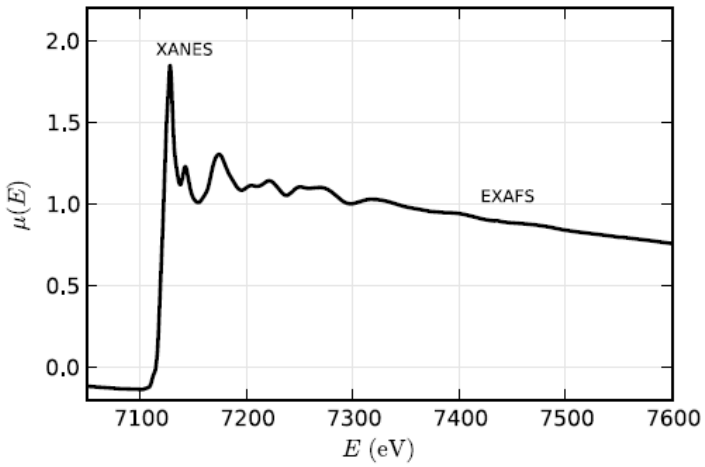

Figure 12: An example XAFS spectrum for the Fe K edge of FeO indicating the XANES and EXAFS regions. [93]

1.7. Project Overview

The work presented in this thesis is an extension of previous work carried out by Hamilton and Warringham.[73,74] Hamilton pioneered the application of INS as an analytical technique for iron Fischer-Tropsch catalysis, which was further explored and defined by Warringham working in partnership with a major supplier of FTS technology (Sasol Technology UK Ltd). The overall aim of this investigation is to use the application of inelastic neutron scattering to further investigate the formation of the hydrocarbonaceous overlayer on iron-based Fischer-Tropsch catalysts. A detailed outline of each chapter of the thesis is given below:

- **Chapter 3**: A standard reference hematite catalyst (**Fe-ref**), containing no promoters or use of support materials, was investigated for an extended period on stream – up to 240 h. This work builds directly on from the previous work by Warringham[94], which examined the same catalyst in the initial 24 h period of reaction. The aim of this chapter is to establish the complete evolutionary profile of a reference material using ambient pressure CO hydrogenation at 623 K as a test reaction.

- **Chapter 4:** Warringham established the groundwork for this chapter, examining a hematite catalyst singly promoted with varying levels of sulfur as this has been reported to alter the product slate of the FT process towards lower olefins, which are highly desirable by the chemical manufacturing industry.[95] This process is known as Fischer-Tropsch to olefins (FTO). This chapter investigates five potential prototype hematite catalysts (**Fe-Na-S_x**, where subscript x refers to sulfur concentration in ppm) doubly promoted with varying levels of sulfur plus the addition of a fixed level of sodium across all five samples. These measurements are compared against the standard reference catalyst sample, using an ambient pressure CO hydrogenation reaction as a representative test reaction.

- **Chapter 5**: Of the five catalysts studied in **Chapter 4**, one was selected for further investigation. This investigation examined the doubly promoted catalyst over an initial 24 h period using an ambient pressure CO hydrogenation reaction that is used in previous chapters (**Chapters 3 & 4**). Further study of this prototype catalyst involved a preliminary measurement involving the addition of a CO_2 feedstream to

the CO hydrogenation reaction conditions. This was investigated over a 24 h period for direct comparison against the standard CO hydrogenation conditions.

- **Chapter 6**: A summary of the main conclusions drawn from this project.

- **Chapter 7**: A brief outline of future work for this project.

Table 3 presents a list of the catalyst tested within this thesis and the chapters in which they are studied. In total, six iron-based catalysts have been investigated. The **Fe-ref** catalyst, as well as the Na/S modified samples (**Fe-Na-S_x**), were examined under full FTS conditions at the industrial centre (4:1 H_2:CO, 603 K, 20 bar). This work determined FTS performance and FTO capability. For reasons of confidentiality, the outcomes of those tests undertaken by the industrial partners are not presented at this time. Instead results on the CO hydrogenation reaction is used throughout the thesis.

Table 3: A list of catalysts used within this investigation and their associated chapters within the thesis.

Catalyst	**Relevant Thesis Chapter**
Fe-ref	Chapter 3
Fe-Na-S_{10}	Chapter 4
Fe-Na-S_{50}	Chapter 4
Fe-Na-S_{100}	Chapter 4 & 5
Fe-Na-S_{175}	Chapter 4
Fe-Na-S_{250}	Chapter 4

Chapter 2 – Experimental

2.1. Catalyst Preparation

All iron catalyst samples were prepared at Sasol laboratories, located in St Andrews, using a co-precipitation method of iron nitrate and sodium carbonate (*Equation 2.1*), followed by a calcination step (*Equation 2.2*) to produce the final catalyst product. The co-precipitation step was controlled using a Mettler Toledo LabMax batch reactor apparatus. The use of this apparatus allows for accurate reproducibility of the samples. Iron nitrate, dissolved in deionised water, was added drop wise to a heated solution (357 K) of sodium carbonate and one litre of deionised water. The resulting solution was continually stirred throughout. The iron nitrate was added until the pH of the solution reached 6.5, which was monitored by the iControl LabMax software. The temperature and agitation speed were maintained for 16 minutes. The reaction vessel was removed from the LabMax apparatus; the solution filtered using a Buchner funnel and washed with warm deionised water for approximately 24 hours until the conductivity of the washed solution is zero. After washings the sample was calcined using a step-wise heating programme, run overnight, reaching a maximum temperature of 623 K (*Equation 2.2*). The catalyst samples were ground to a particle size of 250 – 500 µm. This method produced the standard unpromoted iron oxide catalyst, α-Fe_2O_3, referred to as **Fe-ref** and is analysed for an extended period of time on stream in **Chapter 3**.

$$3Na_2CO_{3(aq)} + 2Fe(NO_3)_{3(aq)} + 3H_2O_{(l)} \rightarrow 6NaNO_{3(aq)} + 2Fe(OH)_{3(s)} + 3CO_{2(g)} \quad (\mathbf{2.1})$$

$$2Fe(OH)_{3(s)} \xrightarrow{\Delta} \alpha Fe_2O_{3(s)} + 3H_2O_{(g)} \quad (\mathbf{2.2})$$

$$(NH_4)_2SO_{4(s)} + Na_2CO_{3(s)} + H_2O_{(l)} \rightarrow Na_2SO_{4(l)} + CO_{2(g)} + 2NH_4OH_{(l)} \quad (\mathbf{2.3})$$

The procedure for preparing the promoted samples containing sodium and sulfur discussed in **Chapters 4** and **5**, is identical to the above procedure but with the addition of a slurry step after the filtering and washings steps. This involves the addition of varying amounts of ammonium sulfate, which alters the final sulfur concentrations within the catalyst, and a fixed amount of sodium carbonate dissolved in 20 ml of deionised water (*Equation 2.3*). The samples were calcined using the same procedure as the unpromoted samples.

2.2. Reaction Testing

2.2.1. Micro-reactor Testing

Micro-reactor testing was carried out at the University of Glasgow on a custom-built stainless-steel gas line (**Figure 13**) encased within a fume hood. The gas line is composed of ⅛ in. O.D. stainless steel Swagelok tubing. The gas lines are heated in order to avoid condensation within the lines. The gas supply is from an external gas manifold and controlled by Hastings mass flow controllers (HFC302) which in turn are controlled by a Chell CCD104 control box. The helium mass flow controller (MFC) has a maximum flow rate of 150 sccm, the oxygen mass flow controller is 50 sccm and the remaining two MFC's have a maximum flow rate of 65 sccm. Catalyst samples are loaded into a 6 mm quartz tube reactor and held in place with quartz wool. The reactor tube is connected to the stainless-steel gas lines via ¼ in. compressed Cajon fittings and is housed within a tube furnace (Carbolite MTF 10/15/30), equipped with a PID control (Eurotherm 2604). Additionally, a thermocouple is placed within the catalyst bed to ensure accurate temperature readings during experiments.

CO hydrogenation reactions used in **Chapters 3, 4** and **5** were carried out using approximately 40 mg of catalyst within the quartz tube reactor. Variations in the catalyst masses were applied and discussed in subsequent chapters. A 2:1 mix of hydrogen (7.93 ml/min, BOC Ltd, 99.8%) and CO (3.91 ml/min, CK gases, 99.8%) were established in a carrier gas, helium (24 ml/min, BOC Ltd, 99.99%) over the bypass before the gases were introduced over the catalyst. A CO detector (3 Year BW Clip, CO 30/200 ppm) was positioned within the fume hood near the gas line, next to the CO cylinder. The weight hourly space velocity (WHSV) is calculated to be 68.57 h^{-1}. Analysis of gas flows is carried out by use of a quadrapole mass spectrometer (Hiden Analytical HPR-20) which is connected to the exit point of the gas line via a heated quartz capillary. A temperature ramp of 5 K min^{-1} was used to reach reaction temperature of 623 K which was held for a set period of time. Reactions were carried out at ambient pressure. After reaction, reactant gases were stopped, and the sample was left to cool to room temperature under a flow of helium.

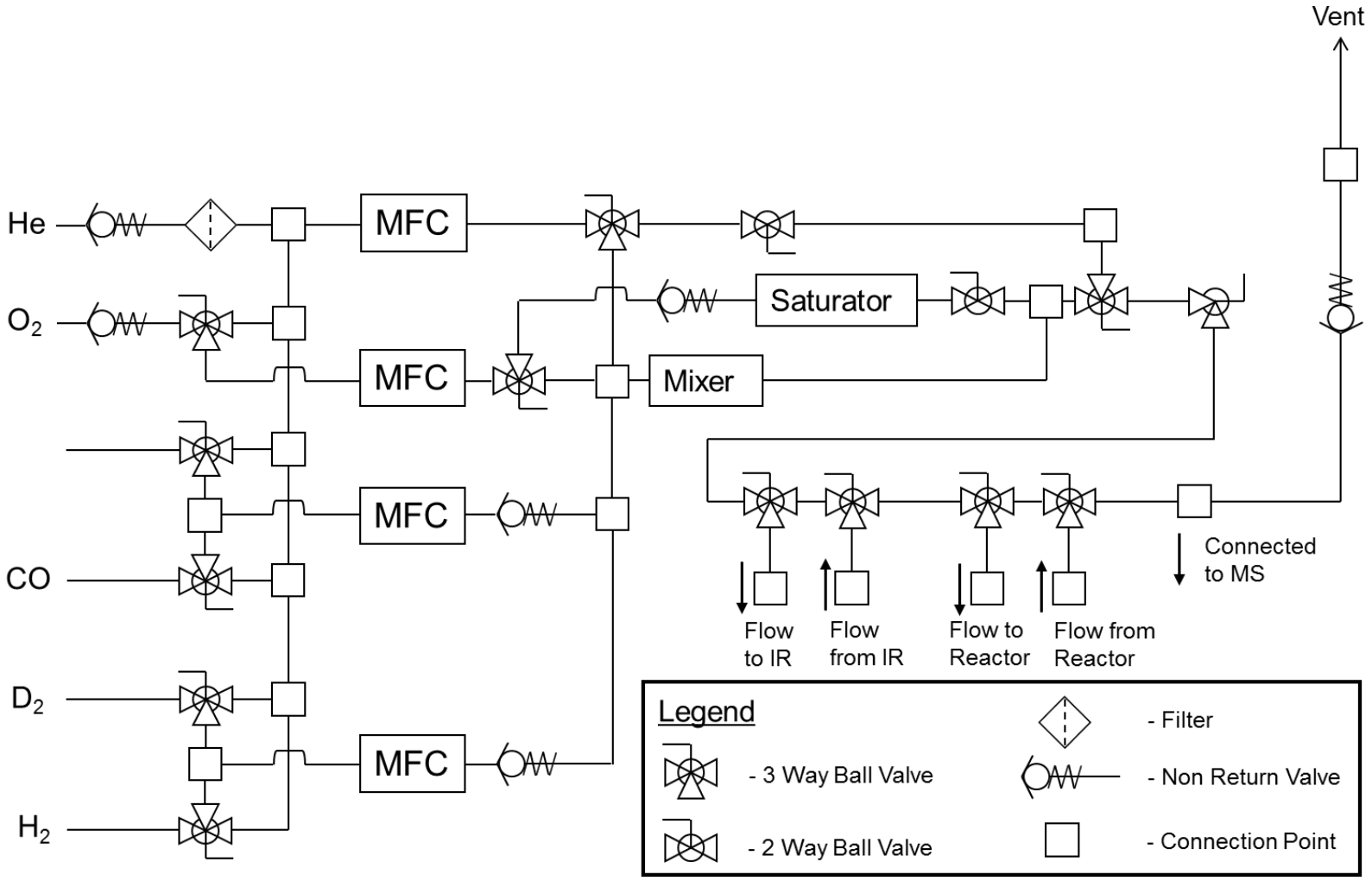

Figure 13: **A schematic line drawing diagram of the gas handling apparatus used for the micro-reactor measurements. Abbreviations include MFC – mass flow controller, IR – infrared spectrometer and MS – mass spectrometer.**

2.2.2. Large-scale Reaction Testing

Large-scale reactions were performed on a custom-built gas line at the ISIS Facility at the Rutherford Appleton Laboratories (Chilton, Didcot, Oxfordshire), and the design is based upon that of the micro-reactor (**Figure 13**). A schematic of the large-scale reactor gas line is shown in **Figure 14**.[66] The gas line is composed of ¼ in. O.D. stainless steel tubing with Swagelok tube fittings. Gas flows are controlled by four Hastings (HFC302) mass flow controllers attached to four individual Chell CCD control boxes. The MFC control boxes are displayed on the front of the reactor unit which is encased within a fume hood. One MFC has a 2000 sccm capacity whereas the other three have a capacity of 200 sccm. Catalyst samples were loaded into an Inconel/stainless steel reactor and attached to the heated gas line.[96] The Inconel cell was suitable for reactions up to 873 K and 20 bar whereas the stainless steel reactor was only suitable for moderate reaction conditions, <623 K and 5 bar pressure.[66] Therefore, both reactors were suitable for reactions within this investigation. The reactor utilised was dependent on reactor availability at the Central Facility. During reaction measurements the reactor was encased within a bucket furnace (Instron SFL, model no: TF105/3/12/F) controlled by a PID module (Eurotherm 3508). The furnace was placed on a heavy-duty automated lab jack in order to raise the furnace during reaction and to lower it from around the cell for cooling and disconnection from the gas lines. The reactant gases are analysed by an in-line mass spectrometer (Hiden Analytical, HPR20 QMS Sampling System).[66] Advances in the sample environment enabled catalyst runs of pyrophoric materials and hazardous gases to be run for extended reaction times (up to 10 days).[66,96] This required close collaboration between ISIS' Pressure and Furnace Section and the Experimental Operational Division. A number of safety devices were put in place to ensure safety of all users at the Central Facility. The laboratory was equipped with two carbon monoxide and two hydrogen detectors connected to isolation valves on the external gas manifold. During the operation of reaction conditions, each user was equipped with a personal CO detector and solo working within the laboratory was forbidden. Hazardous gas notifications were placed on the door to the laboratory that remained locked when the experiment was left unattended. Handheld battery-operated CO detectors (Dräger) were also stored outside the laboratory. The application of these safety procedures allowed for the continual running of an experiment for 10 days; this is believed to be the longest heterogeneous catalyst test reaction ever undertaken at ISIS.

For CO hydrogenation conditions, approximately 10 g of catalyst sample was loaded into an Inconel/stainless steel reactor and plugged with quartz wool. A 2:1 mix of hydrogen (CK Gases Ltd, >99.5%, 150 ml/min) and carbon monoxide (CK Gases Ltd, >99.5%, 75 ml/min) was employed respectively, with helium as a carrier gas (CK Gases Ltd, >99.5%, 600 ml/min), with a total WHSV of 1.18 h^{-1}. This gas mixture was first established over the bypass before flowing over the catalyst. The reaction was carried out at ambient pressure. The reactor was enclosed within the bucket furnace and a temperature ramp of 5 K min^{-1} was utilised until a temperature of 623 K was attained and was held for a set period of time. The standard reaction duration was for 6-8 h. The sample was cooled to room temperature in a flow of helium and isolated. The sample was transferred to an argon filled glove box (MBraun UniLab MB-20-G, [H_2O] <1 ppm, [O_2] <2 ppm) and inserted into an aluminium sample container used for acquiring INS spectra.[66] INS measurements were carried out on the MAPS spectrometer using the A chopper package. Two incident energies were chosen (650, 250 meV) that covered a wavenumber region from 200 – 4000 cm^{-1} and a chopper frequency of 400 or 600 Hz depending on the incident energy selected.[66,69]

Chapter 5 introduces a CO_2 co-feed to the standard ambient pressure CO hydrogenation conditions, therefore the composition of the reaction mixture was altered to H_2: 150 ml/min, CO: 37.5 ml/min and CO_2: 25 ml/min.[97] The flow rate of the carrier gas, helium, and catalyst mass remained the same as the standard CO hydrogenation conditions utilised in **Chapter 3** and **4**.[75] The total flow rate remains unchanged, with a WHSV of 1.48 h^{-1}.

For *ex situ* characterisation to be carried out each sample went through a passivation process, as it is unavoidable that they will be exposed to air and thus causing uncontrolled oxidation to possibly occur. Despite this process potentially resulting in the loss of some species that are present under reactive conditions, for example metallic iron, it is necessary to ensure they are safe to handle. The passivation process involves a standard procedure of slowly increasing the sample exposure to oxygen from zero up to atmospheric levels.[27,98] The standard gas line set up displayed in **Figure 14** did not have an O_2/He inlet and therefore for passivation procedures an O_2/He cylinder (5% in helium, BOC Ltd) was attached to the line specifically for the measurement, sharing an MFC with either CO or CO_2.

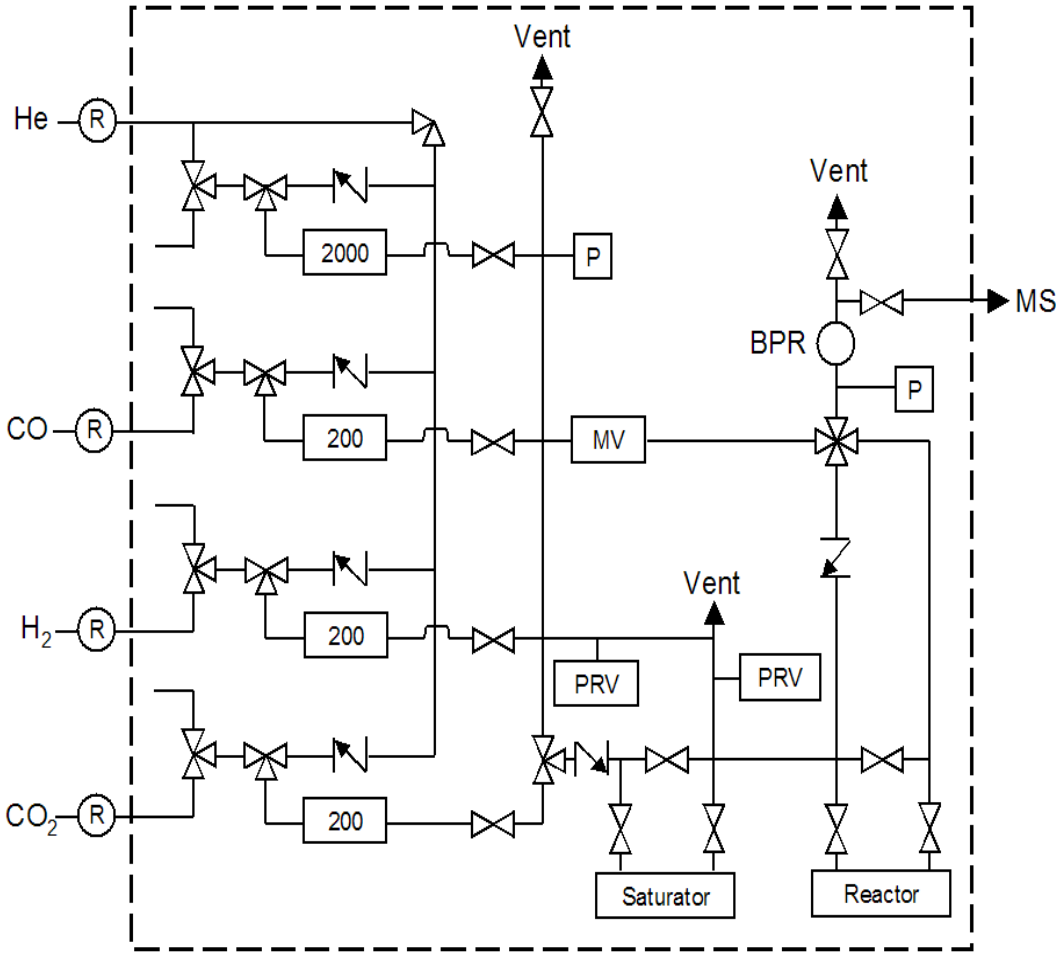

Figure 14: A schematic line drawing diagram of the gas handling apparatus used for the large-scale reaction measurements. Mass flow controllers are indicated by rectangular boxes containing the maximum flow rate (sccm). Other abbreviations include MV – mixing volume, P – pressure gauge, PRV – pressure relief valve, BPR – back pressure relief valve and MS – mass spectrometer. The dotted lines around the schematic show what is encased within the walk in fume hood. [66]

2.3. Catalyst Characterisation

2.3.1. Pre-reaction Catalyst Testing

Before reaction of the prepared iron catalyst samples, characterisation of the samples was carried out using temperature-programmed reduction (TPR), X-ray diffraction (XRD), Raman scattering, Brunauer-Emmett-Teller (BET) analysis, inductively coupled plasma optical emission spectroscopy (ICP OES), scanning electron spectroscopy (SEM), transmission electron spectroscopy (TEM) and X-ray photoelectron spectroscopy (XPS). TPR measurements are carried out using hydrogen as the reductant in a 1:4 mix with helium and are performed on the micro-reactor set-up (**Figure 13**). XRD diffraction measurements have been performed on two separate instruments, both being a Panalytical X'Pert PRO MPD but one using Cu K_α radiation (Glasgow) and the other using Co K_α radiation (Sasol Technology UK Ltd). The cobalt radiation source is the preferred instrument as there is no occurrence of fluorescence with the iron-based samples. Access to this instrument at the Sasol laboratories was not readily available; therefore, some measurements have been performed using the instrument with a copper source. XRD measurements were performed in the 2θ range of 5-90°. Raman scattering was performed on Horiba Jobin Yvon LabRam HR confocal Raman microscope and a 532 nm laser source at <20 mW power. Measurements were performed for approximately 5 minutes. BET – N_2 physisorption measurements were performed on a Quadrasorb evo 3 BET station instrument, with degassing of samples being carried out on a Quantachrome FloVac Degasser. Samples were degassed overnight and analysed on the BET instrument the following day. ICP-OES measurements were performed at Butterworth Laboratories Ltd on behalf of Sasol Technology UK Ltd. SEM measurements were performed using a Philips XL30 ESEM which was also equipped with an Oxford Instruments INCA Energy 250 energy dispersive spectrometer system (EDS) allowing for the examination of the chemical composition of materials (detection limit ~ 0.2 wt. %). TEM was performed using a Tecnai T20 microscope with an accelerating voltage of 200 keV. Samples were suspended in methanol before being positioned on a carbon grid for insertion into the microscope. Elemental analysis was performed on an Exeter CE-440 Elemental Analyser (detection limit ~ 0.1 wt. %). XPS was acquired at Sasol Technology UK Ltd. using Kratos AXIS Ultra DLD, with a monochromatic Al K_α X-ray source (detection limit ~ 0.1 wt. %).

2.3.2. Post-reaction Micro-reactor

For *ex situ* characterisation, the samples have been exposed to a passivation procedure mentioned previously (**Section 2.2.2**) in order to prevent unwanted reactions occurring on exposure to atmosphere.[27]

Ex situ XRD, Raman and TEM are performed as described for pre-reaction samples (**Section 2.3.1**). *In situ* temperature-programmed oxidation (TPO) measurements are carried out on the micro-reactor following a CO hydrogenation reaction, *i.e.* no passivation. The mass of catalyst required to provide qualitative review of the chemistry for *in situ* TPO measurements was investigated further in **Chapter 4, Section 4.3.1**. A flow of oxygen (5% in helium, 75 ml/min, BOC Ltd) is introduced over the sample with a temperature ramp of 5 K min^{-1} up to 1173 K. The carbon dioxide mass trace is measured using the in-line mass spectrometer. The peak areas of the CO_2 trace were quantified by using known weights of graphite (Sigma Aldrich, 99.99%) and exposing to TPO conditions. The integrated areas of the CO_2 trace from the thermally decomposed graphite were plotted against mass of carbon to create a calibration curve (**Figure 15**). The regression line of the linear response links integrated mass spectrometer response with a known weight of carbon. For *in situ* measurements carbon values are normalised to grams of iron present (g_{Fe}^{-1}) in the amount of starting material as opposed to per gram of catalyst (g_{cat}^{-1}). This is due to the fact that the amount of iron oxide present will change over the course of the reaction whereas the amount of iron will stay constant.

For *ex situ* temperature-programmed measurements approximately 10 mg of catalyst is loaded into the quartz tube reactor and exposed to the same reaction conditions as described for the *in situ* measurements. Discussion of the mass utilised for this measurement is presented in **Chapter 3, Section 3.3.2.** It is noted that the micro-reactor TPO arrangements has limitations. Firstly, the degree of oxygen in the feed stream (5% O_2/95% He) is restricted for safety reasons. The concentration level selected ensures that the system is always within the explosive limits for an oxygen/fuel reaction.[99] Secondly, the degree of carbon that is quantifiably detectable within the micro-reactor has an upper limit before it can exhaust the available oxygen supply. Should carbon deposition during reaction testing become excessive, the only way to perform quantitative measurements is to reduce the mass of catalyst being analysed. However, it is observed that the mass of catalyst can influence the gas/solid exchange dynamics that may affect the TPO profiles observed.

Iron samples which contained varying levels of sulfur, and a fixed level of sodium, discussed in **Chapter 4**, were analysed at the Diamond Light Source, Harwell using the B18 beam line measuring the sulfur K-edge. Emma Gibson (University of Glasgow) and Giannantonio Cibin (Diamond Light Source) assisted with these measurements.

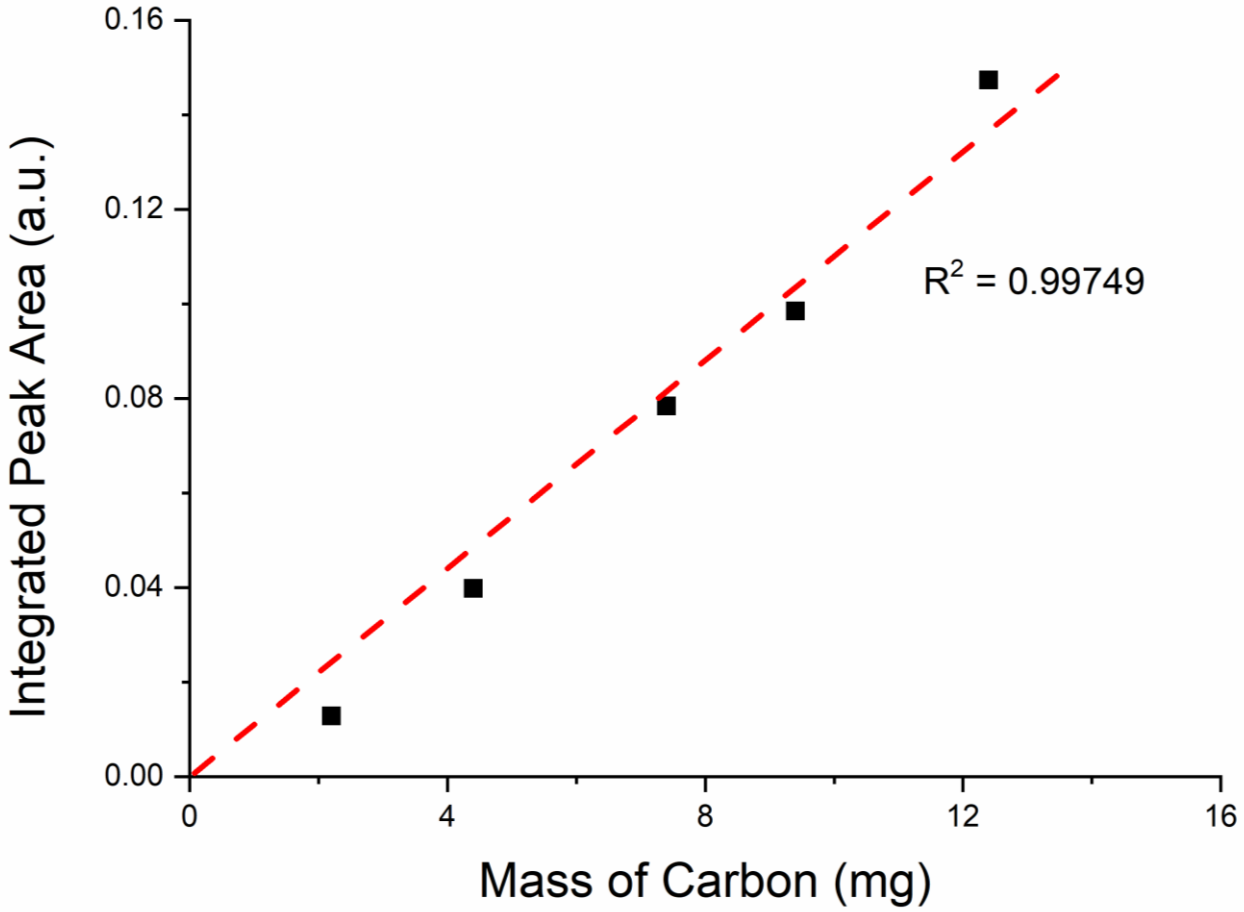

Figure 15: Linear plot ($y = 0.01101x$) of the integrated area of the CO_2 trace of the known weights of graphite exposed to TPO conditions against the mass of the graphite calibration material used. The R^2 value is 0.99749.

2.3.3. Post-reaction Large-scale Reactor

INS analysis was carried out after performing ambient pressure CO hydrogenation reactions on the iron-based catalysts using the scaled-up apparatus as outlined in **Section 2.2.2**. After the heating and flow of reacting gases was stopped, the reactor was cooled to room temperature in a flow of helium. The cell was transferred to an argon filled glove box (MBraun UniLab MB-20-G, [H_2O] <1 ppm,[O_2] <2 ppm) where the catalyst samples were loaded into aluminium cells and sealed using an indium wire gasket.[66] Once assembled in the INS cell, the samples were analysed on the direct-geometry instrument MAPS giving a spectral range of 200 – 4000 cm^{-1}. An aluminium cell is required for INS acquisition as the cell itself gives reduced background in comparison to the Inconel and stainless-steel reactors. However, the Inconel/stainless steel reactors are required for the reaction measurements due to the high temperatures utilised for the reaction of the iron catalysts.[66]

The MAPS spectrometer for INS measurements was calibrated to quantify the number of hydrogen atoms present on the catalyst surface with the quantification procedure previously described within the literature.[100]. Polystyrene (Sigma Aldrich, average M_w = 350,000) was used chosen as a reference material as it provides a reference for ν(C-H) stretching modes and has the presence of two different types of hydrogen, aliphatic (~2900 cm^{-1}) and aromatic (~3100 cm^{-1}). A high molecular weight variant of polystyrene was used to minimise the effect of terminal groups, simplifying the formula mass to $C_6H_5C_2H_3$, corresponding to 8 hydrogen atoms per sub-unit. The simplified formula mass was used in determination of the number of hydrogen atoms per sample mass used. Known weights of polystyrene were selected, loaded into sachets of aluminium, contained within the aluminium sample holders and run on the MAPS spectrometer using the "A" chopper package with a frequency of 600 Hz and an incident energy of 650 meV. As the mass of polystyrene is increased the formation of two distinct peaks at ~3000 cm^{-1} with increasing intensity (**Figure 16(a)**) are observed. The observed bands were fitted and integrated using the Origin graphical software package (OriginPro, version 2018). A plot of the integrated intensity for the ν(C-H) feature as a function of sample mass reveals a straight line (**Figure 16 (b)**, R^2: 0.99896). The spectral response is directly proportional to the number of hydrogen atoms present in the beam which is confirmed from the linearity of the response. During the course of this project the MAPS spectrometer was upgraded which included an installation of a new neutron guide and new choppers which, in turn, increased the flux. Therefore, to ensure the integrity of the calibration measurements, the procedure was repeated after the upgrade and the results are presented within the appendices (**Figure 70**).

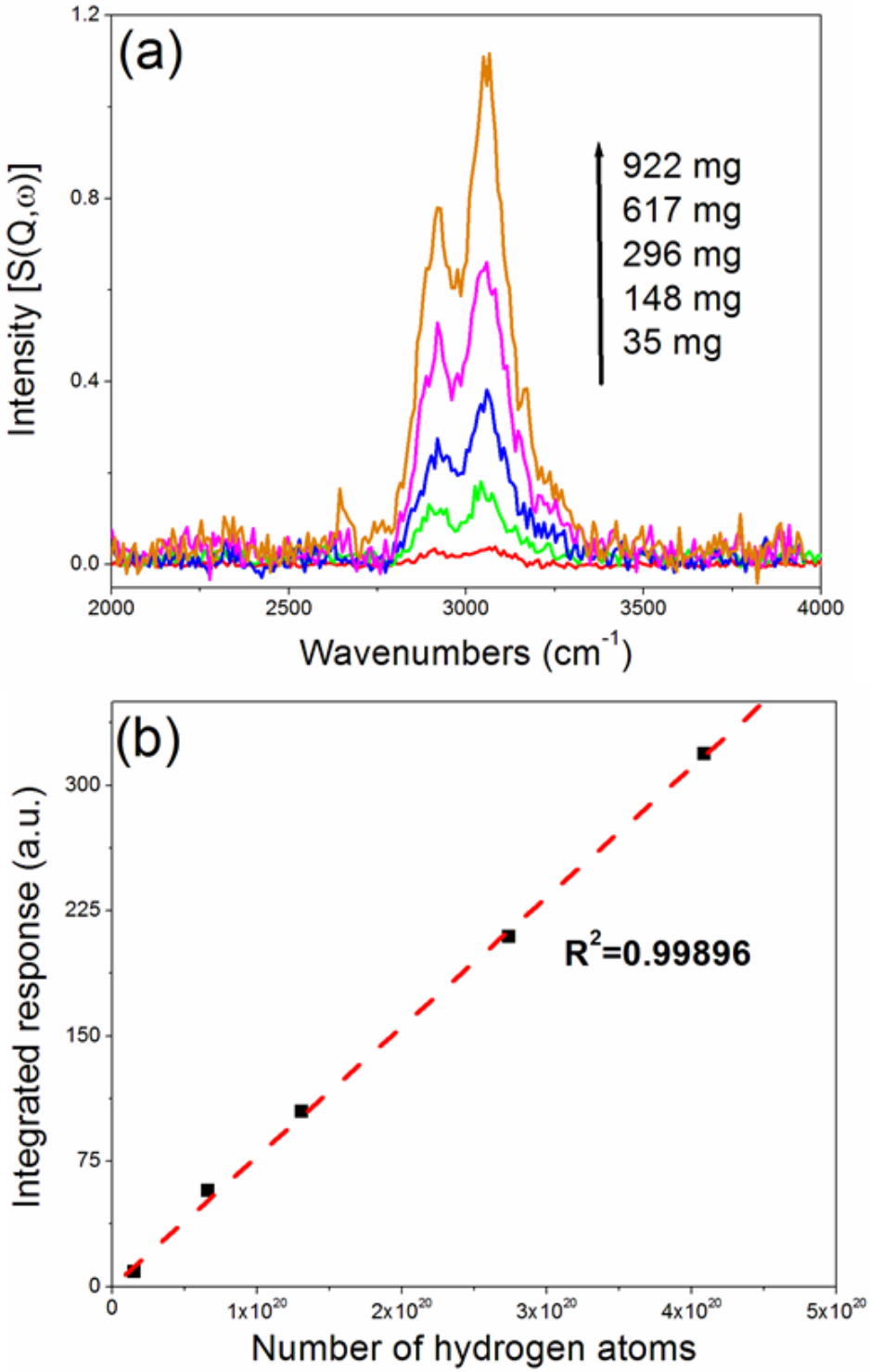

Figure 16: (a) The baseline corrected INS spectra of the varying masses of polystyrene recorded on the MAPS spectrometer at incident energy 650 meV. The spectra were obtained using the 'A' chopper package. (b) Linear plot ($y = 8 \times 10^{-19}x$) of the integrated areas of each of the polystyrene features ν (C-H) present in (a) against the number of hydrogen atoms present in each mass of polystyrene used. The R^2 value is 0.99896.

Chapter 3 – CO hydrogenation at 623 K: temporal behaviour of the hydrocarbonaceous overlayer on a reference hematite catalyst over an extended period of time-on-stream

3.1. Introduction

Highlighted within the thesis introduction (**Section 1.3**), iron-based FTS catalysts are known to go through an evolutionary period during the initial stages of reaction. The pre-catalyst is often composed of hematite or magnetite, which on exposure to a pre-treatment step or under FTS conditions, is reduced towards α-Fe and iron carbides, with the final composition of the catalyst being dependent on the reaction conditions utilised.[2,23–25] The complex nature of iron catalysts will affect FT activity reaching a steady-state as the catalyst progresses through this evolutionary period. Despite there being some debate over the particular active species of an iron catalyst, there is a general consensus that Fischer-Tropsch activity correlates with the formation of iron carbides.[22,26,36] Furthermore, a study by Perez-Alonso *et al*. displayed that FT catalytic activity may initially decrease but, for continuing time on steam (T-o-S), the activity will once again rise and return close to its original activity over a period of *ca.* 120 h; the changes are attributed to variations in the composition of the iron catalyst in the initial stages of the reaction.[101] This is also in agreement with Buker and co-workers who reported an iron FTS catalyst to require approximately 100 h to reach a steady-state.[102] However, it is noted that the extent of the initial conditioning period will be dependent on several factors including reactor configuration, gas hourly space velocity (GHSV), gas composition, pressure and temperature.

Previous work by Hamilton and Warringham *et al*. have described the application of inelastic neutron scattering (INS) to investigate the formation of a hydrocarbonaceous overlayer on both industrial and laboratory prepared iron-based catalysts that can be utilised for FTS reactions.[76,94,103–105] These investigations serve as a basis for the work undertaken within this thesis. The main aim of this chapter is to build upon previous INS investigations of an Fe-based FTS catalyst that correlate CO hydrogenation activity with the formation of a hydrocarbonaceous overlayer. In particular, the work carried out by Warringham who studied the evolutionary profile of a high specification iron catalyst (**Fe-**

ref) up to 24 h.[73] From this initial study, it was identified that growth of the hydrocarbonaceous overlayer was incomplete and the catalyst was still undergoing this evolutionary period that is suggested within the literature. The work presented within this chapter is a direct extension of the afore-mentioned study and, for the first time, examines the formation of the hydrocarbonaceous overlayer over extended time scales (0 – 240 h), more representative of that encountered in the industrial operation. Application of INS, alongside other analytical techniques such as X-ray diffraction, Raman spectroscopy and temperature-programmed oxidation measurements, are utilised to investigate how hydrogen is partitioned within an unpromoted FTS catalyst (**Fe-ref**), the same catalyst utilised by Warringham,[73] for an extended period of time on stream (0 – 240 h), for an ambient pressure CO hydrogenation reaction. A model previously proposed within Warringham's PhD thesis,[73] linking the supply of hydrogen and the hydrocarbonaceous overlayer has since further been developed and will be discussed at the end of this chapter (**Section 3.5**).

3.2. Characterisation of Catalyst As-prepared

A hematite pre-catalyst (α-Fe_2O_3), with no promoters or support was prepared using the procedure outlined in **Section 2.1.1**. and is referred to as **Fe-ref** throughout this chapter. BET, ICP-OES, XRD, Raman spectroscopy, TEM and TPR have all been applied to characterise the sample before exposure to CO hydrogenation conditions. **Table 4** presents a summary of the relevant information obtained from BET, ICP-OES and application of Scherrer equation from the XRD diffractogram (**Figure 17**) to calculate the particle size.

Table 4: Tabulated data of surface area and pore volume obtained from BET, particle size (nm) obtained from application of Scherrer equation to XRD diffractogram and mol % of iron from ICP-OES. Parentheses represent standard deviation from triplicate measurements.

Sample	Surface Area (m^2g^{-1})	Pore Volume ($cm\ g^{-1}$)	Particle Size (nm)	mol % of Fe
Fe-ref	47.51 (± 3.21)	0.230 (± 0.008)	16	68.2

The XRD diffractogram (**Figure 17)** displays reflections at 2θ = 28.2, 38.8, 41.7, 47.9, 58.1, 63.8, 68.1, 74.2, 76.1 and 86.1°. By application of the programme Highscore Plus,[106] reflections are characteristic of highly ordered hematite and by application of the Scherrer equation,[86–88] the mean crystallite size is estimated to be 16 nm as shown in **Table 4** above. This correlates well with that observed previously for this catalyst sample.[105] The high purity and high homogeneity of the sample, *w.r.t.* crystallite size, is achieved through the use of the automated sample preparation apparatus described in **Chapter 2, Section 2.1**.

Figure 18 presents the TPR profile of the **Fe-ref** sample monitoring the water trace on the mass spectrometer as the temperature is increased. Two distinctive peaks are present at 597 and 779 K and are representative of the step-wise reduction process of hematite towards metallic iron (*Equation 3.1*).[107] The first feature at 597 K is indicative of α-$Fe_2O_3 \rightarrow Fe_3O_4$ and the second feature, at 779 K, is representative of $Fe_3O_4 \rightarrow \alpha$-Fe. However, it is proposed that the second step goes through FeO as an intermediate, although this species is difficult to observe in temperatures below 893 K due to it being a metastable compound and disproportionates into Fe_3O_4 and Fe below this temperature (*Equation 3.2*).[108–112]

$$\text{Hematite } (\alpha Fe_2O_3) \rightarrow \text{Magnetite}(Fe_3O_4) \rightarrow \text{Wüstite } (FeO) \rightarrow \alpha Fe \quad (\mathbf{3.1})$$

$$4FeO \rightleftharpoons Fe_3O_4 + Fe \quad (\mathbf{3.2})$$

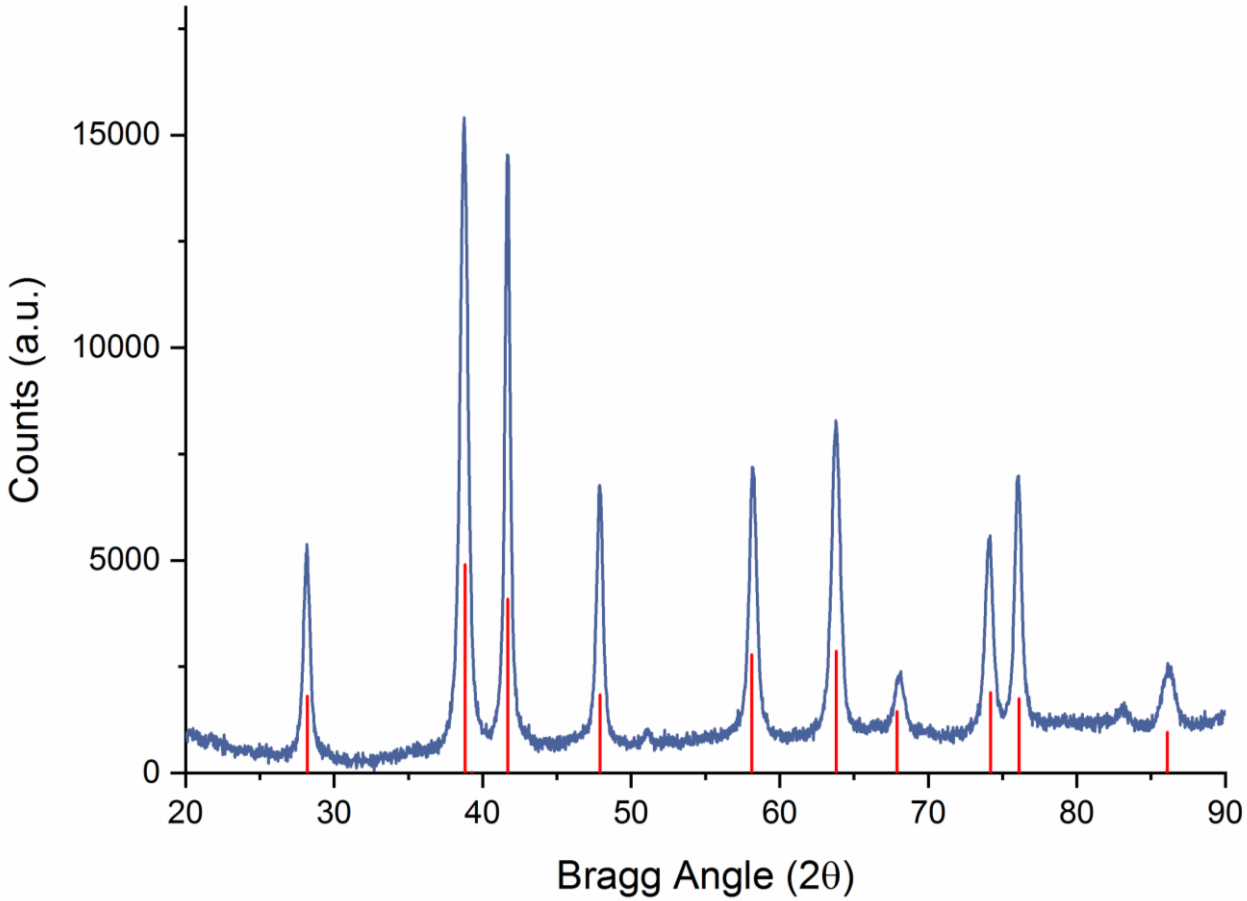

Figure 17: The powder XRD (Co K_α) of the hematite reference catalyst sample (Fe-ref) as-prepared. The red lines are indicative of reflections corresponding to α-Fe_2O_3 reference diffractogram from the programme Highscore Plus.[106]

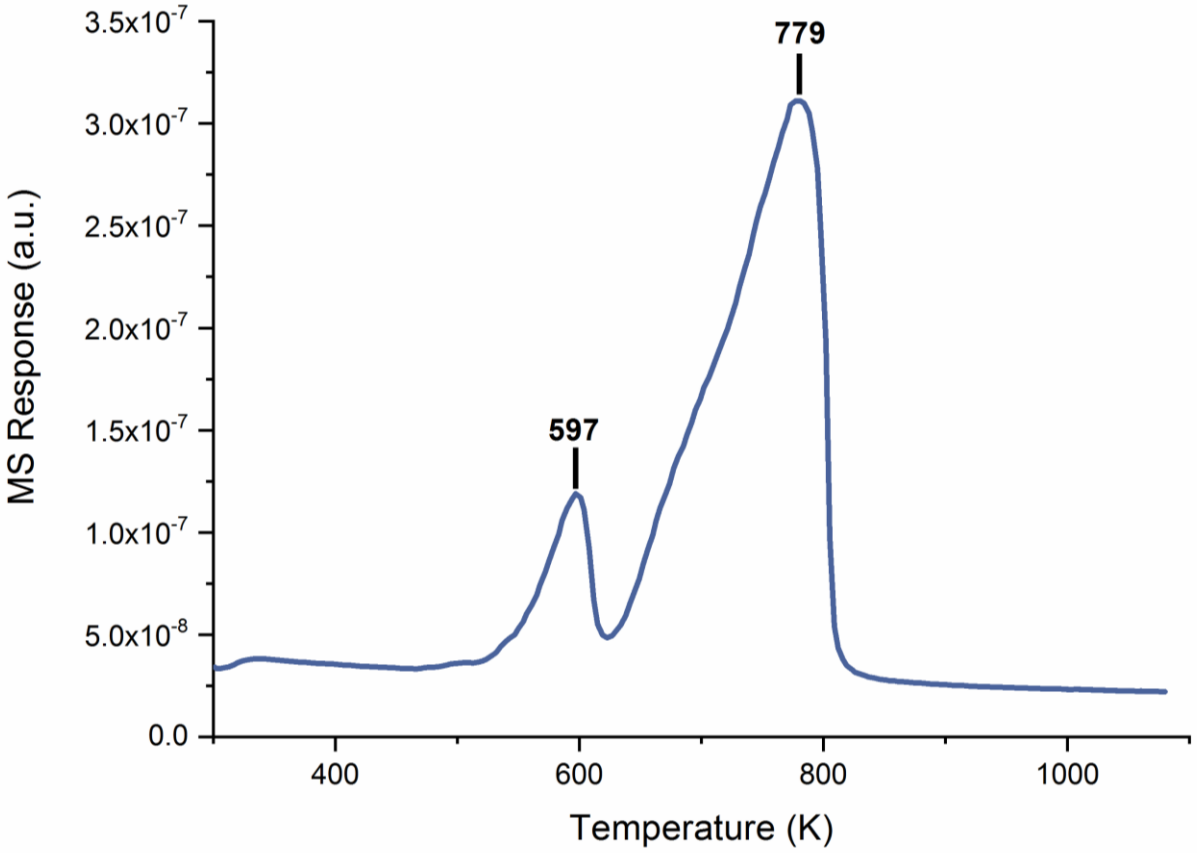

Figure 18: The *in situ* temperature-programmed reduction profile (with hydrogen) of the hematite reference catalyst (Fe-ref).

Upon characterisation of **Fe-ref** by Raman spectroscopy, three other iron-based materials, supplied by Sasol Technology Ltd., were tested: hematite (α-Fe_2O_3), magnetite (Fe_3O_4) and maghemite (γ-Fe_2O_3). The features observed in the reference materials (hematite (**Figure 19 (b)**), magnetite and maghemite (**Figure 20**)) all match closely with values reported within the literature.[113–115] The Raman spectrum of the **Fe-ref** catalyst (**Figure 19 (a)**) has features present at 223, 292, 408, 495, 608, 660, 1316 cm^{-1} which all match closely with the pure hematite sample and also complements the XRD (**Figure 17)**, confirming that the sample prepared consists of α-Fe_2O_3, the intended output. **Table 5** presents a comparison of the bands observed for the **Fe-ref** catalyst (**Figure 19 (a)**) against values reported within the literature.[113-116]

Table 5: A comparison of the bands observed for Fe-ref and of hematite in comparison to that reported within the literature.[113–116]

Observed Raman Shift (cm^{-1})	**Reported Hematite Values (cm^{-1})**
222	222
292	290
407	408
498	498
608	607
1311	1320

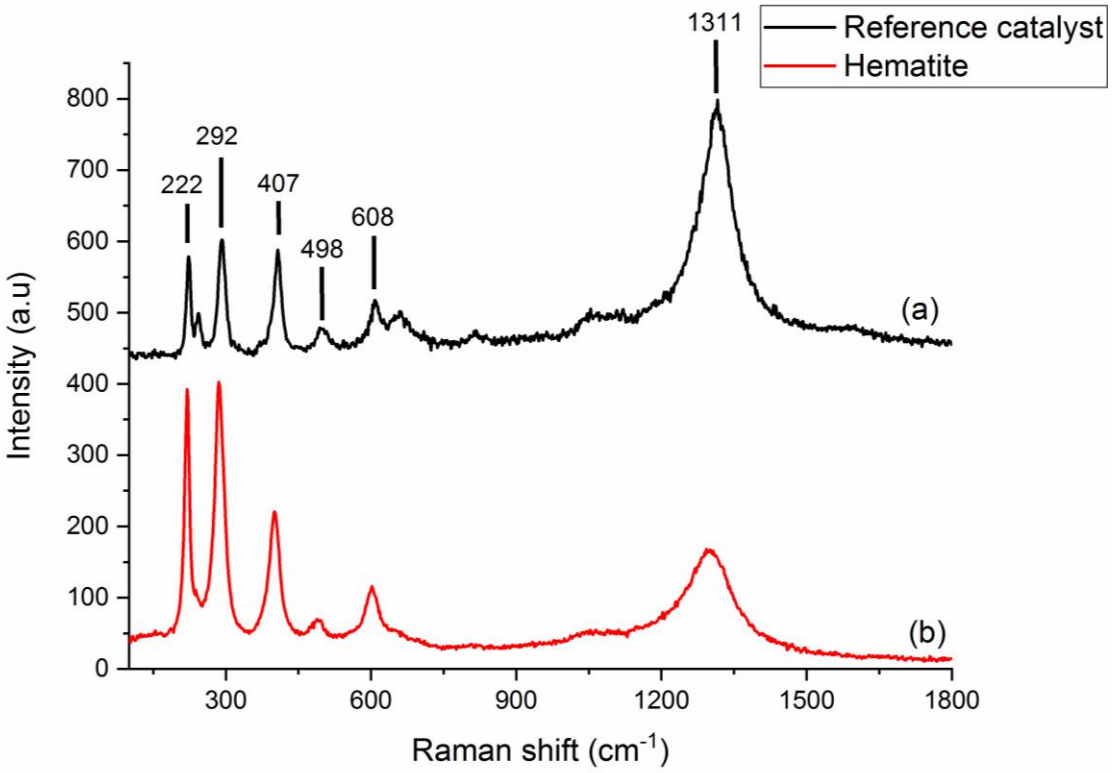

Figure 19: The Raman spectra of (a) the reference catalyst sample (Fe-ref) and (b) a pure hematite sample.

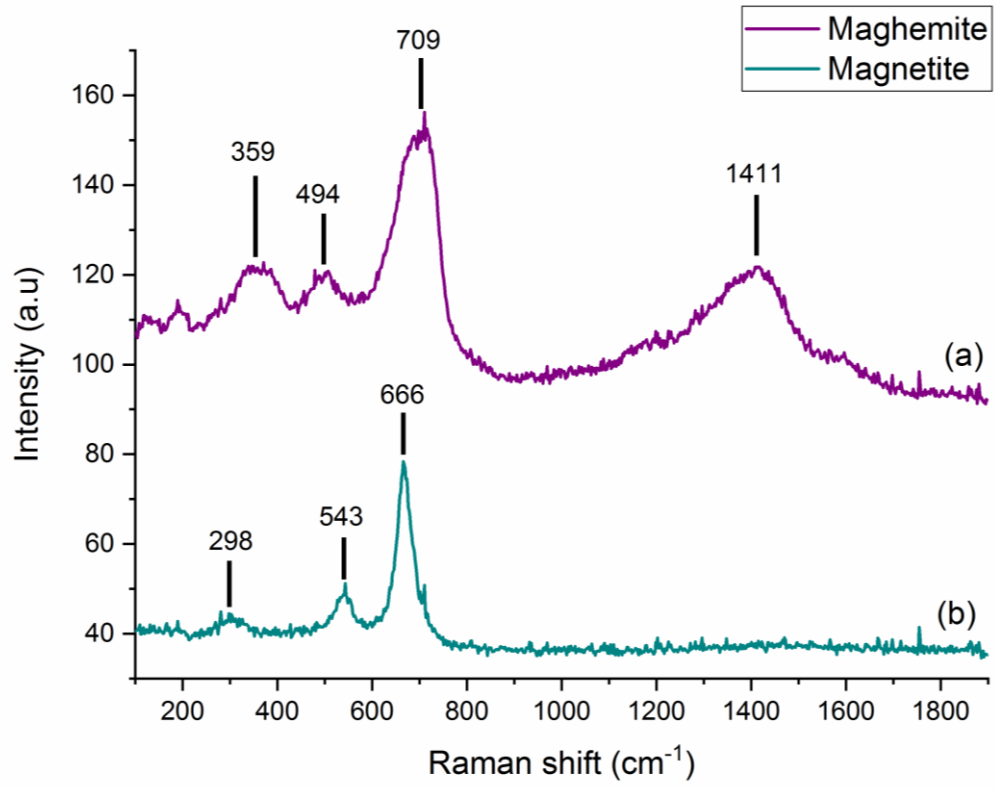

Figure 20: The Raman spectra of (a) maghemite (γ-Fe_2O_3) and (b) magnetite (Fe_3O_4) samples.

Figure 21 presents a transmission electron micrograph (TEM) of the **Fe-ref** sample displaying the micro-crystallinity of the sample which exhibits an average diameter of 16 nm, in agreement with the XRD (**Figure 17**). The indexing of the lattice spacing of the high resolution transmission electron micrograph (HRTEM) shown in **Figure 22** indicates a d-spacing of 0.361 nm and is consistent with α-Fe_2O_3 (d(012) = 0.368 nm).[117] Donald MacLaren and Colin How (School of Physics and Astronomy, University of Glasgow) assisted with these measurements.

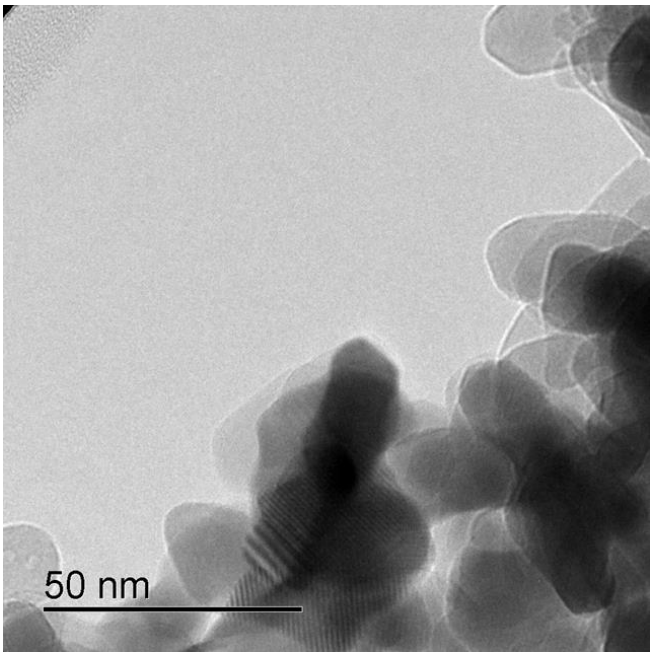

Figure 21: The transmission electron micrograph of the unpromoted α-Fe_2O_3 sample before exposure to CO hydrogenation conditions. The scale bar is indicative of 50 µm

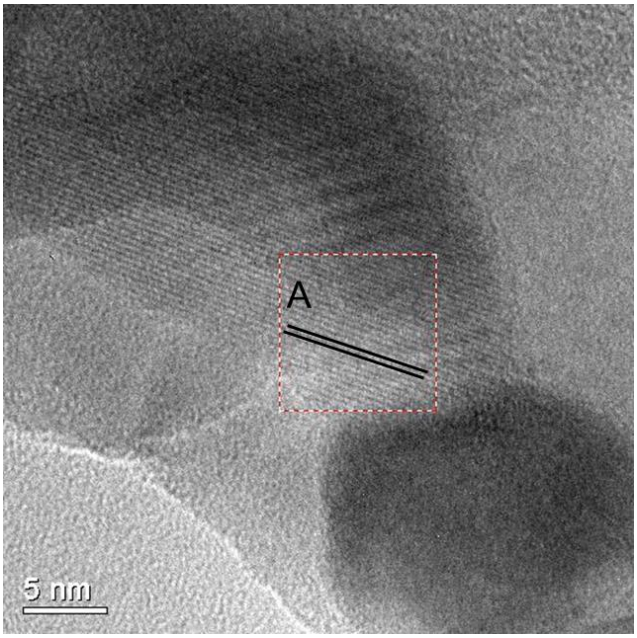

Figure 22: High-resolution transmission electron micrograph of the unpromoted α-Fe_2O_3 sample before exposure to CO hydrogenation conditions. The white scale bar is indicative of 5 nm.

3.3. Large-scale Reaction Testing

The introduction to this chapter (**Section 3.1**) refers to Hamilton and co-workers applying INS to investigate an industrial grade catalyst. This catalyst was supplied by Sasol Ltd and taken from their Secunda coal-to-liquids FTS plant in South Africa, from a reactor operating under steady state conditions. However, before analysis of the catalyst, Soxhlet extraction had to be utilised in order to remove heavy wax residues that had formed on the catalyst surface which would otherwise complicate the INS spectra.[76] This led to the application of a CO hydrogenation reaction as a representative FTS reaction in the future testing of laboratory prepared catalyst samples with the aim to minimise the complexity of the system.[94,103–105] This methodology is applied within this chapter and throughout the thesis for reactions carried out on the large-scale reactor at the ISIS Facility as well as the micro-reactor set-up in Glasgow. Despite not being fully regarded as FTS chemistry as no polymerisation takes place, it allows definition of $Fe/H_2/CO$ surface chemistry which is associated with FTS.

INS is a relatively insensitive technique, therefore a large sample mass, approximately 10 g of catalyst, is required for analysis in order to obtain a reasonable signal to noise.[96] This results in the need for a large-scale reactor system at the ISIS Facility to prepare the samples as outlined in **Section 2.2.2**. For this chapter an unpromoted hematite catalyst (**Fe-ref**) was exposed to CO hydrogenation conditions for varying lengths of time: 48, 96 and 240 h on stream. A sample was also exposed to only dehydration conditions to obtain a comparable background spectrum for the INS data. Giovanni Rossi and James Campbell (School of Chemistry, University of Glasgow) assisted with sample preparation. The reactions were monitored using a Mass Spectrometer (MS) which was connected to the gas line, positioned after the reactor and a representative reaction profile for one of the reactions (96 h on stream) is shown in **Figure 23**. The scaled-up reaction profile can be divided into two main stages. *Stage I* occurs as the reaction approaches the reaction temperature of 623 K and is signified by the simultaneous production of methane, water and carbon dioxide. At this stage the catalyst is undergoing reduction from hematite to magnetite. *Stage II* occurs approximately after 7 h and is identified by the reaction system reaching a pseudo-steady state. No wax products were detected over the course of the measurement, which as stated previously, is indicative that this selected regime (*i.e.* CO hydrogenation at ambient pressure) does not induce long chain hydrocarbons normally associated with FTS chemistry. It is noted that CO_2 production drops quite dramatically over the reaction period. This was also noted by Warringham *et al*.[94] who suggested that

the main route of CO_2 production is predominantly from the reduction of α-$Fe_2O_3 \rightarrow Fe^0$. From the reaction profile (**Figure 23**) the decrease in CO_2 correlates with the CO returning to a steady state regime which would therefore suggest that by approximately 7 h on stream the catalyst has been fully reduced. From reaching a steady-state until the end of the reaction period studied *i.e.* 240 h on stream, the production of CO_2 remains constant which would suggest that the water gas shift (WGS) reaction (*Equation 3.3*) is occurring simultaneously to the methanation pathway. Over the course of the reaction there is also a noticeable depletion in the water feature. This could be caused either by a reduction in the hydrogenation of surface oxygens or the WGS activity has increased.

$$CO_{(g)} + H_2O_{(g)} \rightleftharpoons CO_{2(g)} + H_{2(g)} \quad (\mathbf{3.3})$$

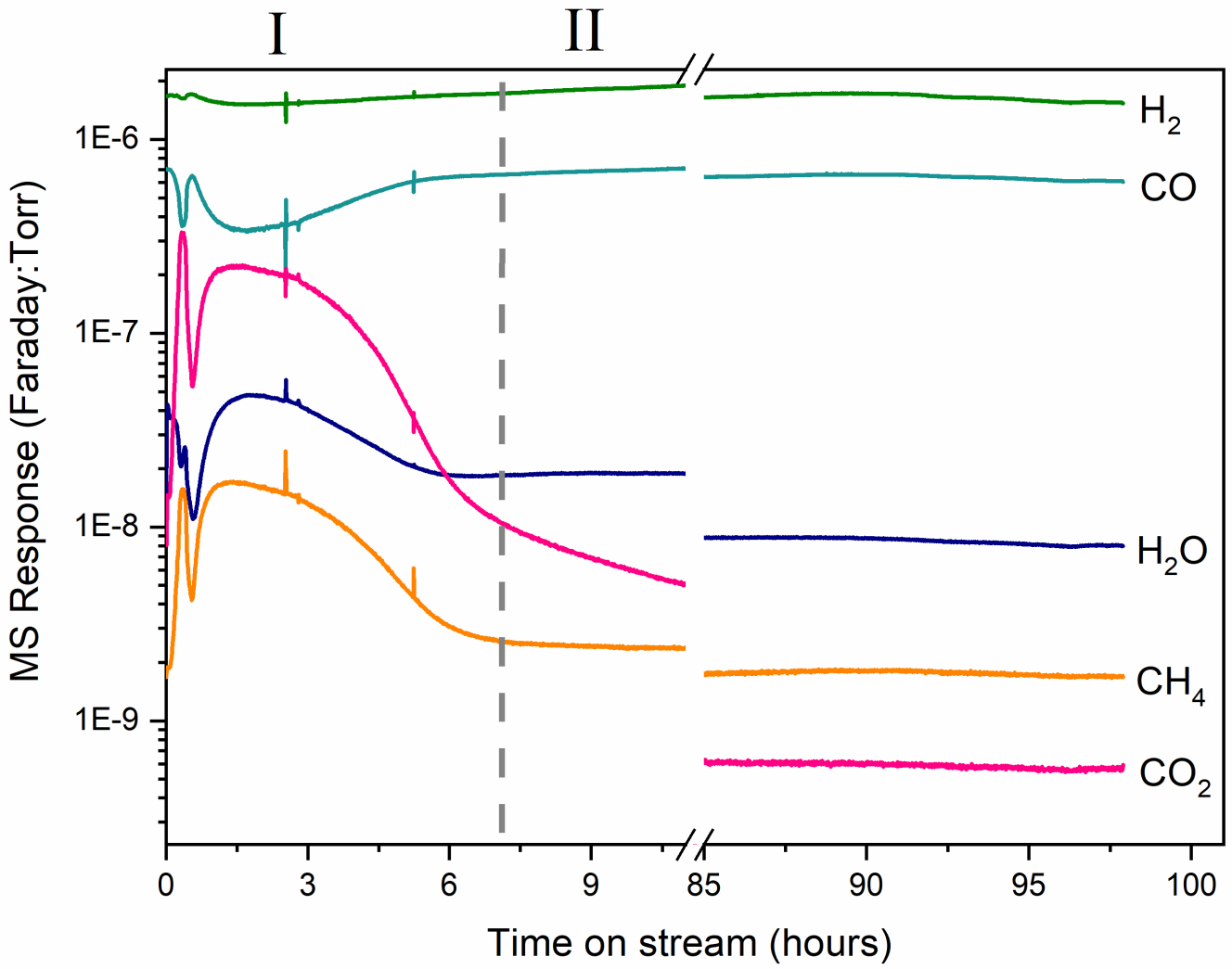

Figure 23: Mass spectrometer reaction profile for a large-scale reactor of a CO hydrogenation reaction over the reference hematite catalyst (Fe –ref) at 623 K, ambient pressure, for 96 h. The mass traces are labelled on the right hand side.

3.3.1. Inelastic Neutron Scattering

Once reaction testing on the catalyst samples was complete, the Inconel/stainless steel reactor was transferred to an argon filled glove box where the sample was removed and placed in an aluminium INS cell and sealed with indium wire.[66] The transfer of the sample to an aluminium cell was necessary as the reactors utilised for reaction (*i.e.* high temperatures) are observable in the INS spectra in the lower energy regions whereas contributions from aluminium is minimal.[66] The sample was measured on the MAPS spectrometer and recorded at two incident energies: 650 meV (5243 cm^{-1}) and 250 meV (2016 cm^{-1}).

Figure 24 displays the υ(C – H) region (2200 – 3750 cm^{-1}) of the INS spectrum recorded at 650 meV. As this is a direct continuation of work previously carried out by Warringham[73], data has been included within this figure, that was obtained from this prior investigation (*i.e.* sample reacted for 3 h) to give a better visual representation of the growth and development of the hydrocarbonaceous overlayer over the full 240 h studied. The figure displays two distinct features at 2932 and 3048 cm^{-1} for INS spectra of all samples that have been exposed to CO hydrogenation conditions. The former feature can be assigned to hydrogen atoms associated with sp^3 hybridised carbon atoms *i.e.* aliphatic. The latter can be assigned to hydrogen atoms that are associated with sp^2 hybridised carbon atoms, *i.e.* olefinic or aromatic υ(C-H).[104,105] In contrast, the sample that was dried and not reacted (0 h) is practically featureless except for a small but noticeable peak at 3633 cm^{-1} which can be assigned to a small population of terminal hydroxyls that are present at the surface of the hematite pre-catalyst.[103] As the sample is exposed to an increased time on stream, this feature disappears and there is the emergence of the peaks at 3048 cm^{-1} and 2932 cm^{-1}. As time on stream is increased (*i.e.* to 96 h) band intensity increases. Between 96 and 240 h, only a modest increase in the intensity is observed.

Figure 25 presents the deformation region (400-1600 cm^{-1}) of the INS spectra recorded at an incident energy 250 meV. Again, the 3 h spectrum obtained by Warringham has been included.[73] The clean, dehydrated sample (0 h) has a noticeably significant peak at 797 cm^{-1}. Following previous studies, this can be attributed to a spinon mode of the hematite pre-catalyst.[105] A spinon can be defined as a collective excitation of spins that comprise of the magnetic sublattice, which in the case of hematite, is antiferromagnetically aligned iron ions.[105] The feature is no longer present at 3 h on stream signifying the loss of the hematite structure as the carburization process advances. The 3 h spectrum is characterised by

features at 591 and 941 cm^{-1} and are indicative of an A_{1g} Fe-O phonon mode of Fe_3O_4 (591 cm^{-1}) and a possible combination of an alkenic δ(C-H) and a magnetic interaction associated with Fe_3O_4 (941 cm^{-1}).[105,115] The feature at 941 cm^{-1} is discussed in depth in a subsequent chapter (**Chapter 4, Section 4.4.2.1**). At 48 h there is the emergence of peaks at 807, 871, 953, 1160, 1389 and 1451 cm^{-1} and assignments are summarised in **Table 6**. Each of the observed features at 48 h on stream was previously observed at 6 h on stream.[94] As time is increased to 240 h the intensity of these features evolve, with little change in the spectral profile between 96 and 240 h. The features present at 1160, 1389 and 1451cm^{-1} are assigned to aromatic δ(C-H) modes.[76,94,103–105] More specifically, the feature at 1160 cm^{-1} can be assigned to a CC-H in plane deformation mode of a polyaromatic hydrocarbon; 1389 cm^{-1} to an in-plane ring deformation of a naphthalene like molecule; 1451 cm^{-1} to a semi-circle deformation mode that is potentially linked with a δ(C-H) mode associated with carbons on the perimeter of an extended polyaromatic network.[94,118] The bands observed at 807 and 871 cm^{-1} can be assigned to out of plane C-H deformation mode of either an olefinic or aromatic group.[119] Finally, the band at 953 cm^{-1} can be assigned to an alkenic δ(C-H).[76,94,103–105]

Table 6: Bands observed in the INS spectra of the Fe-ref sample before and after exposure to CO hydrogenation conditions on the large-scale reactor (Figures 24 and 25) with vibrational assignments.

Feature Observed in INS Spectra (cm^{-1})	Vibrational Assignment
591	Fe-O phonon mode of Fe_3O_4
797	Spinon mode
807	Out of plane δ(C-H)
871	Out of plane δ(C-H)
941	O-H in plane deformation/ Alkenic δ(C-H)
953	Alkenic δ(C-H)
1160	In-plane δ(C-H)
1389	In-plane C-C ring deformation
1451	Semi-circle ring C-C deformation
2932	Aliphatic υ(C-H)
3048	Aromatic/olefinic υ(C-H)
3633	Terminal O-H stretching mode

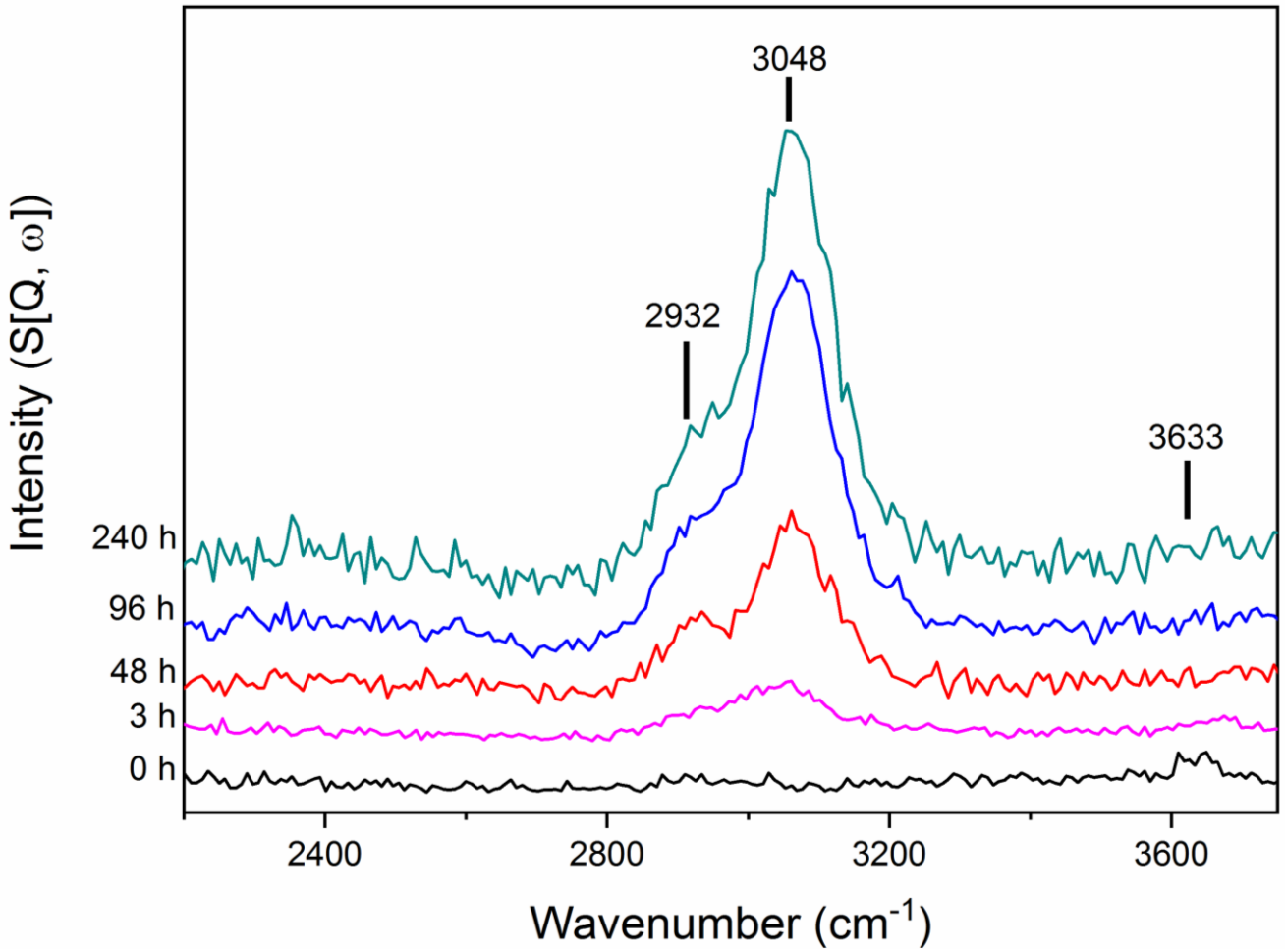

Figure 24: INS spectra (recorded at 650 meV) of the unpromoted α-Fe_2O_3 after CO hydrogenation at 623 K in the large-scale reactor. Spectrum for 3 h on stream obtained by Warringham.[73]

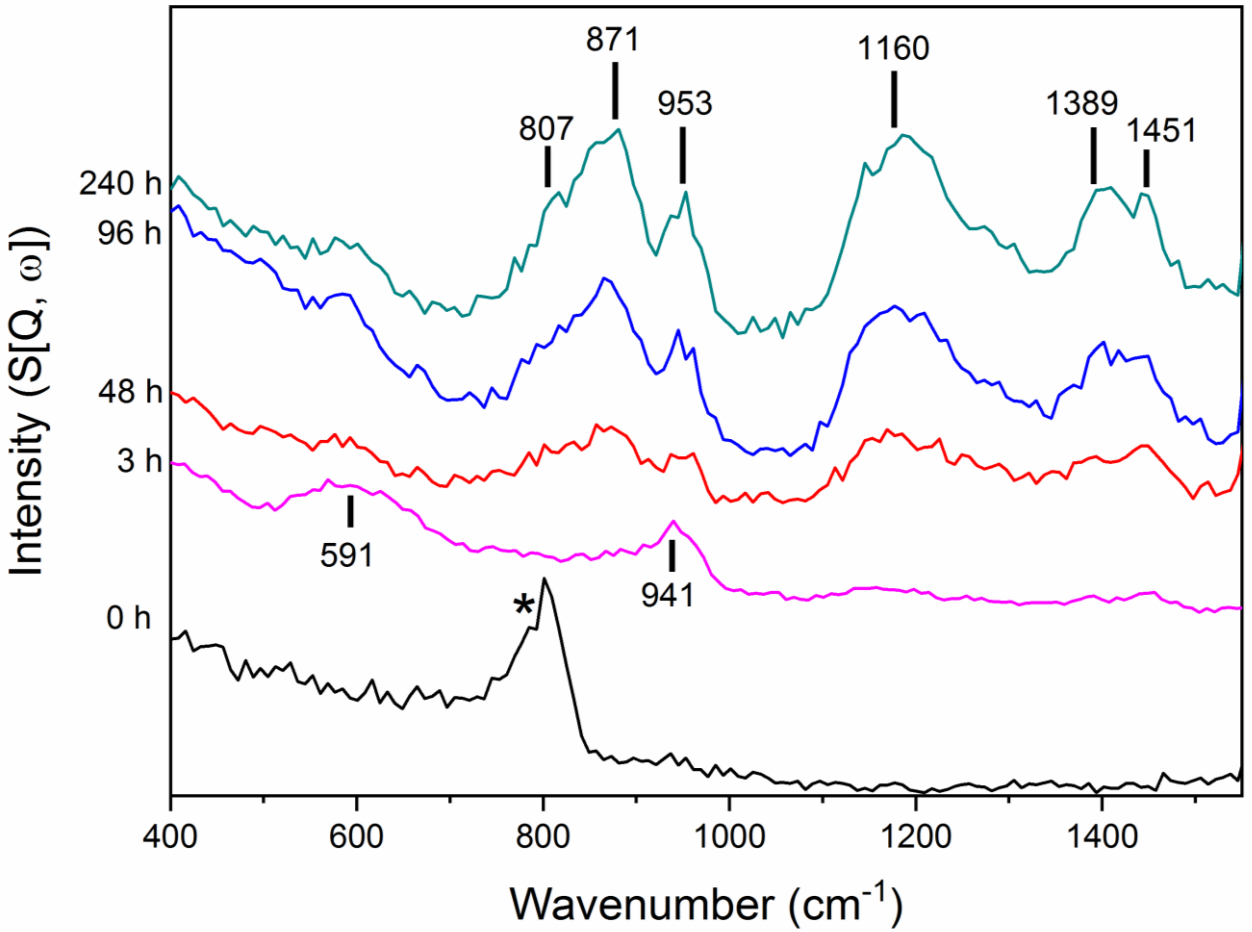

Figure 25: INS spectra (recorded at 250 meV) of the unpromoted α-Fe_2O_3 sample after CO hydrogenation at 623 K in the large-scale reactor over a 240 h period. Spectrum for 3 h on stream obtained by Warringhmam.[73] The asterisks highlights the spinon feature.

The benefit of using INS is the ability to quantify each of the species present as the intensity of each mode is proportional to the hydrogen concentration. Each feature from **Figure 24**, the sp^2 (3048 cm^{-1}) and sp^3 (2932 cm^{-1}) hybridised carbon features, was peak fitted as shown in **Figure 26**. From the calibration procedure outlined in **Section 2.3.3**., the integrated area of each feature was quantified, and the degree of hydrogen retention is presented in **Figure 27**. Incorporation of all data previously obtained by Warringham[73] is included within the plot, again allowing visualisation of the complete hydrocarbonaceous overlayer on the **Fe-ref** catalyst over the full 240 h period studied. Interestingly the aliphatic component (2932 cm^{-1}) is stabilised by approximately 24 h on stream and, thereafter, shows very little change over the course of 240 h. On the other hand, the aromatic component (3048 cm^{-1}) increases quite dramatically up to ~200 h on stream, after which hydrogen content continues to increase but at a slower rate suggesting that it is close to a maximum value about this time. The dip in hydrogen concentration at 48 h on stream can be accounted for by the fact that the measurements from 48 – 240 h on stream were carried out at a different allocation of beam time using a different batch of catalyst than samples recorded for 3 – 24 h. Overall; the formation of the hydrocarbonaceous overlayer approaches saturation after 100-200 h on stream.

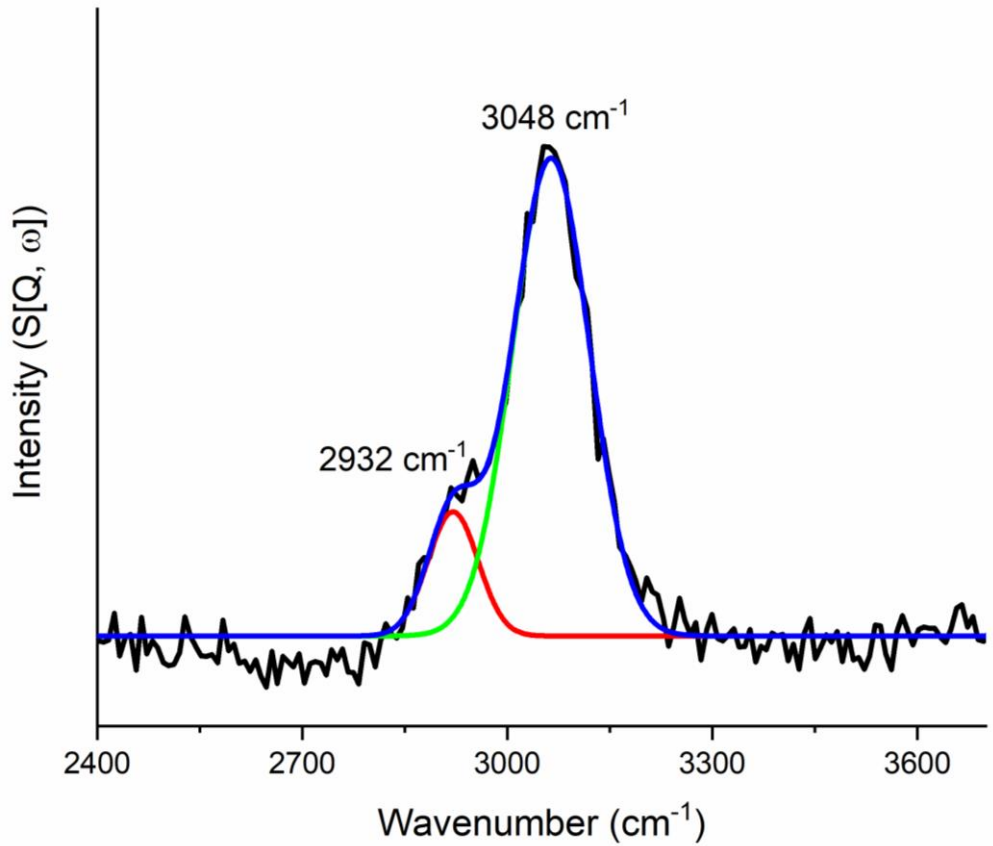

Figure 26: INS spectrum of the Fe-ref sample after exposure to CO hydrogenation conditions at 623 K for 240 h on the large-scale reactor with Gaussian peak fittings (OriginPro 2018) indicating the sp^3 (2932 cm^{-1}) and sp^2 (3048 cm^{-1}) hybridised carbon features.

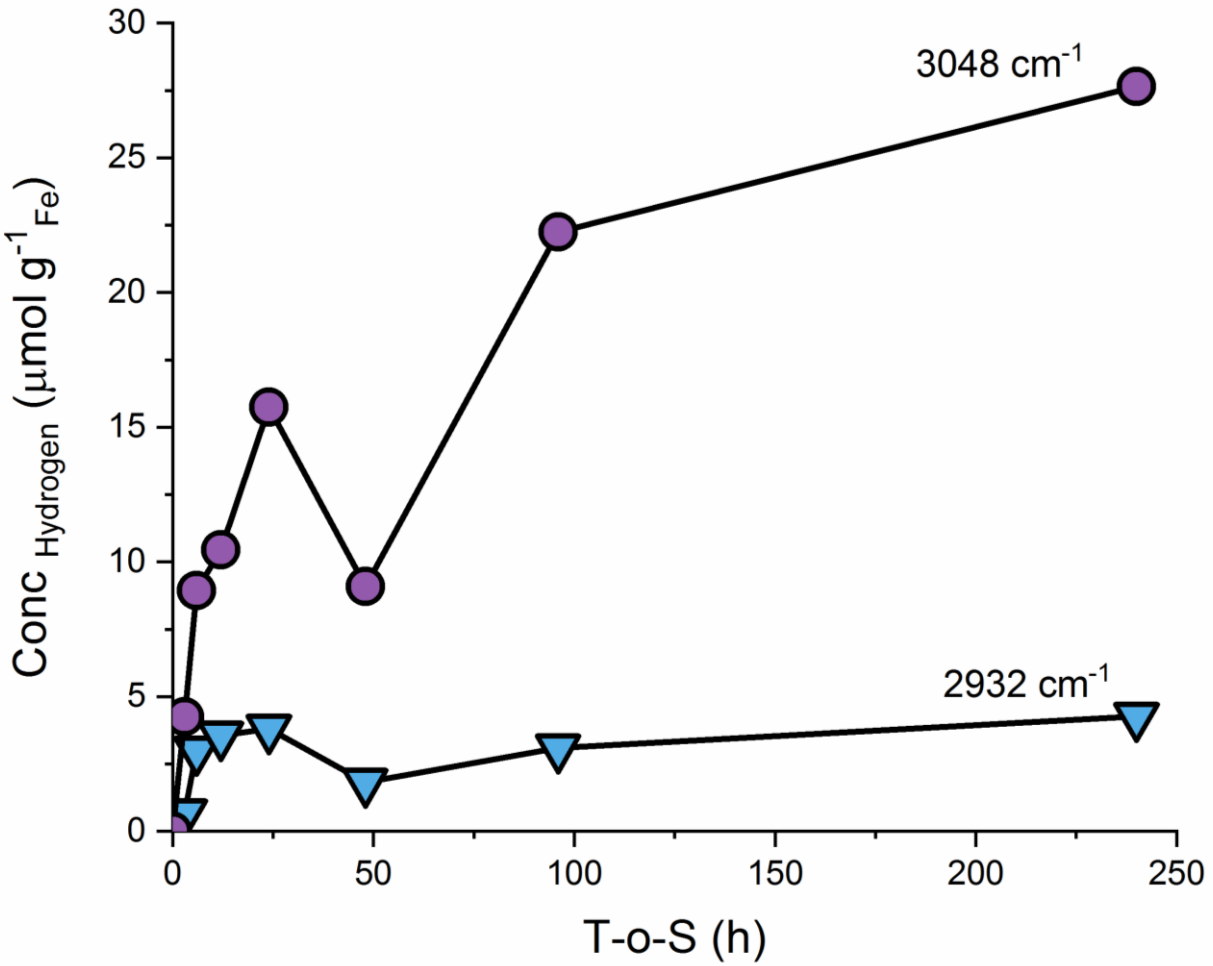

Figure 27: The quantified hydrogen content (µmol g^{-1}_{Fe}) of the features identified in Figure 24: aliphatic, sp^3 hybridised carbon feature at 2932 cm^{-1} (triangles) and aromatic, sp^2 hybridised carbon feature at 3048 cm^{-1} (circles). Data for 3-24 h obtained from Warringham.[73]

3.3.2. *Ex situ* Characterisation of the Large-scale Reactor

Following INS measurements on the MAPS spectrometer, samples underwent a passivation procedure outlined in **Chapter 2, Section 2.2.2**, which involved exposing the sample to small volumes of oxygen up to atmospheric levels.[27] After the passivation process, samples were transferred to a glass sample holder for storage and subsequently analysed *ex situ* by elemental analysis, powder XRD, Raman spectroscopy, TEM and TPO measurements.

3.3.2.1. Elemental Analysis

Elemental analysis of the catalyst before and after exposure to CO hydrogenation conditions for 48, 96 and 240 h time-on-stream enable the degree of carbon and hydrogen retention within the catalyst to be determined; the results are presented in **Table 7**. Minimal C and H are detected in the unreacted sample. On reaction there is a systematic trend of increasing C retention for increasing periods of T-o-S but the degree of which is decreasing for times ≥ 100 h. **Table 7** additionally shows hydrogen retention to be evident but to a much lesser degree than observed for C and also in a less systematic fashion. Collectively **Table 7** indicates increased retention of C (major) and H (minor) up to approximately 100 h T-o-S, with the degree of hydrogen retention just above the detection levels of the elemental analyser (detection limit ~ 0.1 wt. %).

Table 7: Elemental analysis of before and after exposure to CO hydrogenation conditions for 48, 96 and 240 h on stream. The standard deviation from measurements performed in duplicate is shown in brackets.

Time on stream (hours)	Wt % Carbon	Wt % Hydrogen
0	0.11 (±0.08)	0.08 (±0.01)
48	23.42 (±0.21)	0.17 (±0.05)
96	32.83 (±0.86)	0.39 (±0.14)
240	34.89 (±0.66)	0.27 (±0.06)

3.3.2.2. X-ray Diffraction

The *ex situ* XRD diffractograms of the iron oxide samples reacted for 48, 96 and 240 h are presented in **Figure 28**. There is very little difference between each of the reacted diffractograms. Comparing the reacted samples to the sample pre-reaction (**Section 3.2, Figure 17**) there is the loss of the reflections associated with hematite and there is the emergence of features associated with iron carbides in the range of 40 - 60°. In order to determine the specific types of iron carbide present Rietveld refinement was applied by Sasol Technology.[120] This analysis determined that each of the reacted samples, 48 - 240 h on stream, consisted of pure Hägg carbide (χ-Fe_5C_2). Previous work has shown cementite (Fe_3C) to be present in the early stages of reaction at 6 h on stream.[103] However, **Figure 28** establishes the formation of Hägg carbide to be complete by 48 h. Warringham's measurements of the same catalyst up to 24 h on stream using the large-scale reactor, identified iron carbide species to be present with XRD.[94] However, due to poor signal to noise, caused by fluorescence from the Cu K_α radiation with the iron sample, identification of the specific carbide type was not possible. The clarity of the diffractograms utilised within this section of the thesis is due to the fact that Co K_α radiation was used instead of the Cu K_α as this is more suitable for analysis of iron-based samples. Despite Warringham being unable to identify the carbide species through XRD, TEM was utilised and identified Hägg carbide to be present by 24 h on stream, which is in good agreement with the samples analysed post 24 h in this study.

The broad amorphous feature present at ~ 30° is assigned to amorphous carbon. As time on stream increases, this feature shows signs of growth; for extended time on stream this could lead to the deactivation of the catalyst. At ~ 85° there is a small peak which might be associated with metallic iron. This may be expected to be a more prominent feature but due to the analysis being *ex situ* and the catalyst having previously been exposed to a passivation procedure, the reduced iron catalyst may have oxidised slightly and therefore the origins of this feature is not as clear as expected.

The average crystalline size of α-Fe_2O_3 was 16 nm before the catalyst was exposed to reaction conditions. As time on stream is increased to 48 h, there is a decrease in the particle size of χ-Fe_5C_2 to 11 nm. However, this increases as time on stream progresses up to 240 h resulting in a particle size of 15 nm, which could be a sign of sintering of the catalyst, another cause of catalyst deactivation.

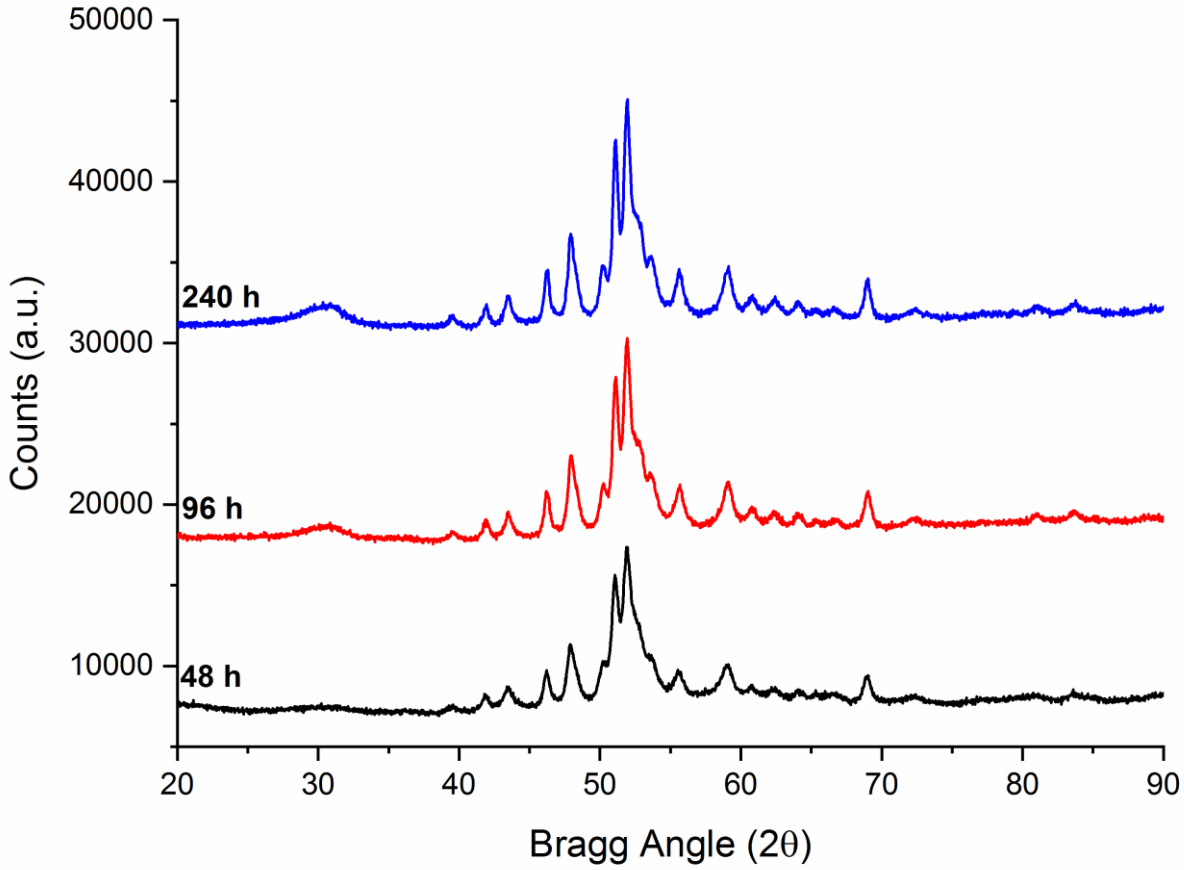

Figure 28: The *ex situ* X-ray diffractogram (Co K_α) of the unpromoted α-Fe_2O_3 after exposure to CO hydrogenation conditions at 623 K in the large-scale reactor for 48, 96 and 240 h.

3.3.2.3. Raman Spectroscopy

The *ex situ* Raman spectroscopy measurements obtained for the samples after exposure to CO hydrogenation condition for 48 – 240 h are presented in **Figure 29**. All spectra are identical and have been peak fitted using a Gaussian line function on the Origin graphical software package (OriginPro, version 2018) to identify the different carbonaceous species present between 1000 and 1800 cm^{-1}. Each of the spectra are indicative of several different carbonaceous species, mainly disordered carbon (D1 and D4 bands), amorphous carbon (D3 band), and graphitic-like carbon (G band). From XRD (**Figure 28**) and TPO measurements (**Figure 31**) there is no indication of the formation of graphitic carbon and therefore, it is proposed that the G band consists of short-range, highly ordered carbon that is graphitic-like in structure but lacks lone-range order to give rise to an extended network of graphitic carbon.[105] The post-reaction samples indicate no presence of residual hematite from the pre-catalyst identified in **Figure 19(a)**, suggesting that all the hematite has undergone reduction by 48 h. As time on stream is increased from 48 to 96 h there is an increase in the intensity of each of these bands but between 96 and 240 h on stream there is very little increase in band intensity. This suggests that carbonaceous build-up has reached an optimum level by approximately 100 h on stream.

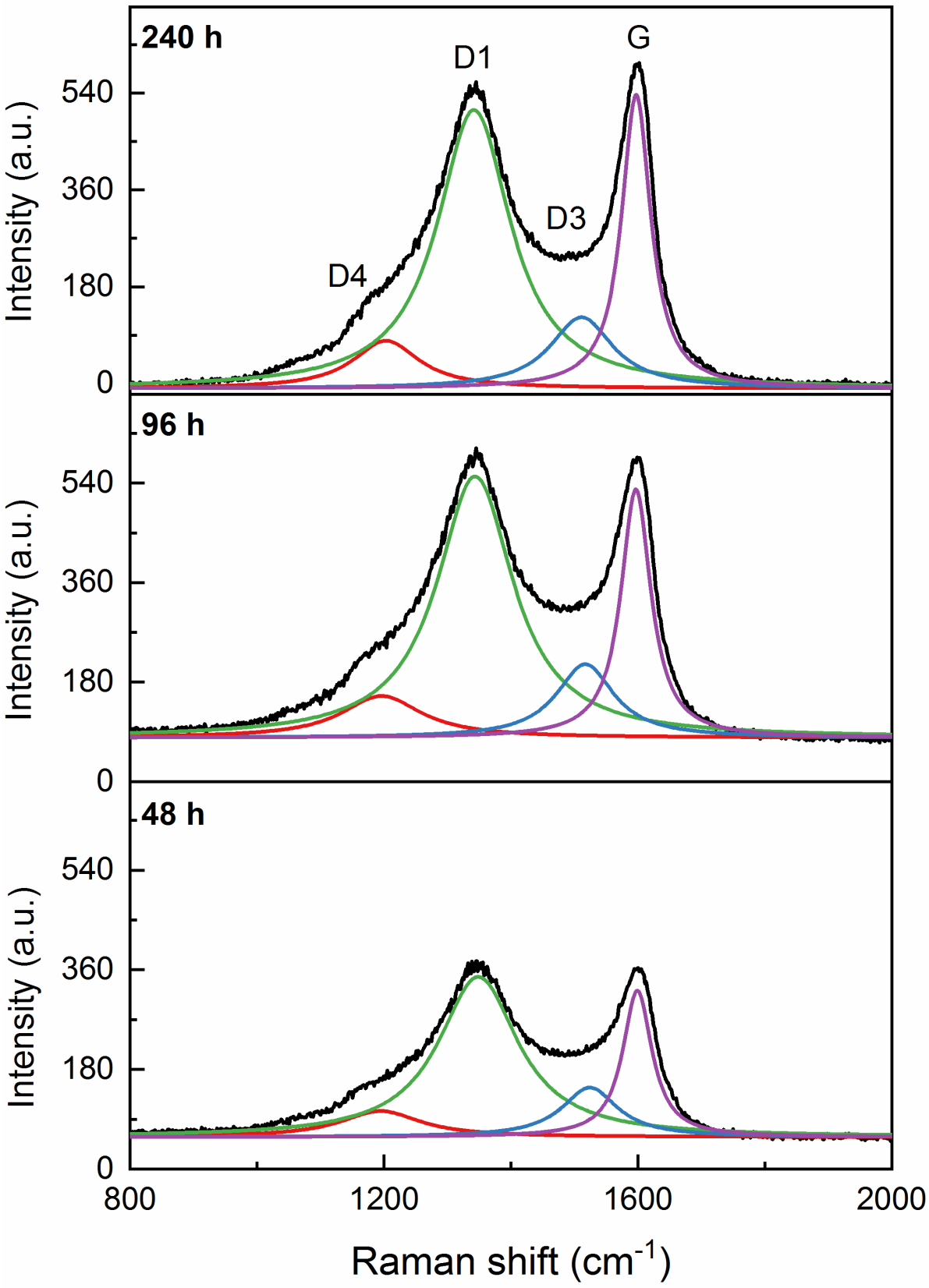

Figure 29: ***Ex situ*** **Raman spectra of unpromoted α-Fe_2O_3 after exposure to CO hydrogenation conditions at 623 K, ambient pressure on the large-scale reactor for 48, 96 and 240 h on stream. The D and G bands are defined with respect to Table 1. The spectrum was fitted by Guassian line shapes using OriginPro 2018.**

3.3.2.4. TEM Analysis

Ex situ TEM was performed on the samples post-reaction and a micrograph for the **Fe-ref** sample exposed to reaction conditions for 240 h on the large-scale reactor is presented in **Figure 30**. The micrograph is characterised by a core shell structure with an outer, less dense layer. Previous studies within the literature have found similar findings.[22,94,103,105,121] The lattice planes are indexed at position A to be 0.205 nm which is characteristic of monocyclic Fe_5C_2 (d (510) = 0.205 nm).[122] The outer layer shell can be attributed to amorphous carbon which has been highlighted in other characterisation techniques (*i.e.* XRD, Raman and TPO studies). This is in agreement with findings by Warringham and the **Fe-ref** sample at 24 h on stream.[94]

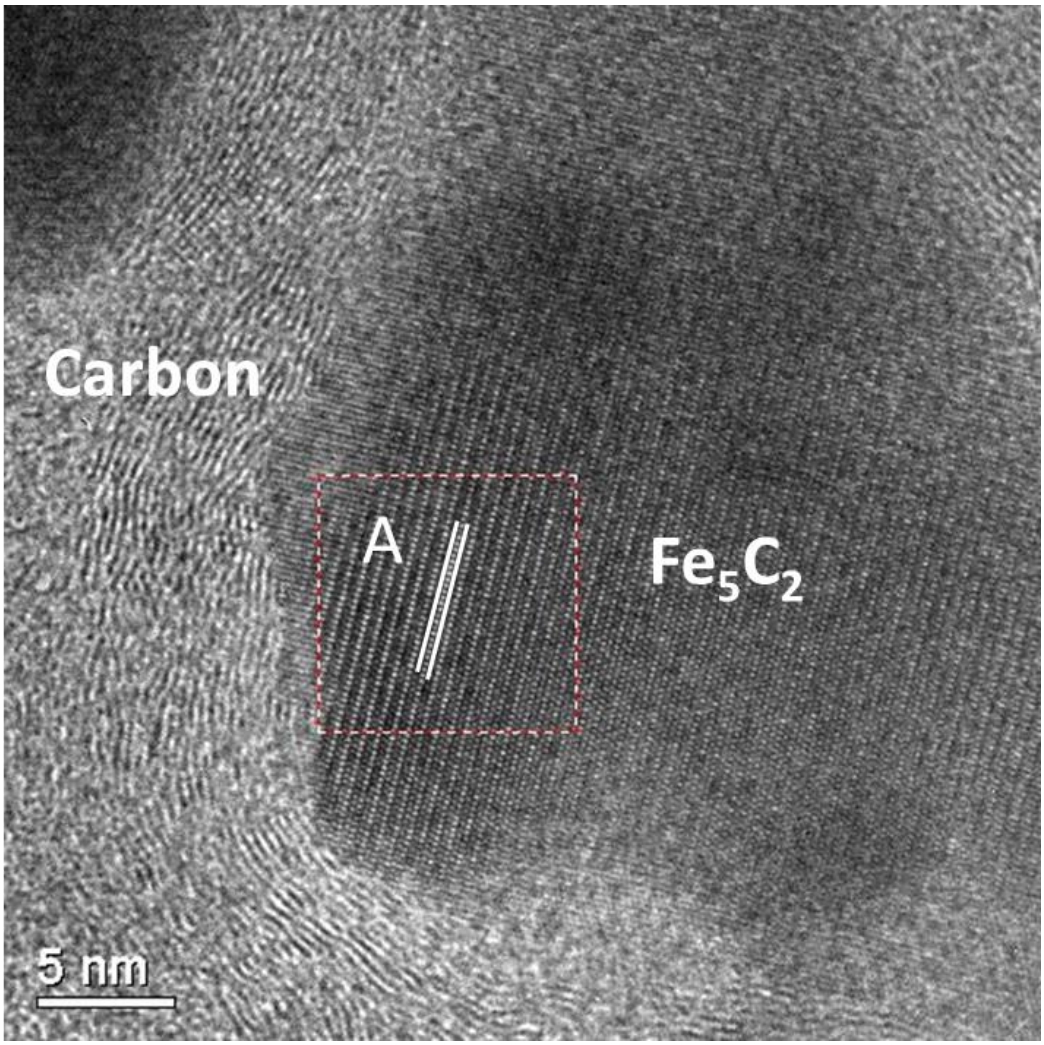

Figure 30: HRTEM of Fe-ref after exposure to CO hydrogenation conditions at 623 K for 240 h on the large-scale reactor. The d-spacing marked by A is 0.205 nm which is indicative of monocyclic Fe_5C_2. The scale bar is indicative of 5 nm.

3.3.2.5. Temperature-programmed Oxidation Measurements

The samples reacted for 48, 96 and 240 h on the scaled-up reactor were analysed *ex situ* on the micro-reactor set-up by temperature-programmed oxidation (TPO). The MS trace for CO_2 was monitored and the resulting profile for each sample is presented in **Figure 31**. Previous work by Warringham[94,105] has identified the presence of three different carbonaceous species from TPO measurements on iron-based FTS catalysts and assigned these as follows: α - reactive carbonaceous material, β - amorphous carbon, and γ - bulk iron carbides. These assignments were based on studies from within the literature examining carbonaceous deposits on iron-based catalysts.[123,124] However, these assignments will be reviewed throughout the thesis. As mentioned previously, this work is a direct continuation of that carried out by Warringham and therefore a procedure had been established for *ex situ* TPO measurements, which involved the use of approximately 40 mg of catalyst. However, this resulted in saturation by complete consumption of the oxygen (**Figure 32 (a)**) which could potentially be due to the excess carbon present on the catalyst surface. The saturation would therefore result in the TPO data becoming qualitative rather than quantitative. It was therefore decided that the mass of catalyst used for these measurements should be reduced in order maintain quantitative analysis, with the end result using 10 mg of sample to be used for *ex situ* studies (**Figure 32 (b)**).

The most noticeable difference between this data set (48 – 240 h), presented in **Figure 31**, and that obtained by Warringham (3 – 24 h) is the absence of the α feature yet the presence of both the β and γ components remain throughout the duration of the extended reaction period under investigation. Each species identified from the TPO profiles is quantifiable through calibration measurements discussed in **Chapter 2, Section 2.3.2. Figure 33** presents the quantified carbon values normalised per gram of iron within the sample. Data obtained by Warringham of the earlier 0 – 24 h dataset, acquired using the same experimental set-up, has once again been included to present a more comprehensive perspective on the dependency of the TPO features to reaction time.[73,94] The α species is only present up to 24 h; thereafter it is no longer observed. This limited presence of the α species has previously been observed by Warringham on the micro-reactor set-up but occurs at a much earlier stage within the reaction, *i.e.* about 6 h on stream.[94] This can be rationalised through the differences in the gas/solid exchange dynamics between the micro-reactor and the large-scale reactor which results in a much slower activation of the catalyst.[105] Previously, this species has been assigned as a precursor to the formation of the hydrocarbonaceous overlayer,[95] its absence post 24 h, correlates with the saturation of the aliphatic component of the hydrocarbonaceous overlayer from the INS dataset discussed in

the previous section (**Section 3.3.1**). Therefore, at this stage, it appears that the α species is more specifically a precursor to the aliphatic component of the hydrocarbonaceous overlayer. However, the α TPO feature may also be linked to iron carbide formation (γ component) as XRD (**Figure 28**) indicates iron carbide formation to have saturated over the period for which the TPO α peak is generated and consumed. On the other hand, **Figure 33** indicates progressive growth of the β and γ TPO features for increasing T-o-S up to approximately 200 h, where saturation of both states is achieved. Indeed, the intensity profiles of the β and γ bands reasonably follow that of the sp^2 hybridised ν(C-H) stretch (**Figure 27**). Thus, it is proposed that it is the development of the β and γ entities over a catalyst conditioning period of *ca.* 200 h that is responsible for the formation of the olefinic and/or aromatic component of the hydrocarbonaceous overlayer. It can also be postulated that the α component could be a precursor to either the β or γ TPO features, as the demise of α correlates with an increased production of these other components (**Figure 33**).

In summary, the assignment of the α feature has been reviewed and is proposed as a possible precursor to (i) the aliphatic component of the hydrocarbonaceous overlayer (ii) precursor to either the β and/or γ features in the TPO measurements. These considerations illustrate the dynamic nature of the evolutionary phase of iron-based FTS catalysts undergoing CO hydrogenation at elevated temperature and atmospheric pressure.

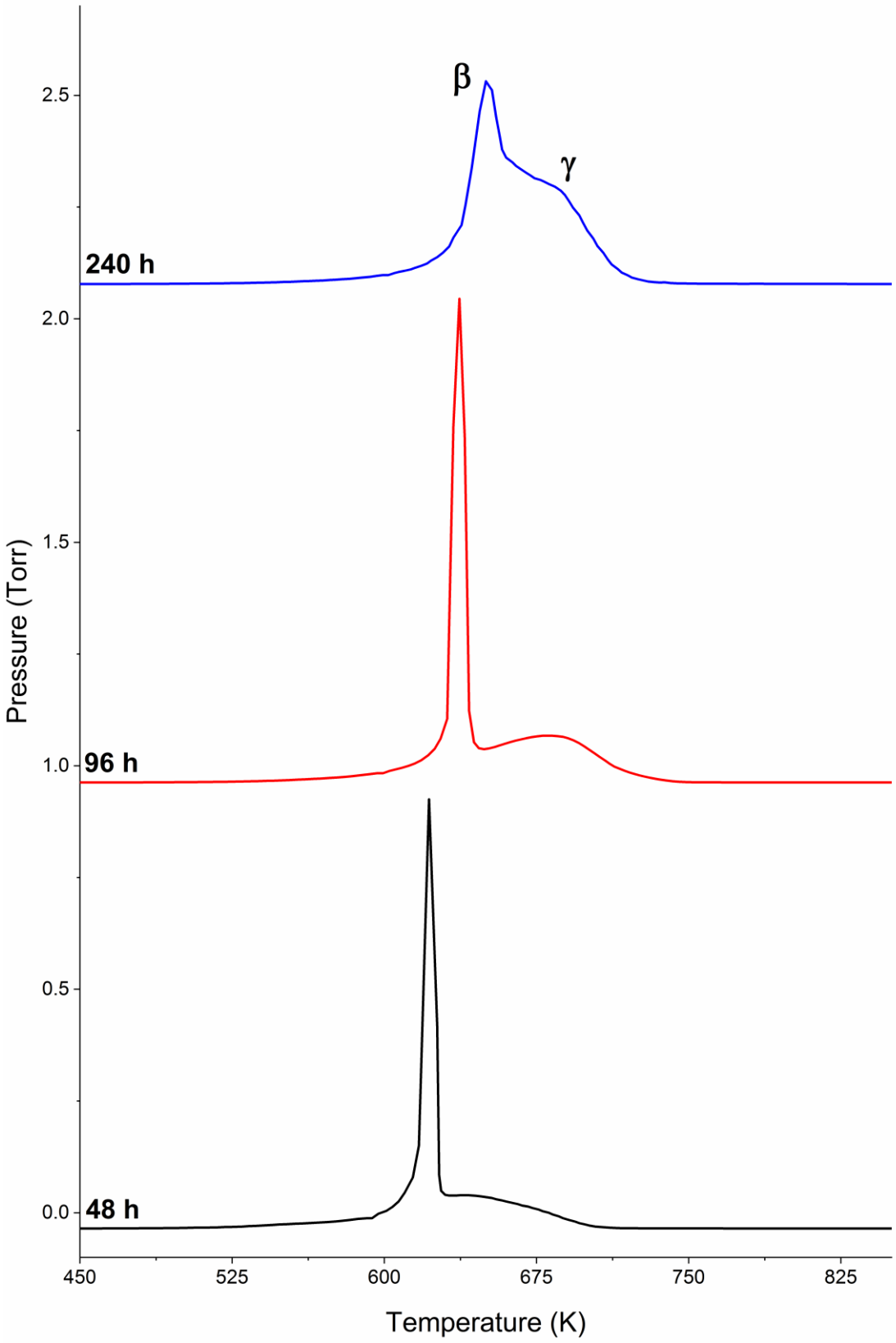

Figure 31: ***Ex situ*** **temperature-programmed oxidation profiles of unpromoted α-Fe_2O_3 (10 mg) taken from the large-scale reactor after exposure to CO hydrogenation conditions at 623 K, ambient pressure for 48, 96 and 240 h on stream.**

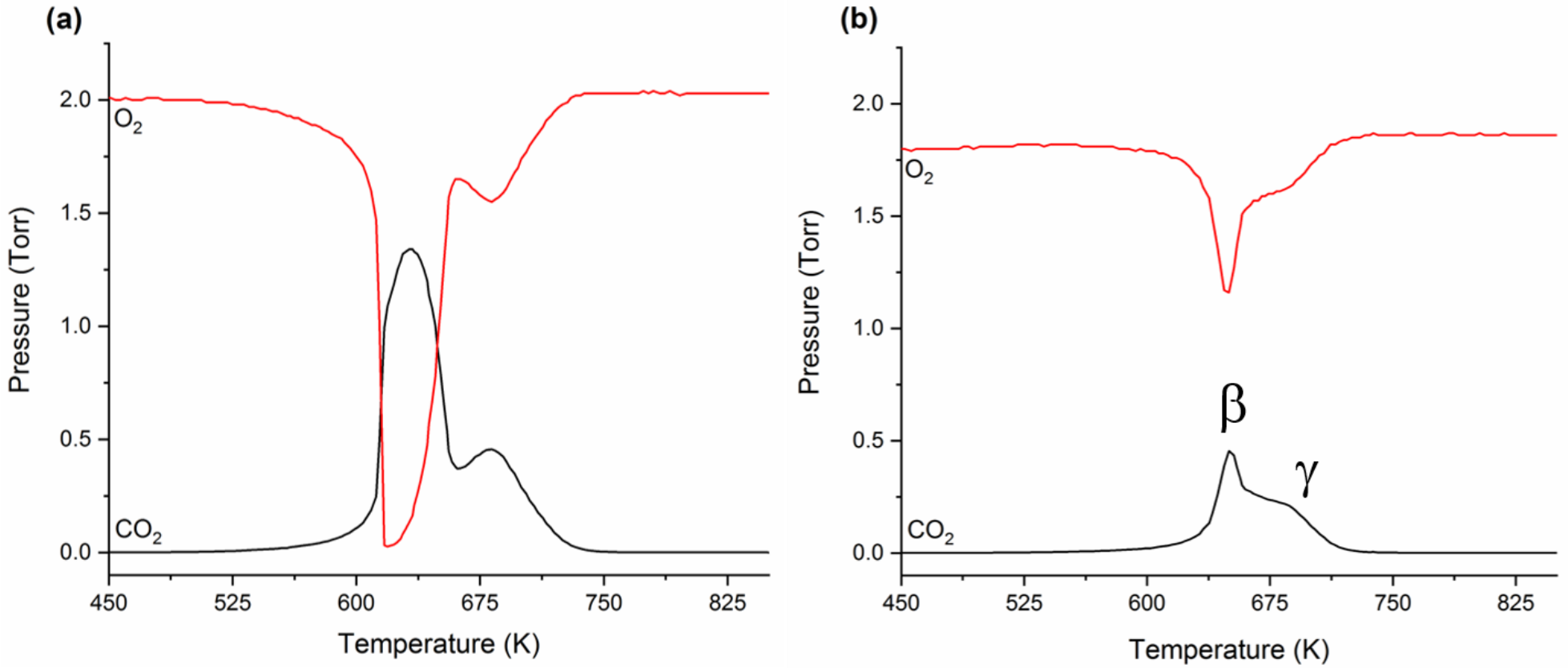

Figure 32: ***Ex situ*** **temperature-programmed oxidation profiles, displaying oxygen consumption of the catalyst samples using (a) 40 and (b) 10 mg catalyst, after exposure to ambient pressure CO hydrogenation reaction conditions at 623 K for 48 h. The black line is indicative of the measured CO_2 and the red line indicative of O_2 consumption.**

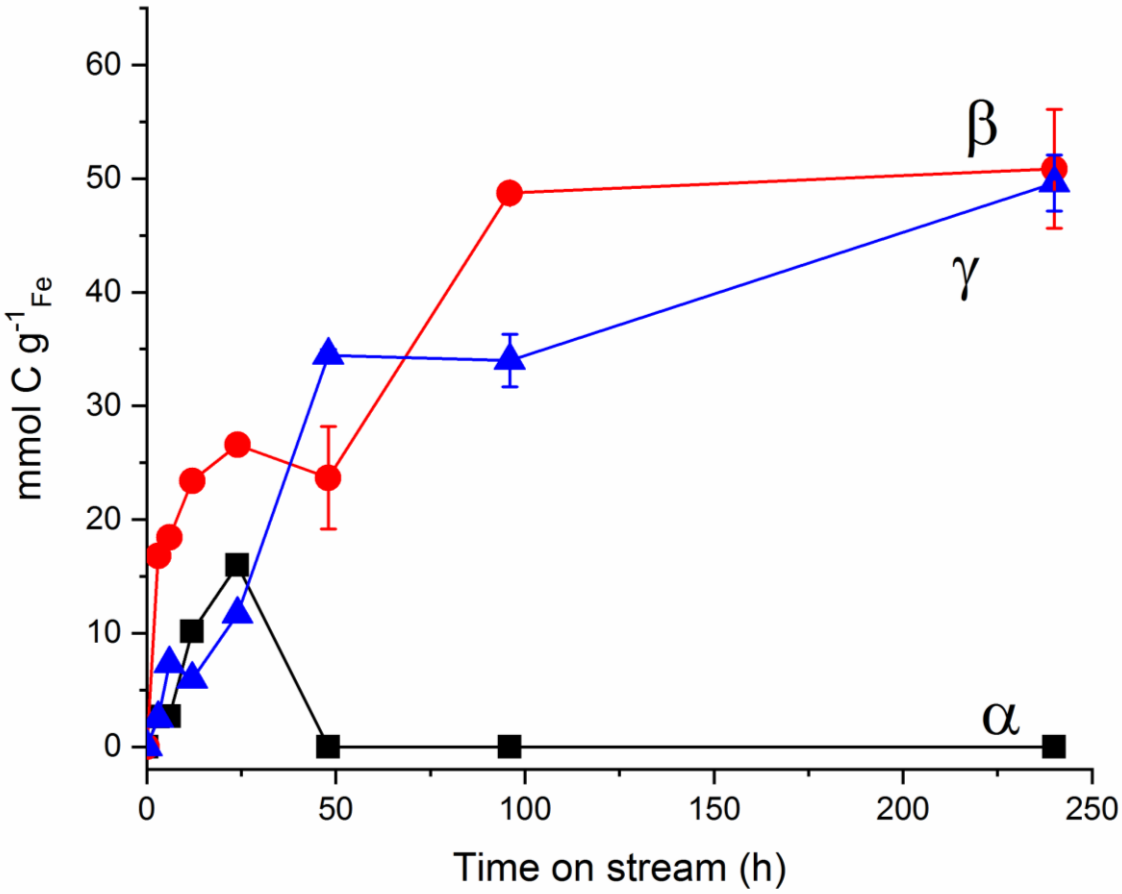

Figure 33: A comparison of the carbon content (mmol g^{-1}_{Fe}) obtained for the reactive carbonaceous material (α), amorphous carbon (β) and bulk iron carbide (γ) components observed from *ex situ* temperature-programmed oxidation profiles of the samples taken from the large-scale reactor after exposure to CO hydrogenation conditions up to 240 h on stream. Data plotted from 3-24 h obtained from Warringham's PhD thesis[73] and included for comparative purposes.

3.4. Micro-reactor Reaction Testing

Reaction testing conditions *i.e.* gas composition (2:1 H_2:CO), temperature and time-scales (48 - 240 h), carried out on the micro-reactor were intended to complement the reactions carried out on the large-scale reactor presented in the previous section of this chapter (**Section 3.3**). However, reaction testing beyond 96 h was not feasible due to an excess build-up of carbon observed in post-reaction analysis and is discussed in more detail in the following section (**Section 3.4.1**). The catalyst mass utilised for this set of reaction testing was varied in order to try and obtain quantifiable data for post-reaction analysis. The reaction profile itself displayed no significant variations with the changing of catalyst mass and a representative profile using 10 mg of **Fe-ref** for a CO hydrogenation reaction for 96 h is presented in **Figure 34**. The reaction profile displayed similar trends to that previously obtained and described by Warringham.[73] As with the reaction profile of the large-scale reactor, the profile can be divided into stages, although the micro-reactor setup has three distinct stages unlike the scaled-up system which has only two stages. *Stage I* is identified by the production of CO_2 at 515 K, which represents the reduction of the hematite starting material (α-Fe_2O_3) towards magnetite (Fe_3O_4). There is a small consumption of CO at this stage and it is therefore proposed that the reduction of hematite occurs by CO (*Equation 3.4*) rather than by dihydrogen.[105] It is of course possible for hematite to be reduced by hydrogen but as consumption is minimal at this stage it is not thought to be occurring via this route.[13,108]

$$CO_{(g)} + 3\alpha Fe_2O_3(s) \rightarrow CO_2(g) + 2Fe_3O_4(s) \qquad (\mathbf{3.4})$$

Stage II is identified by the simultaneous production of CO_2, methane and water as the reaction reaches temperature at 623 K. At this point in the reaction profile there is also consumption of CO and a small proportion of H_2. The production and consumption of materials at this stage in the reaction profile can be accounted for through several surface reactions. Firstly, the continued production of CO_2 in this phase of the reaction may be due to the catalyst further reducing from magnetite towards metallic iron (*Equation 3.5/3.6*). The presence of metallic iron and CO will lead to the CO dissociating on the catalyst surface by either CO dissociation (*Equation 3.7*) or disproportionation (*Equation 3.8*) *i.e.* the Boudouard reaction. [108,125]

$$Fe_3O_{4(s)} + CO_{(g)} \rightarrow 3FeO_{(s)} + CO_{2(g)} \quad (\mathbf{3.5})$$

$$FeO_{(s)} + CO_{(g)} \rightarrow Fe_{(s)} + CO_{2(g)} \quad (\mathbf{3.6})$$

$$CO_{(ad)} \rightarrow C_{(ad)} + O_{(ad)} \quad (\mathbf{3.7})$$

$$2CO_{(ad)} \rightarrow C_{(ad)} + CO_{2(g)} \quad (\mathbf{3.8})$$

The hydrogenation of the increased surface carbon will account for the production of methane (*Equation 3.9*). Surface oxygen on the other hand will either oxidise CO to further produce CO_2 (*Equation 3.10*) or will be hydrogenated to produce water (*Equation 3.11*). The WGS reaction will also play a role in mediating the products (*Equation 3.12*).

$$C_{(ad)} + 4H_{(ad)} \rightarrow CH_{4(g)} \quad (\mathbf{3.9})$$

$$O_{(ad)} + CO_{(g)} \rightarrow CO_2 \quad (\mathbf{3.10})$$

$$O_{(ad)} + 2H_{(g)} \rightarrow H_2O_{(g)} \quad (\mathbf{3.11})$$

$$CO_{(g)} + H_2O_{(g)} \rightleftharpoons CO_{2(g)} + H_{2(g)} \quad (\mathbf{3.12})$$

Stage III can be identified by the reactants and products reaching a steady state. The catalyst stability is highlighted by its ability to maintain this steady state over 96 h on stream. Yet a slight dip is evident in the water feature as seen also in the large-scale reactor (**Figure 23**). It is interesting to note that the CO_2 feature remains at a steady state after approximately 2 h of reaction over the course of the 96 h studied which varies significantly from that observed in the large-scale reactor which took approximately 7 h to reach a steady state. This can be attributed to the differences in the gas/solid exchange dynamics of the two reactor set-ups. The increase in gas exchange dynamics in the micro-reactor reduces the time required for complete reduction of the pre-catalyst towards magnetite.[105] Despite the differences in the exchange dynamics between the two reactors, the reaction profiles obtained from each reactor display similar attributes mainly through two dominant chemical pathways: firstly, the hydrogenation of carbon monoxide to methane, and secondly, evidence of the WGS reaction in the production of CO_2. [105] The conditions used within this study result in a CO conversion of less than 1% with an iron time yield (FTY) of 1.72 x 10^{-4} mmol (CO) $g_{Fe}^{-1}s^{-1}$, which is comparable to that obtained within the literature utilising similar reaction conditions.[50,105]

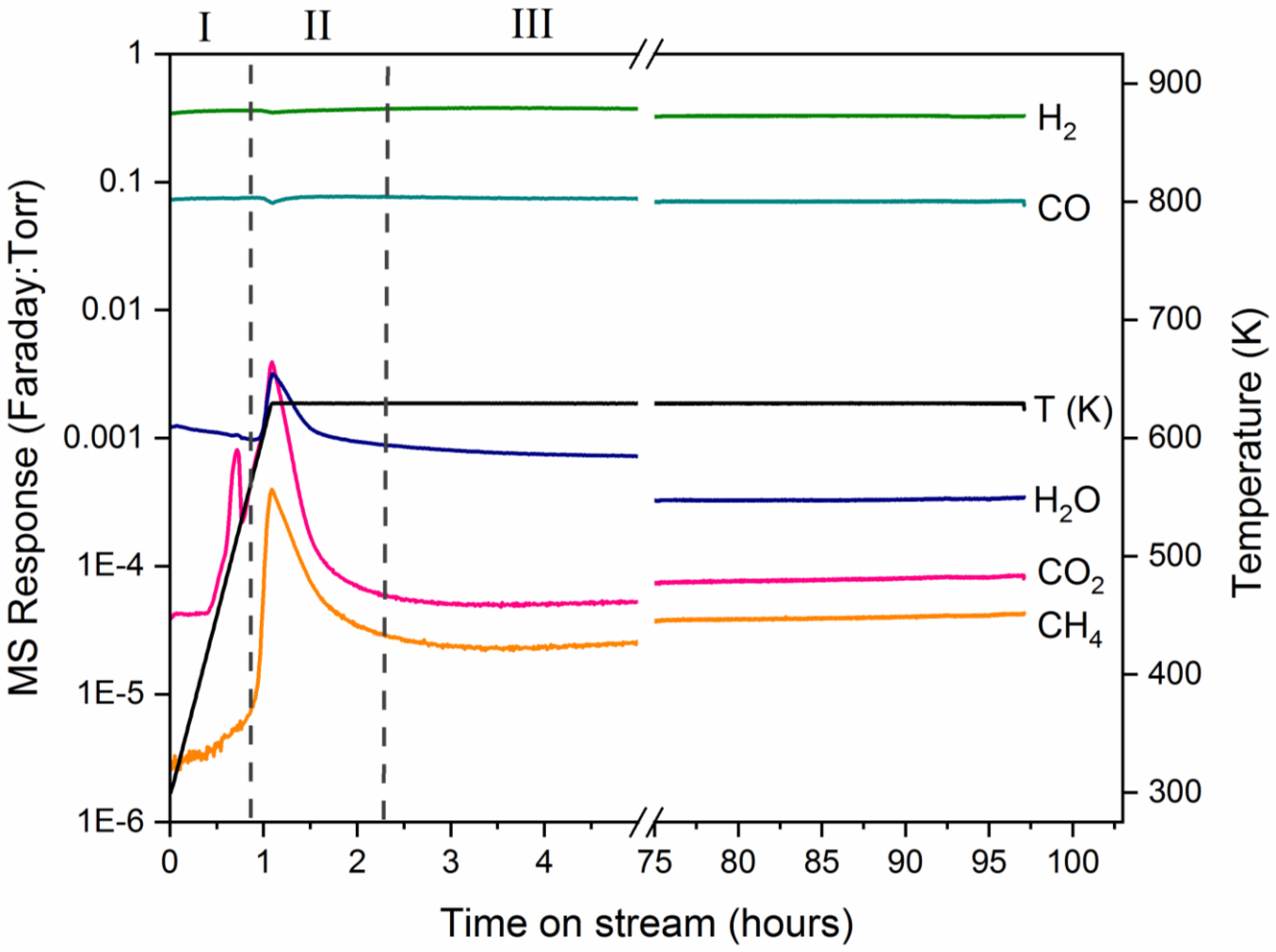

Figure 34: Micro-reactor reaction profile of the upromoted catalysts (10 mg) during a CO hydrogenation reaction, ambient pressure, 623 K for 96 h.

3.4.1. *In situ* Temperature-programmed Oxidation

Despite the reaction profile being almost identical to Warringham's data[94] (0 – 24 h), *in situ* TPO characterisation of samples beyond 48 h on stream resulted in significant difficulties due to the excessive build-up of carbon, which arose from the increased exposure to time on stream of the catalyst samples. For this particular set of experiments, a repeat measurement previously carried out by Warringham, was undertaken to establish a crossover between the two sets of data *i.e.* 0-24 h by Warringham and 48 – 240 h for this study. This repeat measurement utilised 40 mg of catalyst for an ambient pressure CO hydrogenation reaction followed *by in situ* TPO analysis. The resulting data was comparable to that obtained by Warringham highlighting the formation of the β and γ components, as shown in **Table 8**. Note that the α species identified in previous TPO measurements has not been reported at this later stage of the reaction on the micro-reactor set-up utilising **Fe-ref**. It is interesting to observe that the carbonaceous species (β and γ) are identified in both the micro-reactor set up and the catalyst samples from the large-scale reactor, which would suggest that these species will form despite the changes in the gas exchange dynamics that each of the samples are exposed to.

Table 8: A comparison between the quantified carbon (mmol C g^{-1}_{Fe}) obtained from this current study (10 mg catalyst) and that by Warringham[94] (40 mg catalyst) from an *in situ* temperature-programmed oxidation measurement after catalyst exposure to CO hydrogenation conditions for 24 h on stream on the micro-reactor. Carbon content is normalised (g^{-1}_{Fe}) to allow for direct comparison.

Carbon feature in TPO profile	Carbon content Warringham's data set (mmol C g^{-1}_{Fe})	Current study carbon content (mmol C g^{-1}_{Fe})
α	-	-
β	33.43	26.99
γ	24.04	19.33

In situ TPO analysis of 40 mg of catalysts reacted for 48 h on stream indicated saturation of the β feature in the TPO profile shown in **Figure 35 (c)**. This was possibly due to the excessive build-up of carbon resulting from the increased exposure to reaction conditions. Saturation of the features would therefore affect the reliability of the quantified data set.

This resulted in testing various catalyst masses (10, 20, 40 mg) for the 48 h reaction and each of the resulting TPO profiles, alongside oxygen consumption, are presented in **Figure 35 (a)** to **(c)**. From the various catalyst masses tested, the 10 mg sample was most promising and thus was used for a sample exposed to 96 h on stream. Unfortunately, as shown by the *in situ* TPO profile in **Figure 36**, this was unsuccessful. The extent of saturation resulted in no distinguishable features being observed and thus highlighted the limitations of the micro-reactor set-up and concluded that exposure to CO hydrogenation conditions is limited to 48 h on stream with this set-up. Consequently, it is not possible to produce a carbon retention plot vs. T-o-S for the micro-reactor, as was possible for the large-scale INS reactions (**Figure 33**).

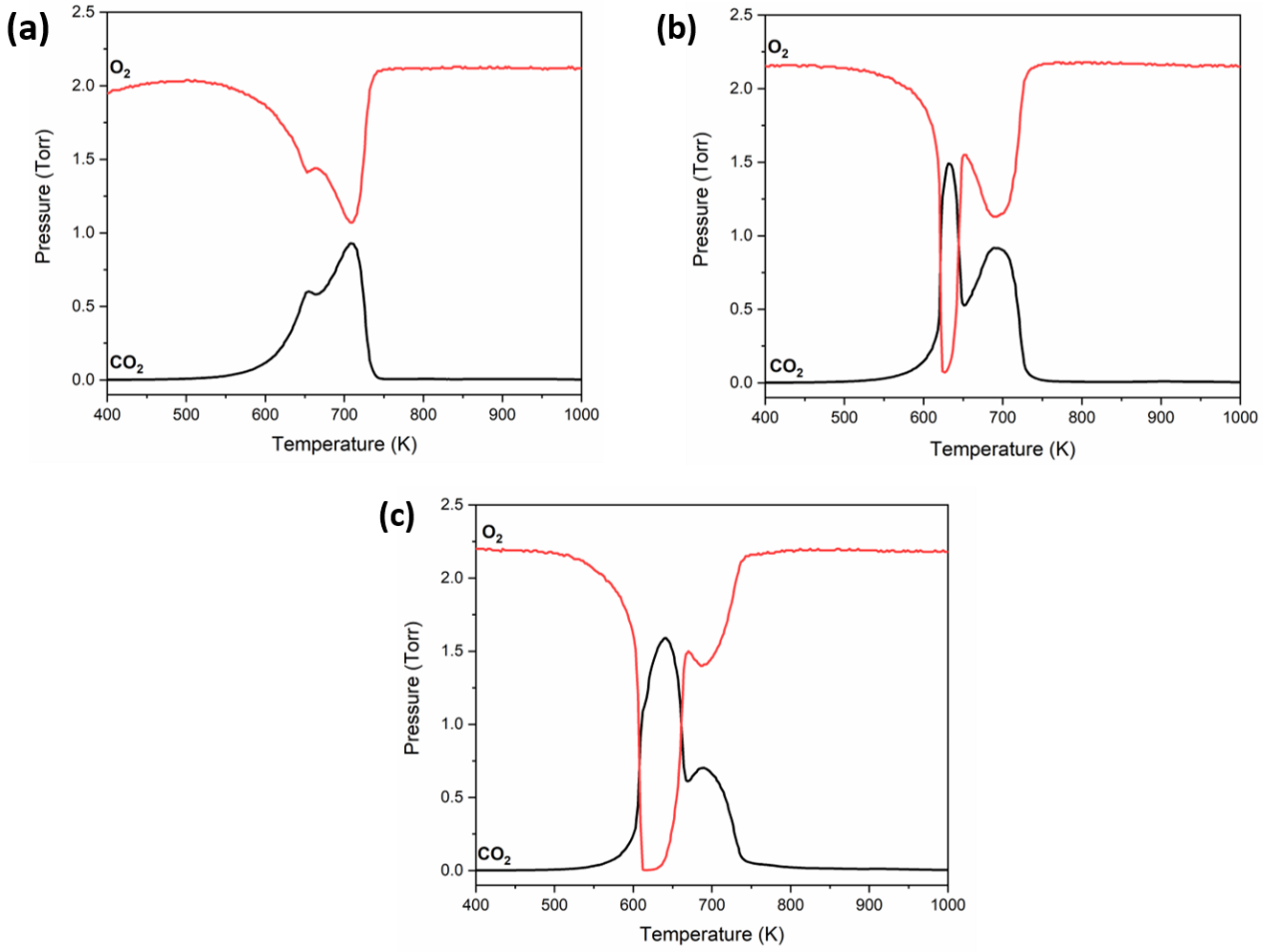

Figure 35: ***In situ*** **temperature-programmed oxidation profiles of the unpromoted α-Fe_2O_3 sample with (a) 10 mg (b) 20 mg and (c) 40 mg of catalyst after exposure to CO hydrogenation conditions on the micro-reactor for 48 h. The black line is indicative of the measured CO_2 and the red line indicative of O_2 consumption.**

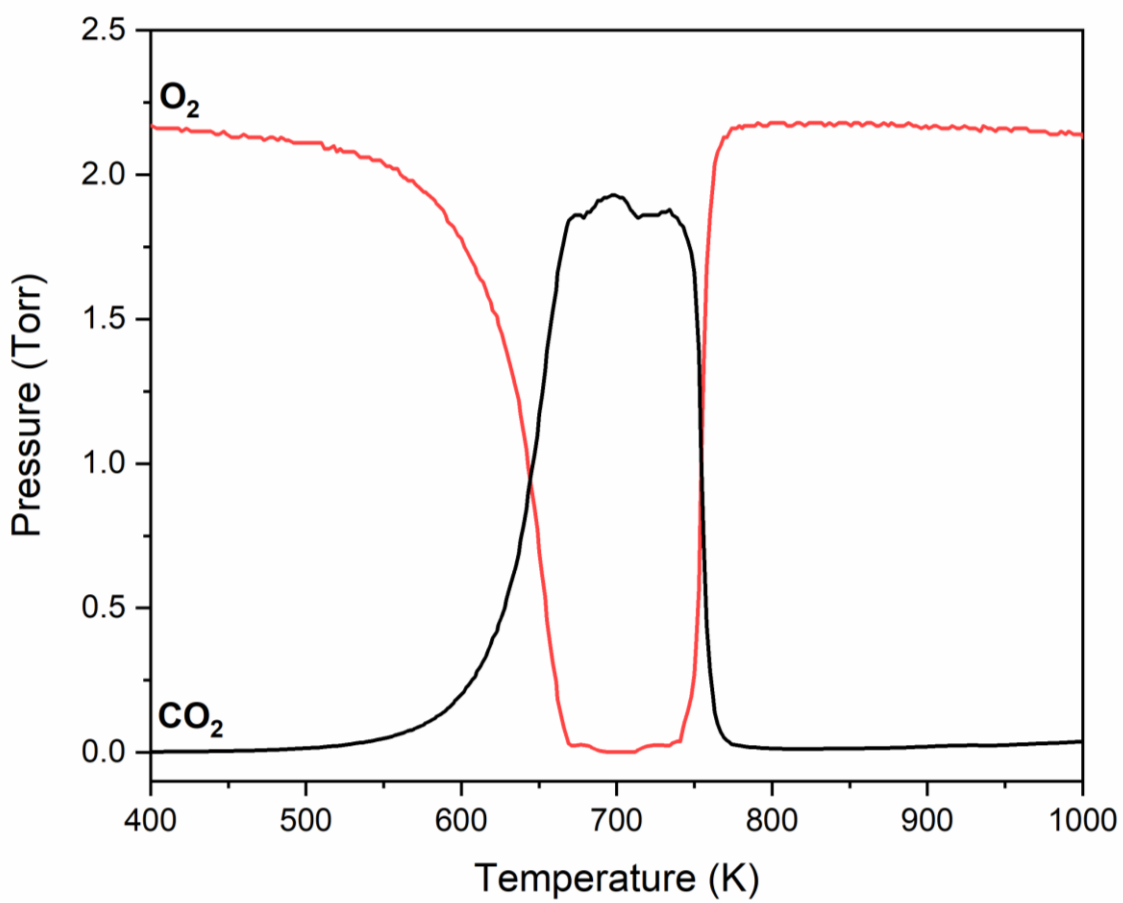

Figure 36: ***In situ*** **temperature-programmed oxidation profile of the unpromoted α-Fe_2O_3 sample with 10 mg of catalyst after exposure to CO hydrogenation conditions on the micro-reactor for 96 h. The black line is indicative of the measured CO_2 and the red line indicative of O_2 consumption.**

3.5. Discussion

Extending the reaction period studied of the **Fe-ref** catalyst from 24 to 240 h has established a complete evolutionary profile of an iron-based catalyst exposed to ambient pressure CO hydrogenation conditions on a large-scale reactor set-up. Unfortunately, the complementary micro-reactor TPO studies beyond 24 h were unable to be carried out due to excessive carbonaceous build-up, which resulted in difficulty in distinguishing features in the *in situ* TPO profiles. Therefore, majority of the focus for this chapter was centred on the large-scale set-up. The XRD diffractograms highlighted the presence of 100 % Hägg carbide for all post-reaction samples, as does the TEM for the 240 h sample, which is consistent with the literature as a potential active phase for FTS reactions.[22,26] The sp^3 hybridised carbon feature from the INS data set, displays limited production as the quantified hydrogen (**Figure 27**) is shown to plateau at a fairly early stage in the reaction (approximately 24 h). On the other hand, the sp^2 hybridised carbon feature displays a steady production of olefinic/aromatic material up until ~ 200 h on stream, concluding that the hydrocarbonaceous overlayer is dominated by olefinic/aromatic character, with a minority aliphatic component, and requires approximately 100 – 200 h for complete hydrocarbonaceous overlayer formation to occur in the large-scale reactor. Interestingly, as the α peak from the *ex situ* TPO measurements ceases to be observed, the aliphatic component of the hydrocarbonaceous overlayer displays signs of saturation. Therefore, suggesting that the α species, previously assigned as a potential precursor to the overlayer formation,[95] is proposed to be specifically a precursor for the aliphatic component of the overlayer. However, the α component is also postulated to be a precursor to the β and/or γ TPO features. On the other hand, the saturation of the aromatic feature from the INS dataset at *ca.* 200 h correlates with the β and γ components from the TPO measurements reaching a steady-state as well as the intensity of the carbonaceous bands observed by Raman spectroscopy plateauing around this time on stream. Therefore, the β and γ features from the TPO measurements are tentatively proposed to be responsible for the formation of the olefinic and/or aromatic component of the hydrocarbonaceous overlayer.

Overall, the post-reaction analysis of the **Fe-ref** catalyst highlights the iron carbide phase to be pure Hägg carbide with the complete evolution of the catalyst, including the evolution of the hydrocarbonaceous overlayer, by approximately 200 h on stream as indicated by INS, *ex situ* TPO and Raman spectroscopy. This is consistent with the literature, which analysed FT catalytic activity as a function of time on stream, indicating

that iron FTS catalysts require a conditioning period of days rather than hours.[101,126] These latter studies did not consider a role for a hydrocarbonaceous overlayer.

Warringham previously proposed a scheme to provide a role of the hydrocarbonaceous overlayer in a CO hydrogenation reaction in relation to the supply of hydrogen within the system.[73] The proposed scheme incorporated a previously established competition model by Niemantsverdriet, which stated that the final carbon product of a Fischer-Tropsch reaction is dependent on the supply of hydrogen, with a hydrogen deficient system leading to competition between the production of carbides (*i.e.* the active phase) and the formation of inactive carbon. [25,127] Within Warringham's PhD thesis it was proposed that the hydrocarbonaceous overlayer forms on the surface of the proposed active site, the iron carbide, and acts as a mediator of the supply of reagents to these sites. Applying Niemantsverdriet's model to this system, a plentiful supply of hydrogen will result in a consistent formation of hydrocarbon products (*Equation 3.13*), and a hydrogen deficiency will result in the formation of amorphous carbon (*Equation 3.14*); suggesting the dominant pathway for a CO hydrogenation reaction would be the formation of amorphous carbon.

$$nC_{x(ad)} + H_{y(ad)} \rightarrow nC_xH_y \quad \textbf{(3.13)}$$

$$nC_{(ad)} \rightarrow C_{n(poly)} \quad \textbf{(3.14)}$$

This proposed scheme has since been further developed. The following hypothesis is represented in a schematic form presented in **Figure 37**. The pre-catalyst (α-Fe_2O_3) on exposure to syngas is reduced towards Fe_3O_4 and Fe^0 where at this stage, iron carbides begin to form, followed by the formation of the hydrocarbonaceous overlayer. As previously mentioned, the overlayer is proposed to form on the surface of the iron carbide layer.[103] It is proposed that the coverage of the overlayer is a 'template' for sites, A and B, which are responsible for hydrogen and carbon monoxide dissociative adsorption respectively. This proposal is similar to that which has been outlined by Borodziński[42,43] (**Chapter 1, Section 1.4, Figure 2**) for olefin hydrogenation reactions over supported Pd catalysts. Here, site A is responsible for providing a continual source of hydrogen atoms within the system. At site B the dissociatively adsorbed oxygen will react with either carbon or hydrogen resulting in the formation of carbon dioxide or water (*Equations 3.15* and *3.16*).

$$C_{(ad)} + 2O_{(ad)} \rightarrow CO_{2(g)} \quad \textbf{(3.15)}$$

$$2H_{(ad)} + O_{(ad)} \rightarrow H_2O_{(g)} \quad \textbf{(3.16)}$$

Furthermore, the final carbon product from site B is highly dependent on the supply of hydrogen, forming either hydrocarbon products (*Equation 3.13*) or amorphous carbon (*Equation 3.14*). Under the conditions utilised in this study, *i.e.* an ambient pressure CO hydrogenation reaction at 623 K, a plentiful supply of hydrogen will result in the formation of methane at site B, whereas a deficiency in hydrogen will result in the formation of amorphous carbon. On the other hand, using this proposed model for an FTS reaction, *i.e.* a high-pressure reaction, at site B C-C propagation will occur resulting in high molecular weight saturated products. It is therefore proposed that the role of the hydrocarbonaceous overlayer is to act as a template in defining the two active sites on the iron carbide. Further work is required to check the validity of these proposals.

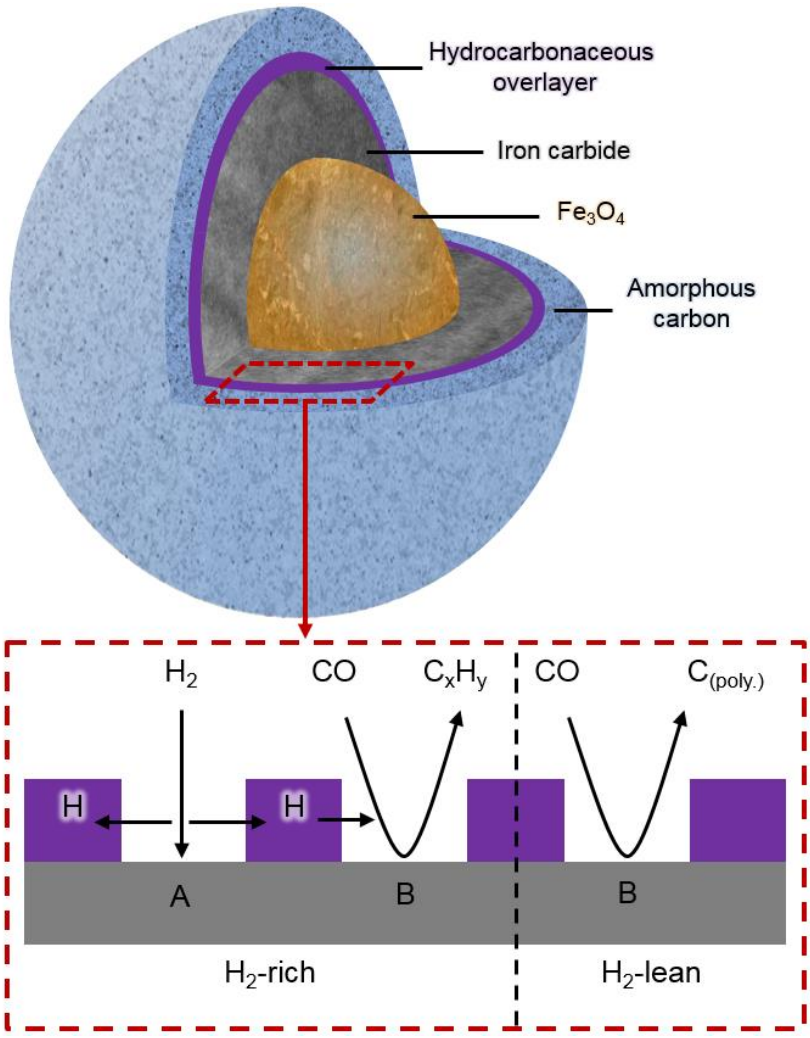

Figure 37: A schematic of the composition of the iron FTS catalyst after exposure to ambient pressure CO hydrogenation conditions at 623 K for *ca.* 6h. The hydrocarbonaceous overlayer (purple) is suggested to mediate the transfer of hydrogen, where the final product output is dependent on the supply of hydrogen within the system.[94]

3.6. Conclusions

An ambient pressure CO hydrogenation has been utilised as a representative FTS reaction to investigate the evolution of an unpromoted hematite catalyst over a 240 h period. Characterisation of the catalyst through INS, TPO, XRD, TEM and Raman spectroscopy have led to the following conclusions to be drawn. Due to issues arising from *in situ* TPO measurements on the micro-reactor, discussed in **Section 3.4.**, the majority of the focus has centred on the large-scale reactor.

- Post-reaction *ex situ* XRD indicates only Hägg carbide to be present within the bulk catalyst from 48 h onwards.
- For reaction times ≥ 48 h, TPO measurements show only amorphous carbon (Peak β) and iron carbide (Peak γ) species to be present. The α peak grows and decays to ultimately zero concentration over the period 0 - 48 h T-o-S.
- INS analysis of the reacted catalyst samples identifies the presence of sp^2 and sp^3 hybridised C-H species, with quantification of the ν(C-H) modes indicating the concentration of aliphatic C-H species to saturate after approximately 24 h T-o-S. In contrast, the concentration of olefinic/aromatic C-H entities progressively increase up to ~ 200 h before appearing to reach saturation.
- The TPO α species is suggested to play an integral part in the catalyst evolutionary process and is proposed to follow one of the following pathways: (i) precursor to the aliphatic component of the hydrocarbonaceous overlayer and/or (ii) precursor to β and γ components.
- The development of the amorphous carbon (β) and iron carbide (γ) entities that develop over a catalyst conditioning period of *ca.* 200 h correlate with the formation of the olefinic and/or aromatic component of the hydrocarbonaceous overlayer.
- From inspection of the TPO and INS intensity profiles, it is concluded that under stated reaction conditions the overall catalyst conditioning process requires approximately 200 h T-o-S to achieve completion.
- Steady-state operation of the catalytic system is not directly coupled to the TPO β and γ features, nor is it connected to the development of the olefinic/aromatic component of the hydrocarbonaceous overlayer.

Chapter 4 – CO hydrogenation at 623 K: the effect of S concentration on doubly promoted hematite catalyst on the formation of a hydrocarbonaceous overlayer

4.1. Introduction

Fischer-Tropsch to olefins (FTO) is a process which could be considered as a viable alternative as a direct route to the production of lower olefins (C_2-C_4) from syngas without a dependency on crude oil.[48] Iron-based catalysts are ideal for the FTO process over cobalt based catalysts due to having a naturally higher selectivity towards olefins in the first instance.[49,50] To assist in shifting the product slate further towards the desired lower olefins, promoters such as alkali metals and sulfur have been reported within the literature, with each promoter suggested in having its own specific role. The addition of alkali metals to iron-based catalysts, such as sodium or potassium, has been suggested to increase olefinicity within the FTS product stream. A study by Ribeiro *et al*. investigated an iron-based FTS catalyst promoted with various alkali metals (Li, Na, K, Rb and Cs), examining the rate of carburization of iron.[61] Ribeiro found that the rate of carburization was not only linked to the basicity of the promoter but also closely linked with the selectivity of olefins. Ribeiro suggested that this increase in selectivity towards olefins could be explained through the Blyholder model.[128] As shown in **Figure 38**, according to this model, the carbon monoxide molecule donates electrons through the filled σ orbital (bonding) to the empty d orbitals of the metal. On the other hand, the electrons from the populated d orbitals of the metal are transferred to the π* (antibonding) orbital of the carbon monoxide. This process, known as back-donation, is enhanced by the addition of alkali metals to the iron catalyst, which decreases the bond strength of C – O by reducing the bond frequency. Therefore, Ribeiro suggested that the inclusion of alkali metals leads to enhanced olefin production due to the increased surface coverage of carbon as a result of the weakened C – O bond. This in turn prevents the readsorption of olefins to the surface by decreasing the surface hydrogen coverage.[61]

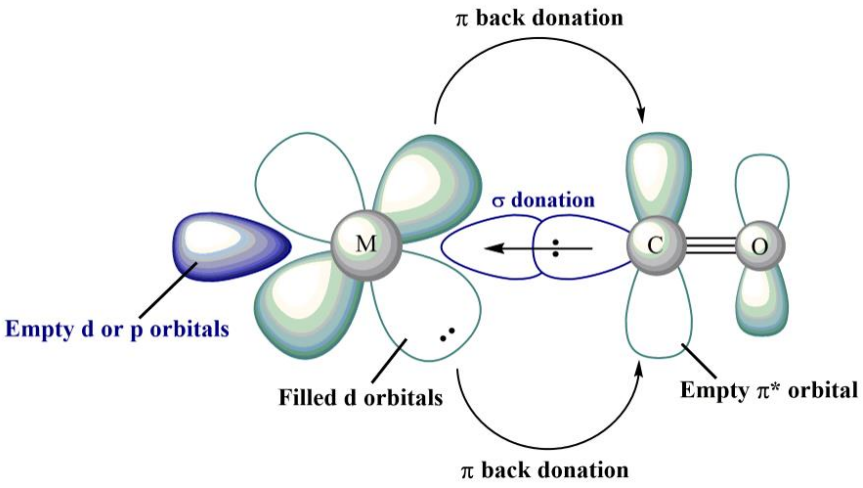

Figure 38: Blyholder model of the molecular orbital bonding of CO to a metal site.

On the other hand, the addition of low levels of sulfur to an iron-based catalyst has also exhibited enhanced olefin selectivity. However, the specific role of the sulfur is still under debate within the literature. De Jong and co-workers suggest the selectivity is a result of the sulfur weakening Fe-C bond at iron-carbide surface, therefore facilitating the formation of short chain hydrocarbons,[50] whereas Kritzinger proposed that S poisons the active sites responsible for the hydrogenation of surface olefins.[129] However, Yuan *et al*. emphasised the need for the combination of both an alkali metal and sulfur to enhance selectivity towards lower olefins but also decrease selectivity towards unwanted by-products such as methane, as discussed in **Chapter 1, Section 1.5.1**.[45]

Warringham *et al*. set the ground work for this investigation, studying a hematite catalyst singly promoted with sulfur.[95] Different concentrations of sulfur were selected and added to the standard iron-based catalyst (**Fe-ref**) which was investigated in **Chapter 3**. The selection of sulfur levels by Warringham were based on a study by Bromfield and Coville[64], highlighting peak catalytic activity in relation to catalyst sulfur concentration (**Chapter 1, Section 1.5, Figure 4**). Warringham's preliminary study highlighted that the addition of sulfur hindered the reduction process of the hematite catalyst, shown from *in situ* XRD measurements, and in turn resulted in the reduction in the formation of the hydrocarbonaceous overlayer as indicated by the INS spectra. Warringham's *in situ* TPO data highlighted that the increased sulfur concentration not only resulted in the delayed retention of the α species but caused a significant increase in the formation of amorphous carbon (β component). Overall, this preliminary study suggested that the inclusion of sulfur within the iron FTS catalyst matrix, impedes the reduction and carburization process of the catalyst, directly impacting the formation of the hydrocarbonaceous overlayer which, in

turn, correlates with reduced catalytic activity of sulfur promoted catalysts investigated by Bromfield and Coville.[64]

This chapter expands from this initial study by Warringham by incorporating an alkali metal, sodium, to the reference hematite sample alongside varying levels of sulfur. Five concentrations of sulfur were selected (10 -250 ppm) with the sodium concentration (*ca.* 2000 ppm) kept constant and are compared against the reference material (**Fe-ref**) examined previously in **Chapter 3**. Each of the promoted catalyst samples have been labelled **Fe-Na-S$_x$**, where subscript *x* refers to the intended sulfur concentration in ppm. The levels of sulfur selected were below the maximum catalytic activity investigated by Bromfield and Coville[64] (**Chapter 1, Section 1.5.1, Figure 4**) and levels of sodium and sulfur are comparable to levels studied within the literature.[45,50] The selection of the catalyst formulations to be investigated was guided by advice from the Industrial Partner (Sasol Technology Ltd.).

The aim of the following chapter is to determine how the addition of this second promoter will affect the Fe/CO/H_2 surface chemistry and in turn, its effects on the formation of the hydrocarbonaceous overlayer.

4.2. Catalyst Characterisation

The promoted catalyst samples were characterised before exposure to CO hydrogenation conditions by ICP, BET, XRD and TPR to establish whether the addition of the low levels of promoters, sulfur and sodium, had a significant effect on the structural and/or behavioural properties of the hematite pre-catalyst. **Table 9** presents a combination of the ICP and BET data obtained for each of the doubly promoted catalysts alongside the reference material from **Chapter 3**, for comparative purposes. The sulfur concentrations utilised within this study are unfortunately below detection limits of ICP (< 300 ppm), however the bracketed values were provided by Butterworth Laboratories as a measured value, but its reliability may be compromised due to being below official detection limits and is provided here as a qualitative value rather than quantitative, *i.e.* indicative of a varying sulfur concentration across the samples. Note that the sodium concentration is of a similar value across all of the doubly promoted samples (*ca.* 2000 ppm) except for **Fe-Na-S$_{100}$** (2890 ppm), which may potentially explain some anomalous results later in this chapter. The surface area and pore volume measured by BET all show similar results to that obtained for the reference hematite sample, suggesting the addition of promoters at these levels has not affected the overall structure of the hematite catalyst. It is noted that the surface area obtained for **Fe-ref** is lower than previously obtained by Warringham *et al*. who reported a value of 70.8 m^2g^{-1}.[105] The differences may be due to slight variations made in the automated programme of the Mettler Toledo LabMax batch reactor apparatus used for catalyst preparation. Nevertheless, a relatively high surface area hematite catalyst has been achieved through use of the batch reactor apparatus in comparison to catalyst preparation without this equipment by Hamilton *et al*. who obtained a surface area of 32.1 m^2g^{-1}.[103]

Table 9: Summary of ICP-OES and BET analysis of Fe-ref (Chapter 3) and of the doubly promoted catalysts utilised within this chapter. BET measurements were performed in triplicate therefore, standard deviation for surface area (m^2g^{-1}) and pore volume (cm g^{-1}) are provided in brackets. Bracketed ICP values are measured values reported by Butterworth Laboratory but below official detection limits and are provided to indicate the varying sulfur concentrations across the samples.

Catalyst sample	ICP-OES S Value (ppm)	ICP-OES Na Value (ppm)	Surface Area (m^2g^{-1})	Pore Volume (cm g^{-1})
Fe-ref	0	0	47.51 (±*3.21*)	0.230 (±*0.008*)
Fe-Na-S_{10}	<100 (*22*)	1855	45.44 (±*4.07*)	0.240 (±*0.011*)
Fe-Na-S_{50}	<100 (*41*)	2120	48.56 (±*0.662*)	0.265 (±*0.005*)
Fe-Na-S_{100}	<100 (*56*)	2890	47.36 (±*1.47*)	0.227 (±*0.028*)
Fe-Na-S_{175}	100 (*96*)	1910	47.89 (±*0.651*)	0.221 (±*0.004*)
Fe-Na-S_{250}	100 (*145*)	1820	46.14 (±*2.16*)	0.248 (±*0.004*)

Analysis of the promoted samples by XRD (**Figure 39**) indicate reflections at 2θ = 24.4, 33.4, 35.9, 41.2, 49.7, 54.2, 57.8, 62.6, 64.2, 69.6, 72.1, 75.7, 80.8, 83.1, 85.2 and 88.9°, which are identical to that observed by the reference catalyst sample. By application of the Highscore Plus programme,[106] reflections are characteristic to that of highly ordered hematite (α-Fe_2O_3). This establishes that the low levels of promotion to the reference catalyst are not having any crystallographic effect on the catalyst matrix. It should be noted that these samples, including **Fe-ref**, were analysed using a different X-ray diffractometer which utilised Cu K_α radiation, whereas XRD measurements in **Chapter 3** used Co K_α radiation and therefore there are slight variation in the reflections associated with hematite.

TPR studies were carried out to establish whether the inclusion of varying levels of sulfur alongside the fixed levels of sodium may have an effect on the reducibility of the catalyst (**Figure 40**). The TPR profile of the reference catalyst (**Fe-ref**) investigated in the previous chapter has been included to highlight the shift to higher temperatures induced by the increasing sulfur concentration of the samples. The TPR profile for **Fe-ref** displayed two features at 597 and 779 K, indicating the reduction of hematite towards metallic iron

(*Equation 4.1*). As the sulfur concentration is increased these features shift to a higher temperature and for the highest sulfur concentration sample (**Fe-Na-S$_{250}$**), features are present at 645 and 832 K.

$$\text{Hematite } (\alpha Fe_2O_3) \rightarrow \text{Magnetite}(Fe_3O_4) \rightarrow \text{Wüstite } (FeO) \rightarrow \alpha Fe \qquad \textbf{(4.1)}$$

The hindered reduction displayed in the TPR profiles correlates well with that observed by Warringham and co-workers who analysed a hematite catalyst promoted with only sulfur. *In situ* XRD analysis of the singly promoted sulfur samples, exposed to CO hydrogenation conditions over a 6 h period, indicated that the increased sulfur levels hindered the formation of iron carbides.[95]

Other characterisation techniques were also applied for these samples including, X-ray photoelectron spectroscopy (XPS), transmission electron microscopy (TEM) and energy dispersive X-ray (EDX) analysis. The low concentrations of promoters within the sample, in particular the sulfur, caused significant challenges in each of these analytical methods. For EDX analysis the only sample in which sulfur was detectable was the sample with the highest sulfur loading (**Fe-Na-S$_{250}$**), with the analysis report for this sample shown in **Figure 41**. All other promoted samples did not indicate the presence of sulfur, suggesting these samples were below the detection limit of the instrument (detection limit ~ 0.2 wt. %). SEM images were also taken of the samples and showed no significant differences to that previously observed by Warringham for the reference sample (**Fe-ref**) displaying rough, textured blocks of material.[73]

An attempt was made to analyse these particular samples using electron energy loss spectroscopy (EELS) on the TEM microscope with the assistance of Donald MacLaren (University of Glasgow, School of Physics). The aim of this was to determine the spatial distribution of the elements within the catalyst sample. However, under the electron beam there was a very rapid build-up of carbon *i.e.* electron beam contamination, which quickly swamped the EELS signal, thus resulting in difficulties in obtaining a spectrum of reasonable resolution for Fe, the main composition of the catalyst, and so obtaining EELS for the small levels of sulfur within the catalyst was not possible.[130]

XPS is a surface sensitive technique and was used to obtain information on the atomic weight percentage of sulfur and to identify the ratio of sodium to sulfur within each of the samples as shown by **Figure 42.** Hervé Ménard (Sasol Technology UK Ltd.) was

responsible for performing these measurements. The ratio of Na:S is negligible for **Fe-ref**, as to be expected, as promoters were not added to this sample. However, the ratio of Na:S across all the doubly promoted samples is fairly consistent, with the exception of **Fe-Na-S$_{100}$**, displaying a slightly higher ratio. This can be accounted for as the ICP analysis, shown in **Table 9**, indicated that this particular sample has a significantly higher sodium content in comparison to the other promoted samples. The atomic weight percentage of sulfur across all samples, including **Fe-ref**, shows little variation. However, it should be noted that these values obtained here are significantly low and are actually below the detection limit of the instrument (detection limit ~ 0.1 wt. %). From the XPS results obtained, it is not possible to comment on the distribution of the sulfur levels as these are below the detection limits of the instrument and that the variation in Na:S is only a reflection of the slight variation in concentration of sodium within the catalyst. Overall, the XPS results suggest that the promoters are evenly distributed at the catalyst surface and this situation may well be applicable throughout the bulk of the iron oxide matrix.

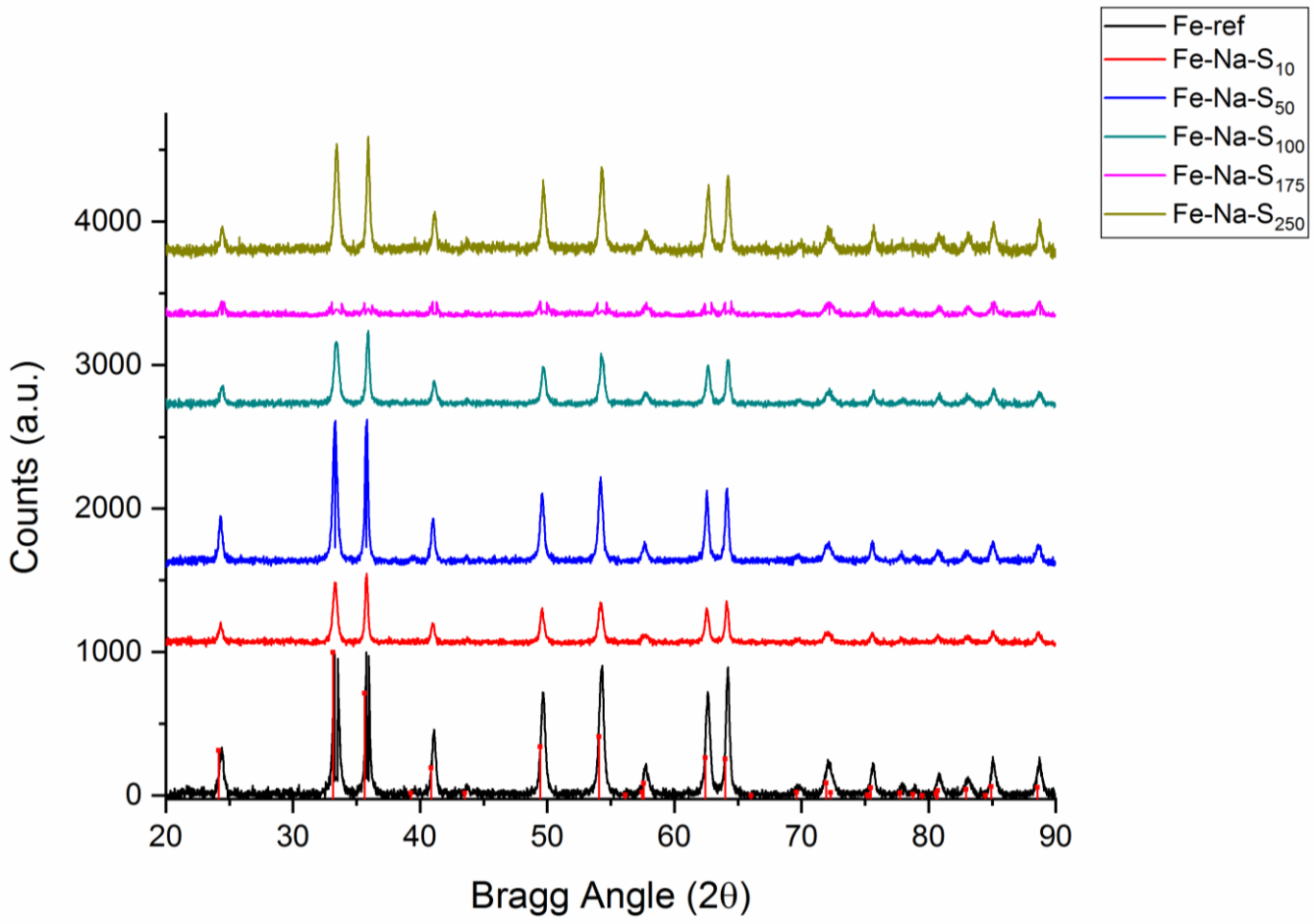

Figure 39: A comparison of the powder X-ray diffractogram (Cu K_α) of the hematite reference catalyst sample (Fe-ref) as-prepared against the five samples promoted with varying levels of sulfur (10-250 ppm) and a fixed level of sodium (2000 ppm). The red lines are indicative of reflections corresponding to α-Fe_2O_3 reference diffractogram from the programme Highscore Plus.[106]

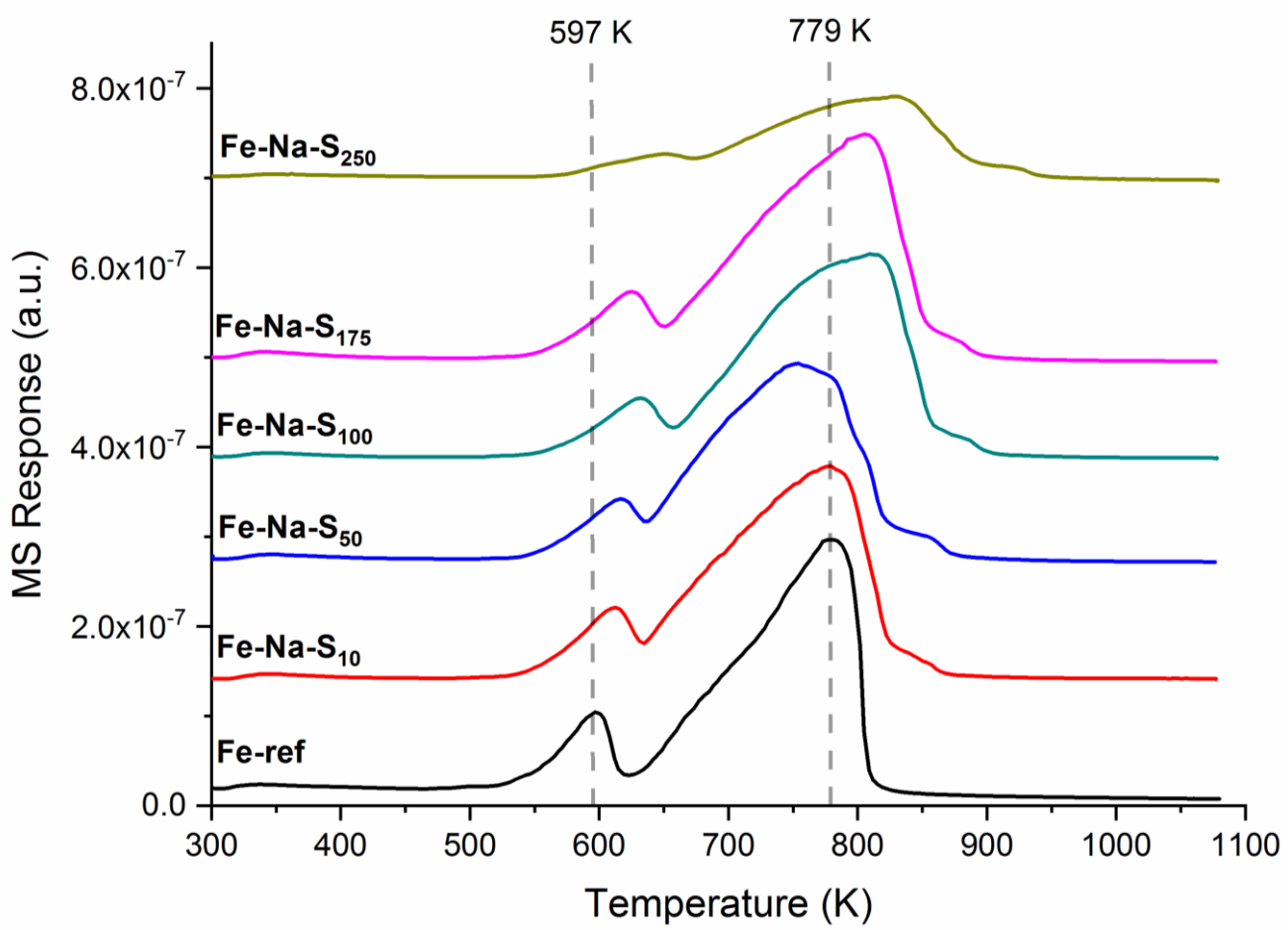

Figure 40: The *in situ* temperature-programmed reduction profile (with hydrogen) of the hematite reference catalyst (Fe-ref) alongside the five samples doubly promoted with varying levels of sulfur and a fixed level of sodium. The dashed lines are indicative of the features of the Fe-ref profile, highlighting the shift to higher temperatures of the promoted samples.

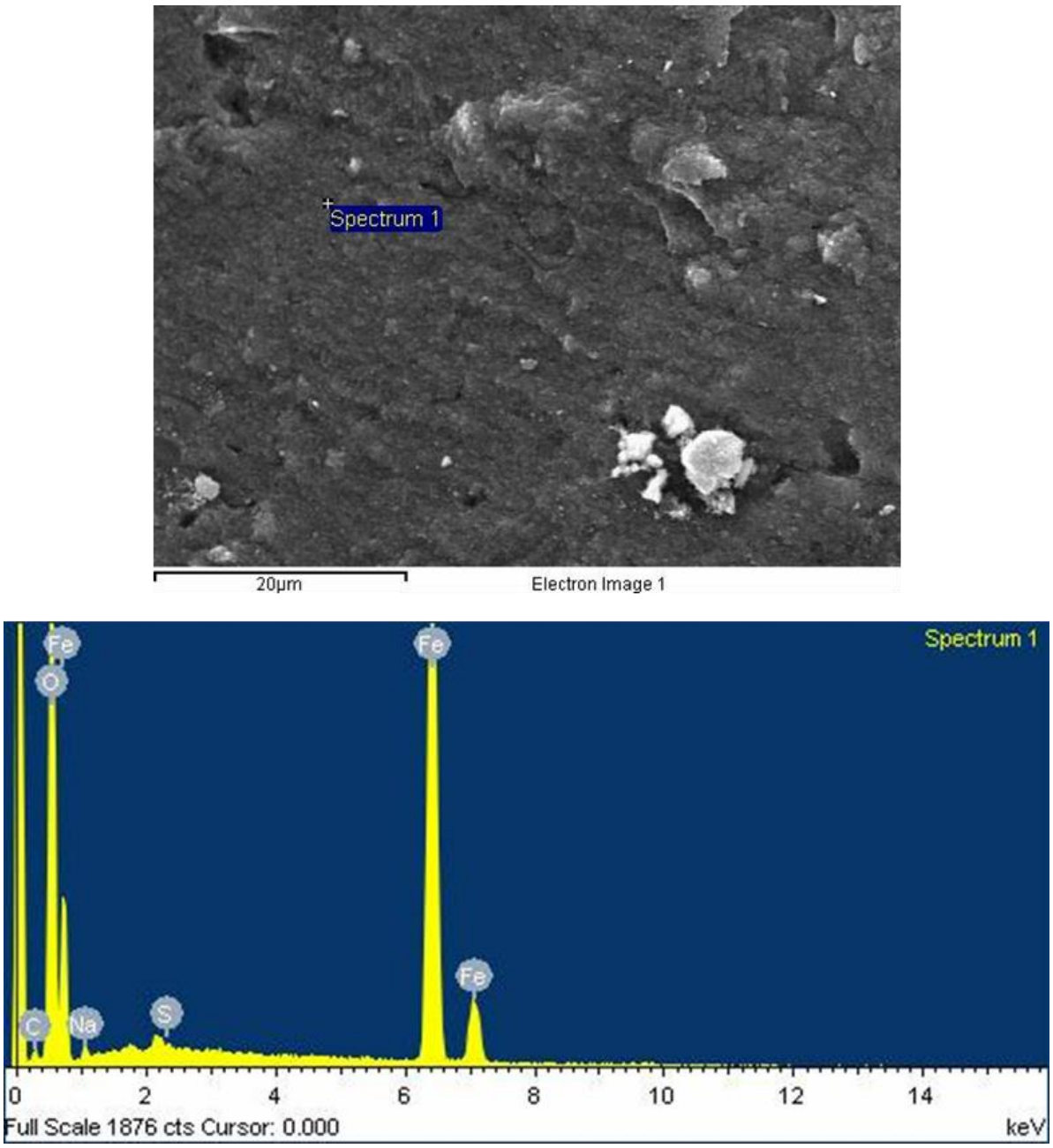

Figure 41: Top image is a scanning electron micrograph of catalyst Fe-Na-S_{250} as-prepared. The bottom image is the EDX analysis of the catalyst sample from the image above, detecting the presence of Fe, O, C, Na, and S.

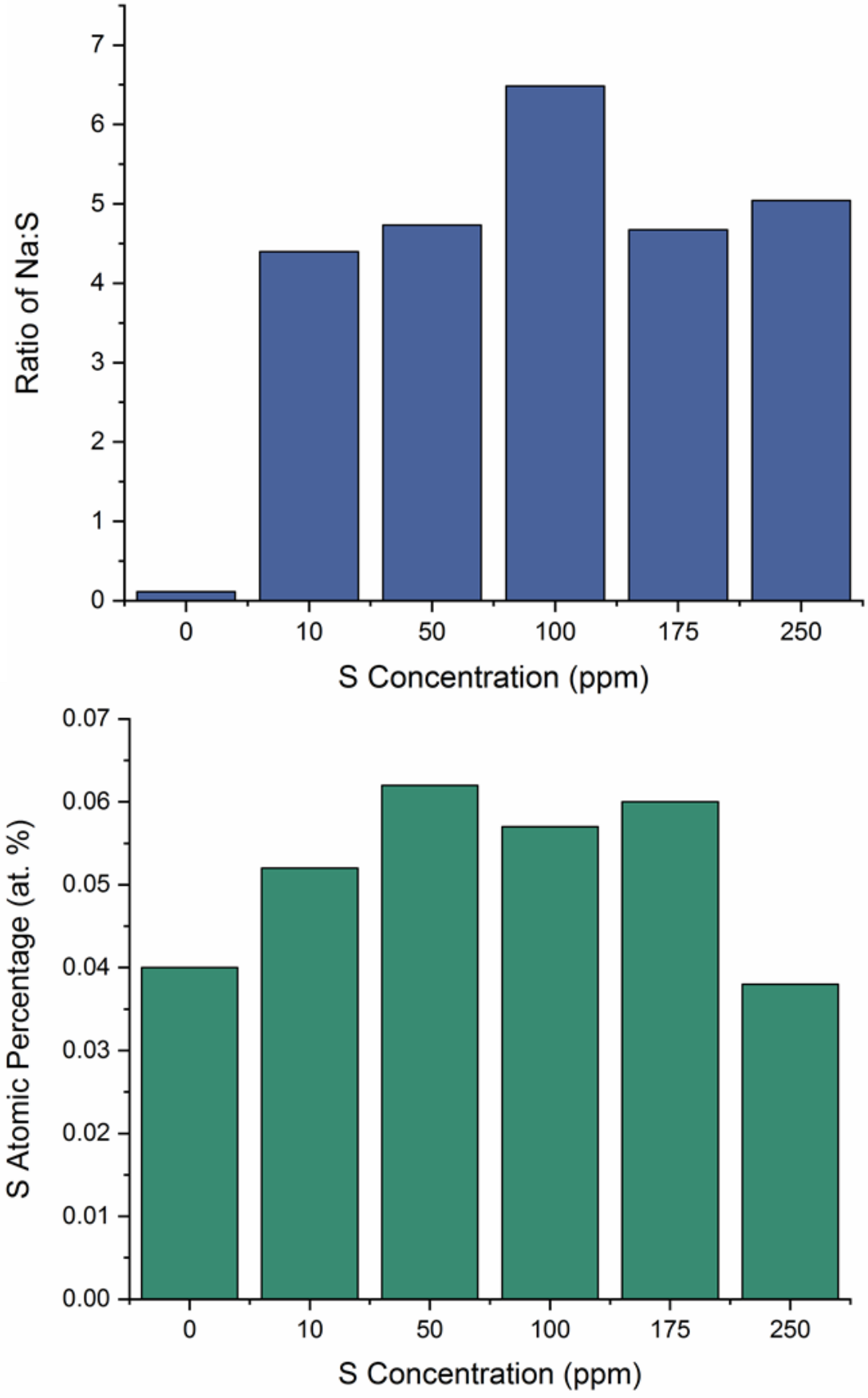

Figure 42: Data obtained from analysis using X-ray photoelectron spectroscopy. The top figure displays the ratio of Na:S across all doubly promoted samples and of Fe-ref. The bottom figure displays the atomic percentage of sulfur across all promoted samples and Fe-ref.

4.3. Micro-reactor Study

The previous chapter discussed the use of a CO hydrogenation reaction as a representative FTS reaction and discussed the reaction chemistry that takes place when utilising the micro-reactor set-up (**Chapter 3, Section 3.4**). The CO hydrogenation reaction has been repeated for each of the doubly promoted catalyst samples using 6 h as a standard reaction test period and 40 mg of catalyst. **Figure 43** presents reaction profiles of the sample containing the lowest (**Fe-Na-S$_{10}$**) and highest (**Fe-Na-S$_{250}$**) sulfur concentrations. In addition to reactants and products normally measured on the mass spectrometer for a CO hydrogenation reaction, masses for sulfur monoxide (SO, m/z 48), sulfur dioxide (SO_2, m/z 64) and hydrogen sulfide (H_2S, m/z 34) were monitored, but not observed. However, it is interesting to note that on removal of the promoted samples from the reactor, a yellow staining was present on the quartz reactor tube, not normally observed after the **Fe-ref** is exposed to CO hydrogenation reaction conditions. It is possible that this may either be elemental sulfur or sodium sulphide (Na_2S), formed as a result of the catalyst exposed to reaction conditions. Both reaction profiles of the promoted samples are generally similar to that observed by the **Fe-ref** sample (**Chapter 3, Section 3.4, Figure 34**), displaying the three stages which can be summarised as follows: *Stage I*, identified by the first production of CO_2 and consumption of CO at 515 K signifying the reduction of α-Fe_2O_3 towards Fe_3O_4 by CO, *Stage II*, identified by the simultaneous production of CO_2, H_2O and CH_4 and consumption of CO and H_2 occurring at 623 K, and finally *Stage III* is indicated by the reaction reaching a steady state regime. Iron time yield (FTY) values for each sample, **Fe-Na-S$_{10}$** and **Fe-Na-S$_{250}$**, are 1.23 x 10^{-4} and 9.40 x 10^{-5} mmol (CO) $g_{Fe}^{-1}s^{-1}$ respectively. Interestingly, the highest sulfur loaded sample (**Fe-Na-S$_{250}$**) displayed an increased production of CO_2 and CH_4 over a longer period of time on stream, than the other doubly promoted samples or of the reference material. This increased production of CO_2 may be due to the fact that the sulfur is inhibiting the reduction process of the catalyst, as shown from TPR measurements (**Figure 40**). As one of the main routes of CO_2 production is from the reduction of α-Fe_2O_3 towards metallic iron, this would result in an increased time on stream before CO_2 reaches a steady state. Due to the low product yields observed from the micro-reactor study, it is not possible to comment on the selectivity of the doubly promoted catalysts in terms of olefin synthesis from these measurements. Higher-pressure measurements using the industrial facilities would be illuminative here but for commercial and contractual reasons are not available for inclusion in this thesis.

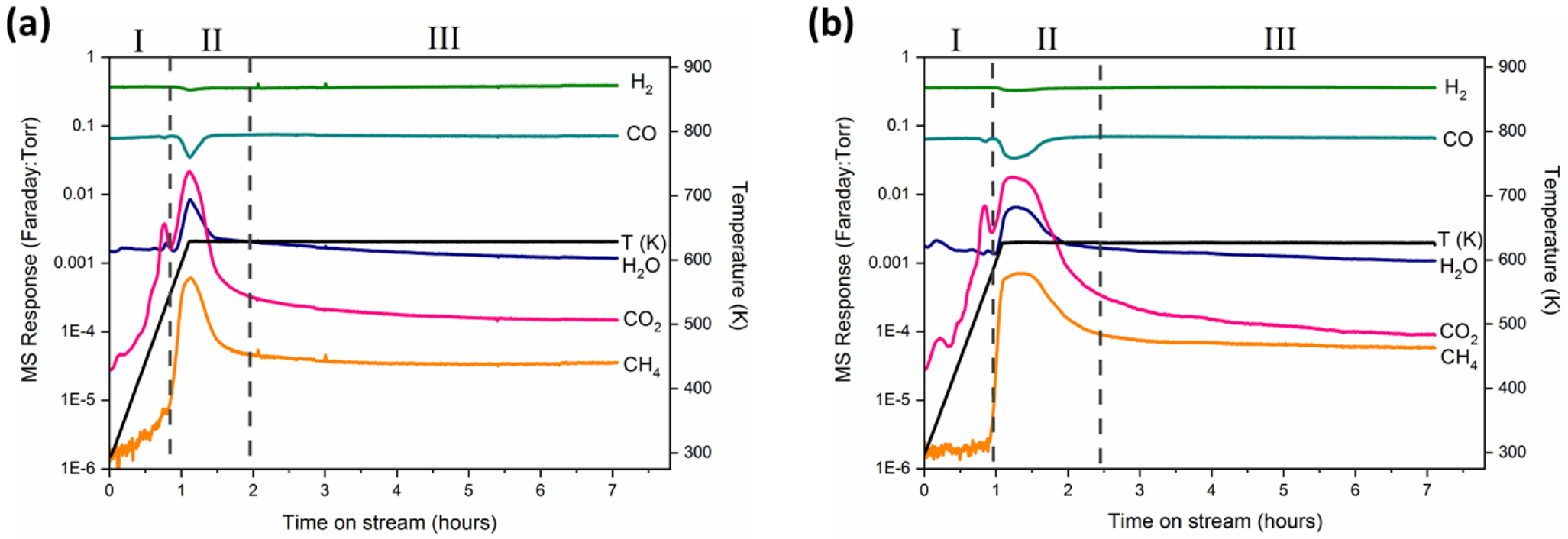

Figure 43: Micro-reactor reaction profiles with a doubly promoted catalysts, a) 10 ppm & b) 250 ppm of S and a fixed level of Na (*ca.* 2000 ppm) during a CO hydrogenation reaction at ambient pressure and 623 K for 6 h.

4.3.1. *In situ* Temperature-programmed Oxidation

The mass of catalyst used for both *ex situ* and *in situ* TPO measurements has previously been explored (**Chapter 3, Sections 3.3.2.3** and **3.4.1**) in order to establish a profile in which, within our experimental constraints, the oxygen is not being completely consumed. This issue once again arose when carrying out *in situ* TPO measurements of the doubly promoted catalyst samples, which led to further investigations varying the sample masses utilised. The lowest sulfur sample (**Fe-Na-S_{10}**) was selected as the test catalyst, varying the sample mass from 20-40 mg with the resulting profiles displayed in **Figure 44**. Despite the issue of oxygen consumption being resolved at the lower catalyst masses (20 and 30 mg), the presence of the α species, is no longer evident, once again highlighting the sensitivity of the micro-reactor set-up to gas/solid exchange dynamics. As this feature may be a key component in the comprehensive understanding of the evolution of the catalyst and the hydrocarbonaceous overlayer, it was decided that a mass of 40 mg should be utilised for measurements of the doubly promoted samples to ensure key components are observed. It is acknowledged that these measurements are therefore qualitative rather than quantitative as the previous measurements have been (**Chapter 3, Section 3.3.2.3, Figure 33**).

Figure 45 presents the TPO profiles of all the doubly promoted samples, identifying the previously observed features, α (precursor species), β (amorphous carbon) and γ (bulk iron carbides). The α species shows very little variation over the range of sulfur concentrations studied. From a qualitative perspective, in comparison to that observed for **Fe-ref**, the α species is more prominent in the promoted catalyst samples, suggesting an increased production of this species. This feature has previously been tentatively assigned as a precursor to the formation of the hydrocarbonaceous overlayer[95], and within **Chapter 3**, is proposed more specifically as either (i) a precursor to the aliphatic component of the hydrocarbonaceous overlayer or (ii) precursor to the β or γ TPO features. Therefore, as there is an increased production of this species in comparison to that of **Fe-ref**, the aliphatic component observed by INS, would be expected to be perturbed. This will be discussed later within this chapter (**Section 4.4.2**).

On the other hand, again from a qualitative perspective, the β component significantly increases upon increasing sulfur concentration whereas the γ feature, displays reduced formation in relation to **Fe-ref** observed previously by Warringham and co-workers.[105] This would imply that the reduction of catalyst has been impeded due to the presence of the sulfur and sodium, correlating with the TPR profiles (**Section 4.2, Figure 40**). This increased production of amorphous carbon and reduced iron carbide formation may be

explained through Niemantsverdriet's competition model as previously discussed in **Chapter 3, Section 3.5**.[25,127] Carbon in a hydrogen deficient environment will result in the formation of amorphous carbon (*Equation 4.2*) over the formation of iron carbides (Fe_xC_y) shown by *Equation 4.3*. Therefore, it is tentatively suggested that the increasing levels of sulfur hinder the mass transport of hydrogen within the system resulting in hydrogen lean conditions, causing the preferred formation of amorphous carbon over bulk iron carbides.

$$nC_{(ad)} \rightarrow C_{n(poly)} \quad (\mathbf{4.2})$$

$$nC_{(ad)} + Fe \rightarrow Fe_xC_y \quad (\mathbf{4.3})$$

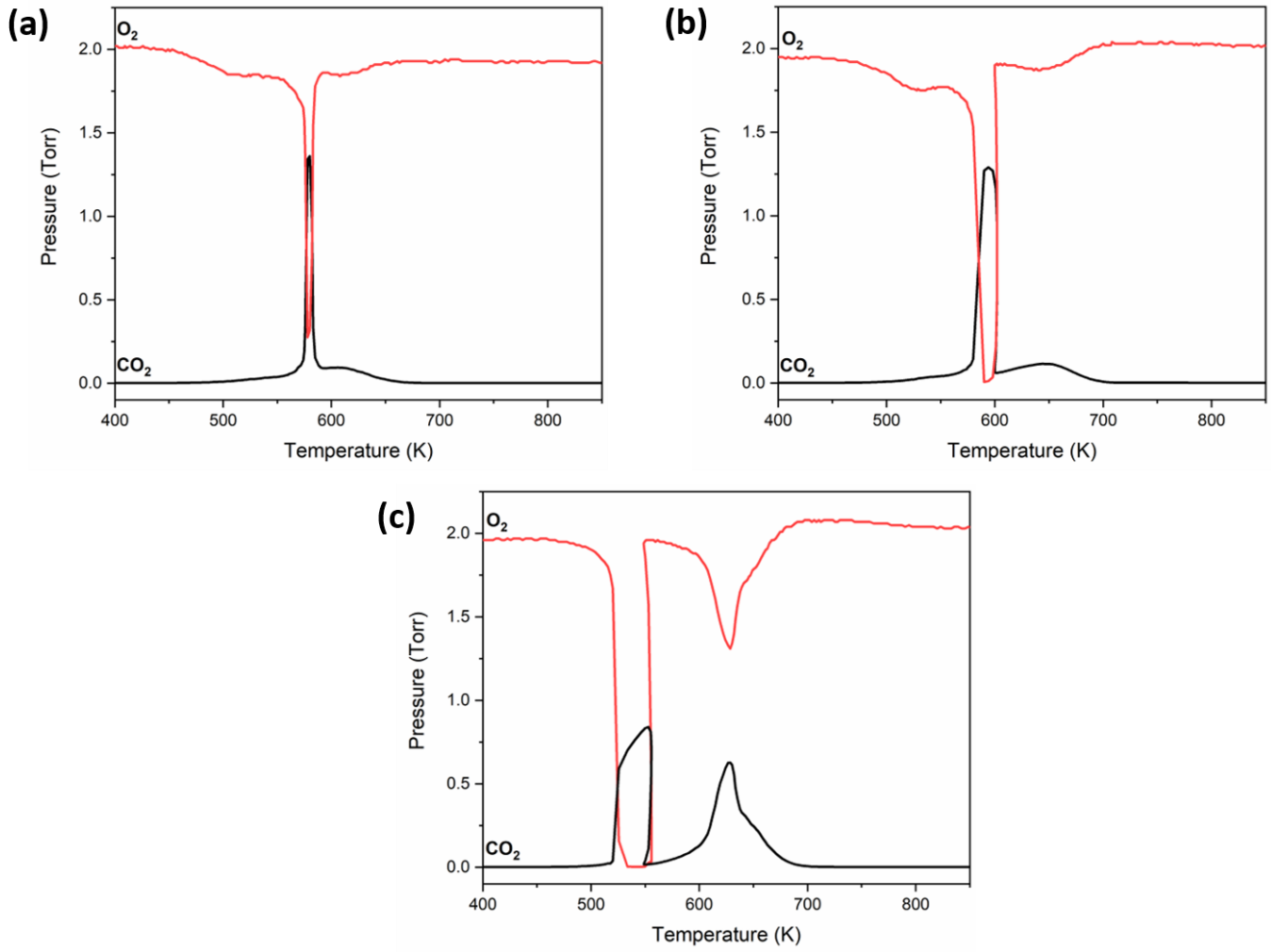

Figure 44: ***In situ*** **temperature-programmed oxidation profiles of a doubly promoted α-Fe_2O_3 sample (Fe-Na-S_{10}) using (a) 20 mg (b) 30 mg and (c) 40 mg of catalyst after exposure to CO hydrogenation conditions on the micro-reactor for 6 h. The black line is indicative of the measured CO_2 and the red line indicative of O_2 consumption.**

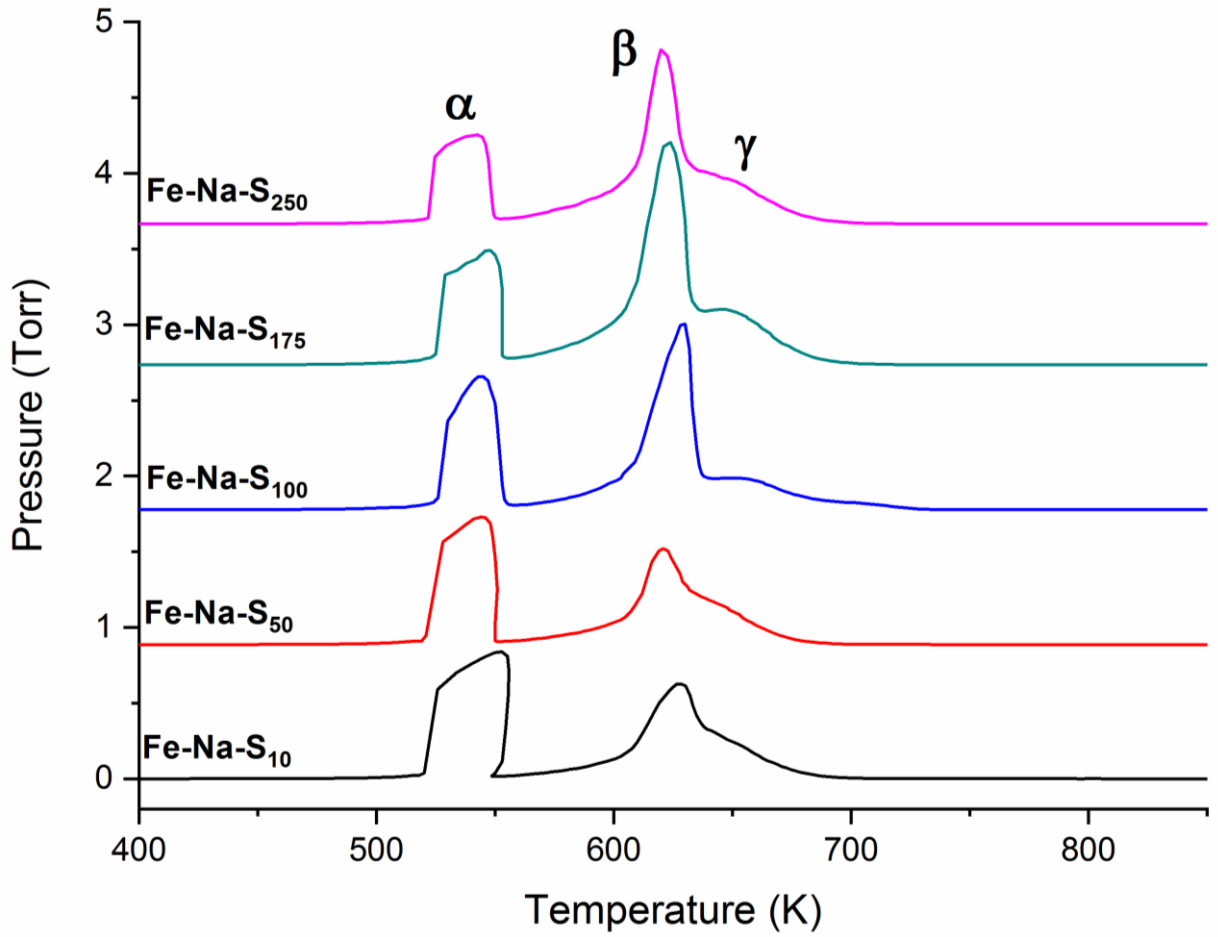

Figure 45: ***In situ*** **temperature-programmed oxidation profiles of the doubly promoted α-Fe_2O_3 (40 mg) after exposure to CO hydrogenation conditions at 623 K, ambient pressure for 6 h on stream on the micro-reactor. Profiles are offset for clarity.**

4.3.2. *Ex situ* Characterisation

4.3.2.1 X-ray Diffraction

The *ex situ* XRD diffractograms shown in **Figure 46** are post-reaction after a 6 h CO hydrogenation reaction in a micro-reactor set-up and have been analysed using a diffractometer with Co K_α radiation at Sasol Technology UK Ltd. Each diffractogram of the doubly promoted catalyst samples displays a fully carbided species. Unfortunately, Rietveld analysis was not carried out in this instance due to the closing of Sasol Technology UK Ltd as discussed in the **Preface** of this thesis. Therefore, the specific carbide present has not been identified. It should be noted that the samples analysed here were not reacted within the micro-reactor set-up in Glasgow (**Chapter 2, Section 2.2.1, Figure 13**) due to time limitations on the visit to Sasol Technology UK Ltd. Therefore, samples were reacted in a micro-reactor set-up at Sasol, which would result in differences in the gas/solid exchange dynamics of the two micro-reactors. Nonetheless, with reference to **Figure 28**, all of the diffractograms in **Figure 46** are consistent with the formation of iron carbide, with Hägg carbide being the most likely molecular entity.

From the TPR profiles discussed in **Section 4.2, Figure 40**, it was shown that the addition of the promoters was hindering the reduction of the catalyst and thus evidence of under reduction in the XRD diffractograms, from increased levels of sulfur, may be expected. However, each diffractogram is identical, despite variations in sulfur concentration. This may suggest that the addition of Na/S is not affecting bulk transformations, indicating the Na/S modification may be exclusively affecting surface properties.

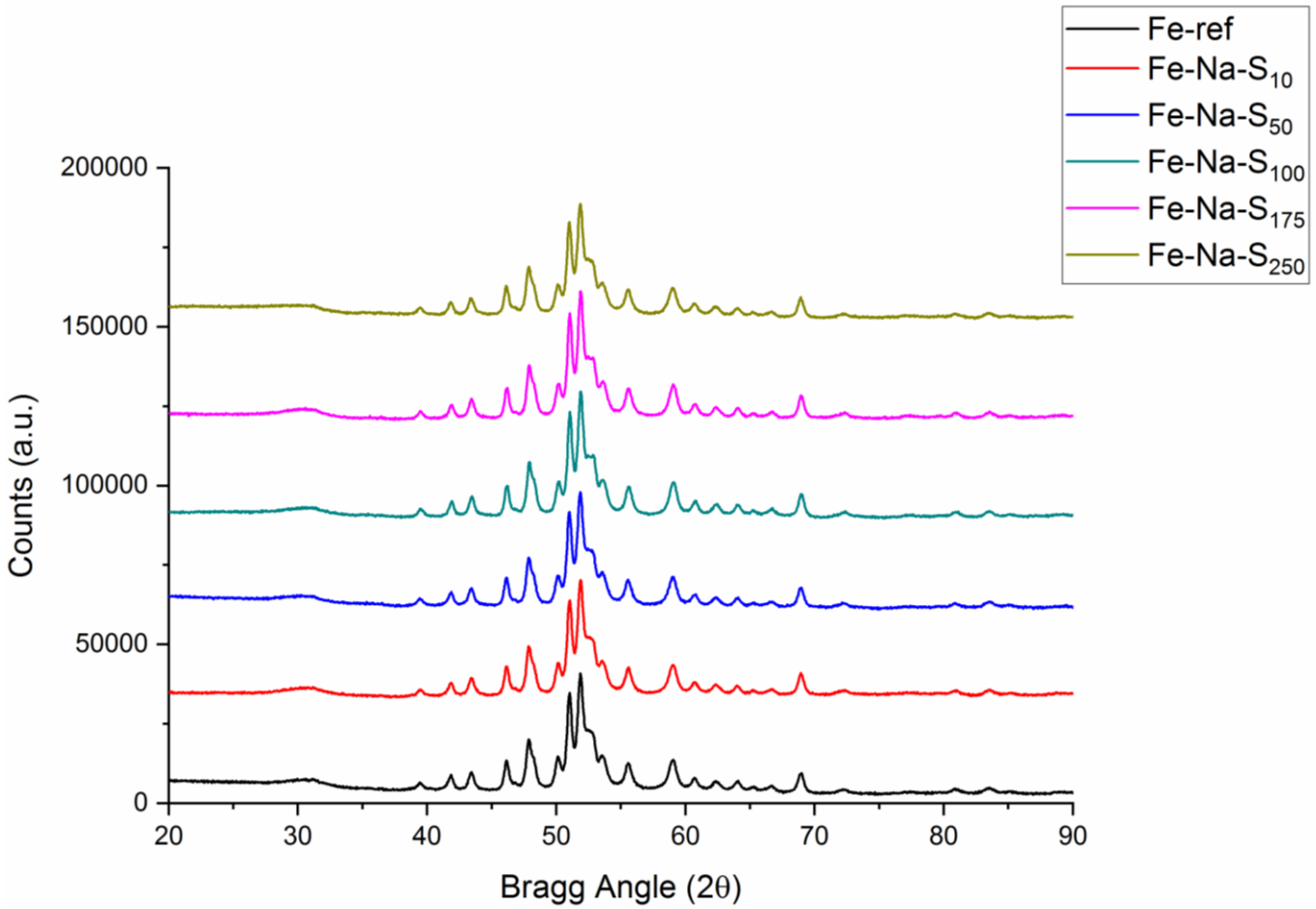

Figure 46: ***Ex situ*** **X-ray diffractograms (Co K_α) of the doubly promoted α-Fe_2O_3 samples and Fe-ref, after exposure to CO hydrogenation conditions at 623 K in a micro-reactor set-up for 6 h.**

4.3.2.2. XANES

The application of XANES was to primarily focus on the sulfur aspect of the catalyst and how this may change on exposure to ambient pressure CO hydrogenation reaction conditions. As sulfur has several known accessible oxidation states (-2, 0, +2, +4, +6),[84] reference samples (S, Na_2SO_3, $Na_2S_2O_3$, $FeSO_4$, and FeS_2) were first measured to gain reference spectra for the various oxidation states which could potentially be present within the catalyst samples. **Figure 47** displays the reference spectra with the data tabulated below in **Table 10** correlating with values reported within the literature.[131,132]

Table 10: Tabulated XANES data for reference materials ($FeSO_4$, Na_2SO_3, S, $Na_2S_2O_3$, FeS_2) detailing peak positions and formal oxidation state of sulfur within the compound.

Reference Material	Peak Position (eV)	Formal oxidation state of sulfur
Iron sulfate ($FeSO_4$)	2483	+6
Sodium sulphide (Na_2SO_3)	2482	+4
	2479	
Sodium thiosulfate ($Na_2S_2O_3$)	2481	+2
	2472	
Elemental sulfur (S)	2473	0
Iron sulphide (FeS_2)	2483	-2
	2472	

All doubly promoted samples (**Fe-Na-S_x**) were analysed as-prepared and the XANES spectra are shown in **Figure 48 (a)**. The sample containing the lowest sulfur concentration (**Fe-Na-S_{10}**) was omitted from this figure and is shown on a separate scale (**Figure 48 (b)**) due to the low intensity in comparison to the other samples. All spectra are indicative of

sulfur to be present in the form of sulfate, *i.e.* S^{6+}. This is to be expected as sulfur is incorporated into the catalyst through impregnation with its final form being sodium sulfate (Na_2SO_4) as highlighted in **Chapter 2**, **Section 2.1**. It's noted that the lower concentrated samples, **Fe-Na-S$_{10/50}$** exhibit a feature at 2473 eV, corresponding to sulfur as S^0 (**Table 11**).

Upon exposure to CO hydrogenation conditions for 6 h on the micro-reactor, there are noticeable changes in the spectra highlighting the change in the sulfur oxidation state within the catalysts (**Figure 49**). Again, **Fe-Na-S$_{10}$** is shown on a separate scale due to the low intensity of the features in comparison to the other samples analysed. Despite the poor signal:noise ratio in comparison to the as-prepared samples, features are observed at 2471, 2473, 2481, 2483 and 2500 eV. The features at 2483 and 2500 eV are observed in the as-prepared samples and have been assigned to sulfur in its highest known oxidation state (S^{6+}), suggesting the presence of some Na_2SO_4 remains within the catalyst. Therefore, the emergence of peaks below this energy indicate that the sulfur has undergone reduction during the exposure to the CO hydrogenation conditions, as for XANES the higher the oxidation state of a species, the absorption edge energy increases correspondently (**Table 10**).[133] The emergence of a peak at 2481 eV indicates that sulfur is additionally present in the +4 oxidation state (S^{4+}) *i.e*. reduced from Na_2SO_4 to sodium sulfide (Na_2SO_3). The final two features at 2473 and 2471 eV are further indicative of sulfur being in 0 and -2 oxidation states, highlighting further reduction of sulfur from the original sulfate species, with Na_2S as the fully reduced species. The data set obtained within this study, before and after exposure to CO hydrogenation conditions, correlates well with a preliminary study by Perdjon-Abel who examined an iron-based FTS catalyst, doubly promoted in a similar concentration range with sulfur (500 ppm) and sodium (4000 ppm) before and after exposure to reduction conditions.[134]

Overall, the XANES spectra within this study, post-reaction, show sulfur to be present in a variety of oxidation states with the bulk composition of the catalyst consisting of Na_2SO_4, Na_2SO_3 and Na_2S, contrasting with that observed from post-reaction XRD, which suggested the addition of promoters did not affect bulk transformations and may be exclusively affecting surface properties. It is acknowledged that XRD and XANES are both bulk techniques and that each technique is emphasising different attributes of the post-reaction samples. The XRD (**Figure 46**) show carburization of the promoted catalysts but show no evidence of S or Na containing species, presumably because these entities are

below detection levels of the laboratory instrumentation. Conversely, the high intensity synchrotron spectrometer is exclusively sampling sulfur containing species and can discern differences in the sulfur populations after reaction.

Table 11: Tabulated XANES data and assignments of features observed in Figure 49 of the doubly promoted samples after exposure to CO hydrogenation conditions at 623 K for 6 h on the micro-reactor set-up.

Feature Observed (eV)	Associated Sulfur Oxidation State	Assigned Sulfur Species
2471	S^{2-}	Na_2S
2473	S^{0}	S
2481	S^{4+}	Na_2SO_3
2483	S^{6+}	Na_2SO_4
2500	S^{6+}	Na_2SO_4

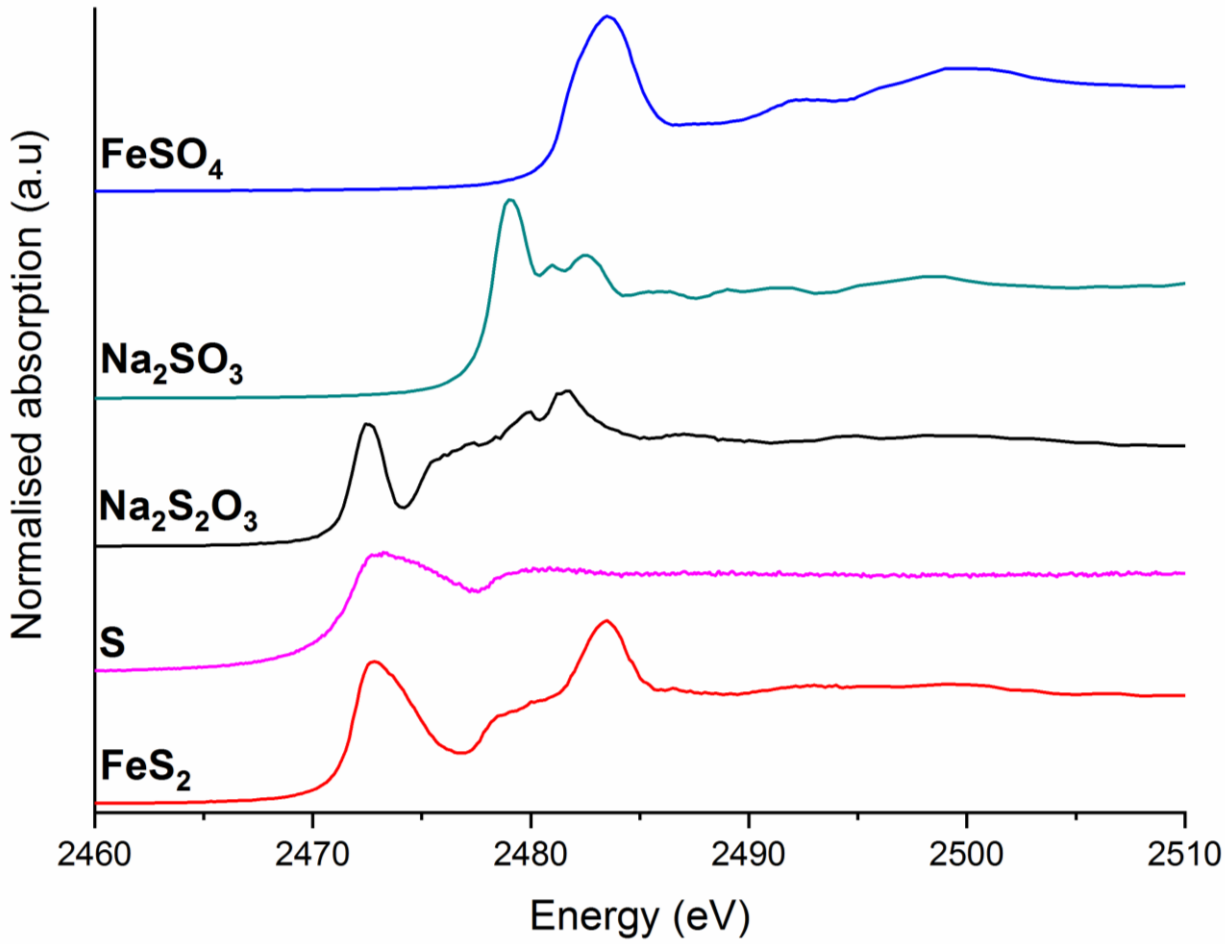

Figure 47: The sulfur K-edge XANES spectra of the reference materials ($FeSO_4$, Na_2SO_3, S, $Na_2S_2O_3$, FeS_2) indicative of sulfur present in various oxidation states.

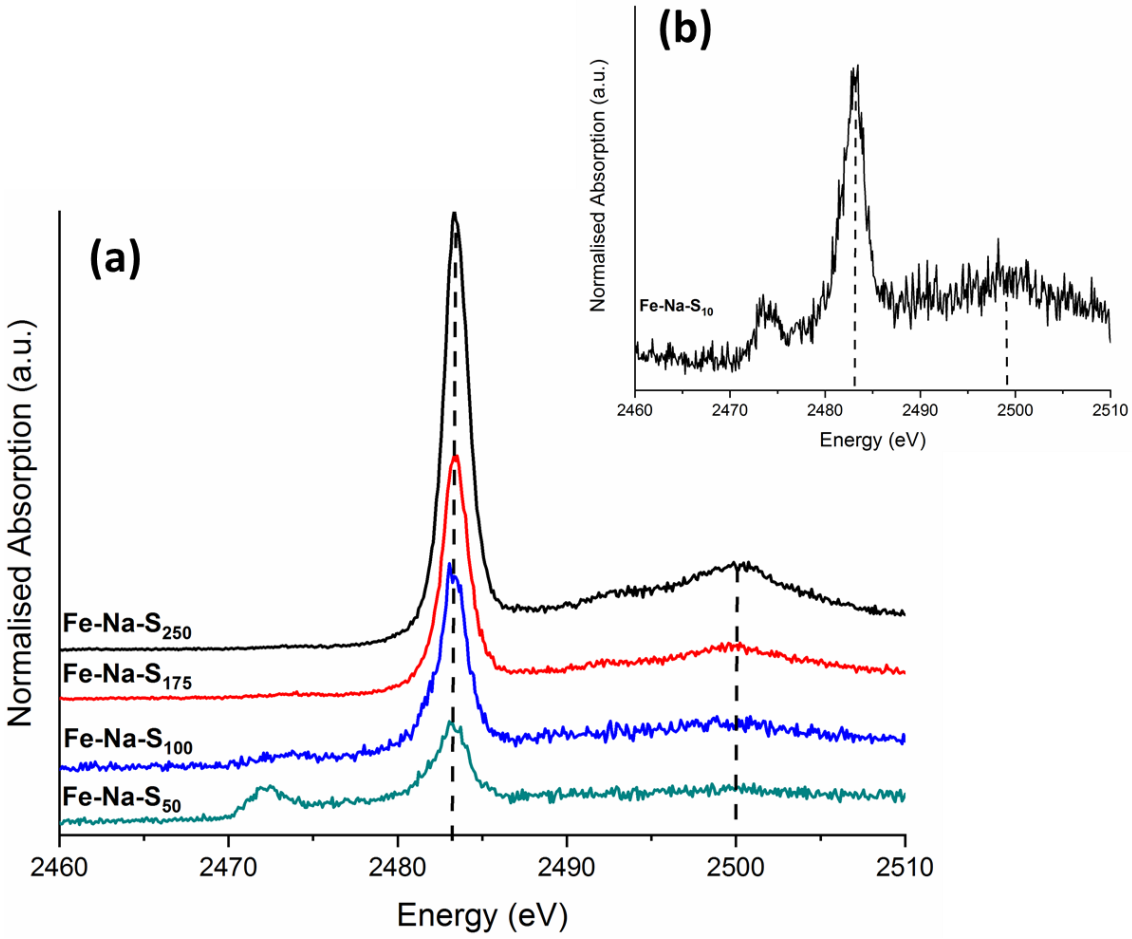

Figure 48: The sulfur K-edge of each of the doubly promoted samples before exposure to reaction conditions. (a) Displays samples Fe-Na-$S_{50\text{-}250}$ (b) Displays sample Fe-Na-S_{10} on a reduced scale.

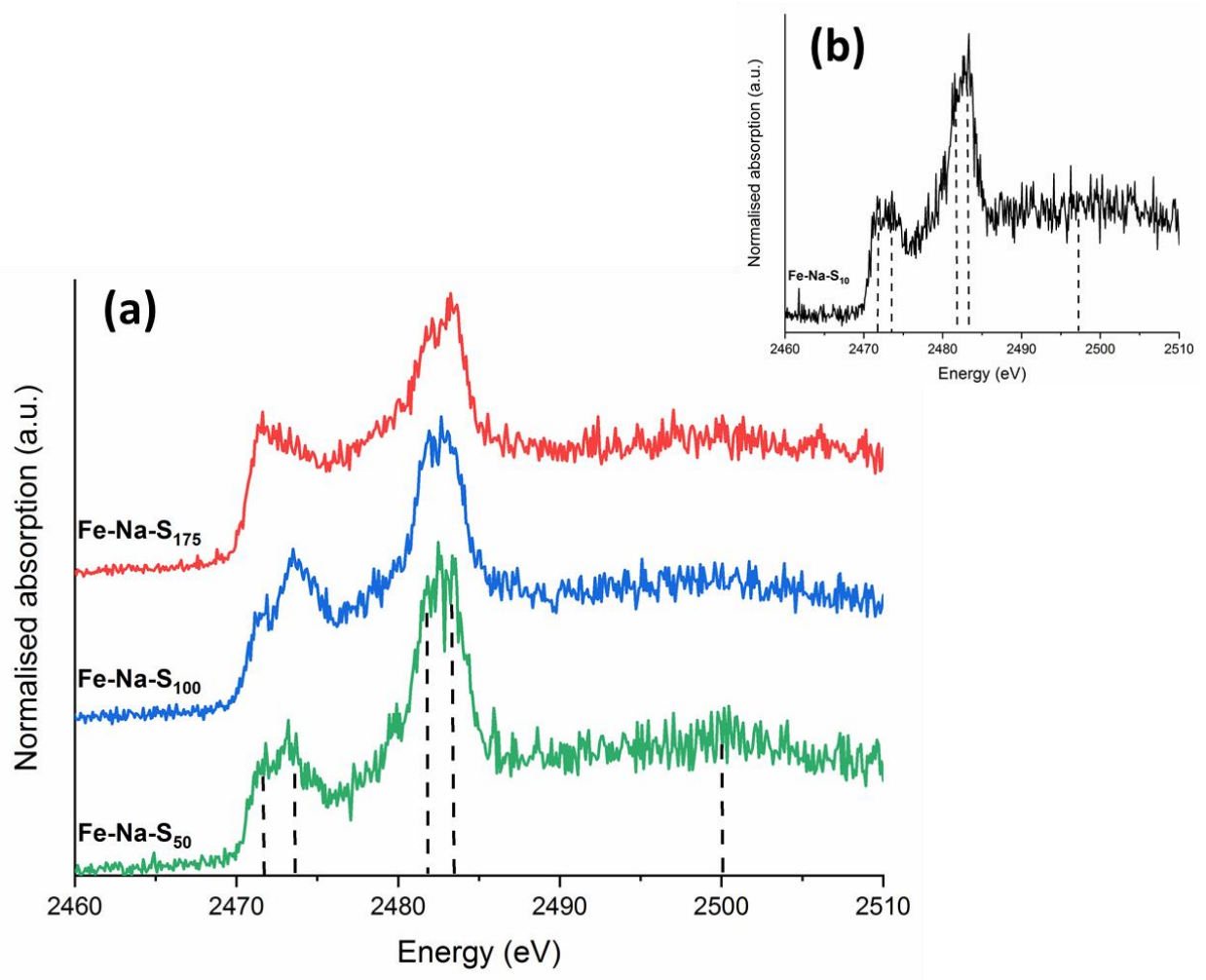

Figure 49: The sulfur K-edge of each of the doubly promoted samples after exposure to CO hydrogenation reaction conditions. (a) Displays samples Fe-Na-$S_{50\text{-}175}$ (b) Displays sample Fe-Na-S_{10} on a reduced scale.

4.4. Large-scale Study

4.4.1. Large-scale Reactor Testing

Before the **Fe-Na-S_x** catalysts were analysed by INS, each sample was first exposed to a 1.5 h dehydration step, followed by CO hydrogenation conditions for 8 h in the large-scale reactor at the ISIS Facility, as discussed in **Chapter 2, Section 2.2.2**. Presented in **Figure 50** is a representative MS reaction profile for one of the doubly promoted samples, **Fe-Na-S_{100}**. Similarly to that observed in the large-scale reaction profile for **Fe-ref** (**Chapter 3, Section 3.3, Figure 23**), two main stages can be identified. Firstly, the simultaneous production of methane, water and carbon dioxide, signifying the reduction of the α-Fe_2O_3 towards Fe_3O_4, followed by the reaction reaching a pseudo-steady state. Over the range of sulfur concentrations analysed, there were no significant variations in the reaction profiles between each of the promoted catalyst samples. As previously stated, the main route of CO_2 production is predominantly from reduction of α-$Fe_2O_3 \rightarrow Fe^0$ and, as observed for **Fe-ref**, there is a steady depletion of CO_2 production in the initial stages of the reaction profile. As discussed previously (**Chapter 3, Section 3.3.)** the decrease in CO_2 correlates with the CO returning to a pseudo-steady state regime. However, unlike **Fe-ref** in which CO returns to steady state by approximately 7 h, the promoted sample has not quite returned to steady state by the end of the 8 h period studied suggesting the catalyst is still undergoing reduction towards Fe^0. The increased gas/solid exchange dynamics of the large-scale reactor in relation to the micro-reactor will result in a slower reduction period.

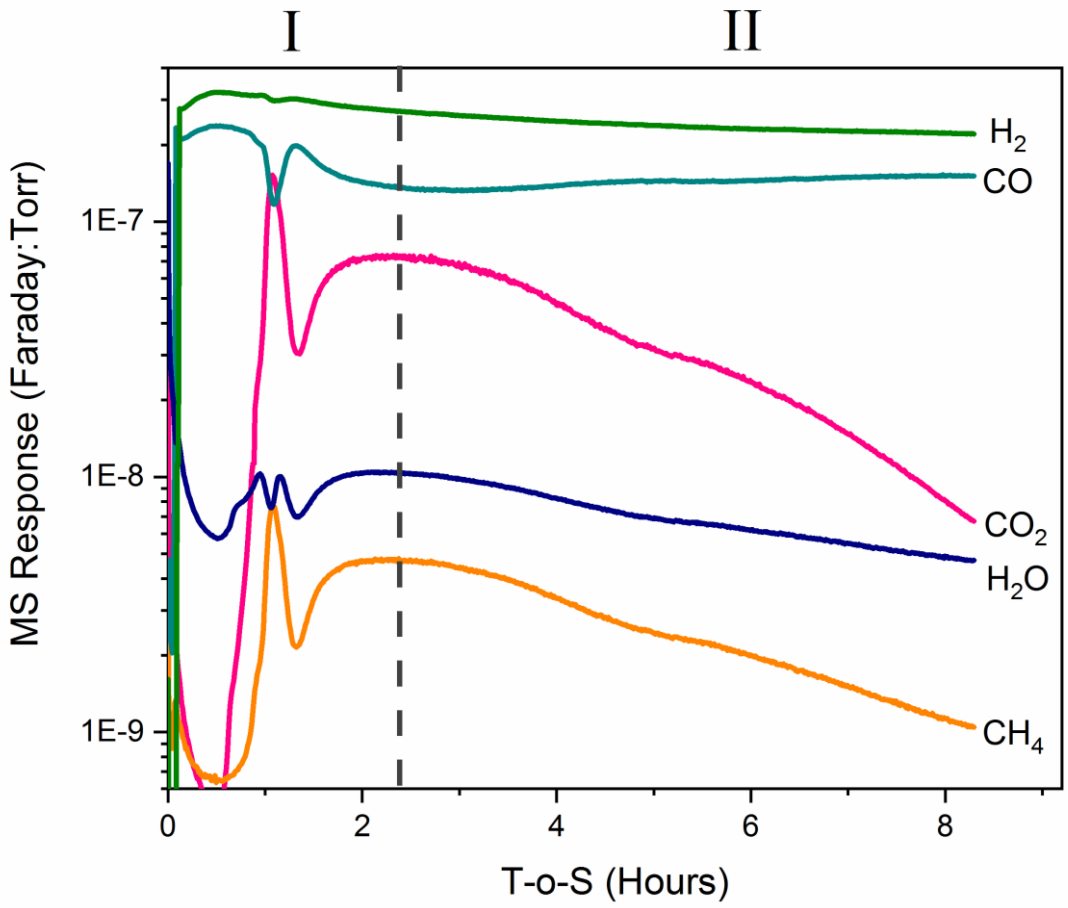

Figure 50: Mass spectrometer reaction profile for the large-scale reactor of a CO hydrogenation reaction over a doubly promoted hematite catalyst (Fe-Na-S_{100}) at 623 K, ambient pressure, for 8 h.

4.4.2. Inelastic Neutron Scattering

Once reaction testing of the catalyst samples was complete, the Inconel/stainless steel reactor was sealed and the sample transferred, in an inert environment, to an aluminium INS cell and sealed with indium wire.[66] Each of the promoted samples were measured on the MAPS spectrometer and recorded at two incident energies: 650 and 250 meV.

The spectra obtained for the samples promoted with S/Na (**Figure 51** and **54**) are not as well defined as previously obtained spectra for **Fe-ref**,[94] indicating the presence of significantly less hydrogen. Albeit, inspection of the stretching region (2400 – 3750 cm^{-1}) presented in **Figure 51**, identifies the presence of hydrocarbon moieties, with a prominent sp^2 hybridised carbon ν(C-H) feature present at 3048 cm^{-1} with a lower frequency sp^3 hybridised carbon ν(C-H) shoulder at 2932 cm^{-1}.[94,95,105] From a visual inspection, the general trend observed is that as the concentration of sulfur within the catalyst is increased there is a decrease in the formation of the hydrocarbonaceous overlayer. However, one sample, **Fe-Na-S$_{100}$**, lies out with this trend and this may be due to the fact that this particular sample has a significantly higher level of sodium, as shown from the ICP data (**Section 4.2, Table 9**), in comparison to the other doubly promoted samples. From previous calibration efforts discussed in **Chapter 2, Section 2.3.3**, each of the identified species in **Figure 51** can be quantified for the amount of hydrogen present. Despite the spectra not being as well defined as that previously obtained for **Fe-ref**,[94] the resolution of the spectra of each sample is maintained, with each of the two species, sp^3 and sp^2, easily identified and peak fitted using Gaussian fittings in the OriginPro 2018 graphical software programme. **Figure 52** displays the peak fittings of each of the hybridised features present for the **Fe-Na-S$_{250}$** sample *i.e.* the sample exhibiting the least defined spectrum, displaying a relatively respectable R^2 value of 0.895. The quantified hydrogen data set is presented in **Figure 53** as well as in **Table 12**. **Fe-Na-S$_{250}$** was repeated due to a number of errors that occurred in the reaction of the sample (initial start-up challenges of the Glasgow University/ISIS catalyst handling operations),[66] therefore questioning the integrity of the measurement. The INS spectrum of both **Fe-Na-S$_{250}$** and **Fe-Na-S$_{250(repeat)}$** is shown in **Figures 51** and **54**. Investigation of these two measurements (**Fe-Na-S$_{250}$** vs. **Fe-Na-S$_{250(repeat)}$**) is discussed further in the following section (**Section 4.4.2.1**). Data obtained by Warringham[94] for the **Fe-ref** sample, for a similar period of time on stream (6 h), has been included in **Figure 53** to display the difference in the hydrocarbonaceous overlayer

formation between promoted and unpromoted catalyst samples. On inclusion of only 10 ppm of sulfur and the fixed concentration of sodium, there is a significant decrease in the sp^2 hybridised feature, which generally decreased upon the increasing sulfur concentrations of the catalysts within this study. On the other hand, the sp^3 hybridised carbon feature initially decreases upon the introduction of promoters to the catalyst, but on the whole remains unaffected by the increasing concentration of promoter. The overall reduction in the formation of the hydrocarbonaceous overlayer, upon increasing sulfur concentrations, correlates with the promoters inhibiting the reduction process of the hematite catalyst as shown from the TPR measurements (**Section 4.2, Figure 40**). Thus, suggesting that the inclusion of these promoters may be hindering the supply of hydrogen necessary for both hematite reduction and formation of the hydrocarbonaceous overlayer.

Table 12: The quantified peak values (µmol H g^{-1}_{Fe}) for the ν(C-H) stretch features observed by inelastic neutron scattering spectra after CO hydrogenation conditions at 623 K for 8 h in the large-scale reactor.

Catalyst	ν(C-H) 2932 cm-1 (µmol H g^{-1}_{Fe})	ν(C-H) 3048 cm-1 (µmol H g^{-1}_{Fe})	ν(C-H) Total (µmol H g^{1}_{Fe})
Fe-ref	3.009	8.929	11.938
Fe-Na-S_{10}	0.2322	4.095	4.3272
Fe-Na-S_{50}	0.2248	2.320	2.5448
Fe-Na-S_{100}	0.2345	3.393	3.6275
Fe-Na-S_{175}	0.4050	2.473	2.8780
Fe-Na-S_{250}	0.05839	0.53552	0.5939
Fe-Na-S_{250} (repeat)	0.01592	1.100	1.1159

The deformation region of the INS spectra (400-1600 cm^{-1}, **Figure 54**) indicates the presence of predominantly aromatic components for all samples except **Fe-Na-S_{250}**, all which have been identified previously for **Fe-ref**.[94] The specific assignments of these features include; 506 cm^{-1} assigned to a C-C torsion mode of edge carbon atoms contained within a polycyclic aromatic network,[118] an out-of-plane C-H deformation of either an olefinic or aromatic group assigned at 871 cm^{-1},[119] a CC-H in plane deformation of a

polyaromatic hydrocarbon at 1160 cm^{-1} and the feature at 1451 cm^{-1} can be assigned to semi-circle ring deformation modes that may be linked to a δ(C-H) mode associated with carbons on the perimeter of an extended polyaromatic network.[94,118] Finally, the feature present at 953 cm^{-1} can be assigned to an alkenic δ(C-H) mode.[94,95,105,115] It should be noted that these features are significantly weaker than that observed for the reference material exposed to a similar time on stream, again indicative of the reduced hydrogen retention that results from S/Na addition.[94]

The sample containing the highest sulfur loading (**Fe-Na-S_{250}**), exhibits a slightly different deformation spectra with peaks displayed at 591 and 941 cm^{-1}. These features have previously been observed for the **Fe-ref** sample after exposure to CO hydrogenation conditions for 3 h on stream (**Chapter 3, Section 3.3.1., Figure 25**). Each of these features are associated with magnetite; 591 cm^{-1} assigned to the A_{1g} Fe-O phonon mode of Fe_3O_4 and 941 cm^{-1} assigned to a possible combination of alkenic δ(C-H) and a magnetic interaction associated with Fe_3O_4.[94,105,115] The latter component is discussed further in the following section (**Section 4.4.2.1**). With reference to **Chapter 3, Section 3.3.1**, the presence of magnetite after 8 h on stream is additional evidence that S/Na is inhibiting the catalyst conditioning process.

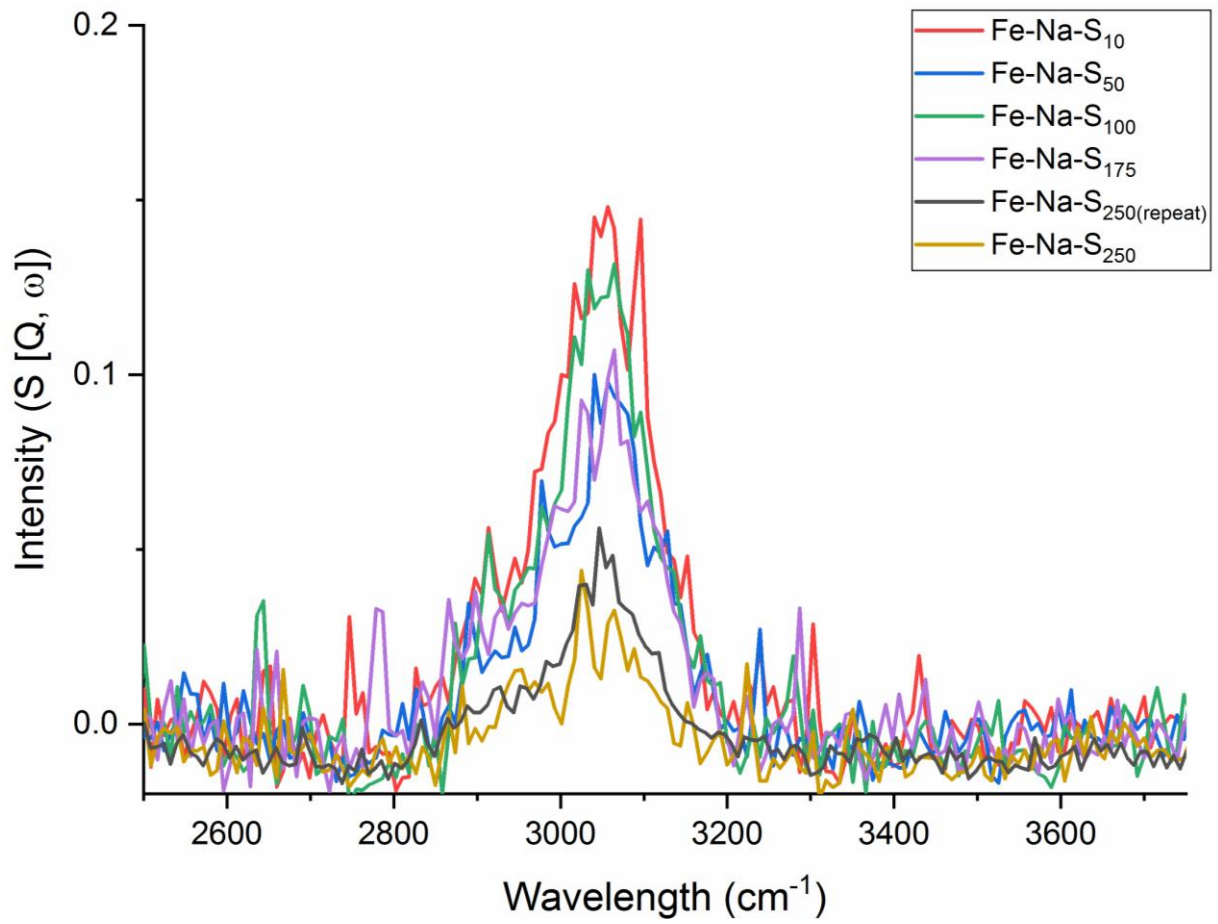

Figure 51: INS spectra (recorded at 650 meV) of α-Fe_2O_3 doubly promoted with a fixed level of sodium (2000 ppm) and varying sulfur concentrations (10 – 250 ppm) after CO hydrogenation at 623 K for 8 h in the large-scale reactor.

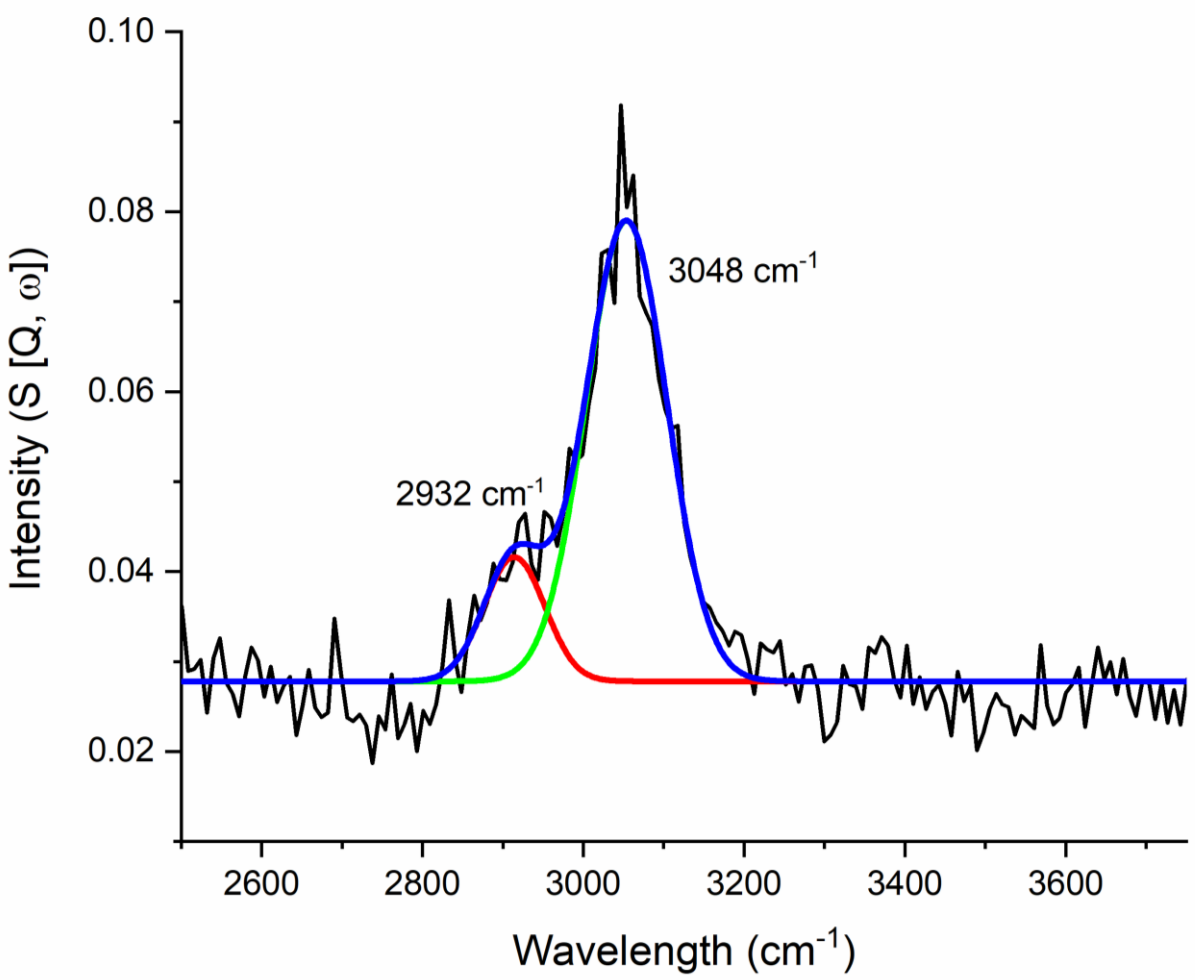

Figure 52: INS spectrum of the Fe-Na-S_{250} sample after exposure to CO hydrogenation conditions at 623 K for 8 h on the large-scale reactor with Gaussian peak fittings (OriginPro 2018) indicating the sp^3 and sp^2 hybridised carbon features.

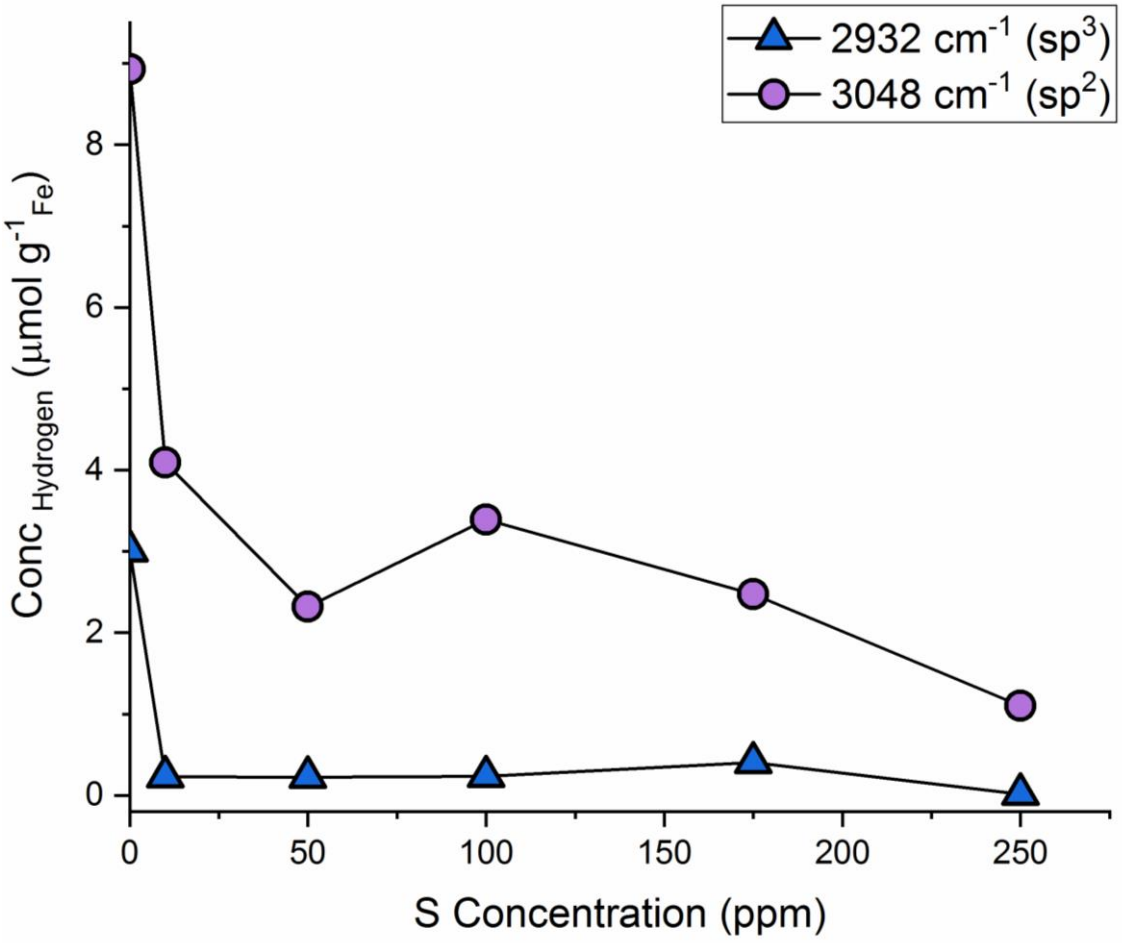

Figure 53: The quantified hydrogen content (µmol g^{-1}_{Fe}) of the features identified in Figure 51: aliphatic, sp^3 hybridised carbon feature at 2932 cm^{-1} (triangles) and aromatic, sp^2 hybridised carbon feature at 3948 cm^{-1} (circles), after exposure to CO hydrogenation conditions at 623 K for 8 h. Data obtained from Warringham[73] for Fe-ref, exposed to the same reaction conditions for 6 h, has been included for comparative purposes between promoted and unpromoted samples.

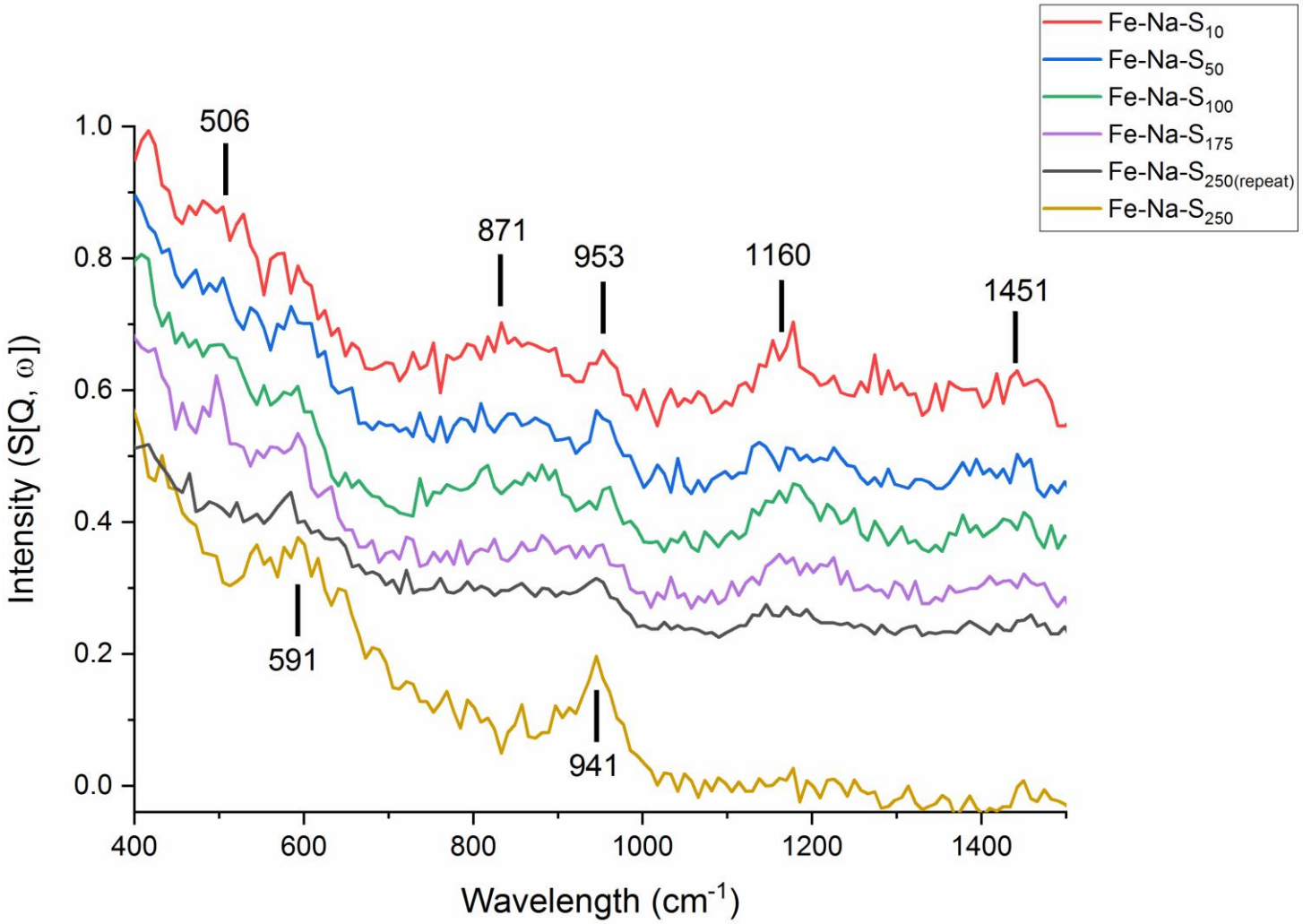

Figure 54: INS spectra (recorded at 250 meV) of α-Fe_2O_3 doubly promoted with a fixed level of sodium and varying sulfur concentrations after CO hydrogenation at 623 K for 8 h in the large-scale reactor. Spectra are offset for clarity.

4.4.2.1. Investigation of a Potential Magnetic Feature

Despite the features identified in the deformation region of **Fe-Na-S$_{250}$** being observed previously in an under reduced reference hematite sample[94], the intensity of the feature at 941 cm^{-1} drew some attention and it was initially postulated that this sharp feature may be a shifted spinon as a result of the high sulfur content within the catalyst. Upon reaction testing of this particular sample on the large-scale reactor, several issues occurred which questioned the integrity and reliability of this measurement. As a result it was decided the best route forward would be to repeat the measurement of this sample. Therefore, a new batch of **Fe-Na-S$_{250}$** was prepared. First, the sample was measured on the MAPS spectrometer, after a dehydration procedure, to ensure that the addition of promoters was not having any effect of the position of the spinon feature, known to form in a hematite sample at approximately 800 cm^{-1}. This was followed by exposing the sample to CO hydrogenation conditions on the large-scale reactor for 8 h. **Figure 55** presents the INS spectra of the ν(C-H) stretching region (2400 – 3750 cm^{-1}) of the sample after exposure to reaction conditions for the original and repeat measurements, alongside the dehydrated sample. As expected **Figure 55** shows the dehydrated **Fe-Na-S$_{250}$** sample to be featureless except for the small presence of terminal hydroxyls associated with hematite at 3633 cm^{-1}. Both the original and repeat measurements of the sample after exposure to reaction conditions show the emergence of the sp^3 and sp^2 hybridised carbon features. Upon quantifying these species it is clear that the hydrocarbonaceous overlayer is further developed on repeat of the measurement (original: 0.5939 vs repeat: 1.1159 μmol H g$^{-1}_{Fe}$) indicating that the initial catalyst tested had not been exposed to the reaction conditions for the full 8 h test period due to initial set-up complications of the apparatus at the Central Facility that was thought to have occurred. On this basis, and with reference to **Table 12**, **Fe-Na-S$_{250}$** is rejected as being unrepresentative. Instead, **Fe-Na-S$_{250(repeat)}$** is deemed to be representative and, consequently, is included in the H concentration vs. T-o-S plot presented previously in **Figure 53**.

Upon analysis of the deformation region (**Figure 56**), the dehydrated sample clearly indicates the presence of a feature at 797 cm^{-1}, which in indicative a spinon feature associated with that of hematite.[105] The loss of this feature upon catalyst exposure to reaction conditions signifies the loss of the hematite structure. Comparing the original and repeat measurements of the sample after reaction testing indicates similar features at 591 and 941 cm^{-1}. However, these features, particularly at 941 cm^{-1}, are significantly less intense upon the repeat measurement. There is also the emergence of a feature at 1160 cm^{-1}

with the repeated sample (**Figure 56(d)**), assigned to a CC-H in plane deformation mode of a polyaromatic hydrocarbon.[94,118] This indicates the formation of aromatic components of the overlayer, which would suggest the catalyst is further along the evolutionary time frame. This confirms that the original catalyst sample was not fully exposed to CO hydrogenation conditions for the full 8 h test period as expected. However, the repeat measurement of **Fe-Na-S$_{250}$** sample still displays features associated with magnetite, confirming that the increased sulfur concentration is in fact impeding the reductive potential of the catalyst.

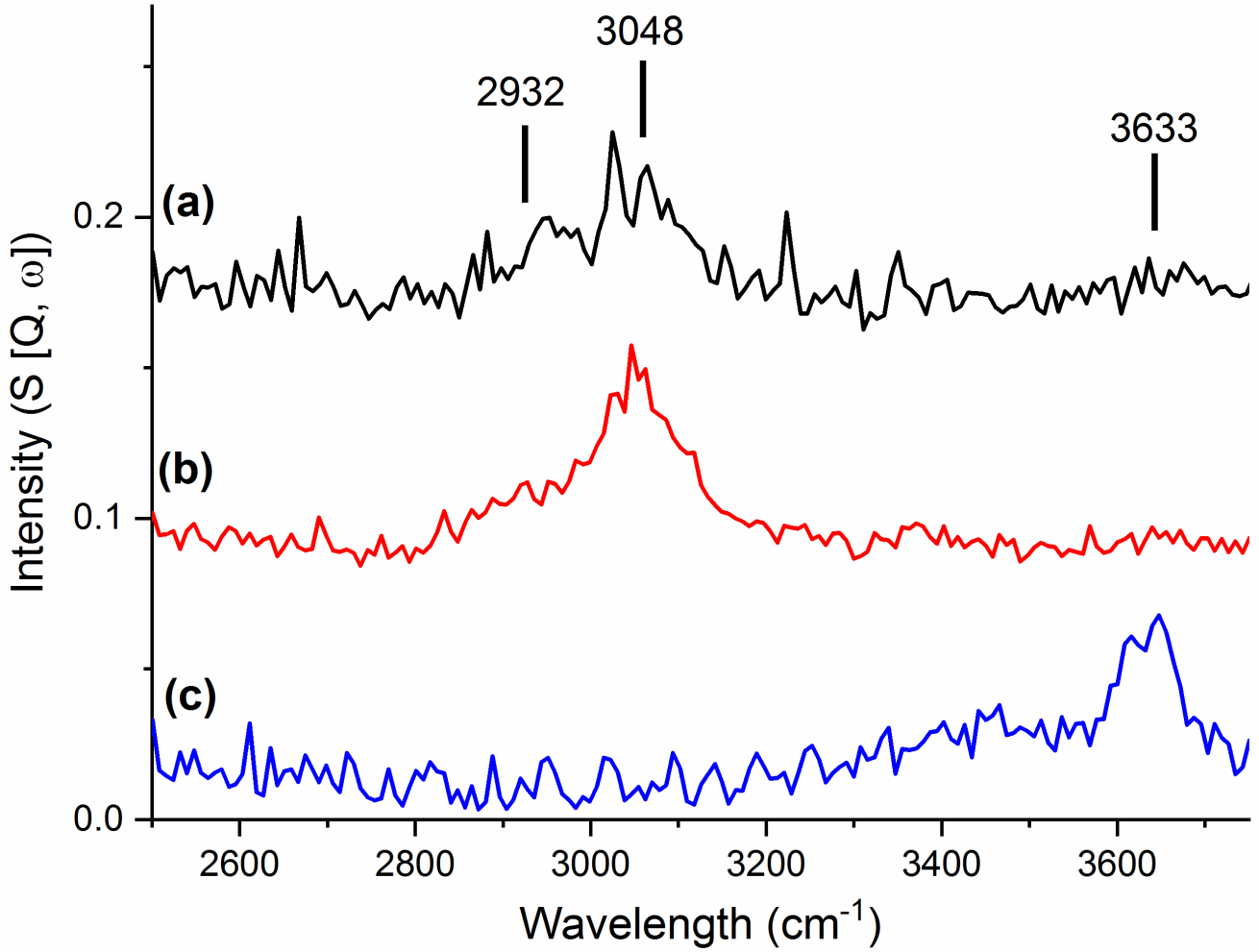

Figure 55: INS spectra (recorded at 650 meV) for (a) the original and (b) repeat measurements of α-Fe_2O_3 doubly promoted with a fixed level of sodium and 250 ppm of sulfur (Fe-Na-S_{250}) after CO hydrogenation at 623 K for 8 h in the large scale reactor. The repeat sample was also exposed to a dehydration step only (c). Spectra have been offset for clarity.

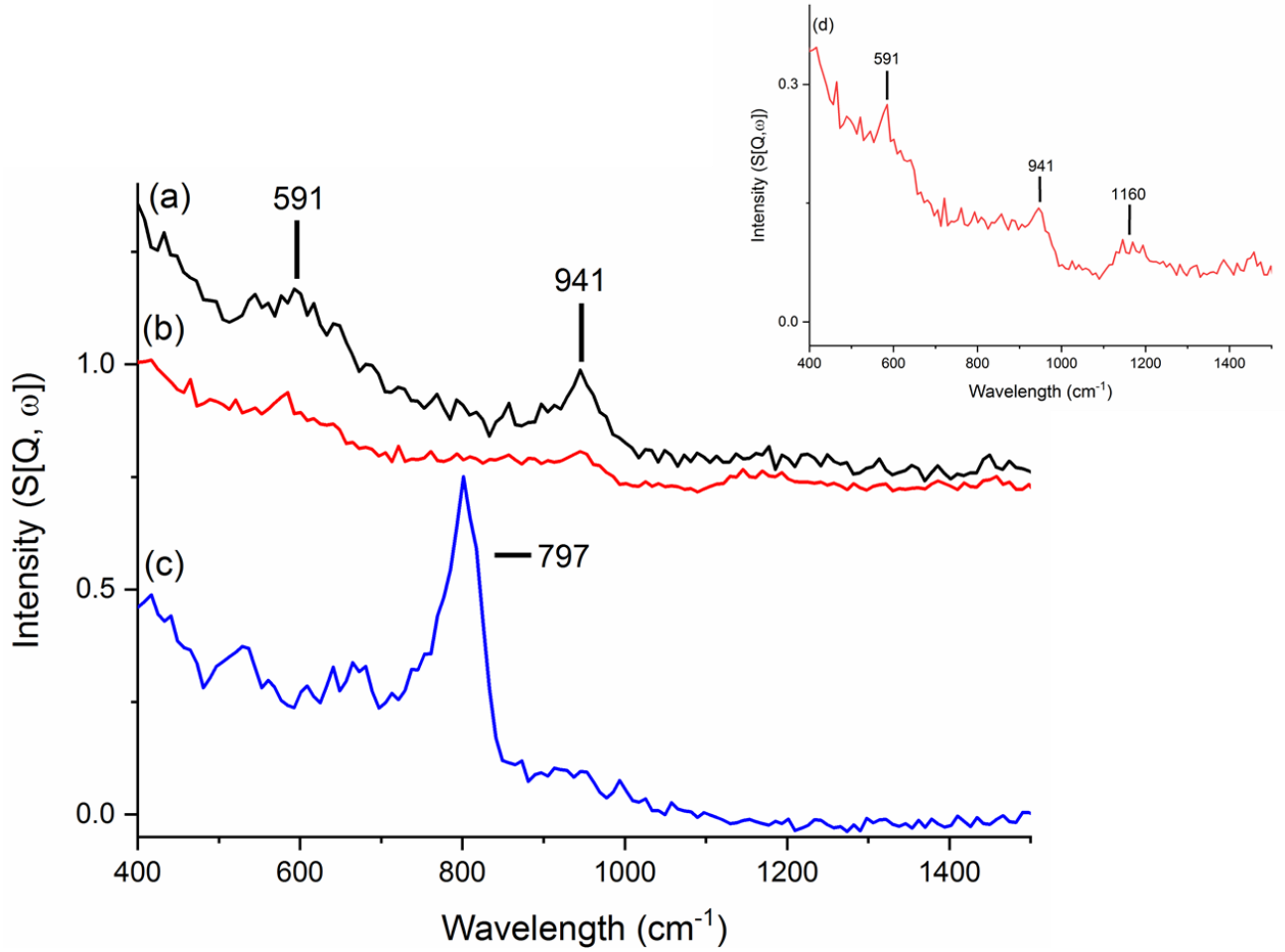

Figure 56: INS spectra (recorded at 250 meV) for (a) the original and (b) repeat measurements of α-Fe_2O_3 doubly promoted with a fixed level of sodium and 250 ppm of sulfur (Fe-Na-S_{250}) after CO hydrogenation at 623 K for 8 h in the large scale reactor. The repeat sample was also exposed to a dehydration step only (c). Spectra have been offset for clarity. (d) displays spectra (b) on a smaller y axis range to define peaks present.

After repeating the measurement of **Fe-Na-S$_{250}$** it was conclusive that the 941 cm^{-1} feature was an aspect of magnetite resulting from under reduction caused by the increased levels of sulfur within the sample. However, curiosity surrounding whether or not this was a magnetic component remained. Previous studies by Parker *et al*. demonstrated a novel method of utilising momentum transfer information, provided from an INS chopper spectrometer (MARI), to be applicable to any molecular system, and highlighted the potential future use of chopper spectrometers within chemistry.[135] This protocol described a method for distinguishing fundamentals from higher order transitions, such as overtones and combinations. Spectra cuts at constant energy transfer allowed for determination of a maximum in *Q*, with different modes exhibiting different maximum values. Later work by McInroy and co-workers used this methodology in validating an adsorbed methoxy feature arising from a second order transition.[136] More recently, Warringham *et al*.[105] utilised this procedure, again with the MARI spectrometer, in the determination of a magnetic component present at approximately 810 cm^{-1} in an unreacted hematite sample. This particular feature is also evident in **Figure 56** for the dried **Fe-Na-S$_{250}$** sample. The neutron scattering intensity for this particular band decreased sharply upon increasing *Q* which confirmed a nuclear spin interaction for this mode. Similarly, to that observed by Warringham, **Figure 57** displays that upon increasing *Q* of the band at 941 cm^{-1} (measured on MAPS), for both the initial and repeat measurements of **Fe-Na-S$_{250}$**, the scattering intensity decreases sharply, establishing this feature as a magnetic interaction associated with magnetite. For an internal consistency check, the neutron scattering intensity of a ν(C-H) band at 3000 cm^{-1}, indicative of the hydrocarbonaceous overlayer, has been included for comparative purposes, highlighting the weak, broad range of momentum transfer with a maximum *Q* value at approximately 10 A^{-1} consistent with a primary vibrational mode of non-magnetic origin.

Overall, the INS data highlights that the increasing sulfur content of the catalyst hinders the formation of the hydrocarbonaceous overlayer by potentially impeding the supply of hydrogen necessary for the reduction of the hematite catalyst towards its active phase and resulting formation of the hydrocarbonaceous overlayer.

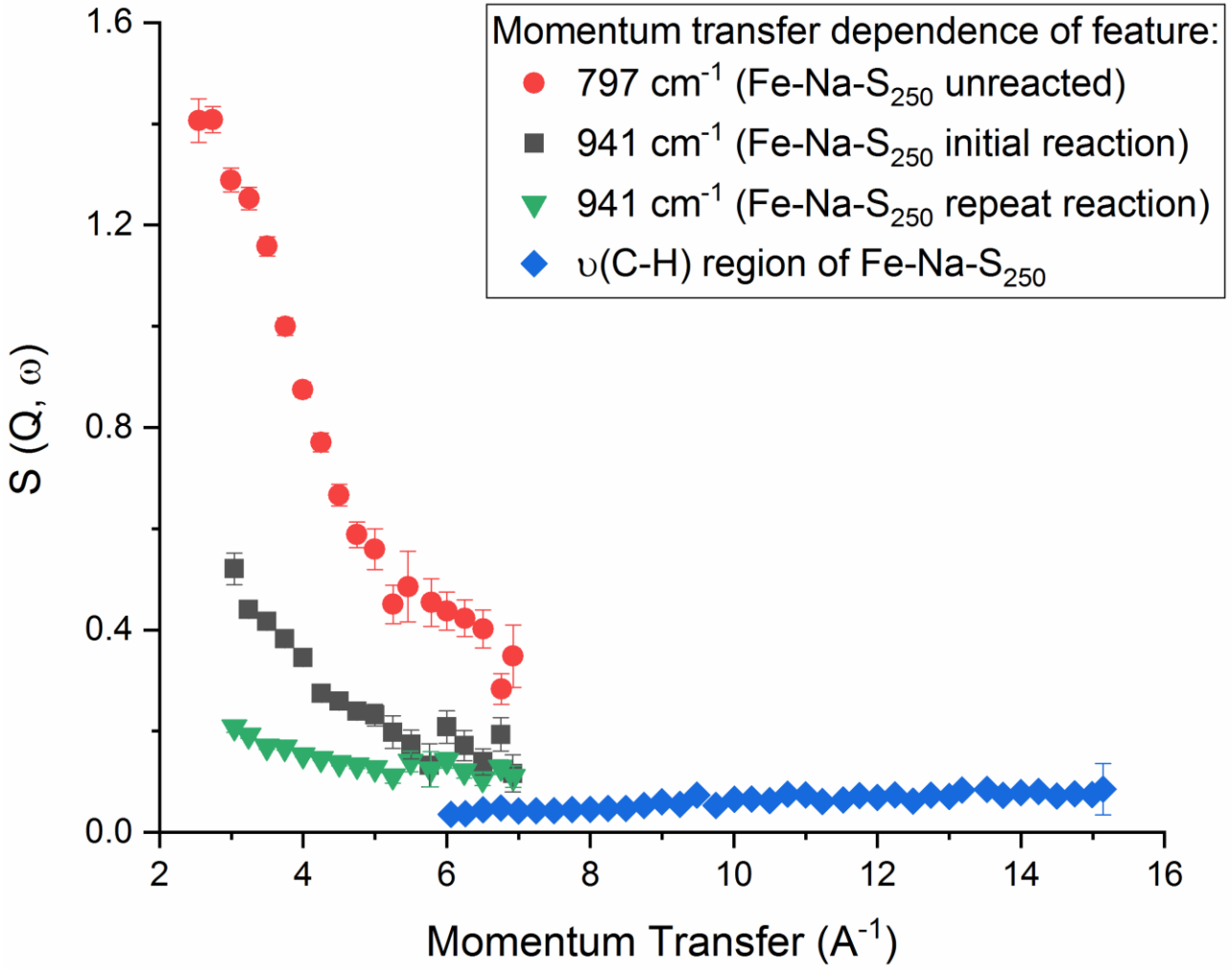

Figure 57: The momentum transfer dependence (MAPS) of the features present at; 797 cm^{-1} of Fe-Na-S_{250} unreacted (red circles), 941 cm^{-1} of the Fe-Na-S_{250} sample, shown in Figure 56, of the initial (black squares) and repeat (green triangles) measurements. The ν(C-H) stretching region of Fe-Na-S_{250} (blue diamond) is shown for comparison purposes.

4.5. Discussion and Conclusions

The introduction to this chapter, **Section 4.1**, discussed the potential roles for sulfur and sodium may play within FTO chemistry. The literature has suggested that the inclusion of sulfur may potentially weaken the Fe-C bond at the iron carbide surface, enhancing shorter chain hydrocarbons and/or act as a poison for the active sites responsible for hydrogenating surface olefins.[50,129] On the other hand, the literature is in good agreement that the addition of sodium enhances olefinicity, with Ribeiro suggesting this is because the addition of alkali metals strengthens the M - C bond while simultaneously weakening C – O, leading to an increase in surface carbon. This in turn lowers the H:C ratio within the catalytic system, enhancing olefinic production.[61] However, Yuan and co-workers emphasised the need for the inclusion of both promoters being vital for the enhancement of lower olefin production as well as simultaneously reducing selectivity towards undesirable by-products such as methane.[45]

On preparation of the catalysts, sulfur is added as a sulfate with the final state of sulfur present as sodium sulfate (Na_2SO_4). Before exposure to reaction conditions, it is proposed that the promoters do not have any crystallographic effect on the catalyst matrix and are evenly distributed on the surface and within the bulk of the catalyst as suggested by XRD (**Figure 39**), XPS (**Figure 42**) and XANES (**Figure 48**). As the catalyst is exposed to reaction conditions, not only is there evolution of the bulk hematite component towards Hägg carbide (**Figure 46**), the promoter species is also shown to go through a reduction process. From the XANES data (**Figure 49, Section 4.3.2**) of the catalyst samples after exposure to CO hydrogenation conditions, a range of various sulfur species are detected including Na_2SO_4, Na_2SO_3 and Na_2S. Over the course of the reaction it is proposed that sulfur is reduced from its initial form of sulfate towards sulfide *i.e.* Na_2SO_4 towards Na_2S in a step-wise manner. Xu *et al.*[65] by application of XPS, have previously reported S^{2-} to be present at the surface of an FTO catalyst after exposure to reduction conditions. Here, it is tentatively proposed that the S^{2-} species is 'capping' the surface of the active site, the Hägg carbide, hindering the 'templating' process of the hydrocarbonaceous overlayer. Throughout this chapter it is demonstrated that upon increasing sulfur concentrations, there is a hindrance in the reduction potential of the catalyst, as shown by TPR (**Section 4.2, Figure 40**), and also a reduced formation of the hydrocarbonaceous overlayer, highlighted by the INS data set (**Section 4.4.2, Figure 53**). This would suggest that the sulfur is constraining the hydrogen supply within the system, and, in turn, hindering the reduction process of the catalyst, and impeding the formation of the hydrocarbonaceous overlayer.

Analysis of the *in situ* TPO data set (**Figure 45**) indicates that upon increasing sulfur concentration there is an increased production of amorphous carbon (β) and under formation of iron carbides (γ). From Niemantsverdriet's competition model, carbon under hydrogen lean conditions will favour production of amorphous carbon over bulk carbides. Thus, further suggesting that the increasing levels of sulfur is constraining the hydrogen supply within the system leading to the increased production of amorphous carbon and restricted iron carbide formation. It is possible that the favourable role of the sodium is to stabilise the sulfur at the catalyst surface, otherwise sulfur may be hydrogenated to form H_2S and desorb from the surface, thus losing the associated benefits.

The following chapter investigates the time dependence (0 – 24 h) of one of the doubly promoted catalysts (**Fe-Na-S_{100}**). By utilising the information obtained within this chapter and that of **Chapter 5**, the model previously discussed in **Chapter 3, Section 3.5** will be adapted to account for the role of promoters, Na and S, within FTO chemistry (**Chapter 5, Section 5.4, Figure 69**).

This chapter has presented a wide range of data, firstly utilising a CO hydrogenation as a representative FTS reaction on both a micro-reactor and large-scale reactor set-up. Various analytical techniques have been employed including TPR, XRD, SEM-EDX, XPS, TPO, XANES and INS. A summary of this chapter is presented below.

- Initial characterisation of each of the doubly promoted catalysts displayed no significant variations in surface (XPS) or bulk structure (XRD and XANES), suggesting that upon preparation of the materials, the promoters are evenly distributed on the surface and throughout the bulk.
- TPR measurements highlighted that the increasing sulfur concentration creates a shift in the reduction temperature of the hematite catalyst to higher temperatures.
- Investigation of varying sample masses for TPO measurements highlighted the sensitivity of the current micro-reactor set-up. The decision to continue to run measurements with 40 mg despite saturation occurring was in order to retain the presence of the α feature, which is proposed to play a key role in the understanding of the Fe/CO/H_2 surface chemistry involved in this process.
- XANES data identified the change in sulfur oxidation state from S^{6+} towards to a mixture of S^{6+}, S^{4+} and S^{2-} after exposure to CO hydrogenation conditions.

- From INS measurements, the presence of higher sulfur loadings inhibits the intensity of sp^2 and sp^3 hybridised carbon species, indicative of a hydrocarbonaceous overlayer.
- The reduced hydrocarbonaceous overlayer links with the increased sulfur concentration inhibiting the reduction of the hematite catalyst suggesting sulfur is negatively affecting the hydrogen supply within the system.
- It is proposed that the Na_2S species formed during reaction blocks the surface of the active phase impeding the formation of the hydrocarbonaceous overlayer.

Chapter 5 – CO hydrogenation at 623 K: investigation of the temporal behaviour of the hydrocarbonaceous overlayer of a prototype FTO catalyst

5.1. Introduction

Chapter 4 established how changing the concentration of sulfur within a doubly promoted iron catalyst would affect the formation of the hydrocarbonaceous overlayer utilising an ambient pressure CO hydrogenation reaction for a set period of time-on-stream. For this investigation, one doubly promoted iron catalyst (**Fe-Na-S$_{100}$**) was selected to be examined over a 24 h period using the micro-reactor and large-scale reactor set-ups. The composition was selected in consultation with the industrial partners as being representative of a prototype FTO catalyst. The chapter can be divided into two sections:

- **Section 5.2**: utilising an ambient pressure CO hydrogenation reaction as used previously in **Chapter 3** and **4** *i.e.* conventional syngas reactant (CO + H_2).

- **Section 5.3**: altering the reactant feed composition of the ambient pressure CO hydrogenation reaction to include a CO_2 co-feed *i.e.* CO_2 addition to syngas reactant (CO + H_2 + CO_2).

As CO_2 is one of the major by-products of an FTS reaction, the purpose of introducing this co-feed was to shift the WGS equilibrium (*Equation 5.1*) towards the left-hand side, maximising the utilisation of carbon towards the desired hydrocarbon products rather than to a CO_2 by-product. A study by Soled *et al*. reported that the inclusion of a CO_2 co-feed to syngas, using a Fe-Zn catalyst, resulted in a diminished formation of CO_2 however, this investigation did not report any mechanistic insight into the process.[137] On the other hand, Liu and co-workers noted that the inclusion of CO_2 altered the product output distribution by decreasing the surface coverage of hydrogen and increased water production. This in turn led to an increased production of olefins and oxygenates.[138] In terms of FTO

chemistry, literature on the addition of a CO_2 co-feed is sparse. However, a recent study by Liang and co-workers (2019), from the Dalian institute in China, known for their contribution to the FTO literature, investigated the addition of Na to an iron-based catalyst for CO_2 hydrogenation. It was observed that upon increasing the concentration of sodium this correlated with an increase in CO_2 conversion and an increase in alkene selectivity.[139] To date, there appears to be no literature for a sulfur promoted FTO catalysts with a CO_2 co-feed.

$$CO_{(g)} + H_2O_{(g)} \rightleftharpoons CO_2 + H_2 \quad (\mathbf{5.1})$$

For **Section 5.3**. of this chapter, adjustments were made to the previously established CO hydrogenation conditions with respect to conditions utilised by Botes and co-workers[97] and as advised by Drochaid Research Services.[140] Details of these adjustments are given in **Chapter 2, Section 2.2.2**. The addition of a CO_2 co-feed was a preliminary measurement towards the end of the research project and therefore only includes scaled-up reaction testing alongside an INS dataset. However, it does allow for direct comparison on how the addition of a CO_2 feedstream affects the formation and composition of the hydrocarbonaceous overlayer over an initial 24 h period of reaction.

5.2. CO hydrogenation at 623 K of a doubly promoted iron catalyst as a function of time on stream

The catalyst sample tested within this section was intended to be promoted with a similar level to the middle range sample (**Fe-Na-S$_{100}$**) from **Chapter 4**. The micro-reactor measurements utilise the same batch of catalyst used for **Chapter 4**, whereas a different batch of catalyst was prepared for the INS measurement and is expected to contain the same sulfur and sodium concentrations as the batch used for micro-reactor measurements.

It should be noted that the MAPS spectrometer was upgraded between the work carried out previously (**Chapter 3** and **4**) and this chapter; therefore calibration measurements were repeated (**Appendices, Figure 70**) and used for quantification of hydrogen in the INS data obtained within this chapter.

5.2.1. Micro-reactor Measurements

5.2.1.1. Reaction Testing

Fe-Na-S$_{100}$ was previously characterised in **Chapter 4, Section 4.2**, and it was established that the addition of sulfur and sodium as promoters did not have an effect on the overall bulk hematite structure but did in fact hinder the reduction potential of the catalyst as shown from the TPR data set (**Chapter, 4, Section 4.2, Figure 40**). The previous study also examined the reaction chemistry during an ambient pressure CO hydrogenation reaction at 623 K for 6 h. This investigation repeated this reaction varying the reaction time intervals over a 24 h period (0, 3, 6, 12 and 24 h). As observed previously with other micro-reactor CO hydrogenation profiles, three stages can be identified in the reaction profile of **Fe-Na-S$_{100}$** (**Figure 58**). Over the 24 period studied the catalyst retains a low activity throughout and does not show signs of deactivation.

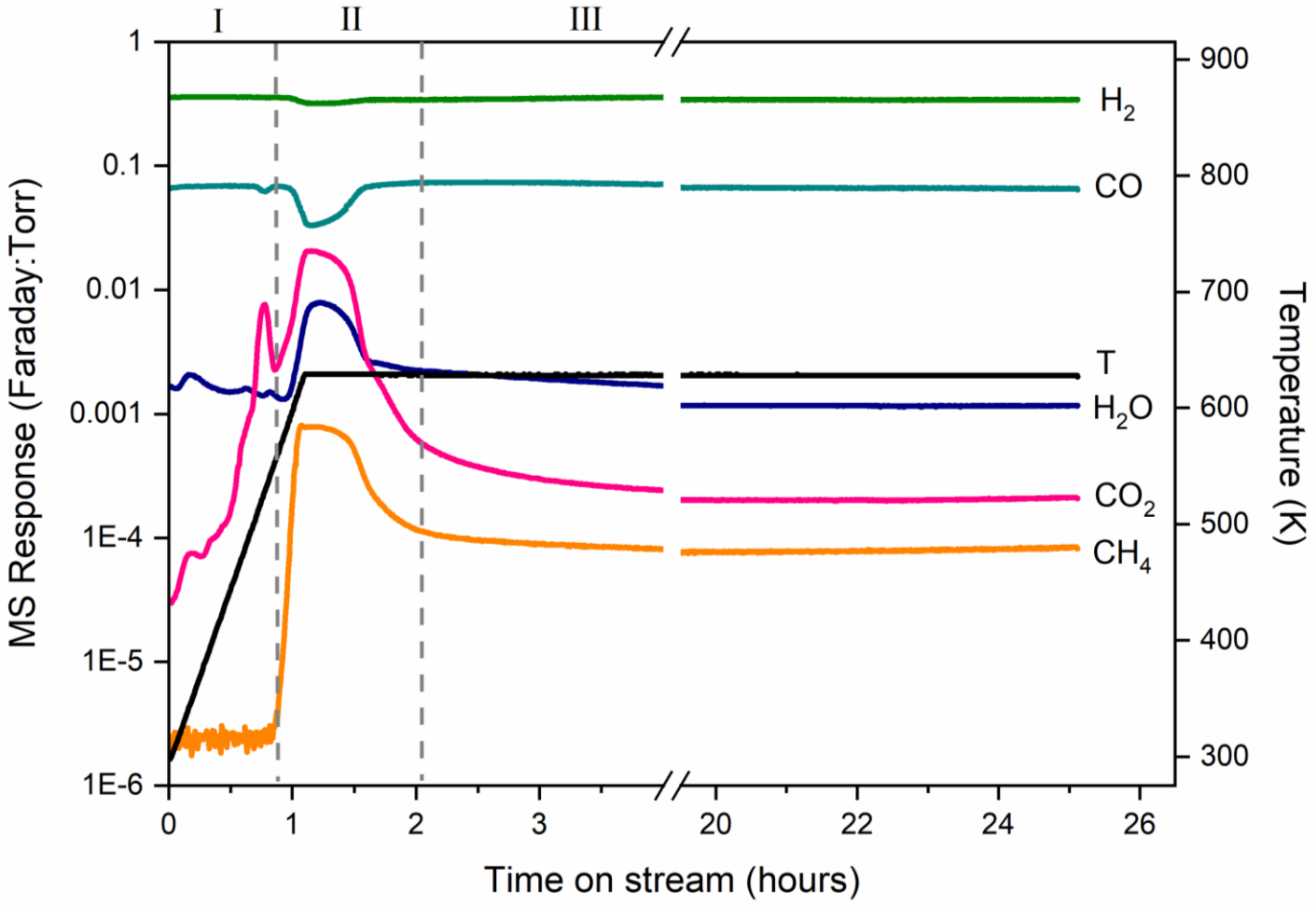

Figure 58: Mass spectrometer reaction profile in the micro-reactor of a CO hydrogenation reaction over a doubly promoted hematite catalyst (Fe-Na-S_{100}) at 623 K, ambient pressure, for 24 h.

5.2.1.2. Temperature-programmed Oxidation Measurements

The *in situ* TPO profiles obtained after exposure to CO hydrogenation conditions for the varying lengths of time on stream (0, 3, 6, 12 and 24 h) are presented in **Figure 59** and identify the previously observed α, β and γ features assigned to a precursor species, amorphous carbon and bulk iron carbides respectively. As with the *in situ* TPO measurements in **Chapter 4, Section 4.3.1.** saturation of the oxygen component occurs when utilising a mass of 40 mg, with a lower mass resulting in a loss of the α component. Again, as this feature may be significant in the comprehensive understanding of the evolution of the catalyst and the hydrocarbonaceous overlayer, a mass of 40 mg has been utilised for these measurements to ensure key components are observed, with acknowledgment that these measurements are therefore qualitative rather than quantitative.

Over the 24 h period under examination, the α species, assigned in **Chapter 3** as a precursor to the formation of the aliphatic component of the hydrocarbonaceous overlayer, as well as a potential precursor to the β and γ TPO feature, displays continual growth over this period of study as does the β component. On the other hand, the γ feature displays limited growth over the 24 h period. Previous work by Warringham examined the unpromoted **Fe-ref** catalyst using the same set-up also over a 24 h period, and thus the two datasets are directly comparable.[94] For the **Fe-ref** sample, the α species is short lived as it's only observable up to 6 h on stream, whereas the doubly promoted sample displays retention of this species for the full 24 h analysis period. From **Chapter 3**, one of the suggested assignments was a potential precursor to the aliphatic component of the hydrocarbonaceous overlayer observed from INS measurements. Therefore, a diminished presence of the aliphatic component would be expected in the INS data set. However, this is not observed and is discussed further in **Section 5.2.3**. Over the 24 h period studied the β feature shows continuous growth whereas the presence or growth of the γ component is minimal. As highlighted in **Chapter 4, Section 4.5**, it was suggested that the inclusion of sodium strengthens the carbon to metal bond and through increased back donation, weakening the C-O bond of the carbon monoxide and thus resulting in an increase in surface carbon.[61] Following this, Niemantsverdriet's competition model[25,127] will play a role as under hydrogen lean conditions, enhanced by the addition of promoters, competition between the formation of amorphous carbon and bulk iron carbides will occur; with the formation of amorphous carbon dominating in a hydrogen lean environment. Therefore accounting for an increase in amorphous carbon production (β) and a reduced formation of iron carbide (γ) in **Fe-Na-S$_{100}$** over the initial 24 h period studied.

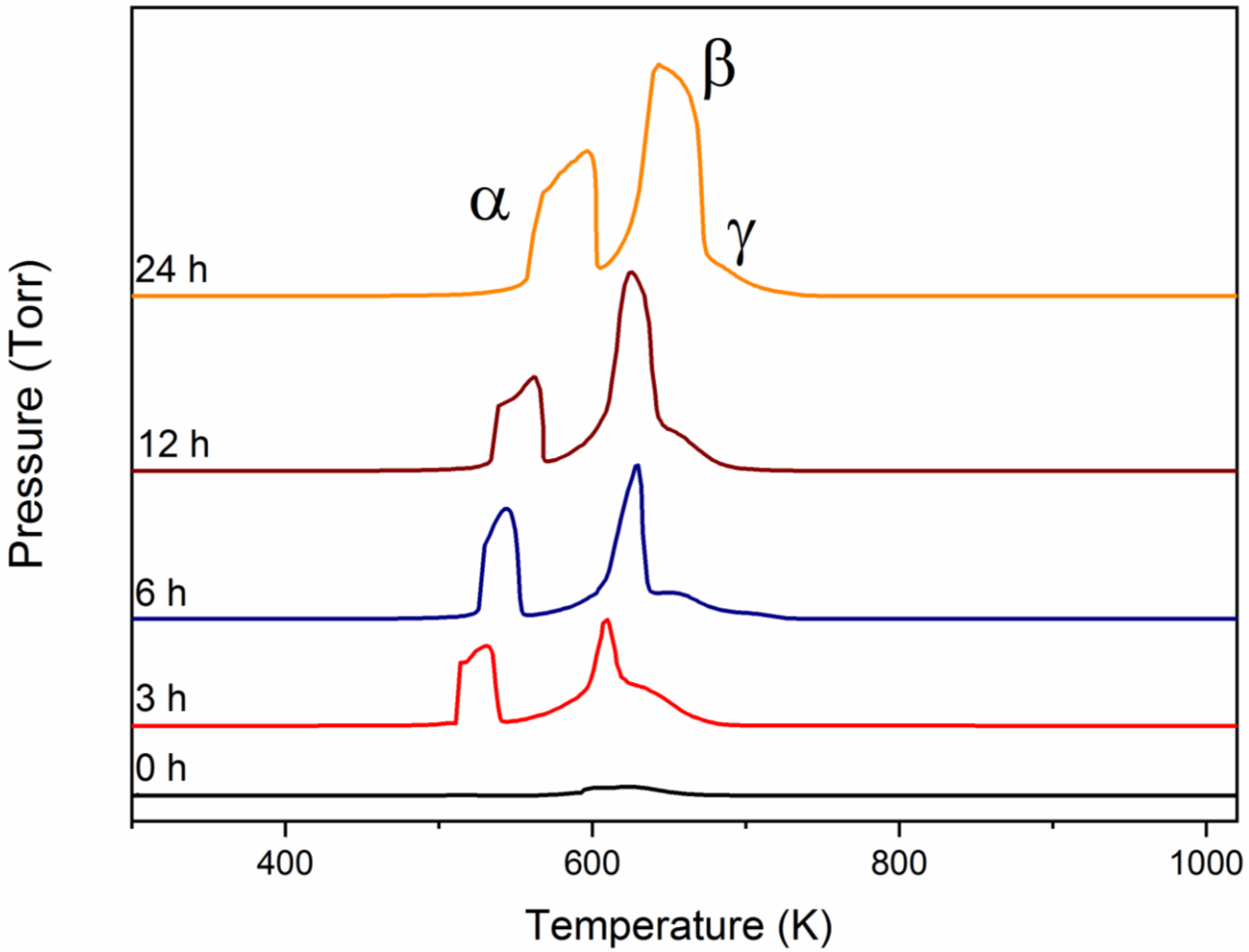

Figure 59: The *in situ* temperature-programmed oxidation profiles (40 mg) of a hematite catalyst doubly promoted with sulfur and sodium (Fe-Na-S_{100}) after exposure to ambient pressure CO hydrogenation conditions at 623 K for 0-24 h.

5.2.2. Large-scale Measurements

5.2.2.1 Reaction Testing

Unfortunately, as the large-scale reactor system at the ISIS Facility is a shared piece of equipment available to a wide range of users, which are restricted to discrete beam time allocations, the mass spectrometer was not operational for the reaction testing measurements in this section (**Section 5.2.2.1**). Due to the limited time available for INS measurements, it was decided that reaction testing should go ahead without access to the mass spectrometer for monitoring the progress of the reaction. Based on previous use of the apparatus, the CO hydrogenation conditions that have previously been employed (**Chapter 3 & 4**) were replicated on the MFC's and the temperature ramp set at 5 K min^{-1} for the furnace. Gas supplies were closely monitored throughout the course of each reaction to ensure a plentiful supply. Throughout the duration of each reaction there were no interruptions of the gas flow to the catalyst within the reactor. The expected reaction profile for this catalyst would be similar to that obtained in **Section 4.4.1.**, **Figure 50**.

5.2.2.2. Inelastic Neutron Scattering

Following reaction testing, the reaction was quenched as described in **Section 2.2.2**, transferred to an aluminium cell in an inert environment and run on the MAPS spectrometer, recording at two incident energies; 650 and 250 meV.

Figure 61 displays the ν(C-H) stretching region (2200-4000 cm^{-1}), recorded at 650 meV, of the INS spectra, identifying the sp^3 (2932 cm^{-1}) and sp^2 hybridised (3048 cm^{-1}) carbon ν(C-H) features observed previously.[94,95,105] As time on stream is increased to 24 h, there is an increase in the intensity of the bands indicating an increased production of the hydrocarbonaceous overlayer. Utilising the new calibration measurements (**Appendices, Figure 70**), each of the identified species observed in **Figure 61**, were quantified and the resulting data presented in **Figure 62**. The aliphatic component (2932 cm^{-1}), shows growth up to 12 h on stream before appearing to reach a steady state. However, the aromatic feature observed at 3048 cm^{-1}, only appears to show growth in the initial stages of reaction (approximately 6 h on stream) before saturation is observed. In comparison to the **Fe-ref** sample (**Figure 63**), containing no structural promoters, the aliphatic component is within

a similar range by 24 h on stream (unpromoted: 3.81 vs. promoted: 3.68 μmol H g^{-1}_{Fe}) whereas the aromatic component by 24 h has significantly diminished with a value of 9.58 vs. 15.74 μmol H g^{-1}_{Fe} for the **Fe-ref** sample.

It was previously proposed, in a recent publication by Warringham, that the α species may be a precursor to the formation of the hydrocarbonaceous overlayer.[95] The retention of this species in the *in situ* TPO measurements, and the overall reduction in the formation of the hydrocarbonaceous overlayer upon the addition of promoters, would agree with this statement. However, in **Chapter 3**, it was proposed more specifically that the α species could be assigned to a precursor to the aliphatic component of the hydrocarbonaceous overlayer, amongst other possibilities. If this was the case then it would be expected that the retention of the α species over the 24 h period would result in a diminished production of the aliphatic component (sp^3 hybridised carbon) observed in the INS dataset in comparison to that previously observed for **Fe-ref**. However, this is not observed. Nevertheless, the retention of the α species correlates with the overall reduced formation of the hydrocarbonaceous overlayer not ruling out its role as a potential precursor to overlayer formation. A possible interpretation of the results, as alluded to in **Chapter 3** and shown in the scheme presented in **Figure 60**, is that the α component is in fact a precursor to either the β or γ TPO features and is highly dependent on the supply of hydrogen within the system *i.e.* the Competition model.[25,127]

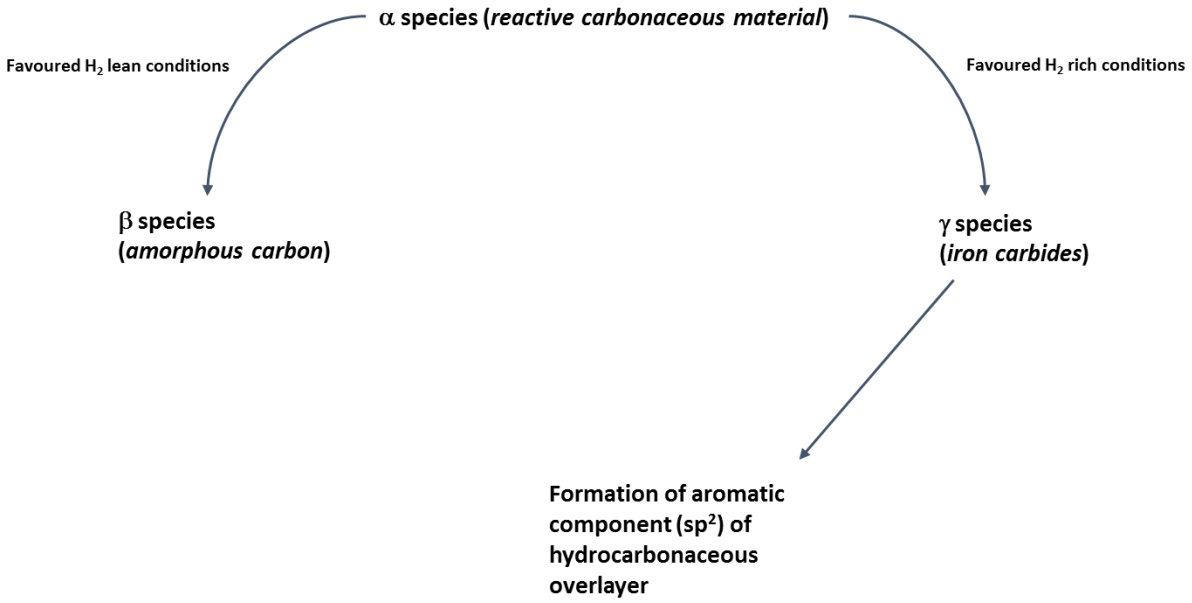

Figure 60: A schematic of the potential pathway of the α species observed in the TPO profiles.

The conclusions from **Chapter 4** indicate that the inclusion of promoters is hindering the supply of hydrogen within the system. Thus, the α precursor is more inclined to produce amorphous carbon (β) over bulk iron carbides (γ). It has been suggested in **Chapter 3** that the formation of the bulk iron carbides may be responsible for the formation of the aromatic component of the hydrocarbonaceous overlayer. Therefore, a reduction in the formation of iron carbides, as observed in the *in situ* TPO measurements, will result in a reduced aromatic component in the hydrocarbonaceous overlayer, in relation to the reference material (**Fe-ref**), which is highlighted by the quantified INS data set (**Figure 62**).

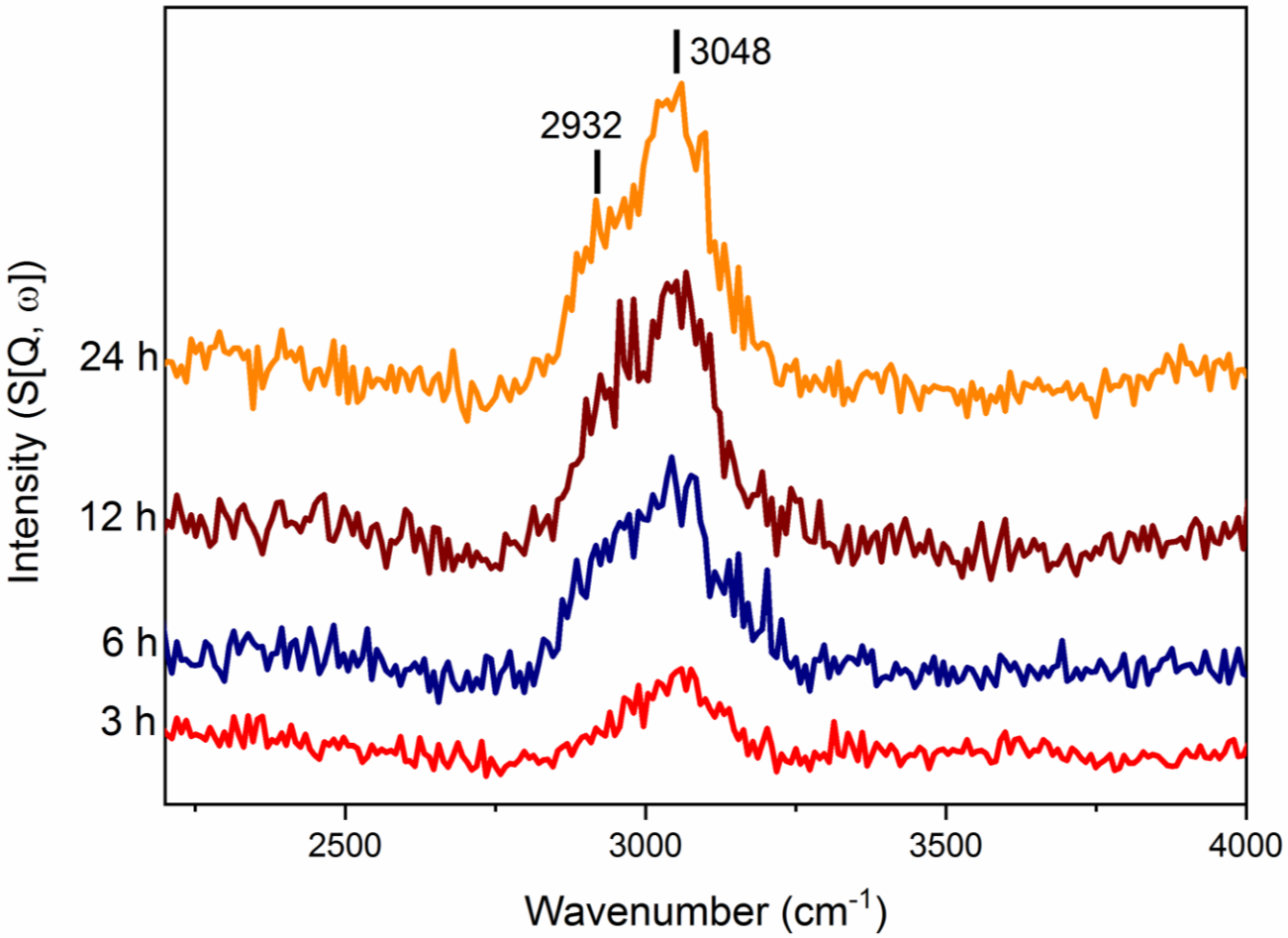

Figure 61: INS spectra (recorded at 650 meV) of a doubly promoted α-Fe_2O_3 (Fe-Na-S_{100}) after ambient pressure CO hydrogenation at 623 K in the large-scale reactor for varying time scales (0 – 24 h).

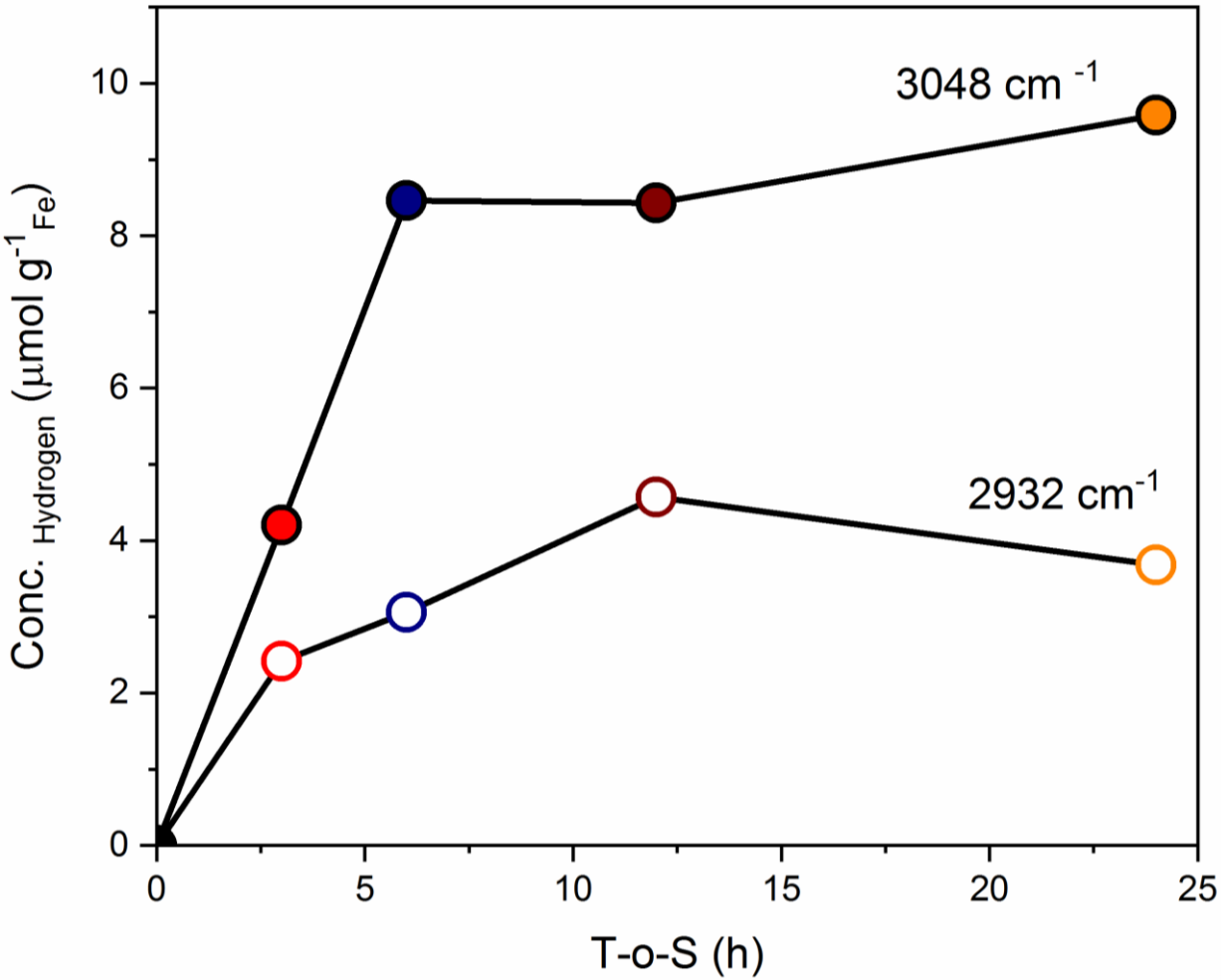

Figure 62: The quantified hydrogen content of the features identified in Figure 61: aliphatic, sp^3 hybridised carbon feature at 2932 cm^{-1} (hollow circles) and aromatic, sp^2 hybridised carbon feature at 3948 cm^{-1} (solid circles) of Fe-Na-S_{100}.

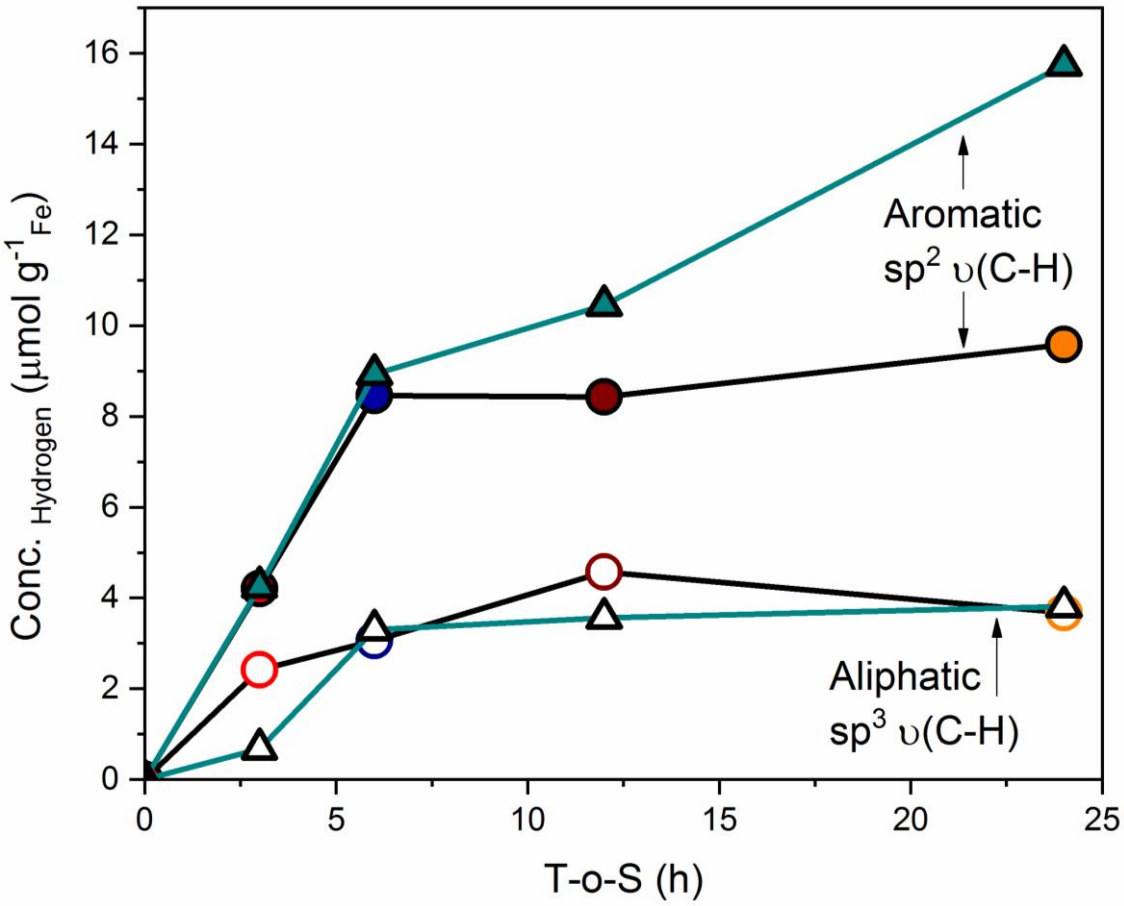

Figure 63: A comparison of the quantified hydrogen content (µmol H g^{-1}_{Fe}) of the sp^2 (solid) and sp^3 (hollow) ν(C-H) features from the INS spectra of Fe-Na-S_{100} (circles) and Fe-ref (triangles).

The deformation region of the spectra (400 - 1600 cm^{-1}) is presented in **Figure 64** and indicates the presence of predominately aromatic components with some aliphatic character. Each of the observed features for samples exposed to CO hydrogenation conditions ≥ 6h, have been previously observed for the **Fe-ref** sample and are detailed in **Chapter 3, Section 3.3.1** and are also referred to in **Chapter 4, Section 4.4.2**. The sample exposed to 3 h on stream displays two prominent bands at 591 and 941 cm^{-1}, indicative of magnetite signifying, the under reduction of the catalyst which was observed for **Fe-ref** in **Chapter 3, Section 3.3.1**. The temporal trends described here are broadly consistent with the conclusions of **Chapter 4**. Namely, that Na_2S present at the surface, after exposure to reaction conditions, impedes formation of the hydrocarbonaceous overlayer via hindering the catalyst reduction process. Over time, the hydrocarbonaceous overlayer can from, with its modified form perturbing the product distribution to favour light olefins.

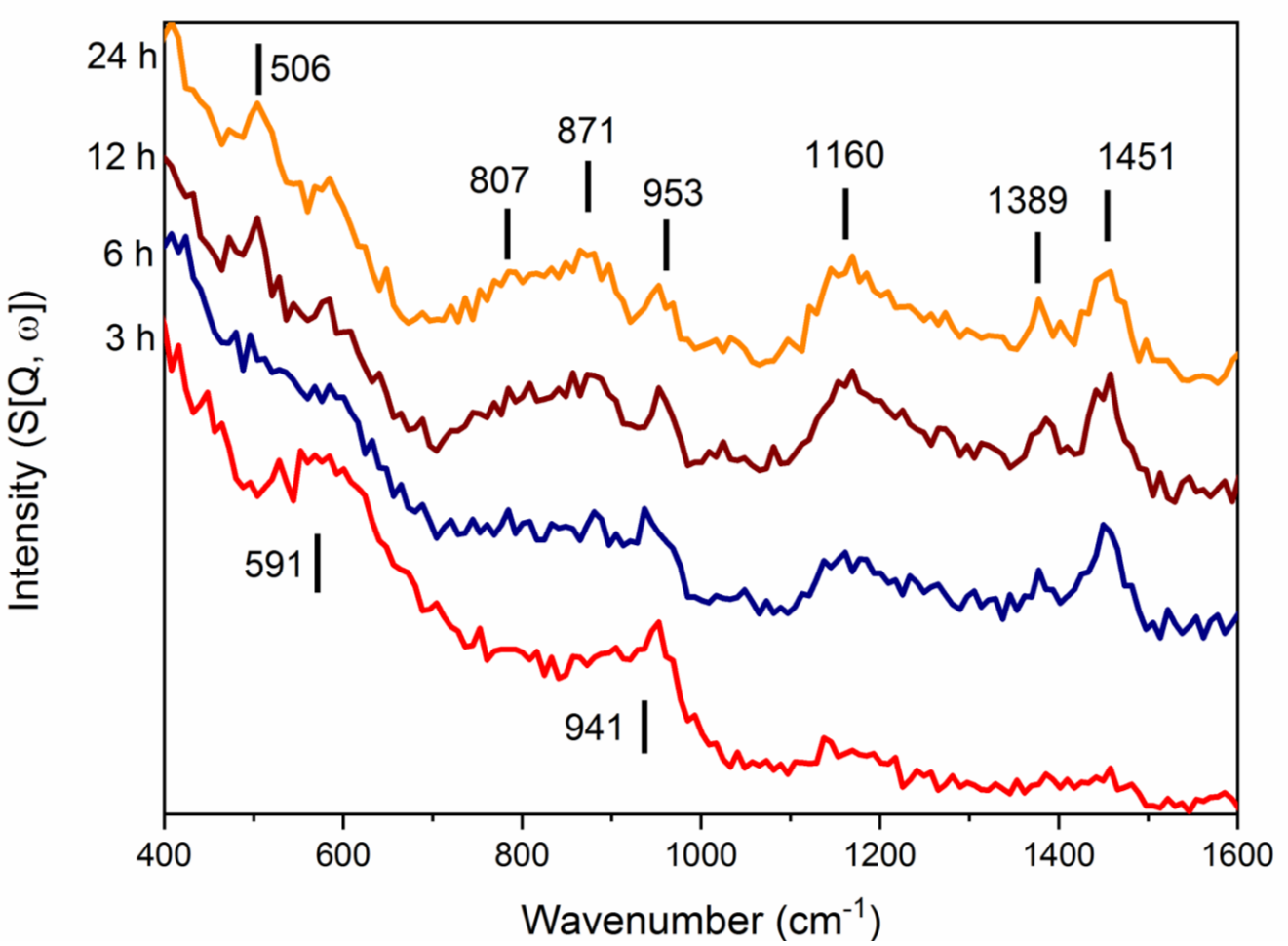

Figure 64: INS spectra (recorded at 250 meV) of a doubly promoted α-Fe_2O_3 sample (Fe-Na-S_{100}) after ambient pressure CO hydrogenation at 623 K in the large-scale reactor over a 24 h period.

5.3. CO hydrogenation at 623 K with a CO_2 co-feed of a doubly promoted iron catalyst as a function of time on stream

5.3.1. Reaction Testing

Due to time constraints towards the end of the project, this preliminary investigation only involved obtaining data for the large-scale reactor followed by INS measurements on the MAPS spectrometer. The reaction testing conditions of this particular set of measurements differed significantly from previous CO hydrogenation conditions utilised on the large-scale reactor. In relation to the conditions applied by Botes[97] and as advised by Drochaid Research Services, the CO flow rate was lowered to compensate for the introduction of a CO_2 co-feed. The reaction continued to be carried out at ambient pressure. As with the previous section (**Section 5.2**) the mass spectrometer at the ISIS Facility was unavailable for majority of our reaction testing measurements. Thankfully, the opportunity arose to analyse one of the samples (12 h T-o-S) at a later date. It should be noted however that this particular sample is a different batch of catalyst to the other samples measured within this section (3, 6 and 24 h samples of a different batch to 12 h sample), although the intended S and Na should be the same. Unfortunately, ICP has not been carried out to confirm this. The facility is not readily available at the University of Glasgow and due to difficulties at Sasol Technology it was not possible to access the previously employed ICP capability (**Chapter 4, Section 4.2**).

The reaction profile presented in **Figure 65** shows minor, but potentially significant differences, to that previously obtained for a doubly promoted sample under ambient pressure CO hydrogenation conditions (**Section 4.4.1., Figure 50**). The profile itself can still be divided into two main sections: *Stage I* highlighting the reduction of the catalyst with the production of water, carbon dioxide and methane and consumption of CO and hydrogen; *Stage II* is indicative of the reaction reaching a steady state regime. Previously, in **Chapter 3, Section 3.3**., for the unpromoted reference catalyst (**Fe-ref**), a steady state regime was operational by approximately 7 h. However, for the doubly promoted catalysts observed in **Chapter 4, Section 4.4**, a steady state regime was not operational by the end of the 8 h time frame studied suggesting the addition of promoters is hindering the reduction process of the catalyst. Interestingly, with the addition of a CO_2 co-feed, the methane feature shown in **Figure 65** is constant throughout the duration of the 12 h period studied. This was not previously observed for the unpromoted (**Section 3.3., Figure 23**) or promoted samples (**Section 4.4.1., Figure 50**) tested without the addition of CO_2. It is

proposed that the inclusion of a CO_2 co-feed will therefore proceed through a two-step reaction scheme: firstly, through the reverse water gas shift (RWGS) as shown by *Equation 5.2*, followed by a CO hydrogenation reaction (*Equation 5.3*).

$$CO_2 + H_2 \rightleftarrows CO + H_2O \quad (\mathbf{5.2})$$

$$CO + 2H_2 \rightarrow (-CH_2-) \ + H_2O \quad (\mathbf{5.3})$$

By enhancing the RWGS reaction (*Equation 5.2*), the preferred route of adsorbed oxygen on the catalyst would be through hydrogenation to form water, rather than oxidise CO to produce CO_2. In turn, the carbon within the system is available for the production of product, *i.e.* methane for an ambient pressure CO hydrogenation reaction, or hydrocarbons in the case of FTS, rather than result in the formation of an undesirable by-product. This proposed pathway would also result in a decrease of hydrogen availability as there would be an increase in hydrogen consumption from *Equation 5.2*.[141] The decreasing H_2/CO ratio could therefore assist in shifting the product slate towards olefins via a constrained hydrogen supply. However, a reduction in hydrogen availability may result in an increased production of coke formation and oxygenates. Unfortunately, as this is a preliminary study this avenue has not yet been explored.

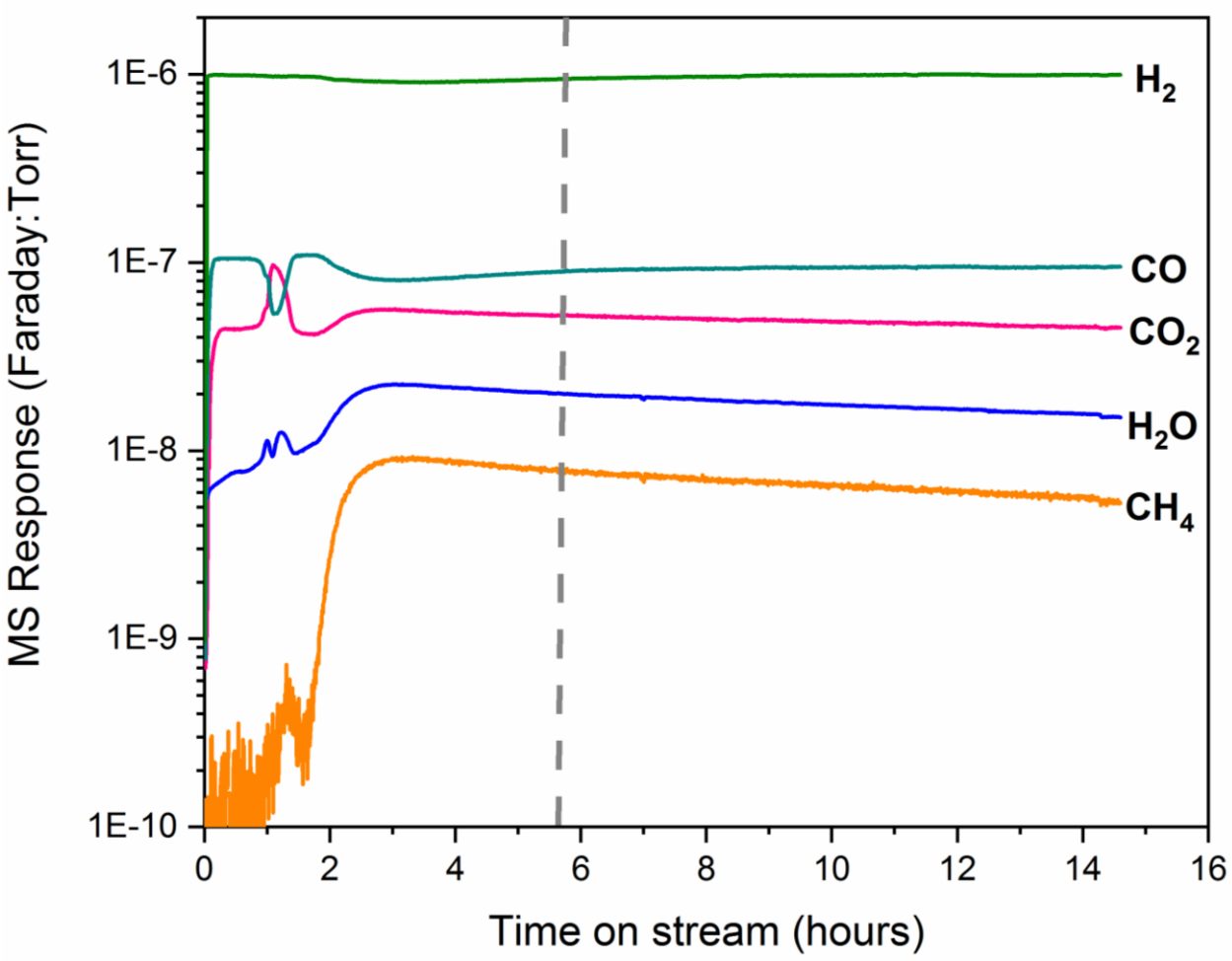

Figure 65: Mass spectrometer reaction profile for large-scale reactor of a CO hydrogenation reaction with a CO_2 co-feed over a doubly promoted hematite catalyst (Fe-Na-S_{100}) at 623 K, ambient pressure, for 12 h.

5.3.2. Inelastic Neutron Scattering

As with previous samples, following reaction testing, the reaction was quenched as described in **Chapter 2 Section 2.2.2**, and transferred to an aluminium cell in an inert environment and run on the MAPS spectrometer, recording at two incident energies; 650 and 250 meV. On transfer from the Inconel cell to the aluminium cell, the catalyst sample exposed to reaction conditions for 24 h, displayed a significant increase in catalyst mass, and is proposed that this particular increase in mass may be as a result of an increase in the production of amorphous carbon.

Inspection of the stretching region (2400 – 3750 cm^{-1}), presented in **Figure 66 (a)**, identifies the presence of hydrocarbon moieties, with a prominent sp^2 hybridised carbon ν(C-H) feature at 3048 cm^{-1} and a lower frequency sp^3 hybridised carbon ν(C-H) shoulder at 2932 cm^{-1} for all reacted samples.[94,95,105] On visual inspection, the intensity of the sample exposed to reaction condition for 24 h is significantly greater than the other samples analysed and thus a secondary plot with the omission of this sample is presented in **Figure 66 (b)** to indicate the presence of the sp^3 and sp^2 hybridised carbon features in the other samples (3, 6 and 12 h). As with previous INS data, the hydrogen concentration of the two features can be quantified with the resulting data presented in **Figure 67**. Due to the reduced intensity of the sample exposed to reaction conditions for 3 h, the peak fitted INS data for this sample is presented within the thesis appendices (**Figure 71**). **Table 13** presents a comparison of the quantified hydrogen content of the sp^3 and sp^2 hybridised carbon features of **Fe-ref** and **Fe-Na-S_{100}**, with and without a CO_2 co-feed, over a 24 h period. In the initial stages of the reaction *i.e.* 3 h on stream, the overall hydrocarbonaceous overlayer in the presence of CO_2 is significantly diminished in comparison to that observed previously for a doubly promoted catalyst sample (**Section 5.2**) or of the reference material (**Fe-ref**) examined in **Chapter 3 Section 3.3.1**. This would suggest that the inclusion of a CO_2 co-feed is reducing the supply of hydrogen within the system at this stage in the reaction. However, from 6 h onwards there is a rapid production of both the sp^2 and sp^3 hybridised carbon features and interestingly by 24 h on stream the total hydrogen concentration for ν(C-H) is approximately an order of magnitude higher than that observed for the same sample (**Fe-Na-S_{100}**) without a CO_2 co-feed from **Section 5.2.2.2.**, 138.65 vs. 13.26 μmol H g^{-1}_{Fe}.

Table 13: Comparison of hydrogen concentration (µmol H g^{-1}_{Fe}) of the aliphatic (2932 cm^{-1}) and aromatic (3048 cm^{-1}) features from INS spectra across different catalysts and reaction conditions employed. Numbers marked with (*) are indicative of values obtained by Warringham.[94]

Time on stream (hours)	CO Hydrogenation: Reference hematite catalyst (Chapter 3)		CO Hydrogenation: Doubly promoted hematite catalysts (Chapter 5, Section 5.2)		CO Hydrogenation with CO_2 co-feed: Doubly promoted hematite catalyst (Chapter 5, Section 5.3)	
	Aliphatic (2932 cm^{-1})	Aromatic (3048 cm^{-1})	Aliphatic (2932 cm^{-1})	Aromatic (3048 cm^{-1})	Aliphatic (2932 cm^{-1})	Aromatic (3048 cm^{-1})
3	0.68*	4.25*	2.41	4.21	1.17	1.31
6	3.01*	8.93*	3.06	8.46	2.91	11.02
12	3.56*	10.45*	4.57	8.43	6.52	28.39
24	3.81*	15.74*	3.68	9.58	22.71	115.94
48	2.21	9.94	-	-	-	-
96	3.09	22.24	-	-	-	-
240	4.26	31.91	-	-	-	-

The deformation region of the spectra (400 – 1600 cm^{-1}), recorded at 250 meV (**Figure 68**), highlights various bands that have been discussed in previous chapters. Interestingly the bands at 591 and 941 cm^{-1}, assigned to features of magnetite, are present for the sample exposed to 3 h on stream as well as 6 h on stream. From previous measurements, of this catalyst (**Section 5.2**) and of the reference material (**Fe-ref, Chapter 3, Section 3.3.1**), these features have only been observed at 3 h on stream, after which the emergence of the other aromatic deformation bands form. This would suggest that the addition of this co-feed is further impeding the reduction process of the catalyst towards the active phase by limiting the hydrogen supply within the system, correlating with the reduction of the hydrogen content of the sp^3 and sp^2 band formation in the initial stages of the reaction. The increase in time on stream to 12 and 24 h displays bands previously observed in the deformation region of other iron FT catalysts tested and are summarised in **Table 14**.[94,95,105] It is noted that the intensity of these features for the 24 h sample are much greater than any previously observed INS measurements of iron-based FTS catalysts, including the **Fe-ref** sample exposed to 240 h on stream (**Chapter 3, Section 3.3.1., Figure 27**).

As this is a preliminary measurement, at this time it is difficult to propose precisely the cause of this unexpected result with the limited reaction testing and catalyst characterisation for this preliminary measurement. A possible explanation could be the phenomenon of a kinetic discontinuity proposed by Moyes *et al*.[142] Moyes examined the hydrogenation of ethyne over palladium catalysts and observed that the initial rates of hydrogenation increased upon increasing ethyne pressure at a given temperature. However, this rate dropped sharply upon reaching a particular pressure after which, the rate slowly declined. Moyes proposed that below this discontinuity the ethyne molecules are not strongly adsorbed on the catalyst surface but on passing to the higher pressure side of the discontinuity, the ethyne molecules are more strongly adsorbed. This in turn, reduces the surface coverage of hydrogen leading to a lower rate of hydrogenation.

A similar result was also observed by Lennon *et al*., which involved an investigation of hydrogen concentration of a propyne hydrogenation reaction.[143] Lennon and co-workers observed that the rate of propyne hydrogenation was critically dependent on the supply of hydrogen. At low hydrogen concentration (hydrogen: propyne, < 6:1), propyne conversion to propane was below 7%, however, upon increasing the hydrogen: propyne ratio to 7:1, the conversion rapidly increased to 100%. It is suggested that the initial low rate of reaction is due to the fact that surface hydrogen is limited, favouring selectivity to propene over propane.[143] A similar result is observed here in the initial stages of reaction, *i.e.* 0 - 6 h on stream. Through a combination of the RWGS reaction (*Equation 5.3*) and FTS (*Equation 5.4*), the system will be deficient in hydrogen, slowing the reduction process and formation of the active phase, the iron carbide, and in turn preventing the formation of the hydrocarbonaceous overlayer. However, referring back to the propyne reaction investigated by Lennon *et al*., the rapid increase in conversion to 100% occurred as the hydrogen concentration reached a specific level *i.e.* > 7:1, and is thought to occur as a result of the hydrogenation of some of the hydrocarbonaceous overlayer which would lead to an increased availability of active sites to facilitate hydrogen adsorption and dissociation.[143] Relating the propyne study to that observed here for reactions > 6 h, it is possible a similar observation is occurring *i.e*. the hydrogenation of the hydrocarbonaceous overlayer and/or surface Na_2S species, due to the increase in hydrogen concentration (H_2:CO:CO_2, 6:1.5:1) in relation to previously utilised CO hydrogenation condition (H_2:CO:CO_2, 2:1:0) therefore, leading to increased number of sites available for H_2 dissociation and adsorption and so an increase in surface hydrogen supply at the catalyst surface. The increased levels of adsorbed hydrogen, as well as possible increased levels of adsorbed carbon, may therefore result in an increased production of the hydrocarbonaceous

overlayer in relation to previous INS measurements as observed in **Chapter 3, 4** and **Chapter 5, Section 5.2**.

This was quite a dramatic outcome that was not expected and, at this period in time is not fully understood. Reaction testing beyond 12 h (**Figure 65**) as well as elemental analysis would be helpful here but, unfortunately, research time was consumed. It may well be possible that the inclusion of promoters is further complicating the situation. However, as the inclusion of a CO_2 co-feed is of real industrial relevance, this unanticipated outcome needs following up and, potentially, it may be more suitable to test **Fe-ref** with a CO_2 co-feed in the first instance.

Table 14: Bands observed in the INS spectra of the Fe-Na-S_{100} sample after exposure to CO hydrogenation conditions with the inclusion of a CO_2 co-feed, on the large-scale reactor (Figures 66 and 68) with vibrational assignments.

Feature Observed in INS Spectra (cm^{-1})	**Vibrational Assignment**
591	Fe-O phonon mode of Fe_3O_4
807	Out of plane δ(C-H)
871	Out of plane δ(C-H)
941	O-H in plane deformation/ Alkenic δ(C-H)
953	Alkenic δ(C-H)
1160	In-plane δ(C-H)
1389	In-plane C-C ring deformation
1451	Semi-circle ring C-C deformation
2932	Aliphatic υ(C-H)
3048	Aromatic/olefinic υ(C-H)

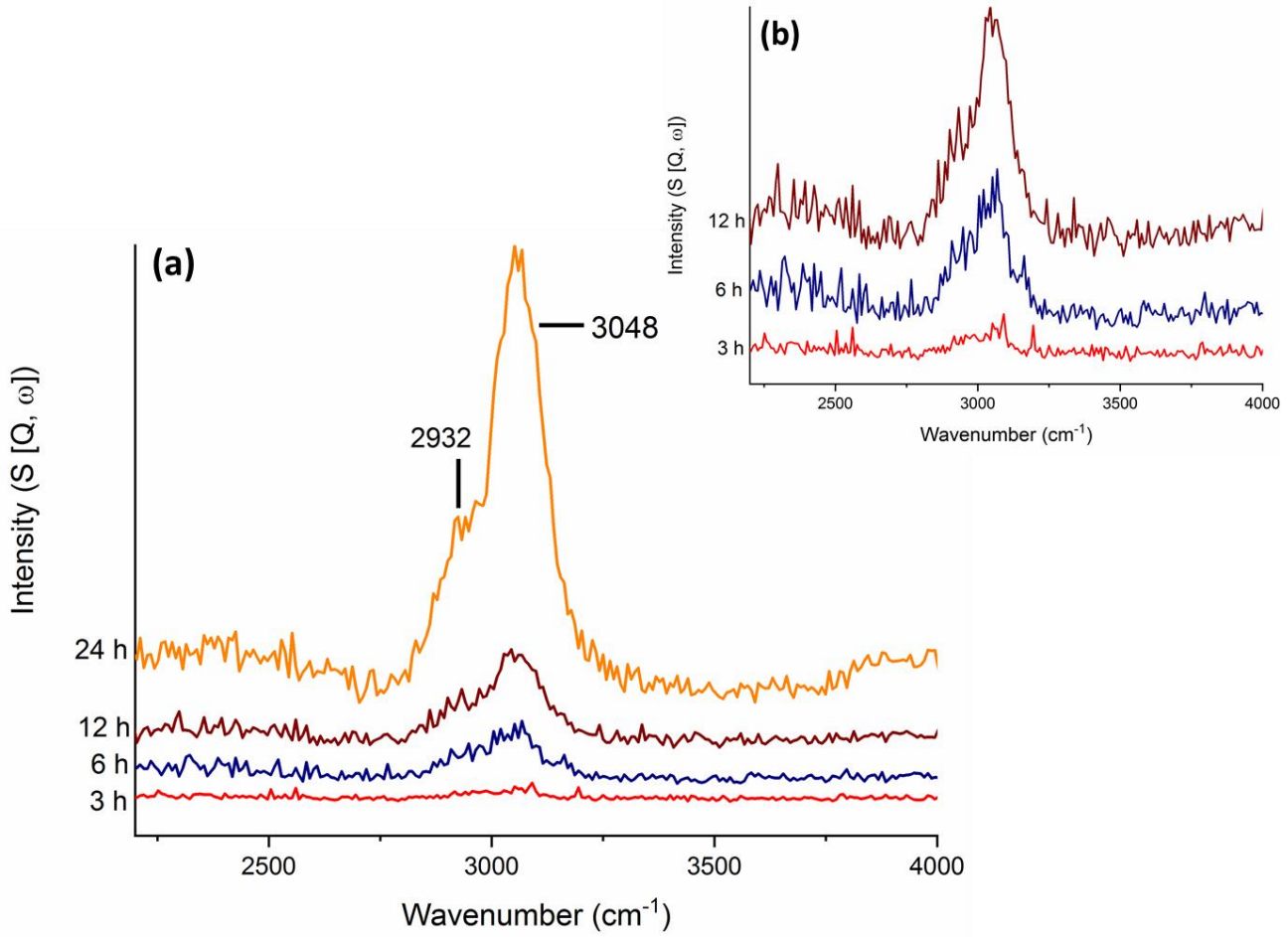

Figure 66: INS spectra (recorded at 650 meV) of the doubly promoted α-Fe_2O_3 (Fe-Na-S_{100}) after ambient pressure CO hydrogenation, with a CO_2 co-feed at 623 K in the large-scale reactor over 24 h period. (b) Enlarged INS spectra from (a) of samples exposed to ambient pressure CO hydrogenation conditions at 623 K between 3 and 12 h.

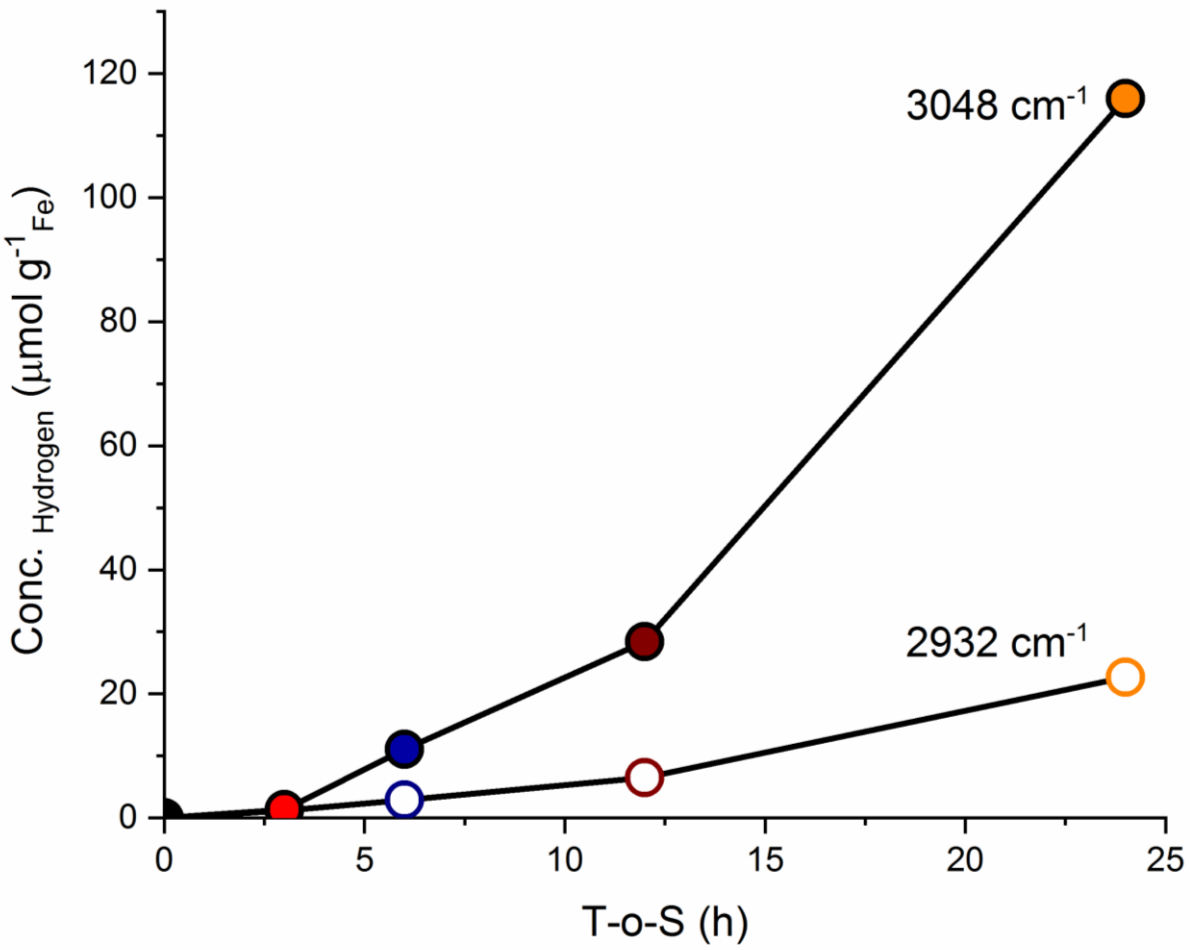

Figure 67: The quantified hydrogen content of the features identified in Figure 66: sp^3 hybridised carbon at 2932 cm^{-1} (hollow circles) and sp^2 hybridised carbon at 3948 cm^{-1} (solid circles) of Fe-Na-S_{100} after exposure to ambient pressure CO hydrogenation conditions at 623 K with the inclusion of a CO_2 co-feed.

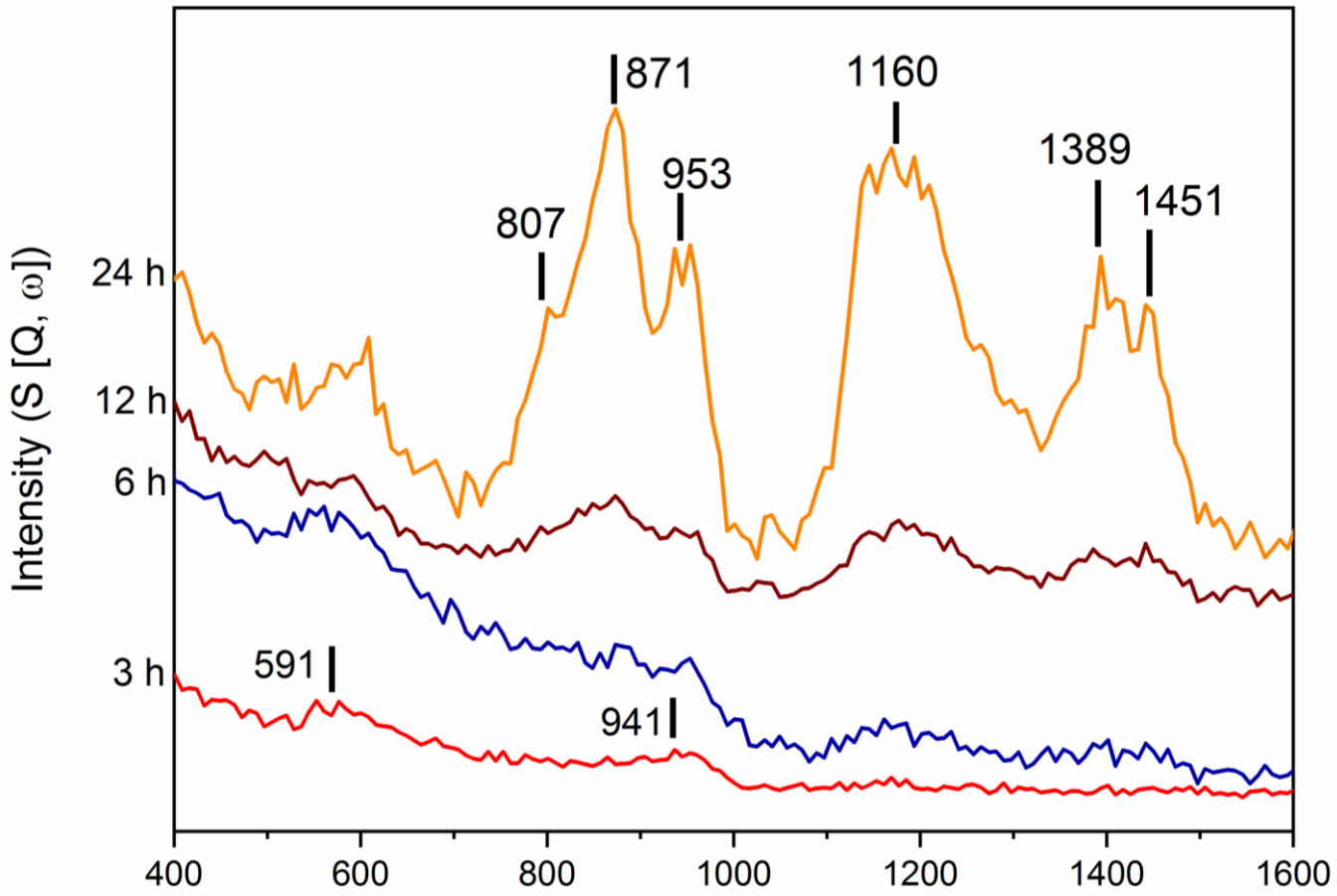

Figure 68: INS spectra (recorded at 250 meV) of the doubly promoted α-Fe_2O_3 sample (Fe-Na-S_{100}) after exposure to ambient pressure CO hydrogenation at 623 K, with a CO_2 co-feed, in the large-scale reactor over a 24 h period.

5.4. Proposed FTO Model

Figure 69 presents an adaptation to the model presented previously in **Chapter 3, Section 3.5** and is representative of a **Fe-Na-S_x** catalyst on exposure to CO hydrogenation conditions. As before, the role of the hydrocarbonaceous overlayer is to define the two proposed active sites on the iron carbide with site A responsible for dihydrogen adsorption and dissociation and site B for carbon monoxide adsorption and dissociation as well as the formation of hydrocarbon products. As discussed previously within **Chapter 4**, before reaction the promoters are suggested to be evenly distributed within the surface and bulk of the catalyst as highlighted by XRD (**Figure 39**), XPS (**Figure 42**) and XANES (**Figure 48**). Upon exposure to reaction conditions it is proposed that the sulfate species is progressively reduced to sulfide *i.e*. forms Na_2S. The Na_2S species then segregates to the surface that can be thought of as an external layer of iron carbide (Hägg carbide). In the absence of a cation, the sulfur at the surface can be hydrogenated to H_2S, which may then progressively desorb from the surface. A previous investigation by Xu *et al*., utilising XPS, indicated the formation of surface S^{2-} of FTO catalysts after exposure to reduction conditions and also noted a loss in the total sulfur surface area, suggesting that sulfur may be lost from the surface as H_2S.[65] Hence, sulfur doping alone is inefficient. However, the Na is able to 'lock' the sulfur at the catalyst surface where it is more resistant to hydrogenation and ultimately sulfur depletion.

With reference to **Figure 69 (a)** at short times (t_1), the partial capping of the Hägg carbide impedes formation of the hydrocarbonaceous overlayer, which delays the 'templating' process that creates the active sites. However, for extended reaction times (t_2), the Na_2S is partially hydrogenated away with sulfur leaving the surface as H_2S; under these conditions a confined hydrocarbonaceous overlayer is able to form (**Figure 69 (b)**). Here, the number of sites able to dissociatively adsorb hydrogen is diminished leading to a reduced hydrogen supply. This will further retard the formation of the hydrocarbonaceous overlayer. Now, with the catalyst effectively operating under hydrogen-lean regime, saturation is less favoured and the C-C bond propagation process is hindered, leading to shorter chain unsaturated products. By increasing the sulfur concentration within the catalyst this results in mass transport limitations of the hydrogen within the bulk of the system, and in turn hinders catalyst reduction towards iron carbides as well as hydrocarbonaceous overlayer formation. The inclusion of sodium within the catalyst increases the surface coverage of carbon as an effect of the Blyholder model, further reducing the surface coverage of hydrogen, and therefore suggesting an increased production of unsaturated hydrocarbons.[61]

At this time, the above conjecture is speculative and requires investigating via the design of further probing experiments. Nevertheless, it does provide a model for how doubly promoted Fe FTS catalysts can be modified to favour the formation of light olefins. An aspect of future work on this project would be to monitor H_2S formation during reaction testing of singly promoted iron-based FTO catalysts to test this hypothesis. It is therefore proposed that the alkali metal may be fulfilling two roles (i) promoting CO dissociation and/or (ii) holding the sulfur in place at the active sites resisting loss of sulfur via H_2S formation.

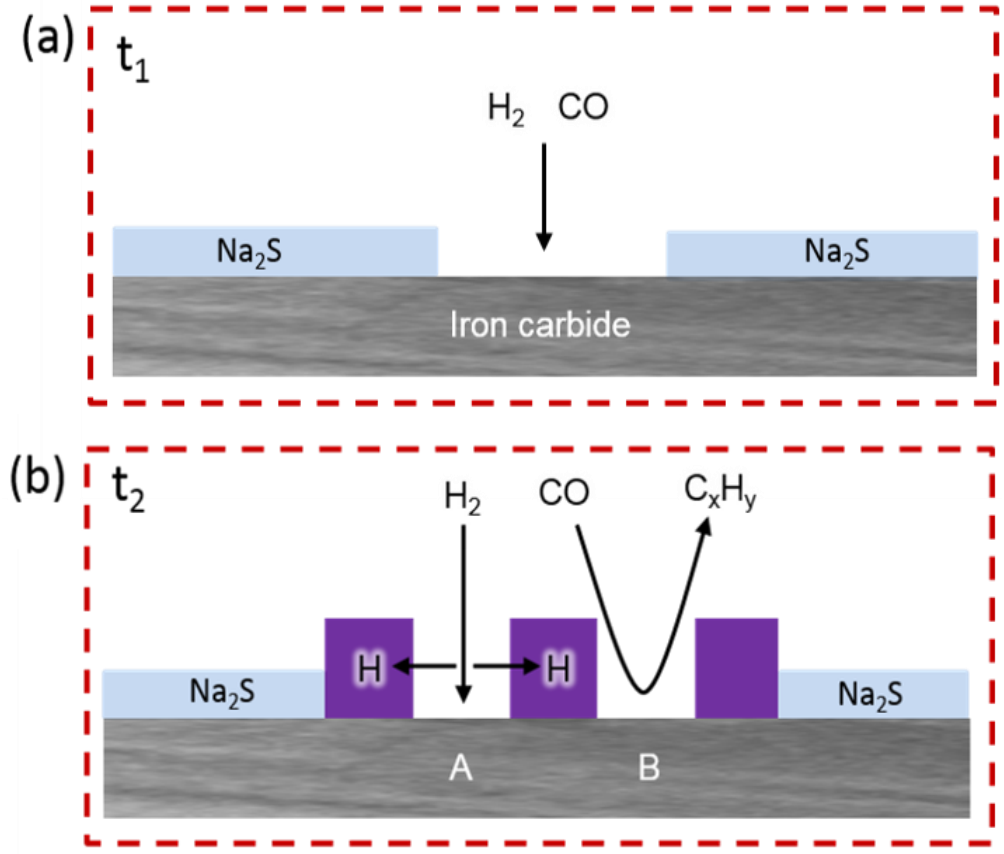

Figure 69: Adapted model from Warringham *et al*[94] to account for the addition of sulfur and sodium as promoters and their role in FTO chemistry, $t_2 > t_1$.

5.5. Conclusions

This chapter selected one of the doubly promoted catalyst samples from **Chapter 4**, **Fe-Na-S$_{100}$**, and examined it over a reaction period of 24 h. **Section 5.2**, made use of the applied ambient pressure CO hydrogenation conditions previously utilised in **Chapters 3** and **4** with post-reaction characterisation involving *in situ* TPO measurements and INS. The main results of this section of the chapter can be summarised as follows.

- *In situ* TPO measurements highlight the retention of the α species over the full 24 h period studied whereas *in situ* TPO measurements for **Fe-ref** only observed this feature up to approximately 6 h on stream.
- Over the 24 h period studied, the β component (amorphous carbon) displays significant growth whereas the γ feature (bulk iron carbides) for the doubly promoted sample displays a diminished response in relation to **Fe-ref**.
- The INS dataset of **Fe-Na-S$_{100}$** displays a reduced formation of aromatic/olefinic band (3048 cm^{-1}) in comparison to **Fe-ref**, whereas the aliphatic component (2932 cm^{-1}) displays little variation.
- The retention of the α species from the TPO measurements correlates with the reduced γ formation and the reduced aromatic component of the hydrocarbonaceous overlayer. It is therefore proposed that the α species may be seen as a precursor to the formation of either the β or γ components, with hydrogen lean environments (a result of the inclusion of promoters) resulting in an increased amorphous carbon production over iron carbides.
- Previously it was suggested that the γ component may be involved in the formation of the aromatic/olefinic component of the hydrocarbonaceous overlayer. Its reduced formation shown in the *in situ* TPO measurements correlates with the reduced aromatic feature in the INS dataset, supporting the assignment of γ feature being responsible for the formation of the aromatic component.

Section 5.3, also utilising **Fe-Na-S$_{100}$**, was a preliminary study which introduced a CO_2 co-feed to the reaction system in order to shift the WGS reaction towards the left-hand side, maximising carbon utilisation for hydrocarbon production rather than as a CO_2 by-product. The work carried out within this section would require further characterisation before any hard conclusions may be drawn from the current obtained data. The results obtained are

interesting, however, pose more questions than answers. Further work of this unanticipated outcome is required.

The main findings of this section can be summarised as follows:

- The large-scale reaction profile of **Fe-Na-S$_{100}$** after exposure to ambient pressure CO hydrogenation conditions with a CO_2 co-feed appears to leads to an increased methane production in comparison to previously studied catalysts without a CO_2 co-feed.
- The presence of the bands observed at 591 and 941 cm^{-1} in the deformation region of the INS spectra, associated with an under-reduced catalyst, are observed for a longer period of time-on-stream (6 h) in comparison to reactions carried out with the inclusion of CO_2 in the feed stream (3h). This suggests potential limitations of hydrogen within the system in the initial stages of reaction.
- The total hydrogen concentration of ν(C-H) region of the INS data by 24 h on stream is an order of magnitude higher than that observed at the same time on stream for the same catalyst observed in **Section 5.2**. However, following up of this outcome is required before any hard conclusions can be made.

The final section of this chapter, **Section 5.4.**, proposed a model to account for the role of the promoters within the catalyst sample suggesting that as time-on-stream is increased the sulfur species within the catalyst, Na_2SO_4 is reduced in a stepwise manner towards Na_2S. The Na_2S species impedes formation of the hydrocarbonaceous overlayer which otherwise, facilitates surface hydrogen supply. This induces hydrogen-lean conditions that favour unsaturation and impede C-C chain propagation so that the selectivity to light olefins is increased as is reported in the literature.

Chapter 6 – Concluding Remarks

Inelastic neutron scattering has been applied alongside other complementary analytical techniques such as temperature-programmed oxidation, X-ray diffraction, transmission electron microscopy and Raman spectroscopy, to firstly investigate a standard hematite catalyst, containing no structural promoters or support (**Fe-ref**), using a representative FTS reaction (ambient pressure CO hydrogenation (**Chapter 3**)). The aim of this investigation was to form a complete evolutionary profile of the reference catalyst by analysing it over an extended period of time on stream (0 - 240 h). The CO hydrogenation test data indicates *the full* system to be operating at a steady state at *ca.* 200 h on stream. From this data set (**Chapter 3**), the previously assigned precursor to the formation of the hydrocarbonaceous overlayer, the α peak from TPO measurements, appears to be, at this stage, more specifically assigned as a precursor to the aliphatic component in the INS measurements. However, it is also suggested as a potential precursor to the β and γ TPO features. On the other hand, correlation is observed between the saturation of the aromatic/olefinic feature of the INS data with the intensity profiles of the β and γ components from TPO measurements. However, observations from **Chapter 5** provide further refinement of these concepts. These considerations illustrate the dynamic nature of the evolutionary phase of iron-based FTS catalysts undergoing CO hydrogenation at elevated temperature. A model was developed to account for a role of the hydrocarbonaceous overlayer proposing it to 'template' the active sites on the iron carbide, depending highly on the supply of hydrogen within the system.

From this initial investigation of a standard reference iron catalyst (**Fe-ref**), the addition of promoters, sulfur and sodium, known to shift the product stream towards lower olefins, were added to investigate the potential effect they could have on the formation of the hydrocarbonaceous overlayer (**Chapter 4**). The inclusion of such promoters was shown to affect the reducibility of the catalyst and, consequently, hinder the hydrocarbonaceous overlayer formation upon increasing concentration of the sulfur component. By application of XANES, the sulfur species present in the catalyst is shown to progress through a reduction process on exposure to reaction conditions, highlighting the presence of a range of sulfur species including sulfate (S^{6+}), sulfite (S^{4+}) and sulfide (S^{2-}). From this, it was proposed that the formation of Na_2S may play a crucial role in the FTO chemistry.

Of the five catalysts tested within **Chapter 4**, one sample was selected, **Fe-Na-S$_{100}$**, as a potential prototype for FTO chemistry. This sample was further analysed as a function of

time on stream utilising ambient pressure CO hydrogenation conditions (**Chapter 5, Section 5.2**). *In situ* TPO measurements of this sample highlighted an extended retention period of the α component (precursor species) in comparison to the **Fe-ref** sample. In combination with the quantified hydrogen data obtained from the INS, it was proposed that this species is in fact a precursor to either the β or γ features and the formation of either species is highly dependent on the supply of hydrogen. Following from this, a previously proposed hypothesis from **Chapter 3**, that the formation of the aromatic component of the hydrocarbonaceous overlayer is dependent on the formation of bulk iron carbides (TPO γ peak) was confirmed.

The latter aspect of this project introduced CO_2 into the feed stream of a CO hydrogenation reaction, using a doubly promoted iron-based catalyst (**Chapter 5, Section 5.3**). The purpose of the addition of CO_2 was to promote the reverse WGS reaction enhancing the utilisation of carbon for hydrocarbon output; with the main aim here to gauge the effect it will have on the formation of the hydrocarbonaceous overlayer. Initially the inclusion of a CO_2 co-feed appeared to hinder the overlayer formation after which the rate of formation of the overlayer is significantly accelerated. By 24 h the total hydrogen concentration was an order of magnitude higher than that previously observed for other iron-based samples tested. Reaction testing (at pressure) and *ex situ* TPO measurements are required to provide further information on this preliminary investigation.

Finally, the model proposed in **Chapter 3** for FTS was further developed to account for FTO chemistry suggesting roles for sodium and sulfur within the catalyst and is presented in **Chapter 5**. This model suggested that initially upon addition of promoters to the catalyst, the sulfur species is evenly distributed throughout the bulk and surface of the catalyst as indicated by XPS, XRD and XANES. Upon exposure to reaction conditions, the sulfur species is reduced to form Na_2S, which migrates to the catalyst surface, initially impeding the hydrocarbonaceous overlayer formation by partially capping the surface of the Hägg carbide, delaying the 'templating' process that creates the active sites. With an increasing time on stream, the Na_2S is partially hydrogenated away as H_2S, allowing for a limited formation of the hydrocarbonaceous overlayer. Overall, the available sites for hydrogen adsorption are diminished creating a hydrogen-lean environment, favouring unsaturated short chain products. The inclusion of the sodium within the catalyst anchors the sulfur within the catalyst resisting loss through hydrogenation as H_2S. Further testing is required to test the validity of this hypothesis.

Chapter 7 – Future Work

Future work for this project could potentially take two routes. Firstly, a logical direction would be a continuation of the FTO based chemistry investigated in **Chapters 4** and **5**. This would involve optimising the S/Na concentrations required for increasing and maintaining a high selectivity towards lower olefins. Reaction testing (at pressure) would be key in order to have a better understanding of the influence these promoters may have on the product distribution. Furthermore, the preliminary study involving the addition of a CO_2 co-feed to the reaction and its effect it has on the formation of the hydrocarbonaceous overlayer needs further investigation as this is of real industrial relevance. Again, utilising reaction testing (at pressure) would be beneficial to test how the product distribution may be altered by this addition.

Secondly, the application of INS to investigate hydrogen spillover on cobalt FTS catalysts. Early investigations in this area have utilised Raney cobalt and supported cobalt catalysts, which have highlighted a substantial role of hydroxyl groups: Co-H surface chemistry. Moving forward, focus should be on the skeletal metal in the first instance.

Appendices

Covered within the Appendices is a description of various calculations utilised within this thesis including WHSV and FTY. Additional figures include the repeated INS calibration measurements on the MAPS spectrometer as a result of the upgrade of the spectrometer and also the peak fitting of the INS spectrum, detailed in **Chapter 5, Section 5.3.2.**, of the sample exposed to CO hydrogenation conditions with a CO_2 co-feed for 3 h on stream.

Weight Hourly Space Velocity (WHSV) Calculation

Values for WHSV were calculated from a rearrangement of the ideal gas law[79]:

$$n = \frac{PV}{RT} \qquad (\mathbf{A.1})$$

Where P = Pressure (1 bar)

V = Flow rate (L min^{-1})

R = Gas constant (8.314 x 10^{-2} L.bar.K^{-1}.mol^{-1})

T = 293 K

By completing *Equation A.1* for each of the gas flows yields a molar flow (mol.min^{-1}) which can then be converted to a mass flow (g.h^{-1}) to be used in *Equation A.2*. [144]

$$\text{Weight Hourly Space Velocity} = \frac{\text{Mass Flow (total)}}{\text{Mass of Catalyst}} \qquad (\mathbf{A.2})$$

Iron Time Yield (FTY) Calculation

$$\mathrm{FTY} = \frac{\text{moles CO}}{\text{g}_{\mathrm{Fe}}\text{in catalyst}}\ \mathrm{s}^{-1} \qquad (\mathbf{A.3})$$

Equation A.3[44] will result in the following units: (CO) g_{Fe}^{-1} s^{-1}.

Additional Figures

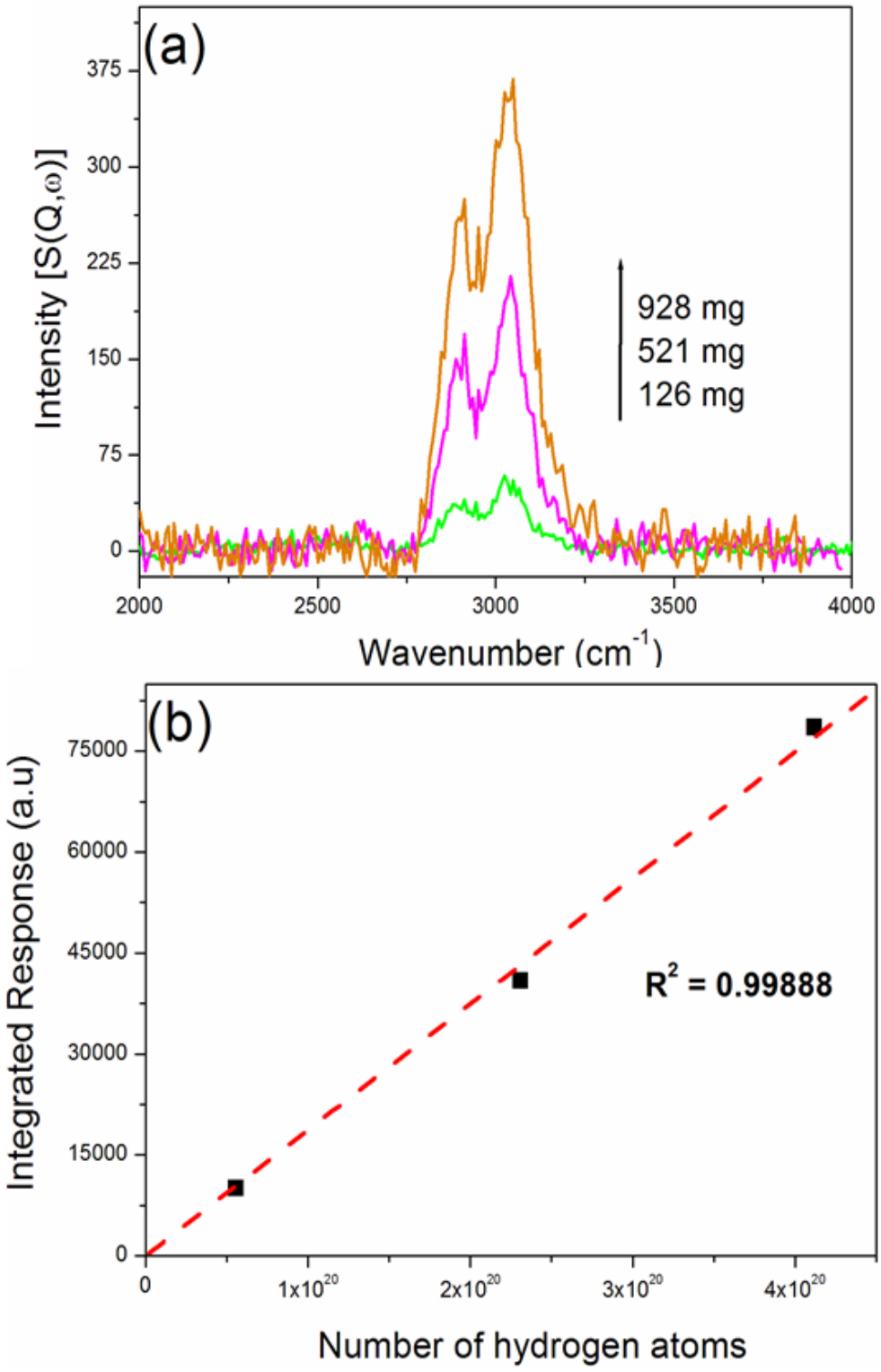

Figure 70(a) The baseline corrected INS spectra of the varying masses of polystyrene recorded on the MAPS spectrometer after the spectrometer upgrade at incident energy 650 meV. The spectra were obtained using the 'A' chopper package. (b) Linear plot ($y = 2 \times 10^{-16}x$) of the integrated areas of each of the polystyrene features ν (C-H) present in (a) against the number of hydrogen atoms present in each mass of polystyrene used. The R^2 value is 0.99888.

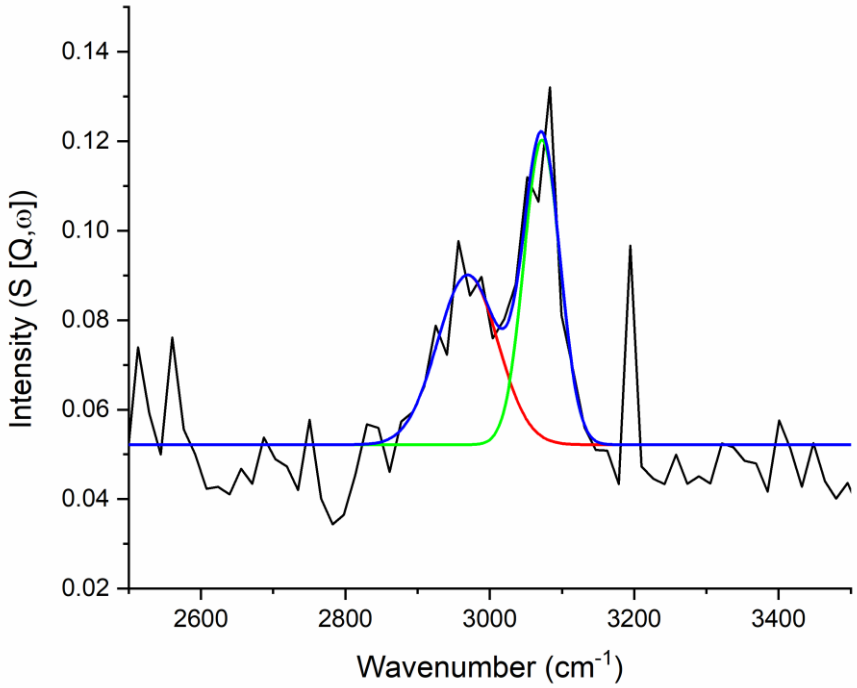

Figure 71: INS spectra (recorded at 650 meV) of the doubly promoted α-Fe_2O_3 after CO hydrogenation, with a CO_2 co-feed at 623 K in the large scale reactor over 3 h period. Peak fitting of the sp^3 and sp^2 hybridised carbon features is shown.

References

1 S. F. Parker (ISIS Instrument Scientist), *Personal Communication*, 2016.

2 J. van de Loosdrecht, F. G. Botes, I. M. Ciobica, A. Ferreira, P. Gibson, D. J. Moodley, A. M. Saib, J. L. Visagie, C. J. Westertrate and J. W. Niemanstsverdriet, *Comprehensive Inorganic II, Vol 7.*, Elsevier, Oxford, 2013.

3 P. Sabatier and J. B. Senderens, *C. R. Acad. Sci. Paris*, 1902, **134**, 514.

4 B. H. Davis, *Catal. Today*, 2002, **71**, 249–300.

5 J. L. Casci, C. M. Lok and M. D. Shannon, *Catal. Today*, 2009, **145**, 38–44.

6 P. M. Maitlis and A. de Klerk, *Greener Fischer-Tropsch Processes for Fuels and Feedstocks*, Wiley-VCH, 2013.

7 M. E. Dry, 2002, **71**, 227–241.

8 Q. Zhang, J. Kang and Y. Wang, *ChemCatChem*, 2010, **2**, 1030–1058.

9 H. Schulz, *Appl. Catal. A Gen.*, 1999, **186**, 3–12.

10 A. K. Dalai and B. H. Davis, *Appl. Catal. A Gen.*, 2008, **348**, 1–15.

11 D. B. Bukur, B. Todic and N. Elbashir, *Catal. Today*, 2016, **275**, 66–75.

12 A. P. Steynberg and M. Dry, Eds., *Fischer-Tropsch Technology*, Elsevier, First Edit., 2004.

13 D. B. Bukur, K. Okabe, M. P. Rosynek, C. Li, D. Wang, K. R. P. M. Rao and G. P. Huffman, *J. Catal.*, 1995, **155**, 353–365.

14 R. Guettel, U. Kunz and T. Turek, *Chem. Eng. Technol.*, 2008, **31**, 746–754.

15 H. Jahangiri, J. Bennett, P. Mahjoubi, K. Wilson and S. Gu, *Catal. Sci. Technol.*, 2014, **4**, 2210–2229.

16 A. de Klerk, *Fischer-Tropsch Refining*, Wiley-VCH, First Edit., 2011.

17 B. Y. F. Morales and B. M. Weckhuysen, in *Catalysis*, eds. J. J. Spivey and K. M. Dooley, Royal Society of Chemistry, Cambridge, 2006, vol. 19, pp. 1–40.

18 D. L. King, *J. Catal.*, 1978, **51**, 386–397.

19 V. V. Ordomsky, A. Y. Khodakov, B. Legras and C. Lancelot, *Catal. Sci. Technol.*, 2014, **4**, 2896–2899.

20 E. De Smit and B. M. Weckhuysen, *Chem. Soc. Rev.*, 2008, **37**, 2758–2781.

21 C. Perego, R. Bortolo and R. Zennaro, *Catal. Today*, 2009, **142**, 9–16.

22 M. D. Shroff, D. S. Kalakkad, K. E. Coulter, S. D. Kohler, M. S. Harrington, N. B. Jackson, A. G. Sault and A. K. Datye, *J. Catal.*, 1995, **156**, 185–207.

23 W. Ning, N. Koizumi, H. Chang, T. Mochizuki, T. Itoh and M. Yamada, *Appl. Catal. A Gen.*, 2006, **312**, 35–44.

24 E. de Smit, F. Cinquini, A. M. Beale, O. V Safonova, W. van Beek, P. Sautet and B. M. Weckhuysen, *J. Am. Chem. Soc.*, 2010, **132**, 14928–14941.

25 J. W. Niemantsverdriet, A. M. van der Kraan, W. L. van Dijk and H. S. van der Baan, *J. Phys. Chem.*, 1980, **84**, 3363–3370.

26 J. Zhang, M. Abbas and J. Chen, *Catal. Sci. Technol.*, 2017, **7**, 3626–3636.

27 M. D. Shroff and A. K. Datye, *Catal. Letters*, 1996, **37**, 101–106.

28 J. B. Butt, *Catal. Letters*, 1990, **7**, 61–81.

29 F. Blanchard, J. P. Reymond, B. Pommier and S. J. Teichner, *J. Mol. Catal.*, 1982, **17**, 171–181.

30 J. P. Reymond, P. Mbriaudeau and S. J. Teichner, *J. Catal.*, 1982, **75**, 39–48.

31 C. S. Kuivila, P. Stair and J. B. Butt, *J. Catal.*, 1989, **118**, 299–311.

32 S. Li, G. D. Meitzner and E. Iglesia, *J. Phys. Chem. B*, 2001, **105**, 5743–5750.

33 M. Ding, Y. Yanga, B. Wu, J. Xua, C. Zhang, H. Xiang and Y. Li, *J. Mol. Catal. A Chem.*, 2009, **303**, 65–71.

34 A. K. Datye, Y. Jin, L. Mansker, R. T. Motjope and T. H. Dlamini, *Stud. Surf. Sci. Catal.*, 2000, **130**, 1139–1144.

35 T. R. Motjope, H. T. Dlamini, G. R. Hearne and N. J. Coville, *Catal. Today*, 2002, **71**, 335–341.

36 J. M. Gracia, F. F. Prinsloo and J. W. Niemantsverdriet, *Catal. Letters*, 2009, **133**, 257–261.

37 Q. Chang, C. Zhang, C. Liu, Y. Wei, A. V. Cheruvathur, A. I. Dugulan, J. W. Niemantsverdriet, X. Liu, Y. He, M. Qing, L. Zheng, Y. Yun, Y. Yang and Y. Li, *ACS Catal.*, 2018, **8**, 3304–3316.

38 S. J. Thomson and G. Webb, *J. Chem. Soc. Chem. Commun.*, 1976, 526–527.

39 G. Webb, *Catal. Today*, 1990, **7**, 139–155.

40 S. D. Jackson, B. J. Brandreth and D. Winstanley, *J. Catal.*, 1987, **106**, 464–470.

41 S. M. Davis, F. Zaera and G. A. Somorjai, *J. Catal.*, 1982, **77**, 439–459.

42 A. Borodziński, *Catal. Letters*, 1999, **63**, 35–42.

43 A. Borodziński and A. Cybulski, *Appl. Catal. A Gen.*, 2000, **198**, 51–66.

44 H. M. Torres Galvis, A. C. J. Koeken, J. H. Bitter, T. Davidian, M. Ruitenbeek, A. I. Dugulan and K. P. De Jong, *Catal. Today*, 2013, **215**, 95–102.

45 Y. Yuan, S. Huang, H. Wang, Y. Wang, J. Wang, J. Lv, Z. Li and X. Ma, *ChemCatChem*, 2017, **9**, 3088–3089.

46 J. Schneider, M. Struve, U. Trommler, M. Schlüter, L. Seidel, S. Dietrich and S. Rönsch, *Fuel Process. Technol.*, 2018, **170**, 64–78.

47 I. Amghizar, L. A. Vandewalle, K. M. Van Geem and G. B. Marin, *Engineering*, 2017, **3**, 171–178.

48 H. M. Torres Galvis and K. P. De Jong, *ACS Catal.*, 2013, **3**, 2130–2149.

49 Y. Cheng, J. Lin, K. Xu, H. Wang, X. Yao, Y. Pei, S. Yan, M. Qiao and B. Zong, *ACS Catal.*, 2016, **6**, 389–399.

50 H. M. Torres Galvis, A. C. J. Koeken, J. H. Bitter, T. Davidian, M. Ruitenbeek, A. I. Dugulan and K. P. de Jong, *J. Catal.*, 2013, **303**, 22–30.

51 X. Chen, D. Deng, X. Pan and X. Bao, *Chinese J. Catal.*, 2015, **36**, 1631–1637.

52 F. Jiao, J. Li, X. Pan, J. Xiao, H. Li, H. Ma, M. Wei, Y. Pan, Z. Zhou, M. Li, S. Miao, J. Li, Y. Zhu, D. Xiao, T. He, J. Yang, F. Qi, Q. Fu and X. Bao, *Science*, 2016, **351**, 1065–1068.

53 H. M. T. Galvis, J. H. Bitter, C. B. Khare, M. Ruitenbeek, A. I. Dugulan and K. P. De Jong, *Science*, 2012, **335**, 835–838.

54 P. Zhai, C. Xu, R. Gao, X. Liu, M. Li, W. Li, X. Fu, C. Jia, J. Xie, M. Zhao, X. Wang, Y.-W. Li, Q. Zhang, X.-D. Wen and D. Ma, *Angew. Chemie Int. Ed.*, 2016, **55**, 9902–9907.

55 S. Li, A. Li, S. Krishnamoorthy and E. Iglesia, *Effects of Zn, Cu, and K promoters on the structure and on the reduction, carburization, and catalytic behavior of iron-based Fischer-Tropsch synthesis catalysts*, 2001, vol. 77.

56 M. Saglam, *Ind. Eng. Chem. Res.*, 1989, **28**, 150–154.

57 Y. Liu, B.-T. Teng, X.-H. Guo, Y. Li, J. Chang, L. Tian, X. Hao, Y. Wang, H.-W. Xiang, Y.-Y. Xu and Y.-W. Li, *J. Mol. Catal. A Chem.*, 2007, **272**, 182–190.

58 B. Chen, X. Zhang, W. Chen, D. Wang, N. Song, G. Qian, X. Duan, J. Yang, D. Chen, W. Yuan and X. Zhou, *Ind. Eng. Chem. Res.*, 2018, **57**, 11554–11560.

59 J. Xie, J. Yang, A. I. Dugulan, A. Holmen, D. Chen, K. P. De Jong and M. J. Louwerse, *ACS Catal.*, 2016, **6**, 3147–3157.

60 H. Arakawa and A. T. Bell, *Ind. Eng. Chem. Process Des. Dev.*, 1983, **22**, 97–103.

61 M. C. Ribeiro, G. Jacobs, B. H. Davis, D. C. Cronauer, A. J. Kropf and C. L. Marshall, *J. Phys. Chem. C*, 2010, **114**, 7895–7903.

62 M. E. Dry and J. C. Hoogendoorn, *Catal. Rev. Eng.*, 1981, **23**, 265–278.

63 C. H. Bartholomew and R. M. Bowman, *Appl. Catal.*, 1985, **15**, 59–67.

64 T. C. Bromfield and N. J. Coville, *Appl. Catal. A Gen.*, 1999, **186**, 297–307.

65 J. D. Xu, Z. Y. Chang, K. T. Zhu, X. F. Weng, W. Z. Weng, Y. P. Zheng, C. J. Huang and H. L. Wan, *Appl. Catal. A Gen.*, 2016, **514**, 103-113

66 R. Warringham, D. Bellaire, S. F. Parker, J. Taylor, R. A. Ewings, C. M. Goodway, M. Kibble, S. R. Wakefield, M. Jura, M. P. Dudman, R. P. Tooze, P. B. Webb and D. Lennon, *J. Phys. Conf. Ser.*, 2014, **554**, 012005

67 P. W. Albers and S. F. Parker, *Adv. Catal.*, 2007, **51**, 99–132.

68 P. C. H. Mitchell and J. Tomkinson, *Catal. Today*, 1991, **9**, 227–235.

69 S. F. Parker, D. Lennon and P. W. Albers, *Appl. Spectrosc.*, 2011, **65**, 1325–1341.

70 P. C. H. Mitchell, S. F. Parker, A. J. Ramirez-Cuesta and J. Tomkinson, *Vibrational Spectroscopy with Neutrons With Applications in Chemistry, Biology, Materials Science and Catalysis*, World Scientific, Singapore, 2005.

71 S. F. Parker, A. J. Ramirez-Cuesta and L. Daemen, *Spectrochim. Acta - Part A Mol. Biomol. Spectrosc.*, 2018, **190**, 518–523.

72 http://www.isis.stfc.ac.uk. Accessed March 2019.

73 R. Warringham, PhD thesis, *An investiagtion of iron-based Fischer-Tropsch catalysts using inelastic neutron scattering*, University of Glasgow, 2015.

74 N. G. Hamilton, PhD thesis, *The application of inelastic neutron scattering to the investiagtion of industrial heterogeneous catalysts*, University of Glasgow, 2010.

75 T. Herranz, S. Rojas, F. J. Pérez-Alonso, M. Ojeda, P. Terreros and J. L. G. Fierro, *J. Catal.*, 2006, **243**, 199–211.

76 N. G. Hamilton, I. P. Silverwood, R. Warringham, J. Kapitán, L. Hecht, P. B. Webb, R. P. Tooze, S. F. Parker and D. Lennon, *Angew. Chemie - Int. Ed.*, 2013, **52**, 5608–5611.

77 P. W. Albers, D. Lennon and S. F. Parker, in *Neutron Scattering - Applications in Biology, Chemistry and Material Science*, 2017, vol. 49, pp. 279-348

78 S. F. Parker, A. J. Ramirez-Cuesta, P. W. Albers and D. Lennon, *J. Phys. Conf. Ser.*, 2014, **554**, 012004.

79 P. Atkins and J. de Paula, *Atkins' Physical Chemistry*, Oxford University Press, 9th edn., 2010.

80 F. Tuinstra and J. L. Koenig, *J. Chem. Phys.*, 1970, **53**, 1126–1130.

81 A. Sadezky, H. Muckenhuber, H. Grothe, R. Niessner and U. Pöschl, *Carbon N. Y.*, 2005, **43**, 1731–1742.

82 M. A. Pimenta, G. Dresselhaus, M. S. Dresselhaus, L. G. Cançado, A. Jorio and R. Saito, *Phys. Chem. Chem. Phys.*, 2007, **9**, 1276–1291.

83 Y. Wang, D. C. Alsmeyer and R. L. McCreery, *Chem. Mater.*, 1990, **2**, 557–563.

84 P. W. Atkins and D. F. Shriver, *Shriver & Atkins' Inorganic Chemistry*, Oxford University Press, Oxford, 5th edn., 2010.

85 A. L. Patterson, *Phys. Rev.*, 1939, **56**, 978–982.

86 J. S. J. Hargreaves, *Catal. Struct. React.*, 2016, **2**, 33–37.

87 J. S. J. Hargreaves, *Crystallogr. Rev.*, 2005, **11**, 21–34.

88 J. I. Langford and A. J. C. Wilson, *J. Appl. Crystallogr.*, 1978, **11**, 102–113.

89 J. D. Grunwaldt and A. Baiker, *Phys. Chem. Chem. Phys.*, 2005, **7**, 3526–3539.

90 G. Bunker, *Introduction to XAFS: A Practical Guide to X-ray Absorption Fine Structure Spectroscopy*, Cambridge University Press, 2010.

91 J. Evans, *X-ray Absorption Spectroscopy for the Chemical and Materials Sciences*, John Wiley & Sons, 2017.

92 R. C. Nelson and J. T. Miller, *Catal. Sci. Technol.*, 2012, **2**, 461–470.

93 M. Newville, *Rev. Mineral. Geochemistry*, 2014, **78**, 33–74.

94 R. Warringham, A. L. Davidson, P. B. Webb, R. P. Tooze, R. A. Ewings, S. F. Parker and D. Lennon, *RSC Adv.*, 2019, **9**, 2608–2617.

95 R. Warringham, A. L. Davidson, P. B. Webb, R. P. Tooze, S. F. Parker and D. Lennon, *Catal. Today*, 2020, **339**, 32–39

96 I. P. Silverwood, N. G. Hamilton, A. McFarlane, R. M. Ormerod, T. Guidi, J. Bones, M. P. Dudman, C. M. Goodway, M. Kibble, S. F. Parker and D. Lennon, *Rev. Sci. Instrum.*, 2011, **82**, 034101.

97 G. F. Botes, T. C. Bromfield, R. L. J. Coetzer, R. Crous, P. Gibson and A. C. Ferreira, *Catal. Today*, 2016, **275**, 40–48.

98 M. E. Dry, *Appl. Catal. A Gen.*, 1996, **138**, 319–344.

99 H. F. Coward and G. W. Jones, *Limits of Flammability of Gases and Vapours*, Bulletin 503, US Bureau of Mines, Washington D.C., 1952.

100 I. P. Silverwood, N. G. Hamilton, C. J. Laycock, J. Z. Staniforth, R. M. Ormerod, C. D. Frost, S. F. Parker and D. Lennon, *Phys. Chem. Chem. Phys.*, 2010, **12**, 3102–3107.

101 F. J. Pérez-Alonso, T. Herranz, S. Rojas, M. Ojeda, M. López Granados, P. Terreros, J. L. G. Fierro, M. Gracia and J. R. Gancedo, *Green Chem.*, 2007, **9**, 663–670.

102 D. B. Bukur, L. Nowicki and S. A. Patel, *Can. J. Chem. Eng.*, 1996, **74**, 399–404.

103 N. G. Hamilton, R. Warringham, I. P. Silverwood, J. Kapitán, L. Hecht, P. B. Webb, R. P. Tooze, W. Zhou, C. D. Frost, S. F. Parker and D. Lennon, *J. Catal.*, 2014, **312**, 221–231.

104 R. Warringham, N. G. Hamilton, I. P. Silverwood, C. How, P. B. Webb, R. P. Tooze, W. Zhou, C. D. Frost, S. F. Parker and D. Lennon, *Appl. Catal. A Gen.*, 2015, **489**, 209–217.

105 R. Warringham, A. R. Mcfarlane, D. A. Maclaren, P. B. Webb, R. P. Tooze, J. Taylor, R. A. Ewings, S. F. Parker and D. Lennon, *J. Chem. Phys*, 2015, **143**, 174703.

106 The HighScore suite, T. Degen, M. Sadki, E. Bron, U. Konig, G. Nenert; Powder Diffraction/Volume 29/ Supplement S2/ December 2014, pp S13-S18106 G. E. Batley, A. Ekstrom and D. A. Johnson, *J. Catal.*, 1974, **34**, 368–375.

107 G. E. Batley, A. Ekstrom and D. A. Johnson, *J. Catal.*, 1974, **34**, 368–375.

108 W. K. Jozwiak, E. Kaczmarek, T. P. Maniecki, W. Ignaczak and W. Maniukiewicz, *Appl. Catal. A Gen.*, 2007, **326**, 17–27.

109 G. K. Reddy, K. Gunasekara, P. Boolchand and P. G. Smirniotis, *J. Phys. Chem. C*, 2011, **115**, 920–930.

110 F. J. Perez-Alonso, I. Melián-Cabrera, M. López Granados, F. Kapteijn and J. L. G. Fierro, *J. Catal.*, 2006, **239**, 340–346.

111 G. Munteanu, L. Ilieva and D. Andreeva, *Thermochim. Acta*, 1997, **291**, 171–177.

112 A. J. H. M. Kock, H. M. Fortuin and J. W. Geus, *J. Catal.*, 1985, **96**, 261–275.

113 S. Das and M. J. Hendry, *Chem. Geol.*, 2011, **290**, 101–108.

114 D. L. A. de Faria and F. N. Lopes, *Vib. Spectrosc.*, 2007, **45**, 117–121.

115 I. Chamritski and G. Burns, *J. Phys. Chem. B*, 2005, **109**, 4965–4968.

116 D. L. A. de Faria, S. Venâncio Silva and M. T. de Oliveira, *J. Raman Spectrosc.*, 1997, **28**, 873–878.

117 Joint Committee on Powder Diffraction Standard Card number 86-0550.

118 P. W. Albers, J. Pietsch, J. Krauter and S. F. Parker, *Phys. Chem. Chem. Phys.*, 2003, **5**, 1941–1949.

119 D. Lin-Vien, N. B. Colthup, W. G. Fateley and J. G. Graselli, *The handbook of infrared and Raman characteristic frequencies of organic molecules*, Academic Press, Boston, 1991.

120 *Sasol Technical Report*, 2016.

121 P. C. Thüne, C. J. Weststrate, P. Moodley, A. M. Saib, J. Van De Loosdrecht, J. T. Miller and J. W. Niemantsverdriet, *Catal. Sci. Technol.*, 2011, **1**, 689–697.

122 Joint Committee on Powder Diffraction Standard Card number 36-1248.

123 J. Galuszka, T. Sang and J. A. Sawicki, *J. Catal.*, 1992, **136**, 96–109.

124 J. Xu and C. H. Bartholomew, *J. Phys. Chem. B*, 2005, **109**, 2392–2403.

125 E. Kawasaki, J. Sanscrainte and T. J. Walsh, 1962, 48–52.

126 D. B. Bukur and R. F. Brown, *Can. J. Chem. Eng.*, 1994, **49**, 4615–4625.

127 J. W. Niemantsverdriet and A. M. van der Kraan, *J. Catal.*, 1981, **72**, 385–388.

128 G. Blyholder, *J. Phys. Chem.*, 1964, 2772–2777.

129 J. A. Kritzinger, *Catal. Today*, 2002, **71**, 307–318.

130 D. A. MacLaren (Senior Lecturer, Physics & Astronomy, University of Glasgow), *Personal Communication*, 2019.

131 B. Debret, M. Andreani, A. Delacour, S. Rouméjon, N. Trcera, E. (Edinburgh I. M. Facility) and H. Williams, *Earth Planet. Sci. Lett.*, 2017, **466**, 1–11.

132 F. Farges, P. Lens, M. Lenz, S. Rossano, J. Labanowski, A.-M. Flank, E. van Hullebusch and P. Lagarde, *J. Phys. Conf. Ser.*, 2009, **190**, 012184.

133 J. E. Penner-Hahn, in *Comprehensive Coordination Chemistry II, Volume 2*, eds. J. A. MCCleverty and T. J. Meyer, Elsevier Ltd., 2nd ed., 2003, pp. 159–186.

134 M. Perdjon-Abel, PhD thesis, *The role of addetives in Fischer-Tropsch reactions*, University of Southampton, 2011.

135 S. F. Parker, S. M. Bennington, A. J. Ramirez-Cuesta, G. Auffermann, W. Bronger, H. Herman, K. P. J. Williams and T. Smith, *J. Am. Chem. Soc.*, 2003, **125**, 11656–11661.

136 A. R. McInroy, D. T. Lundie, J. M. Winfield, C. C. Dudman, P. Jones, S. F. Parker, J. W. Taylor and D. Lennon, *Phys. Chem. Chem. Phys.*, 2005, **7**, 3093–3101.

137 S. L. Soled, E. Iglesia, S. Miseo, B. A. DeRites and R. A. Fiato, *Top. Catal.*, 1995, **2**, 193–205.

138 Y. Liu, C. H. Zhang, Y. Wang, Y. Li, X. Hao, L. Bai, H. W. Xiang, Y. Y. Xu, B. Zhong and Y. W. Li, *Fuel Process. Technol.*, 2008, **89**, 234–241.

139 B. Liang, H. Duan, T. Sun, J. Ma, X. Liu, J. Xu, X. Su, Y. Huang and T. Zhang, *ACS Sustain. Chem. Eng.*, 2019, **7**, 925–932.

140 *Personal Communication*, Drochaid Research Services, October 2018.

141 F. Jiang, B. Liu, S. Geng, Y. Xu and X. Liu, *Catal. Sci. Technol.*, 2018, **8**, 4097–4107.

142 R. B. Moyes, D. W. Walker, P. B. Wells and D. A. Whan, 1989, **55**, 5–8.

143 D. Lennon, R. Marshall, G. Webb and S. D. Jackson, in *Studies in Surface Science and Catalysis*, eds. A. Corma, F. V Melo, S. Mendioroz and J. L. G. Fierro, Elsevier B.V., 2000, vol. 130, pp. 245–250.

144 C. H. Bartholomew and R. J. Farrauto, *Fundamentals of Industrial Catalytic Processes*, Wiley, New Jersey, 2006.